UNIVERSITY OF SOUTHAMPTON

FACULTY OF PHYSICAL SCIENCES AND ENGINEERING

School of Electronics and Computer Science

Microfluidic Airway On-chip

Volume 1 of 1

by

Riccardo Reale

Thesis for the degree of Doctor of Philosophy

08/2017

UNIVERSITY OF SOUTHAMPTON

ABSTRACT

FACULTY OF PHYSICAL SCIENCES AND ENGINEERING

Electronics and Computer Science

Thesis for the degree of Doctor of Philosophy

MICROFLUIDIC AIRWAY ON-CHIP

by Riccardo Reale

Organs-on-chip are a new class of *in vitro* devices aimed at improving the predictivity of preclinical drug testing models by integrating physiologically relevant features in cell culture devices using microfabrication techniques. In human bodies, epithelial tissues are the first line of defence against the external environment and act as barriers by expressing inter-cellular protein complexes called tight junctions (TJ). The epithelial physical barrier has selective permeability properties which can experimentally be measured by electrical means. In this thesis, the design, simulation, modelling, optimisation, fabrication and experimental characterisation of a novel organ-on-chip device for epithelial cell culture and epithelial barrier monitoring are described. In the device, cells are cultured on top of a nanoporous support, fed by constant perfusion of growth medium and barrier properties are monitored in real-time with integrated coplanar Pt/Pt-black electrodes. Finite element method (FEM) simulations were used to develop a new coplanar electrode design which achieved greater sensitivity (45-fold) compared to the other coplanar designs presented in the literature. This design was formed by 2 circular segments electrodes divided by a polymeric septum. The high sensitivity of the novel electrode design enabled the measurement of epithelial electrical properties directly at the air-liquid interface (ALI) and was used to monitor disruptions in the barrier properties of primary bronchial epithelial cells (PBECs) cultured on commercial supports (Transwell®) induced by a calcium chelator (EGTA). The measured barrier disruption was comparable to those measured by standard systems without requiring a submerged culture. The microfluidic device was used to monitor the establishment of the physical barrier under submerged conditions for 6 days of the human bronchial epithelial cell line (16HBE14o-) and disruption of the physical barrier induced by stimulation with a viral mimic (poly(I:C)). All results were comparable to the ones measured by standard systems. This platform is an easy-to-manufacture alternative to available systems with the unique potential to enable the real-time epithelial barrier monitoring under submerged or ALI conditions.

Table of Contents

List of Figures

List of tables

Declaration of authorship

I, Riccardo Reale declare that this thesis and the work presented in it are my own and has been generated by me as the result of my own original research.

Microfluidic Airway On-Chip

I confirm that:

1. This work was done wholly or mainly while in candidature for a research degree at this University;
2. Where any part of this thesis has previously been submitted for a degree or any other qualification at this University or any other institution, this has been clearly stated;
3. Where I have consulted the published work of others, this is always clearly attributed;
4. Where I have quoted from the work of others, the source is always given. With the exception of such quotations, this thesis is entirely my own work;
5. I have acknowledged all main sources of help;
6. Where the thesis is based on work done by myself jointly with others, I have made clear exactly what was done by others and what I have contributed myself;
7. Parts of this work have been published as:

C. Blume, R. Reale, M. Held, T. M. Millar, J. E. Collins, D. E. Davies, H. Morgan and E. J. Swindle, "Temporal Monitoring of Differentiated Human Airway Epithelial Cells Using Microfluidics," PLoS ONE, vol. 10, no. 10, 2015.

C. Blume, R. Reale, M. Held, M. Loxham, T. M. Millar, J. E. Collins, E. J. Swindle, H. Morgan and D. E. Davies, "Cellular crosstalk between airway epithelial and endothelial cells regulates barrier functions during exposure to double-stranded RNA.," Immunity, Inflammation and Disease, 2017.

R. Reale, C. Blume, D. E. Davies, E. J. Swindle and H. Morgan, "A microfluidic platform for the culture and analysis of epithelia", International conference of microfluidics, nanofluidics and lab-on-a-chip, 2016 (oral presentation).

Signed: .....

Date: .....

Acknowledgements

First of all, I would like to thank my main supervisor, Prof. Hywel Morgan, for the possibility to undertake this Ph.D in the Southampton University. His guidance and constant high expectations kept me motivated during this period. Always fair and direct, he taught me the difference between a good and a bad work.

Secondly, I would like to thank my second supervisor, Dr. Emily J. Swindle, for the invaluable support and kindness during this time. Our scientific discussions will hardly be forgotten.

Moreover, I would like to thank Prof. Donna E. Davies for the useful discussions on biological aspects, and the technicians of the Brooke Lab, Dr. Natalie P. Smithers and Dr. Robert A. Ridley for their help in establishing primary cell cultures.
In the same way, I would like to thank the various technicians of the Southampton Nanofabrication centre, Miss. Katie Chamberlain, Mrs. Sarah Helps and Miss. Ying Tran, for the great amount of help, in particular with platinum deposition.

A special thank goes to Dr. Marie Held and Dr. Cornelia Blume who introduced me to the basics of experimental work and gave me important insights on how to approach research.

I thank all my lab mates, especially Josip, Roel, Anna, Carlos, Miguel and Catarina, always friendly, who never spared a laughter in the time of need.

Lastly and most importantly, my thought goes to Marta and to my family who helped me enduring these times. I know they suffered as much as I did for the distance between us.

List of Abbreviations

ALI	Air- Liquid Interface
ADME	Adsorption, Distribution, Metabolism and Elimination
APTES	3-Aminopropyltriethoxysilane
DIV-BBB	Dynamic *in vitro* Blood-Brain Barrier
ECIS	Electric cell-substrate impedance sensing
ECM	Extra-Cellular Matrix
EDTA	Ethylenediaminetetraacetic acid
EEC	Equivalent Electrical Circuit
EGFR	Epidermal Growth Factor Receptor
EGTA	Ethylene glycol-bis(β-aminoethyl ether)-N,N,N',N'-tetraacetic acid
EVOM	Epithelial Voltohmmeter
FEM	Finite Element Method
GPTES	3-Glycidoxypropyltriethoxysilane
JAM-A	Junctional Adhesion Molecule-A
µBBB	Microfluidic Blood-Brain Barrier
MDCK	Madin-Darby Canin Kidney
MEA	Microelectrode Array
OSTE	Off-stoichiometry thiol-ene
PBEC	Primary Bronchial Epithelial Cells
PDMS	Polydimethylsiloxane
PET	Polyethylene terephthalate
PMMA	Polymethyl methacrylate
Poly(I:C)	Polyinosinic-polycytidylic acid
PPy/PSS	Polypyrrole/poly(styrenesulphonate)
PTFE	Polytetrafluoroethylene
SD	Standard deviation
SE	Standard error
TER (TEER)	Trans-epithelial Electrical Resistance
Tg	Glass-Transition Temperature
TJ	Tight Junction
ZO – 1	Zonula Occludens-1
16HBE	Human Bronchial Epithelial Cell Line (16HBE14o-)

Chapter 1: Organ-on-a-chip for drug development

In the last 50 years, the R&D cost of developing a new drug has been increasing steadily [1], with estimated values of 231 million US$ in 1987 [2], of 802 million US$ in 2000 [3] and 1.8 billion US$ in 2010 [4]. Research and preclinical testing of a new candidate account for approximately a third of the total cost, while the clinical development accounts for the remaining two thirds [4]. Studies suggest that the increased cost of the clinical development stage in recent years is related to the type of drugs that are being developed. For example, drugs aimed at degenerative diseases require longer trials. At the same time, drugs aimed at obtaining better performances of already-existing ones, have smaller incremental benefits and require larger samples sizes to achieve statistical significance [5].

Another reason why the figures for the drug development costs are so high is the fact that for each successful candidate there are several unsuccessful ones that are accounted for in the total cost i.e. high rates of attrition. Attrition rates have substantial effects on the total costs especially in the clinical stage, where the average probability for a new drug candidate to reach the market is ≈11% [5]. One of the cause of high attrition rates at the clinical stage is the lack of good models at the preclinical stage: drugs that passed the preclinical stage are often found ineffective or with harmful side-effects during clinical trials. A way to reduce the overall process cost is to reduce the number of failures during the clinical stage by developing more predictive *in vitro* models during drug development pre-clinically. In this way the attrition is shifted from the expensive clinical stage to the faster, high-throughput preclinical stage [4].

Currently, models adopted in the preclinical stage consist of *in vivo* animal models and simple *in vitro* models. *In vivo* models use animals as complete representations of biological systems. One advantage of these models is that the effectiveness of drug candidates is regulated by absorption, distribution, metabolism and elimination (ADME) processes which are also relevant for the human physiology [6]. At the same time, due to their complexity, these models are not able to provide detailed information on underlying physiological mechanisms. Their experimentations are usually low-throughput, expensive, labour-intensive and are often burdened by ethical implications on animal use [7]. Additionally, it has recently been observed that preclinical findings obtained with animal models translate poorly to humans due to crucial genetic, molecular, immunologic and cellular differences [8, 9, 10]. Traditional 2D *in vitro* models focus on cultures in simple environments of immortalised cell lines or primary cells which are derived from patients. Their experimentation is high-throughput, but they fail to recapitulate the overall complexity of the *in vivo* physiological conditions (e.g. spatial orientation, cell-cell communication and cell-matrix interactions) and may lead to inaccurate results [11].

The study of asthma is particularly affected by the lack of appropriate models. Asthma is a medical condition of the conducting airways which leads to symptoms of coughing, wheezing, chest tightness and breathlessness. Symptoms can range from mild to severe with large variations among different patients. Individuals sometimes undergo a temporary significant worsening of the symptoms called exacerbations that can lead to life-threatening conditions which requires medical assistance. Only two new treatments targeting new drug pathways have made it into clinical practice over the past 50 years (anti-IgE, omalizumab, and a bronchodilator targeted at leukotriene receptors, montelukast)). Many drug candidates that passed the preclinical tests on animal models failed in the clinic because of safety or efficacy issues. Mice are the most commonly used animal models for asthma, but have substantial differences in lung structure and genetic background compared to humans which causes them fail to recapitulate the human disease [12, 13]. Current human *in vitro* models should be more predictive, but fail to recapitulate interactions between cells and their environment normally found *in vivo* [14].

A new class of devices called organs-on-chip has recently been developed in an attempt to fill the gap between traditional *in vitro* and *in vivo* models. These systems use the latest advancement in

microfabrication techniques to create complex features *in vitro*. Spatial, chemical, mechanical and biological stimuli are designed within these systems to emulate physiological conditions [15]. Cells cultured in these devices exhibit tissue-level properties that closely resembles the ones found *in vivo*. At the same time, these systems, are designed for highly parallelised applications, greatly increasing experimental throughput [16]. Compared to traditional investigation methodologies, these devices aim to obtain biological information that are more finely detailed and with higher throughput than the animal models and more realistic and reliable than the traditional *in vitro* studies [17].

1.1 The epithelial barrier

The epithelium is one of the most examined tissues in drug testing studies because it is the first barrier that the human body has against the external environment and drug candidates that require absorption through the skin, gastrointestinal (GI) tract or airways need to be able to pass through this barrier. These include orally administered drugs in the form of tablets for absorption through the GI tract and locally administered drugs e.g. inhaled drugs for absorption through the airway and drugs in creams and ointments for absorption through the skin. These drug candidates require absorption through the epithelium in order to reach their target and exert their pharmacological effect.

Epithelia line every cavity in the human body that interfaces the external (skin, gastrointestinal tract, airways) and internal (liver, kidney) environment. A schematic diagram of the epithelium is shown in Figure 1-1 [18]. The epithelial barrier is formed by closely packed cells connected to each other by intercellular protein complexes. Focal adhesions and hemi-desmosomes are macromolecular complexes (based on proteins of the integrins family) which fix the position of the cell by anchoring the actin filaments of the cytoskeleton to the extracellular matrix (ECM). Desmosomes and adherens junctions are complexes (based on the calcium-dependent cadherin protein) which form the initial connection between neighbouring cells by connecting the actin filaments of each cells cytoskeleton [19, 20]. Gap junctions are complexes that allow the exchange of molecules between adjacent cells, while tight junctions (TJ) regulate the communication between the inner part of the tissue and the external environment and regulate the permeability of the epithelial barrier [21].

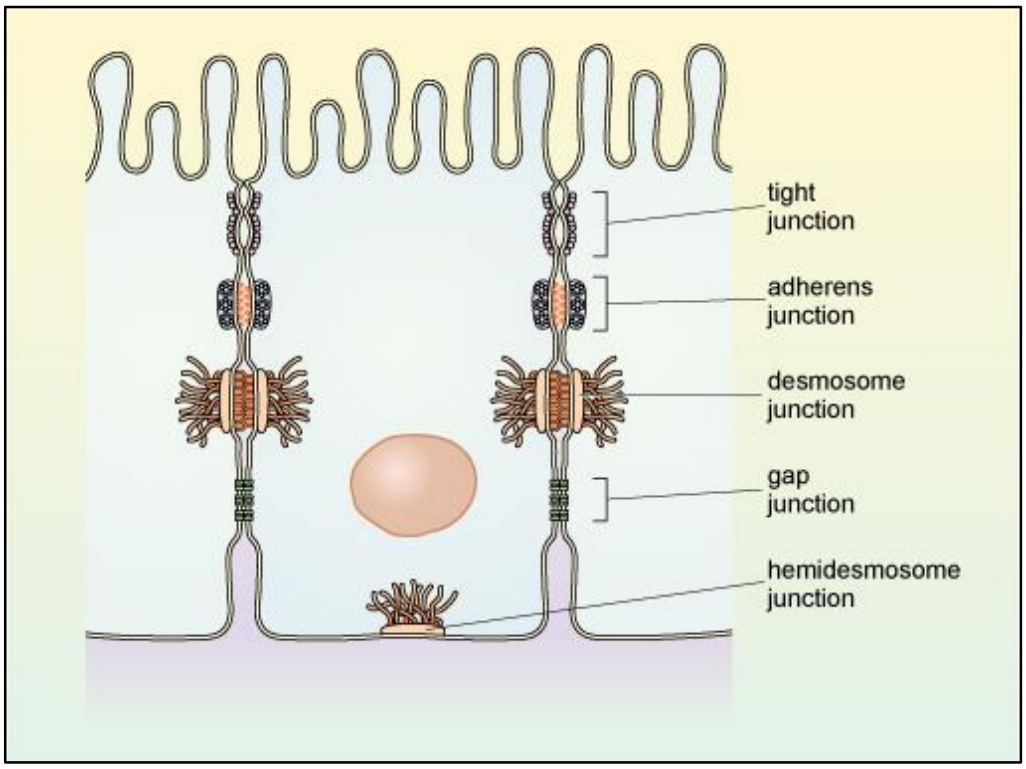

Figure 1-1 Schematic representation of an epithelium. Neighbouring epithelial cells contact each other with TJs, adherens junction, gap junctions and desmosomes, whereas they bind to the ECM with hemidesmosomes and focal adhesions. Copied from [18].

1.1.1 Tight junctions

TJs are protein complexes that hold epithelial cells together forming an epithelial sheet and separates the inside of tissues from external cavities. They divide the epithelial cell layer into two distinct compartments, the apical compartment which is in contact with the external environment and the basolateral compartment which is in contact with the inner tissue and the basement membrane. This separation between the two compartments allows the polarisation of the epithelial barrier which consists of the differential expression of protein complexes from the apical to basolateral compartments. This polarisation is important for the establishment of gradients of ions across the membrane and to maintain specialised functions of each compartment. Currently, there are more than 40 proteins which are associated with the tight junctional complex (Figure 1-2) [22]. These include: zonula occludens (ZO) which are intracellular proteins which connect transmembrane proteins with the actin cytoskeleton; claudins which are transmembrane proteins and play a fundamental role in selective ion permeability and electrical resistance, occludin which is a transmembrane protein of unknown function and the junctional adhesion molecule A (JAM-A) which is a transmembrane protein [23, 24]. Electron microscopy of freeze fractures of TJs show that they consist of rows of 10 nm wide junction points [23].

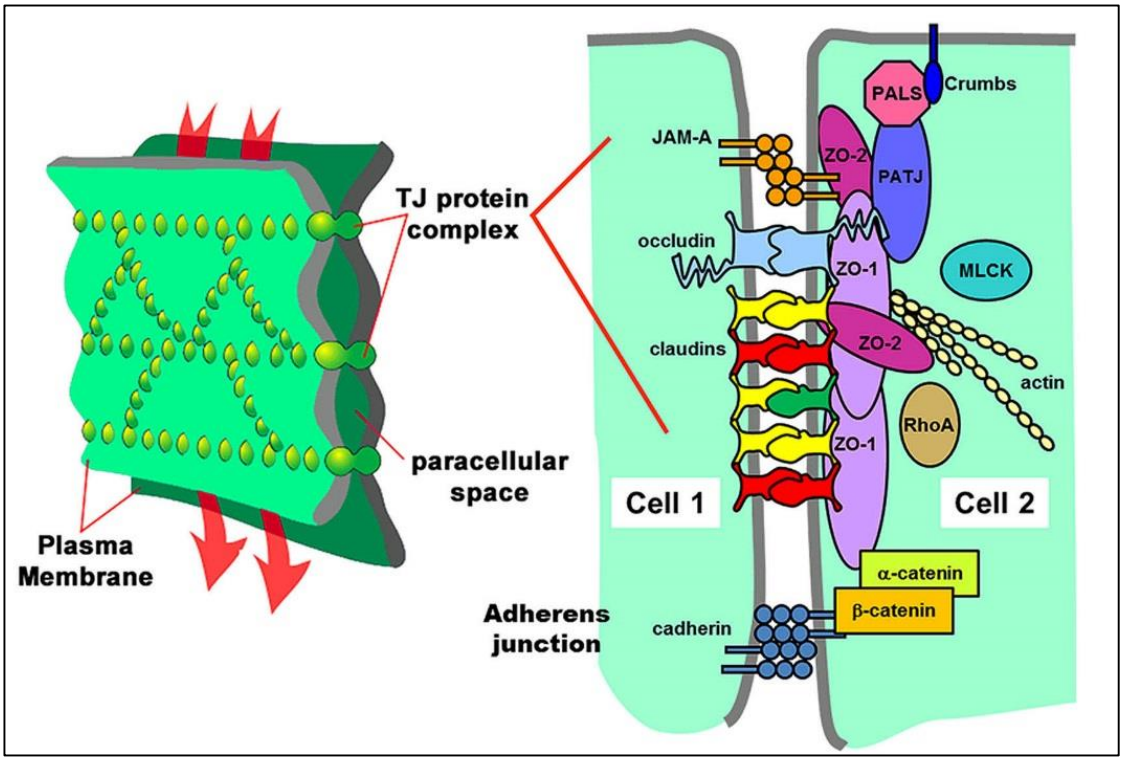

Figure 1-2 TJs structure. TJs are protein complexes that seal the intercellular space between two cells, yielding selective permeability to ions and macromolecules. They consist of rows of 10 nm wide junction points. More than 40 intra-cellular and transmembrane proteins are involved in forming TJs. Copied from [22].

In virtue of the fact that TJs have selective permeability to ions, they have often been studied by electrical means [25]. This method of characterisation consists of applying an electric potential difference across the tissue and measuring the resulting current. The electric resistance of the tissue is the resistance offered to the movement of ions by the TJs and is called the Trans-epithelial Electrical Resistance (TER or TEER).
With this characterisation it is possible to determine that different epithelia in the body have different TER depending on the tissue function [21]. For example, epithelia in the intestine which need to absorb nutrients are quite leaky and have low TER, whereas epithelia from the conducting airways which are exposed to dust and pathogens and need to act as strong barriers are tighter and have a higher TER.

On a microscopic level the tightness of a barrier can be related to the structure of its TJs. Tight epithelial barriers have strong, uninterrupted pericellular distributions of TJs whereas leaky barriers have redistrbution of the TJs leading to an interrupted, reorganised pericellular distribution [25]. If TJs are disrupted via redistribution or downregulation in protein expression, the epithelium loses its selective absorption properties. The disruption of the epithelial barrier is in fact associated with many diseases including asthma and Crohn's disease [26].

1.1.2 Examples of epithelia

Epithelia have different structures depending on their functions. Here structures of intestinal epithelium and of airway epithelium are analysed.

The intestinal epithelium
The main function of the intestine is to absorb nutrients from the food passing through the gastrointestinal tract. In order to effectively perform this function, the intestinal epithelium has two key features: (1) it has a cylindrical structure and (2) each epithelial cell has microvilli protruding

from the apical region of the membrane. The presence of these microvilli is fundamental to increase the effective surface area of the epithelium that can absorb nutrients.

The airway epithelium

The airway epithelium is a multi-layered cellular structure comprising a number of cell types. It has the unique feature of being exposed to an air-liquid interface (ALI) formed by tissue on the basolateral side and air on the apical side. In the gas-exchange region of the airways these include alveolar epithelial cells which comprise a single layer of epithelial cells in close proximity to a single layer of endothelial cells comprising blood vessels. In the conducting airways these cells include basal epithelial cells, ciliated columnar epithelial cells and mucus-producing goblet cells.

In the conducting airways, the main function of the epithelium is to act as a physical barrier against particulates, dust and noxious gases that can be contained in the environmental air we breathe and prevents their entrance in the inner part of the airways. These cells have been known for a long time to achieve this function by means of TJs. Another function of the epithelial barrier is to act against chemicals that might be inhaled. This chemical barrier is performed by the presence of antioxidant agents and by the secretion of mucus, which is a viscoelastic gel that contains many proteins able to prevent dehydration and sequester pathogens. The last function of the epithelial barrier is to act against pathogens that might be inhaled by regulating the innate and adaptive immune responses of the body. If the homeostasis is disrupted, the barrier secretes cytokines and chemokines which are proteins that lead to the recruitment and activation of immune cells and the removal of the pathogens.

Disruption of TJs leading to alterations in the airway epithelial barrier is associated with many human respiratory diseases. For example, in asthma differences in the structure of TJs between a healthy and an asthmatic epithelium are shown in Figure 1-3 [27]. This figure shows the structure of an epithelial tissue obtained with a bronchial biopsy which allows to obtain information on cell nuclei and TJs spatial organization. In a healthy epithelium, TJs are well organised. TJs are formed around the apical side of each cell (pericellular) forming a regular honeycomb network on the XY plane. On the XZ plane, they are confined in the apical side of the first cell layer. In contrast, the asthmatic epithelium shows a marked decrease in the number of TJs and they are redistributed. Moreover, the existing asthmatic TJs are less organised in the XZ plane, thus causing a further decrease in the barrier properties towards external agents.

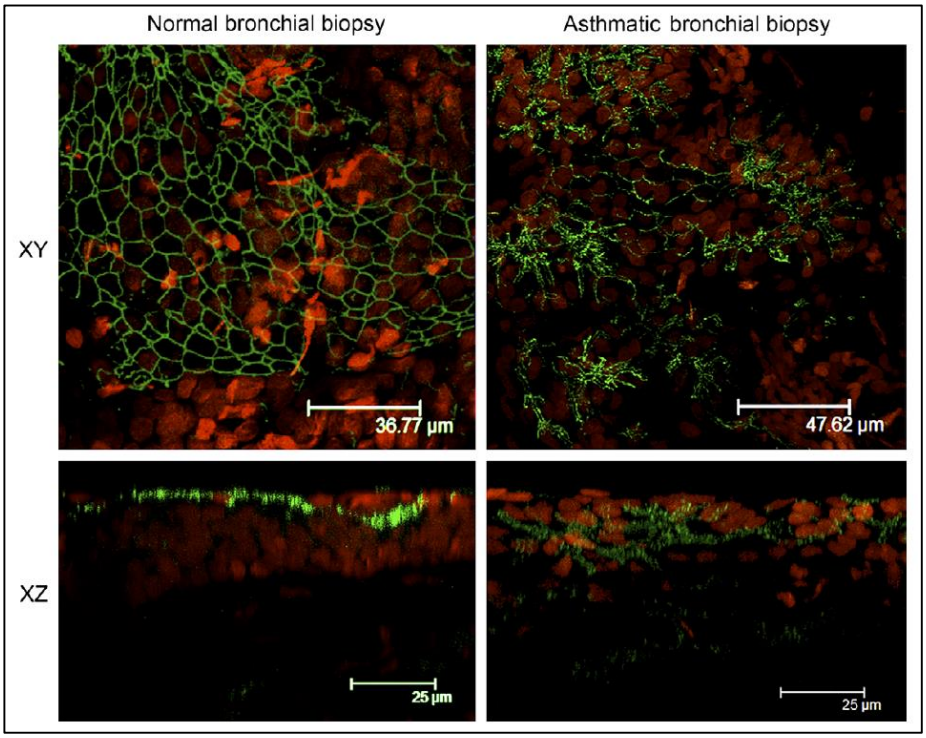

Figure 1-3 Differences in TJ distribution from patients with the respiratory disease asthma and a healthy control. Image of a healthy epithelium (Left) and an asthmatic epithelium (Right) obtained from a bronchial biopsy. A top view (XY) and a cross sectional view (XZ) are shown. The TJ protein ZO-1 is stained using an antibody conjugated to a green fluorescent dye while nuclei are stained in red. Copied from [27].

Experimentally, *in vitro* studies of asthma use primary bronchial epithelial cells (PBEC) cultures from asthmatic donors. Epithelial cells are collected from volunteers, expanded and used to investigate epithelial barrier function *in vitro*. Using this technique, it was demonstrated that primary cells from asthmatic donors retained the defects of the original culture (e.g. increased ionic and macromolecular permeability [28]), indicating this as a model capable of fully recapitulating the *in vivo* complexity [29, 30].

1.2 Commercial systems for investigating epithelial barrier function

Several systems for the *in vitro* analysis of epithelial barrier function are available commercially. Transwell® supports are the most commonly used system for long-term culture of polarised cells. Permeability of the epithelial layer to macromolecules is usually assessed using fluorescently labelled macromolecules (e.g. FITC-dextran) whereas permeability of the epithelial layer to ions can be assessed with three systems: the Epithelial Voltohmmeter (EVOM) system, the CellZscope® system and the Electric Cell-substrate Impedance Sensing (ECIS®) system.

1.2.1 The Transwell® system

The standard *in vitro* system used in biology for studying epithelial barrier function in tissue cultures are the Transwell® supports by Corning. The structure of a Transwell® consists of a microporous membrane mounted on the bottom of a polymeric holder. Transwell® membranes are available with different pore sizes (0.4-8 µm), pore densities (10^5-10^8 holes/cm^2), thickness (10-50 µm) and growth area (0.143-44 cm^2) [31]. The design of the Transwell® holder allows the culture to be suspended in a well of a conventional microplate as shown in Figure 1-4. Cells are cultured on top of the membrane and are exposed to separate basolateral and apical compartments filled with growth medium. The support has open access to both compartments enabling simple medium

replacement and apical or basolateral challenges. Epithelial cells cultured on this support polarise and form a physical barrier with expression of tight junctional proteins at their apical surface. PBEC cultured on Transwell® systems at the ALI in presence of retinoic acid are known to differentiate and form pseudostratified structures with basal cells supporting ciliated cells and mucus-producing goblet cells [32, 33].

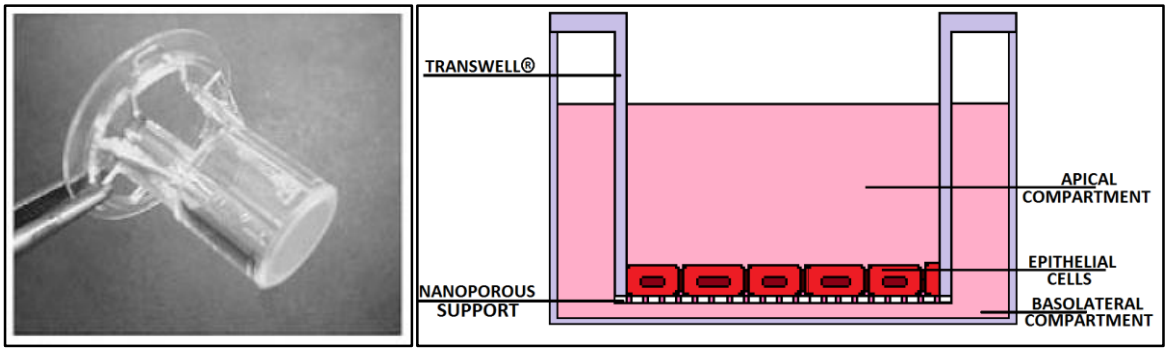

Figure 1-4 Commercial Transwell® tissue culture support used for investigating epithelial barrier formation. Picture of a commercial support [31] and a schematic of cells cultured on a commercial support. Cells are grown on top of a nanoporous membrane in the apical compartment and are exposed to two separate compartments (i.e. apical and basolateral).

1.2.2 The Epithelial Voltohmmeter (EVOM) system

A widely adopted tool for the measurement of the physical barrier of epithelial cells cultured on porous membrane supports is the EVOM system of epithelial voltohmmeters which contain STX2 'chopstick' electrodes connected to an EVOM meter, as shown in Figure 1-5. This was the first instrument designed to perform routine TER in tissue culture research. This is a hand-held system with two Ag/AgCl electrodes mounted on the tips of two parallel polymeric sticks. To perform the measurement one stick is placed into the basolateral compartment of the culture, while the other is placed into the apical compartment. The chopstick electrodes are connected to an epithelial Volt-Ohmmeter which applies the electric stimulus and measures the response of the system. The commercial EVOM2 epithelial Volt-Ohmmeter by World Precision Instruments uses a 12.5Hz square current wave with nominal amplitude ±10 μA as stimulus. The main drawback of this system is that the position of the electrodes relative to the culture affects the current pathway and thus the reading of the resistance and the accuracy of this system is influenced by the skill of the operator [34]. Moreover, the intrinsic non-homogeneity of the electric field can cause overestimation of the cellular resistance [35]. Lastly, this system requires a submerged apical compartment and is therefore not suitable for continuous measurements at the ALI.

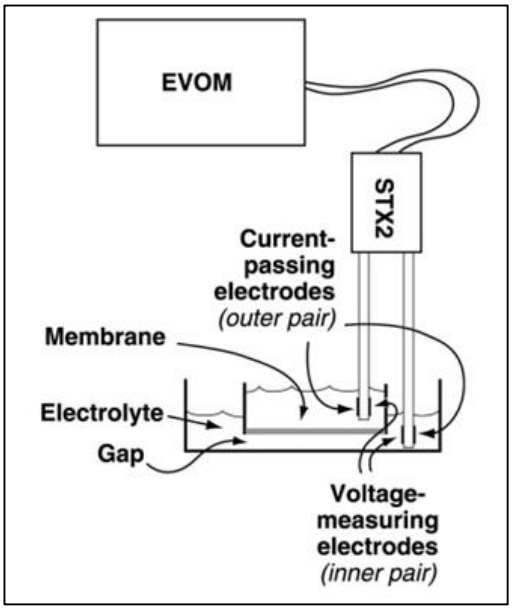

Figure 1-5 Schematic of the commercial EVOM epithelial Volt-Ohmmeter for the measurement of epithelium electrical properties. The two ends of the chopstick electrodes STX2 are submerged in the basolateral and in the apical compartment. The resulting current flows through the cell layer and probes the epithelium [34].

1.2.3 The CellZscope® system

CellZscope® by nanoAnalytics GmbH is a commercial system to measure trans-epithelial impedance spectra of tissues cultured on Transwell® supports, as shown in Figure 1-6. It is formed by 2 parts. The bottom part has steel culture wells which define the basolateral compartments (similarly to a microplate) and act as electrodes. The top part is a removable lid with integrated steel electrodes which are submerged in the apical compartments. To measure the culture electrical properties, a potential difference is applied between the electrodes and the resulting current is measured, similarly to the conventional measurement system. Several advantages that this system has over the conventional measurement system include an automated and parallelised measurement, a homogeneous electric field and the possibility to apply signals with different frequencies, obtaining information on both the tissue resistance and capacitance [36, 37]. The main limitation of this system is that it can only be used to analyse submerged cultures grown on Transwell® supports and therefore is not suitable for continuous measurements at the ALI.

1.2.4 The Electric Cell-substrate Impedance Sensing (ECIS®) system

Another commercially available system that uses impedance spectroscopy to monitor cellular properties is the ECIS® (Electric Cell-substrate Impedance Sensing) system by Applied BioPhysics. In this system, adherent cells are grown directly on top of planar gold electrodes, as shown in Figure 1-6. When a potential difference is applied between the electrodes, the resulting current depends on the cellular coverage and properties. The system can be used to observe several phenomena such as cell spreading and proliferation, cellular micro-motion and wound healing. Different electrodes geometry are needed to study different effects [37, 38]. The main limitation of this system is that it cannot analyse cultures grown on porous supports, which is a necessary condition for cell polarisation (i.e. TJ assembly) and differentiation (i.e. ciliated cells and mucus producing goblet cells).

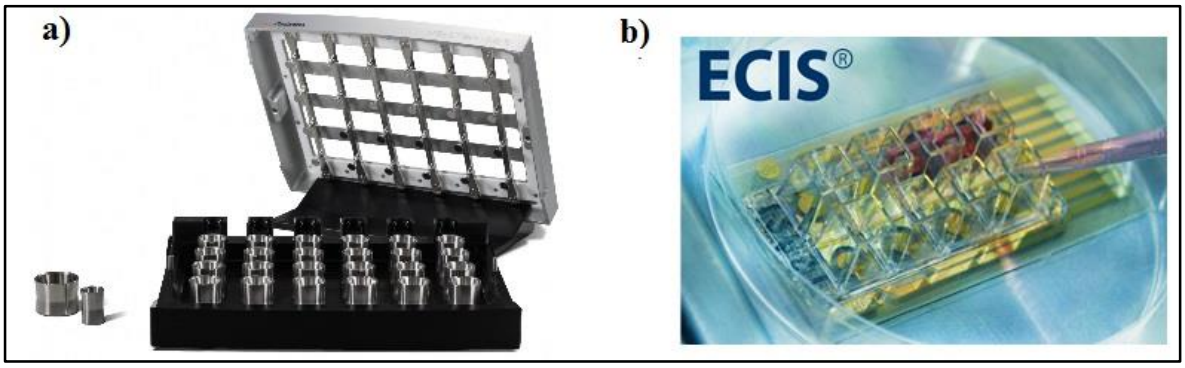

Figure 1-6 Schematics of commercially available setups for the electrical impedance spectroscopy. (a) The cellZscope® is formed by a bottom plate with integrated Transwell® basolateral reservoir and steel electrodes, and by a removable lid with integrated apical steel electrodes [36]. (b) The ECIS® system is formed by planar gold electrodes for the measurement of adherent cells [38].

1.3 Organ-on-a-chip devices for monitoring the epithelial barrier

Organ-on-a-chip are a new class of micro-devices which aim to replace conventional tissue culture systems. These models use cutting edge microfabrication technologies to recreate *in vitro* physiologically relevant features of the *in vivo* cellular environment. In this section some capabilities of the organs-on-a-chip that have been demonstrated in the literature are presented.

1.3.1 Constant perfusion

The main limitation of conventional static cultures lies in the non-physiological way they are fed. In such systems, the cells are submerged by growth medium which is replaced every 2-3 days. In the human body instead, cells are fed by constant perfusion of blood through the tissue. This difference leads to different concentration profiles of chemicals across the system. In a static system the concentration of nutrients is high when the growth medium is added and starts decreasing during the following days until the medium is replaced, leading to a saw-tooth profile. In a perfusion system the inlet concentration is constant and, if the consumption is stable, the nutrients reach a steady-state concentration profile which is stable over time. A similar reasoning can be applied to waste produced by the cells, which build-up until the medium is replaced in static cultures, or are constantly removed reaching a steady concentration in a constant perfusion environment. Since an inhomogeneous concentration profile can affect cellular regulation mechanisms and inhibit cellular proliferation, constant perfusion is adopted in all organ-on-chips trying to recreate *in vivo*-like conditions.

1.3.2 Air-liquid interface systems

One of the most relevant physiological features of the airways is the coexistence of a gaseous and liquid phase. While some cell lines can polarise under submerged conditions, primary bronchial epithelial cells (PBEC) require the presence of an ALI in order to polarise, differentiate and form a physical barrier. Several organ-on-chip devices enabling this feature have been developed, providing a more physiological representative model of the airways.

Nalayanda *et al.* [39] developed an open access device where epithelial cells can be cultured with the apical side open to the atmosphere while they are fed by cell culture medium by flow on the basolateral side. In this system, a nanoporous polymeric membrane is sandwiched between two layers of poly-dimethylsyloxane (PDMS). The opening is created by punching a hole through the PDMS. Cells cultured in this platform demonstrated a higher degree of monolayer integrity and a decrease in surface tension of the hypophase as compared to cells cultured under conventional

media exposure. In another study Huh *et al.* investigated the effects that the ALI induces in a cell culture with two devices in which the gaseous phase was confined in closed channels and flow condition were applied [40, 41]. Schematic structure of the analysed systems are shown in Figure 1-7. These studies proved the feasibility of the recapitulation of an ALI culture and the replication of the alveolar space in a microfluidic device. Moreover, using fluorescence microscopy, TER measurements and analysis of the surface tension they showed that this configuration yields a culture with responses to microbial infection and nanoparticles that partially recapitulate the *in vivo* situation. In all these studies, a direct measurement of barrier integrity at the ALI with the standard EVOM® system was not possible due to the lack of an apical electrolyte. To enable the measurement, apical compartments of cultures were temporarily submerged with medium and left to stabilise for 10 minutes.

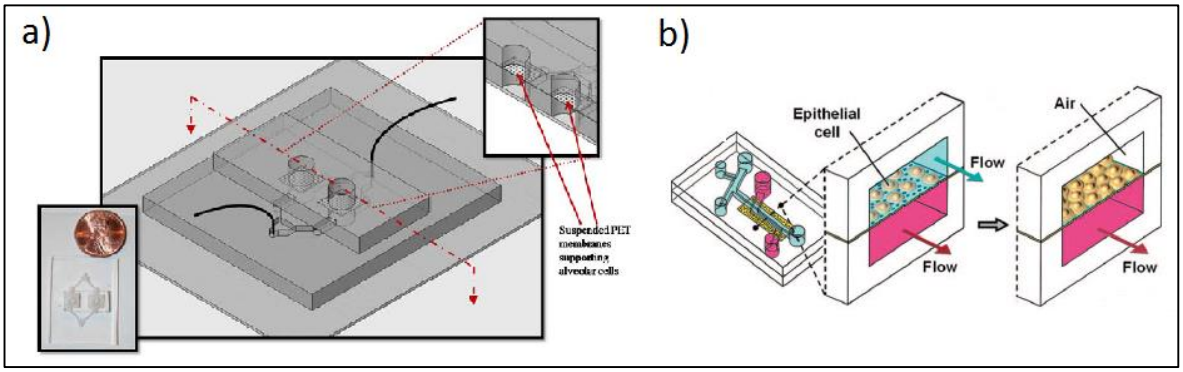

Figure 1-7 Examples of lung-on-a-chip devices from the literature of epithelial cells cultured at the ALI. A device with an open access chamber for an ALI monoculture of bronchial epithelial cells [39] (a). The ALI recapitulates the *in vivo* situation and is required for the differentiation of PBECs. A device with a channel for the air flow [41] replicating the alveoli (b).

1.3.3 Chemical stimulation

In order to minimize the cost of testing new drugs, the throughput of any device should be maximised. One way to improve the drug testing throughput of a device is by increasing the number of different concentrations of the drug to be tested at the same time in parallel. Different engineering approaches capable of testing several drug concentrations at once have been proposed and 3 examples are discussed below and are shown in Figure 1-8.

Xu *et al.,* [42] developed a system that can test in parallel a discrete number of concentrations of a chemical. Each concentration to be tested has a separate submerged culture chamber. All the chambers have common inlets for the target chemical and for the eluent. The different concentrations are generated in different channels running from the chemical inlet to the culture chambers. The number of different concentrations that can be tested in one run depends on the design of the device (12 in the device reported in this study). In this study, a human non-small cell lung cancer cell line (SPCA-1) was used. Kim *et al*., [43] developed a system that creates a continuous gradient of a chemical across a cell culture. This device relies on diffusion to create the gradient. It is formed from two channels, with different inlets and outlets but common middle tract. Once steady state is reached, the chemical has a constant concentration profile across the channel section that ranges from zero to the inlet concentration. This device was used to study induced epithelial to mesenchymal transition in A549 human lung alveolar epithelial cells. In a similar study, Sip *et al*., [44] developed a platform for the application of a continuous gradient to cell cultured on the bottom of a multi-well plate. This system used commercial supports and PDMS inserts to produce a diffusion based gradient on submerged cultures. This system was used to study the induced migration of a neutrophil cell line (HL-60). A common advantage shared by the last two devices is the flexibility in timing and orientation of the gradient, because both of them are

untethered from the substrate. All these systems provide valuable approaches for high-throughput studies of concentration-dependent effects.

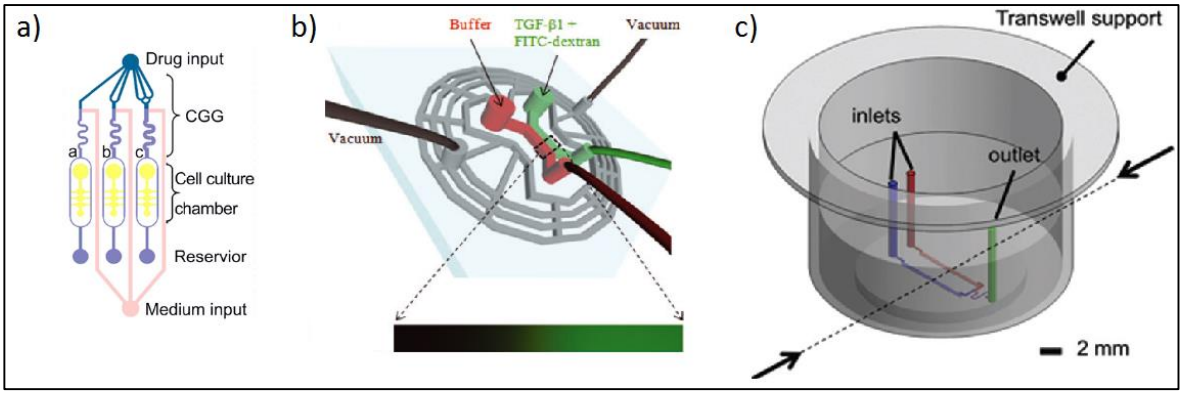

Figure 1-8 Examples from the literature of high throughput devices for drug testing. (a) A device with separate chambers to generate a discrete number of concentration [42]. (b,c) Two devices to generate continuous gradients on cells cultured on the bottom of a culture well [43, 44].

1.3.4 3D environments

Cells are greatly influenced by their surrounding environment. In physiological conditions, they are surrounded by the extracellular matrix (ECM), which is a mixture of macromolecules and proteins (of which collagen I is the most abundant [45]) which has structural and regulatory effects on the cell. The recapitulation of this physiological environment is an aspect which is often pursued in tissue engineering. Three dimensional (3D) structures are usually adopted in cell cultures in order to maximize the degree of fidelity of the model. A 3D culture can be achieved through the use of 3D features, through culture of multiple cell types or through 3D differentiation (e.g. PBEC ALI cultures).

Zhang *et al.,* developed a device for the culture of cells in different types of 3D scaffolds [46]. Among other findings, the culture of osteocytes on polystyrene (PS) microbeads and the culture of primary murine intestine epithelial cells on an electrospun nanofibrous mesh were successfully achieved, highlighting the high adaptability of the platform. In another study, Wu *et al.,* reported different morphologies for PBECs grown in different environments [47]: cells cultured on a thin layer of type IV collagen-coated membranes showed a cobblestone appearance whereas cells cultured on a thicker layer of growth factor-reduced Matrigel (a commercially available mixture of ECM proteins secreted by mouse sarcoma cells) assumed a 3D spheroid configuration. Osei *et al.,* performed a 3D co-culture on commercial supports [48]. Human bronchial epithelial cells (16HBE14o-) and human fibroblast (MRC-5) were cultured in different compartments of the system. The interaction between the two types of cells led to increased levels of produced pro-inflammatory cytokines (IL-8). Examples of 3D cultures from the literature are reported in Figure 1-9.

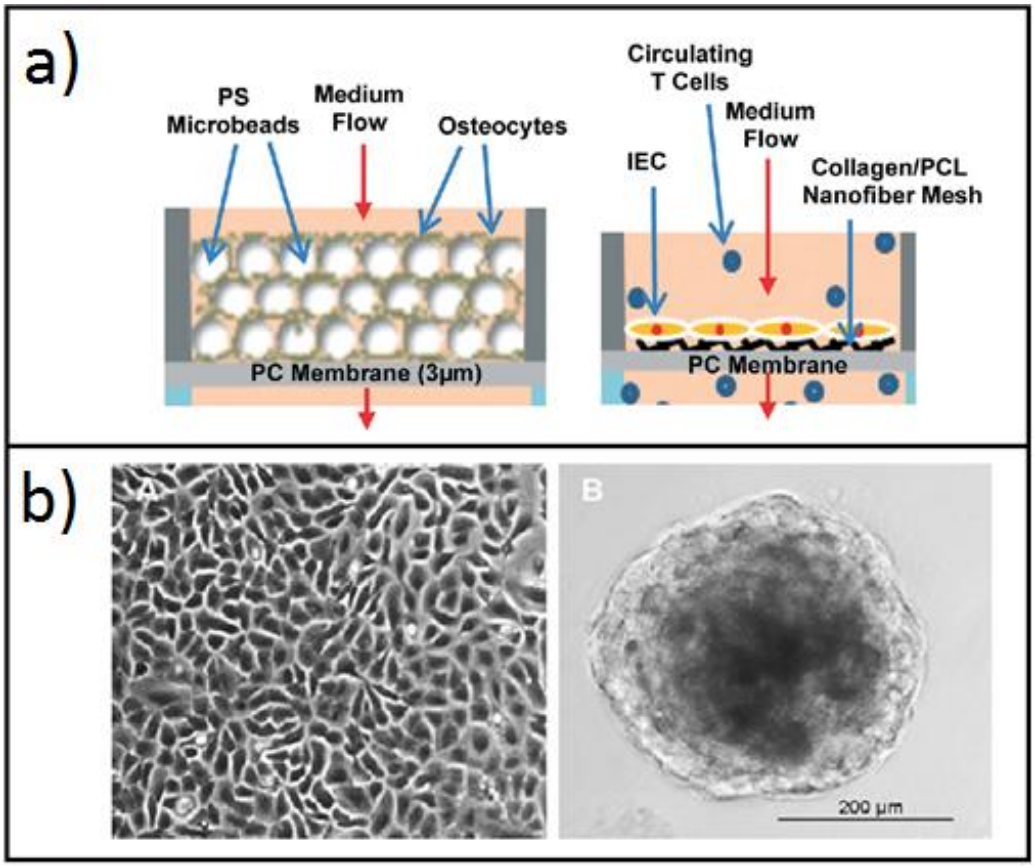

Figure 1-9 Examples of 3D cultures from the literature. (a) A system for the culture on PS microbeads or on electrospun polymer [46]. (b) Differences between cobblestone and globular appearances of HBECs cultured on different substrates [47].

1.3.5 Membrane permeation

A key aspect of the effectiveness of a drug is its ability to reach the systemic circulation. In order to do so, drugs need to have high permeability through the epithelium and to be substantially absorbed [49]. Drugs can be absorbed either by passive diffusive or active transport by membrane proteins. Both epithelial cell lines and primary cells have been used to perform *in vitro* permeation studies on the culture [50].

Forbes *et al.,* [51] performed permeation studies on the human bronchial epithelial immortalised cell line (16HBEs) which were polarised by growing on commercial supports. They reported a decrease in the permeability of the culture to mannitol as the TJs were established over time, as shown in Figure 1-10. Moreover, they studied the relation between membrane permeability and hydrophobicity using drugs with different partition coefficients (i.e. the equilibrium solubility in the cells), namely: mannitol, sotalol, salbutamol, atenolol, metoprolol, timolol, betaxolol and propranolol . Jang *et al.,* reported the development of a microfluidic tubule-on-a-chip as an *in vitro* model to study drug permeation through a culture of primary human kidney proximal tubular epithelial cells [52]. The study highlighted the importance that the continuous flow has in maintaining the physiological properties of the culture such as cell polarisation, primary cilia formation, albumin transport, glucose reabsorption, and recovery from a cytotoxic compound (Cisplatin).

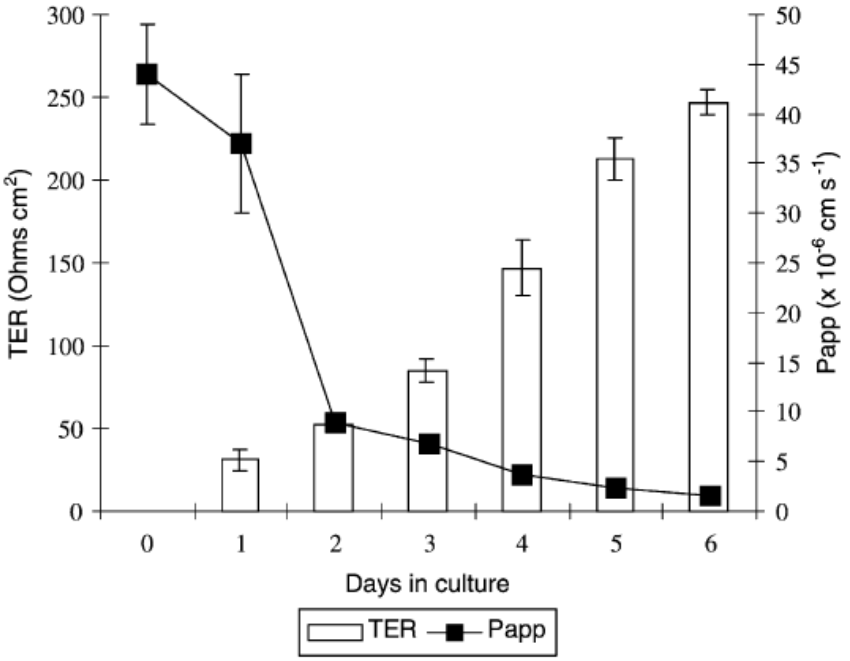

Figure 1-10 Correlation between TER and mannitol permeability. As TJs are established over time, the electrical resistance of the culture increases whereas the permeability decreases [51].

1.3.6 Mechanical stresses

Mechanical stresses are known to play an important role in cellular physiology [53]. Cells all over the body are affected by shear stresses caused by blood flow. In the lungs, alveoli naturally undergo cyclical mechanical stretch associated with breathing while in chronic respiratory disease the airway bronchial epithelium undergoes compression as a result of bronchoconstriction.

The stretching associated with breathing in the alveoli compartment was recreated in a PDMS chip by Huh *et al.,* [40]. Human alveolar epithelial cells and human pulmonary microvascular endothelial cells were cultured on the different sides of a porous membrane sandwiched between two layers of PDMS. In addition to the channels for the liquid phase and for the gaseous phase, there were two ancillary channels located either side. The cyclical application of vacuum in the side channels caused a deformation of the thin PDMS walls and the subsequent stretching and relaxation of the culture. Another study by the same author [41] reported the development of a device to investigate the noxious effects that the formation and implosion of air plugs might have on the culture. This condition is observed in several pulmonary diseases, including chronic obstructive pulmonary disease and asthma. This device has the capability to create small plugs of liquid in a flow of air and to push them along the culture. As the liquid plugs advance in the channel they lose liquid on the wall: this will cause consumption of the plugs which will eventually implode enforcing mechanical stresses to the cells. Schematics of the devices used in the 2 studies are reported in Figure 1-11.

Compression associated with bronchoconstriction in the bronchial compartment was recreated by Chu *et al.,* [54] and by Ressler et al. [55], who used the same model to apply compression stress on a culture of normal PBECs and to a culture of rat tracheal epithelial (RTE) cells, respectively. To obtain the transcellular compression they injected a stream of compressed air in the apical compartment of a standard Tranwell® system sealed with a silicon plug. Using immunofluorescence and total RNA analysis, they observed that under compression conditions epidermal growth factor receptor (EGFR) shows an autocrine activation process in PBECs [54] and that RTE upregulate expression of mRNAs for Egr-1, ET-1, and TGF-b1 in a magnitude- and time-dependent manner [47]. In these studies, mechanical stresses were found to have great effects on the culture, having a direct impact on cellular viability and on transport properties.

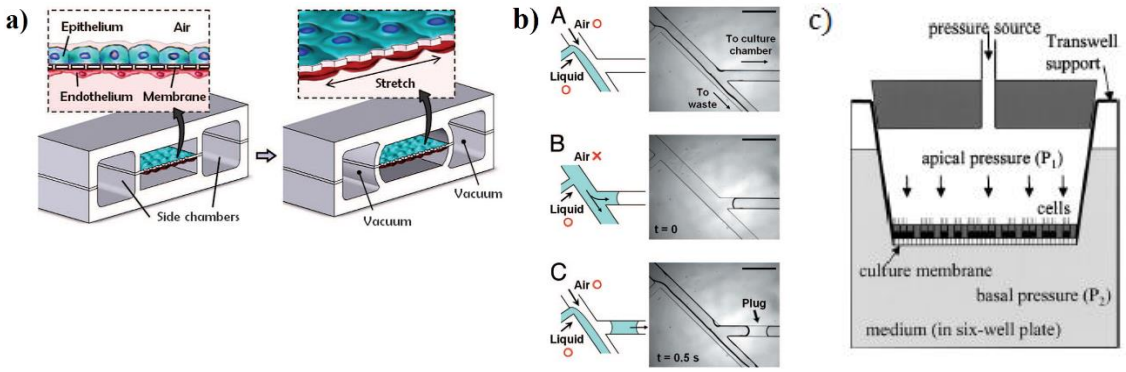

Figure 1-11 Examples from the literature of devices which recreates physiological mechanical stresses. (a) A cyclical stretching of the membrane equivalent to the one caused by breathing is achieved by applying cyclical vacuum in the side channels [40]. (b) A device to generate air plugs and implode them on the culture [41]. (c) A system to apply compression stress on a static culture of epithelial cells on Transwell® [47].

1.3.7 Body-on-a-chip

The human body is a complex network of interacting organs: biological studies that focus only on one tissue can miss important effects stemming from multi-organs interaction. For example, in the human body the plasma concentration of a drug over time is controlled by its ADME processes [56]. Tissues deriving from different organs are required to recapitulate these effects *in vitro.* A micro-engineering approach to overcome this issue is the body-on-a-chip, where different tissues are culture in separate chambers and are exposed to the same medium. In this way, synergic interactions can be analysed [15].

Li *et al.,* [6] developed an integrated discrete multiple organ cell culture (IdMOC) system, where cells derived from 6 different tissues (normal human primary hepatocytes (liver, metabolism), kidney proximal tubule cells (kidney, excretion), small airway epithelial cells (lung), aortic endothelial cells (heart), aortic endothelial astrocytes (brain) and MCF-7 human breast adenocarcinoma cells) were cultured in segregated wells with an overlying common layer of culture medium. This system was used to compare the toxicity of an anti-cancer drug (tamoxifen) toward each cell type, and found that, based on the concentration needed to cause 99% drop in survival, MCF-7s were the most affected by the drug and the hepatocytes were the least affected. In another study, Sung *et al.,* [57] developed a micro cell culture analog (μCCA) where cells derived from the liver, the marrow and colon cancer were cultured in three separate chambers connected by the medium flow. Flow residence times for each chamber and for an external reservoir (which mimicked the hold-up of the remaining part of the body) were designed to resemble physiological conditions. This system was able to reproduce the physiological metabolism of an anti-cancer drug (Tegafur®, a prodrug of 5-fluorouracil), as opposed to cells cultured in standard systems. In another study, Imura *et al.,* [58] designed a PDMS microsystem that integrated intestinal cells on a porous support, liver cells on beads and cancer cells on glass connected by the medium. A pro-drug candidate (epirubicin) was introduced in the apical compartment of the intestinal cells: in order to have an effect on the cancer culture it needed to be absorbed by the intestinal cells and be metabolised by the liver cells. The results obtained with this system were comparable with the pre-existing clinical ones demonstrating its capability to obtain *in vitro* physiological response to drugs. Schematics of the 3 systems are shown in Figure 1-12. While these body-on-a-chip systems are still far from recapitulating the *in vivo* complexity of the human body, they can be used in conjunction with mathematical pharmacokinetic models to obtain predictions of drug effectiveness and toxicity during the preclinical development stage that are more reliable than current models [59].

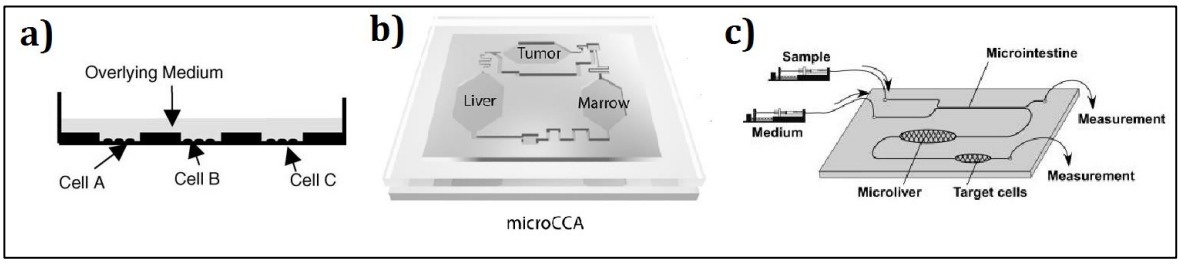

Figure 1-12 Schematics of body-on-a-chip systems. (a) Static wells exposed to the same static medium (6 cell types) [6]. (b) Microfluidic system with cells cultured on glass surface (3 cell types) [57]. (c) Microfluidic system with cells cultured on porous support, beads or glass surface (3 cell types) [58].

1.3.8 Electrical characterisation of barrier properties

The TER of an epithelial cell layer is a variable that yields information on the status of the TJs, on the tightness of the barrier and on cellular viability. The monitoring of this value is extremely useful to assess effects of positive or negative stimuli, and many studies proposed different systems for its measurement. Schematics of 4 systems from the literature used to measure cellular electrical properties are shown in Figure 1-13.

Hediger *et al.,* [60, 61] proposed two studies aimed towards the development of a device produced in a clean room environment with integrated electrodes for the measurement of TER. In these studies, they produced and tested both platinum and Ag/AgCl electrodes. The integration of the polymeric porous support into the system was reported as the critical step in the manufacturing process: to ensure the absence of the glue on the culture surface during assembly a custom gluing procedure was developed. These systems could detect an increase in the measured resistance after the submerged culture of Madin-Darby canine kidney (MDCK) cells (Figure 1-13a). In another study, Booth *et al.,* [62] developed a PDMS microfluidic device with integrated Ag/AgCl electrodes to monitor the development of the blood brain barrier (Figure 1-13b). The system used the commercial EVOM2 epithelial volt-ohmmeter to perform a TER measurement every 12 hours, and compared the electrical properties of endothelial cells mono-cultures and co-cultures of endothelial cells and astrocytes. The microfluidic blood brain barrier (μBBB) showed significantly higher TEER levels than in static models, with a comparatively short time to steady state TEER compared to dynamic *in vitro* blood brain barrier (DIV-BBB). The same system was used to assess the time required for the culture to recover from stimulation with Histamine.

Odijk *et al.,* [63] performed a study on the modelling and measurement of TEER in a gut-on-a- chip (Figure 1-13d). They used standard Ag/AgCl chopstick electrodes to measure electrical properties of human intestinal epithelial Caco-2 BBE cells on parallel cultures of standard and microfluidic systems. In the study they observed that the confined environment of the microfluidic channel and small tissue imperfections can greatly affect measured TEER values, stating that a 1% hole in the cell coverage can induce a 90% drop in TEER. Henry *et al.,* [64] reported the development of a microfluidic device with integrated gold electrodes for the four-points measurement of TEER (Figure 1-13e). Using this system, they were able to follow the differentiation of human primary small airway epithelial cells at ALI culture conditions and human intestinal epithelial cells under submersion. They were also able to monitor the disruption of cell–cell junctions after exposure to a chelating agent (EGTA). In this study, the culture was temporarily submerged before the measurement of the barrier electrical properties. Maoz *et al.,* [65] reported a microfluidic heart-on-a-chip for integrated measurements of electrical activity, barrier function and conformational changes (Figure 1-13f). This device featured Pt/Pt-black electrodes for TEER and micro-electrodes array (MEA). The MEA was used to monitor the spontaneous beating frequency of an endothelialised myocardium.

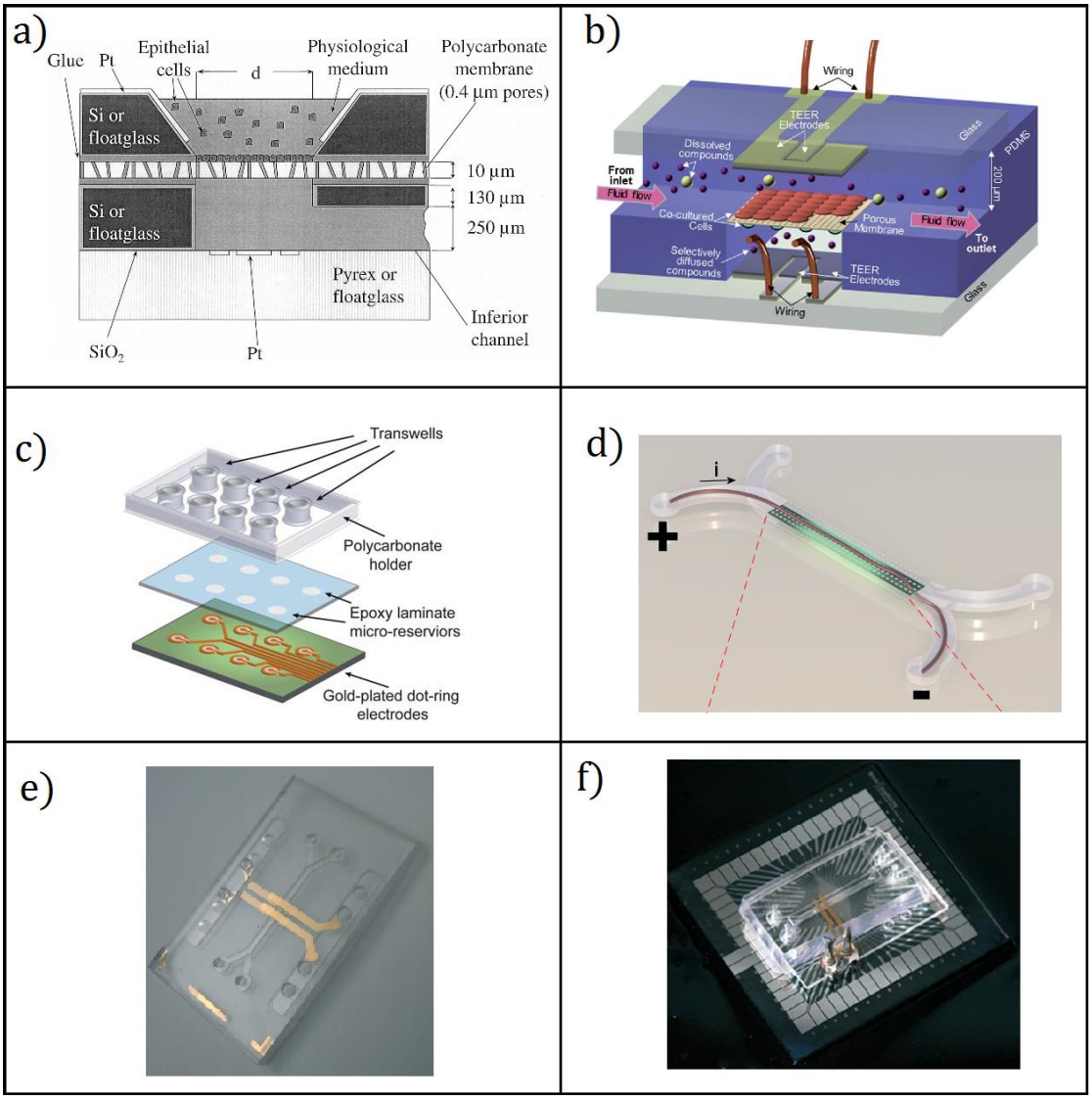

Figure 1-13 Systems for the measurement of cellular electrical properties from the literature. (a) Glass system for the measurement of trans-epithelial resistance of cell cultured in static condition with Ag/AgCl electrodes [60]. (b) PDMS system for the measurement of trans-endothelial resistance of cell cultured under constant perfusion with Ag/AgCl electrodes [62]. (c) PCB based system for the measurement of trans-epithelial resistance of cell cultured in static condition with Cu/Au electrodes [66]. (d) Gut-on-a-chip system for the measurement of trans-epithelial resistance of cell cultured under constant perfusion with external Ag/AgCl electrodes [63]. (e) Microfluidic system for the four-points impedance measurement of epithelia [64]. (f) Heart-on-a-chip with integrated TEER and MEA electrodes for epithelial electrical measurement and spontaneous beating frequency analysis [65].

All the systems for barrier characterisation described so far, used electrodes placed in the two different compartments of the epithelial culture. Therefore, none of those systems can be used to perform real-time barrier measurements of ALI cultures, because they all required the apical electrodes to be submerged. Sun *et al.,* [66] reported the development of a PCB-based device for the measurement of the electrical properties of epithelial cells cultured on a commercial culture support (Figure 1-13c). The system used coplanar gold electrodes coated with a conductive polypyrrole-polystyrene sulfonate (PPy-PSS) to improve electrode performances. In contrast with standard measurements, in this system both electrodes were placed on the basolateral side of the

culture. Measurements of the barrier electrical properties after the stimulation with two chemicals known to have different effects on the barrier was successfully reported and demonstrated that barrier properties of epithelial cells could be continuously monitored in real-time. Currently, full integration of electrodes within organ chip microfluidic culture devices remains challenging and the location, dimensions and geometry of the electrodes is non-optimized [64].

1.4 State of the art limitations

Organs-on-chip are a new class of devices which improve the standard system by integrating a wide range of physiologically relevant features, such as electrical, chemical, environmental and mechanical stimuli. An ideal device featuring all these aspects is currently out of technological reach due to manufacturing and operation complexities. Instead, platforms upgraded with few application-specific features are within reach and have the potential to improve the system reliability and to improve our basic understanding of complex biological systems.

Currently, there are no systems able to perform the electrical real-time monitoring of epithelia cultured at the ALI. Existing organ-on-chip with electrodes on both side of the culture can't perform a measurement directly at the ALI and require a momentary submersion of the culture to perform the measurement, thus achieving poor temporal resolution. The only existing system having both electrodes on the same side of the culture provides a poor representation of the in *vivo* physiology and lacks the sensitivity necessary to measure ALI cultures. Moreover, most systems reported in the literature adopt manufacturing technologies not suitable for mass manufacturing, thus having poor scalability.

In summary, there is the need to create a better *in vitro* platform for epithelial cell culture yielding high-throughput and reliable information on epithelial barrier properties. Such device could reduce the attrition rate at the clinical stage of drugs development and greatly reduce the costs associated with it.

1.5 Aim of the project

The aim of this project is to develop a microfluidic device for the culture and electrical analysis of barrier properties of epithelial cells. The device provides a physiologically relevant representation of the cellular environment and is capable to sustain the growth of an epithelial cell culture under constant perfusion for the time required for the establishment of a physical epithelial barrier. It enables cell culture and electrical monitoring under submerged or ALI conditions, and is capable to detect fine variations of epithelial barrier properties. The device is automated and capable to perform real-time (minutes-scale) and long-term (weeks-scale) measurements. It is produced adopting scalable manufacturing technologies, making it apt to mass-manufacturing. Moreover, the device is compact and suitable to parallelization to increase the system throughput.

Chapter 2: Theory of Lab-on-a-chip

Organs-on-chip are a subset of the lab-on-a-chip class, which refers to devices that can perform a wide range of tasks, with the common feature of being miniaturised (μm size) and fabricated using standard semiconductor technologies. This technology has found applications in many fields, especially in life sciences. The design of such devices involves several branches of physics, combining the "wetness" (Fluid Dynamics, Biology, Chemistry) of life sciences with the "dryness" (Mechanics, Electrics, Electronics) of the semiconductor industries. This chapter provides a theoretical background of fluid dynamics and of electrical measurement in biological systems.

2.1 Fluid dynamics in microsystems

The behaviour of fluids at the microscale differs from the macroscale that we observe every day. Many effects such as turbulence, mixing, time-dependence, etc. have completely different dynamics at the two scales. This peculiar fluid mechanic at the microscale is called microfluidics. Lab-on-a-chip systems take advantage of the special properties of microfluidics to perform cheaper, faster and more controlled operation compared to macroscale. In this section the equation which rules the microscale is derived as a particular case of the more complex general equation, and dispersion phenomena which are negligible at the macroscale but important at the microscale are also examined.

2.1.1 Navier-Stokes equation

The equation that governs the behaviour of an incompressible Newtonian fluid (i.e. a fluid where the viscous stress are proportionally to the local strain rate, such as water) is known as the Navier-Stokes equation [67]:

$$\rho_0 \left(\frac{\partial u}{\partial t} + u \cdot \nabla u\right) = -\nabla p + \mu_0 \nabla^2 u \qquad (2.1)$$

Here $u(\vec{x}, t)$ is the velocity field which depends on the spatial coordinates $\vec{x} = [x, y, z]$ and on the time t, $p(\vec{x}, t)$ is the pressure field, ρ_0 is the density and μ_0 is the dynamic viscosity of the fluid. The system of equations must be coupled with the mass conservation constraint. If the density is constant (i.e. negligible thermal expansion and incompressible fluid) the mass conservation can be expressed as:

$$\nabla \cdot u = 0 \qquad (2.2)$$

2.1.2 Dimensionless Navier-Stokes equation

The Navier-Stokes equations can be made dimensionless by rearranging the constant terms. Dimensionless equations are useful because they are independent of the scale of the system and allow for qualitative comparisons. To obtain a dimensionless equation, characteristic quantities specific to the system are introduced:

- L_0 is a characteristic length scale. It is usually either the biggest spatial dimension (length of the device) or the dimension of a small part in the system (valve seat, restriction in a channel).
- U_0 is a characteristic velocity in the system.
- T_0 is a characteristic timescale. If the system is subject to an external periodic perturbation with frequency f_0, it is $T_0 = 1/f_0$. If the steady state is considered, it is $T_0 \to \infty$.
- P_0 is a characteristic pressure in the system.

Using the following normalisations:

$$u^* = \frac{u}{U_0}\ ;\ t^* = \frac{t}{T_0}\ ;\ p^* = \frac{p}{P_0}\ ;\ \nabla^* = L_0\nabla \qquad (2.3)$$

the Navier-Stokes equations in dimensionless form become [68]:

$$\rho_0\left(\frac{U_0}{T_0}\frac{\partial u^*}{\partial t^*} + \frac{U_0^2}{L_0}u^*\cdot\nabla^* u^*\right) = -\frac{P_0}{L_0}\nabla^* p^* + \frac{U_0}{L_0^2}\mu_0\nabla^{2^*}u^* \qquad (2.4)$$

Rearranging the constant terms gives:

$$\frac{\rho_0 L_0^2}{U_0\mu_0}\left(\frac{U_0}{T_0}\frac{\partial u^*}{\partial t^*} + \frac{U_0^2}{L_0}u^*\cdot\nabla^* u^*\right) = -\frac{P_0 L_0}{U_0\mu_0}\nabla^* p^* + \nabla^{2^*}u^* \qquad (2.5)$$

Which can be expressed as:

$$Re\left(St\frac{\partial u^*}{\partial t^*} + u^*\cdot\nabla^* u^*\right) = -\frac{Re}{Ru}\nabla^* p^* + \nabla^{2^*}u^* \qquad (2.6)$$

Where Re, St and Ru are three dimensionless numbers:

- $Re = \frac{\rho_0 U_0 L_0}{\mu_0}$ is the Reynolds number. It represents the ratio between inertial and viscous forces and will be analysed in more detail in the next section.

- $St = \frac{L_0}{T_0 U_0}$ is the Strouhal number. It represents the ratio between the advection time and the timescale of an external force applied to the system. If no external force is present, then $T_0 = \frac{L_0}{U_0}$ and $St = 1$. If the system is in a steady state, then $T_0 \to \infty$ and $St = 0$, which makes velocities independent of time.

- $Ru = \frac{\rho_0 U_0^2}{P_0}$ is the Ruark number. It represents the ratio between advection (transport by bulk motion) forces and a characteristic pressure.

2.1.3 Reynolds number

The Reynolds number is a dimensionless quantity that characterises the degree of turbulence of a flow. In the original experiment of Reynolds [69], there were two pipes that ended in a single transparent pipe generating a coaxial flow. Water and a tracer dye were pumped through the system. At low flow rates the trace of the dye was stable along the pipe, whereas at high flow rates the water formed vortices resulting in an unstable trace and quick mixing, as shown in Figure 2-1.

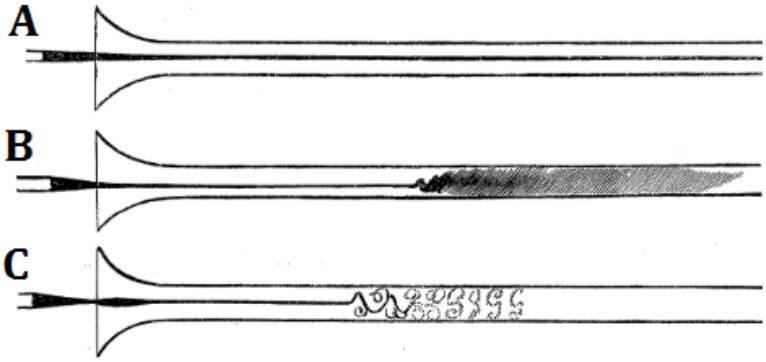

Figure 2-1 Different flow regimes highlighted by Reynolds (adapted from [69]). A coloured tracer (black) is flown coaxially with a flow of water. (A) Laminar flow: if the flow rate is low the tracer is stable across the pipe. (B) Turbulent flow: if the flow is increased the tracer flow breaks at a certain distance from the inlet causing the water to colour down. If this flow is observed with a reduced shutter time (C) it is possible to observe ripples of the tracer flow.

From these observations it was concluded that there are two possible types of flow for a fluid:

- A laminar regime where the fluid flows in an ordered manner with each particle following a parallel trajectory or streamline.
- A turbulent regime where the fluid flows in a chaotic manner forming vortexes.

For a horizontal pipe in laminar regime the vertical components of the velocities are always zero, whereas in turbulent regime the instantaneous local velocities might be different from zero but with a zero mean.

It is possible to predict which kind of flow occurs in a system by analysing the Reynolds number:

- For $Re > 10000$ the flow will be turbulent.
- For $Re < 10$ the flow will be laminar.
- For $10 < Re < 10000$ there will be a mixed flow with transition from one behaviour to the other.

In microfluidic systems the typical dimension is in the order of 10-100 µm and the typical velocity is in the order of 1 mm/s, which for water-based systems yields:

$$Re = \frac{\rho v d}{\mu} = \frac{10^{-6}\frac{Kg}{mm^3}\ 1\frac{mm}{s}\ 10^{-1}mm}{10^{-6}\frac{Kg}{mm\,s}} \sim 0.1 \qquad (2.7)$$

which is well within the laminar flow regime.

2.1.4 Stokes equation

If no external time-dependent perturbation is applied, then $T_0 = \frac{L_0}{U_0}$ and $St = 1$: in a microfluidic systems where $Re \ll 1$, then $\frac{Re}{Ru} \sim 1$ to apply the mass conservation constraint. The Navier-Stokes equation then simplifies into the Stokes equation [70]:

$$-\nabla p + \mu_0 \nabla^2 u = 0 \qquad (2.8)$$

$$\nabla \cdot u = 0 \qquad (2.9)$$

2.1.5 Boundary conditions

Boundary conditions (BC) are required to solve the differential Stokes equation. Here are presented some of the most commonly used BC for different boundaries:

- No-Slip: for a flow along a smooth wall it is assumed that fluid particles do not move with respect to the wall. If the wall is still, then fluid particles will be still. If the wall is moving, fluid particles will move with the same velocity of the wall.

$$u_x^{STILL\,WALL} = 0 \qquad (2.10)$$

$$u_x^{MOVING\,WALL} = u^{WALL} \qquad (2.11)$$

- No-Stress: for a flow along a gas surface it is assumed that no shear stress is applied.

$$\frac{\partial u_x^{GAS}}{\partial y} = 0 \qquad (2.12)$$

- Slip-Length: for a flow along a rough wall the contact will be formed by regions of liquid/wall and regions of liquid/trapped air, therefore the result will be a mixture of the previous BC. An empirical parameter called slip length l which represents the amount of slip can be defined.

$$u_x^{SLIP} = -l\frac{\partial u_x}{\partial y} \qquad (2.13)$$

- Impermeability: no flow into the wall is allowed.

$$u_y^{IMPERMEABILITY} = 0 \qquad (2.14)$$

2.1.6 Poiseuille flow profile

Consider the system in Figure 2-2, which shows water flowing in a microchannel of height 2h. The walls are still, impermeable and infinitely along the z-axis. The flow is driven by the pressure difference P1-P2.

Figure 2-2 Schematic for the pressure-driven flow between two still plates. The origin of the y-axis is in the centre of the channel. The channel height is 2h. Pressure P1 is applied at one end and pressure P2 is applied on the other.

To find the velocity profile, the Stokes equation must be solved:

$$\frac{\partial u_x}{\partial x} + \frac{\partial u_y}{\partial y} = 0 \qquad (2.15)$$

$$\mu\left(\frac{\partial^2 u_x}{\partial x^2} + \frac{\partial^2 u_x}{\partial y^2}\right) = \frac{\partial p}{\partial x} \qquad (2.16)$$

$$\mu\left(\frac{\partial^2 u_y}{\partial x^2} + \frac{\partial^2 u_y}{\partial y^2}\right) = \frac{\partial p}{\partial y} \qquad (2.17)$$

The boundary conditions are:

- No-slip on the wall

$$u_{x,(y=-h)} = 0 \qquad u_{x,(y=h)} = 0$$

- Impermeability of the wall

$$u_{y,(y=-h)} = 0 \qquad u_{y,(y=h)} = 0$$

- Pressure

$$p_{(x=0)} = p_1 \qquad p_{(x=L)} = p_2$$

From symmetry *u=u(y)*. This means that the velocity depends only on the y-axis. Therefore, the mass balance becomes:

$$\frac{\partial u_y}{\partial y} = 0 \qquad (2.18)$$

which when integrated considering the impermeability boundary conditions, yields:

$$u_y = constant = 0 \qquad (2.19)$$

The equation with the u_y components of the Laplace operator gives:

$$\frac{\partial p}{\partial y} = 0 \qquad (2.20)$$

Which means that the pressure is only a function of the x-axis. The two partial derivatives in the Equation 2.17 are now total derivatives, becoming:

$$\mu\frac{d^2 u_x}{dy^2} = \frac{dp}{dx} \qquad (2.21)$$

The term on the left is a derivative with respect to the y-axis, whereas the term on the right is a derivative with respect to the x-axis: the only solution for this equation is for both terms to be constant.

$$\mu\frac{d^2 u_x}{dy^2} = \frac{dp}{dx} = Const_1 \qquad (2.22)$$

Integrating the pressure:

$$p = Const_1\, x + Const_2 \qquad (2.23)$$

Using the boundary conditions for the pressure:

$$Const_2 = p_1 \qquad Const_1 = \frac{p_2 - p_1}{L} = \frac{\Delta p}{L} \qquad (2.24)$$

Integrating the velocity:

$$\frac{du_x}{dy} = \frac{Const_1}{\mu}\, y + Const_3 = \frac{\Delta p}{\mu\, L} y + Const_3 \qquad (2.25)$$

$$u_x = \frac{\Delta p}{2\mu\, L} y^2 + Const_3 y + Const_4 \qquad (2.26)$$

Using the boundary conditions for the velocity:

$$Const_3 = 0 \qquad Const_4 = -\frac{\Delta p}{2\mu\, L} h^2 \qquad (2.27)$$

The velocity profile becomes:

$$u_x^{PLATES} = \frac{\Delta p}{2\mu\, L}(y^2 - h^2) \qquad (2.28)$$

Which is the parabolic Poiseuille flow profile observed for flow between two parallel plates as shown in Figure 2-3 [71]. The total flow rate can be found by integrating the velocity profile over the cross-section (d is the depth of the channel):

$$Q^{PLATES} = 2\int_0^h u_x^{PLATES}\, d\, dy = \frac{2\, d\, h^3}{3\,\mu}\frac{\Delta p}{L} \qquad (2.29)$$

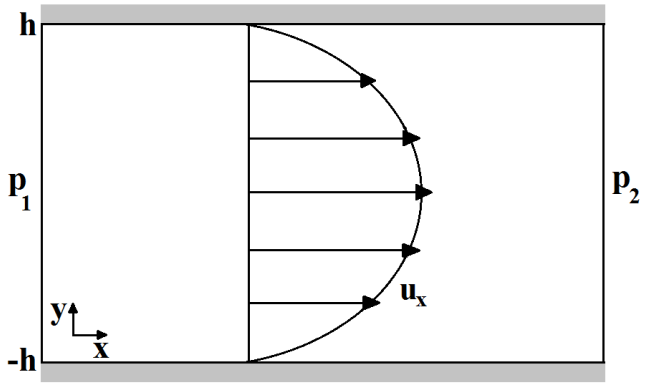

Figure 2-3 Poiseuille parabolic flow profile for a pressure-driven flow between two still parallel plates.

The same procedure can be applied to find the laminar profile in a pipe of diameter R:

$$u_x^{PIPE} = \frac{\Delta p}{4\mu\, L}(r^2 - R^2) \qquad (2.30)$$

Which can be integrated to find the equation for the pressure drop:

$$\frac{\Delta p}{L} = \frac{128\,\mu\, Q}{\pi\, D^4} \qquad (2.31)$$

where $D = 2R$ is the diameter. The pressure drop depends on the fourth power of the diameter: if the diameter is halved, a 16-fold pressure difference is required to obtain the same flow rate.

2.1.7 Diffusion

Consider two species of gas placed inside a box and separated by an impermeable septum as in Figure 2-4. Inside each compartment gas molecules experience random motion due to thermal agitation. When a molecule hits a wall or the septum, it bounces off elastically. When the septum is removed, the two compartments are no longer separated and the molecules that would have bounced off the septum will now move into the other compartment. The molecules will mix due to fluctuations of the thermal random motion. The steady state will be reached when the number of molecules moving from one compartment to the other is statistically equivalent: this only happens when the concentration of each is species is the same across all the system. This process is called diffusion.

The diffusive flux of a species A into a species B can be quantified from Fick's law as [72]:

$$J_A^{Diff} = -D_{AB}\frac{dC_A}{dx} \qquad (2.32)$$

Where J_A^{Diff} is the diffusive flux of the species A $\left[\frac{mol}{s \cdot m^2}\right]$, C_A is the concentration of the species A$\left[\frac{mol}{m^3}\right]$, and D_{AB} is the diffusivity (or diffusion coefficient) of the species A in the species B $\left[\frac{m^2}{s}\right]$. The minus sign in front of the second term means that the flux is from regions of high concentration towards regions of low concentration.

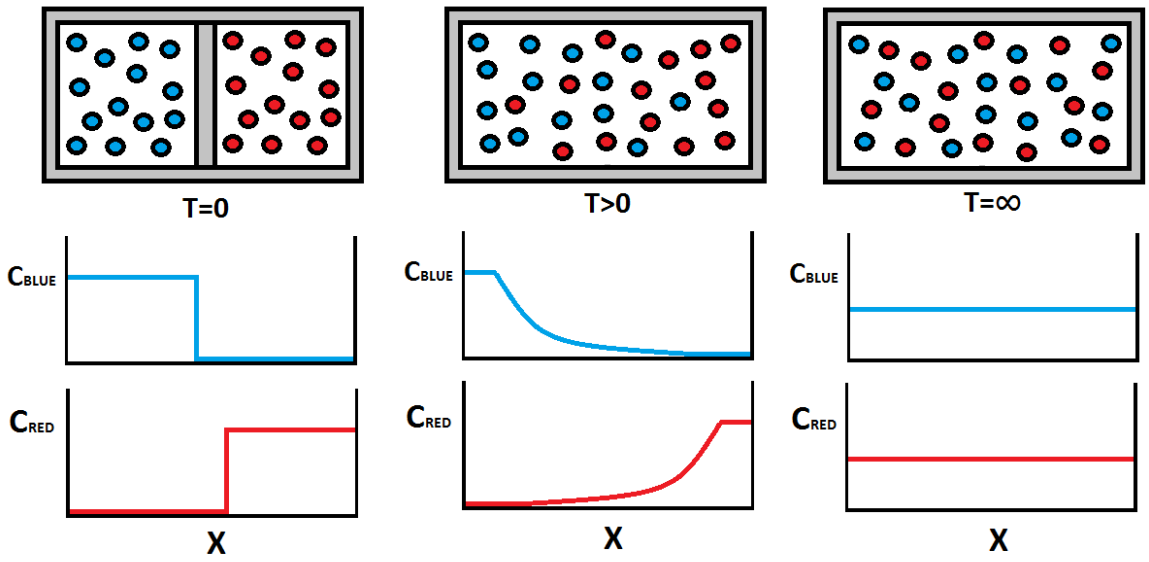

Figure 2-4 Diffusion process - Two different species of gas are placed inside a box and separated by a septum. Inside each compartment the gases are experiencing random motion due to thermal fluctuations and are bouncing on the walls. When the septum is removed the gases will no longer be able to bounce on the septum and they will start mixing due to thermal fluctuations. The steady state is reached when the concentration is uniform in the system.

The diffusivity D_{AB} :

- Is not symmetrical ($D_{AB} \neq D_{BA}$). This means that the diffusivity of the component B into component A is not equal to the diffusivity of the component A into component B.
- Depends on the temperature. The higher the temperature is, the more thermal agitation the molecules will experience, leading to faster diffusion and higher diffusivity.

Analysing Brownian motion, Einstein developed an equation (the second moment of the solution for the density to the diffusion equation) that relates the diffusion coefficient, time and mean squared displacement [73]:

$$\overline{x^2} = 2Dt \qquad (2.33)$$

Which states that the displacement that molecules will on average experience is proportional to the diffusivity and to the time squared. A Gaussian concentration impulse increase its variance over time due to diffusion, and reaches the steady state when the concentration is uniform across the domain.

2.1.8 Péclet number

A fluid in a microchannel will undergo the combined effects of diffusion and convection (i.e. the transport by bulk motion). A dimensionless number that indicates the relative importance of the two effects is the Péclet number, defined as [70]:

$$Pe = \frac{U_0 L_0}{D} = \frac{\tau_{diff}}{\tau_{conv}} \qquad (2.34)$$

Where $\tau_{diff} = \frac{L_0^2}{D}$ is the characteristic diffusion time and $\tau_{conv} = \frac{L_0}{U_0}$ is the characteristic convection time. If *Pe* is small the characteristic transport time of diffusion is small and diffusion will strongly affect the system; vice-versa if *Pe* is high convection will prevail and diffusion will be negligible. At the microscale Péclet numbers are usually 10^2-10^4 times smaller than at the macroscale, therefore diffusion effects can't be neglected [74].

2.1.9 Total dispersion

The parabolic Poiseuille flow leads to dispersion of a solute. As an example, consider the temporal evolution of a flow in a horizontal pipe with an initial concentration impulse. After a given time unit, the distance travelled by the solute in the centre of the pipe will be greater compared to the distance travelled by the solute close to the walls. The solute spreads, and is no longer contained in a single section. This dispersion combines with the dispersion induced by diffusion. This synergic effect was studied by Taylor and Aris [75, 76] who found that for a cylindrical pipe it is possible to introduce an effective diffusivity:

$$D_{EFF} = D\left(1 + \frac{Pe^2}{192}\right) \qquad (2.35)$$

which takes into account both effects. The effective diffusivity is always bigger than the normal diffusivity, and it increases with increasing Péclet number (higher velocities lead to a greater dispersion induced by the parabolic profile).

2.2 Electrical measurement of biological systems

The organ-on-a-chip described in this work will perform electrical measurements of an epithelial tissue. In this section the basics of electrical measurement of biological systems as well as specific aspects of measuring epithelial cells are discussed.

In direct current (DC) measurement, a constant potential difference is applied. All the capacitors in the system are completely charged and act as open circuits. The amount of current flowing is affected only by the resistive components and is proportional to the applied voltage:

$$I = \frac{V}{R} \qquad (2.36)$$

where *R* is the resistance of the system. In alternating current (AC) measurements, the impedance depends on the frequency of the applied signal:

$$I(f) = \frac{V(f)}{Z(f)} \qquad (2.37)$$

Analysis of the frequency dependence of the complex impedance can be used to characterise the different components of the system.

2.2.1 Geometric cell constant

The current flowing in an electrolyte depends on the applied voltage, on the solution conductivity and on the geometry of the electrodes. For two infinite planar electrodes facing each other (Figure 2-5), the resistance and capacitance is related to the dimensions according to:

$$R = \frac{d}{\sigma A} \qquad C = \varepsilon_0 \varepsilon_r \frac{A}{d} \qquad (2.38)$$

where, d is the distance between the plates, A is the surface area of each plate, σ is the solution conductivity, ε_0 and ε_r are the vacuum and the relative dielectric constant respectively. The geometrical parameters can be grouped into a single term called geometric cell constant K:

$$K = \frac{d}{A} \qquad (2.39)$$

It follows:

$$R = \frac{K}{\sigma} \qquad C = \frac{\varepsilon_0 \varepsilon_r}{K} \qquad (2.40)$$

In practical cases it is impossible to determine exactly the cell constant due to fringing field effects and a calibration with a solution of known conductivity or numerical simulations are used for its determination.

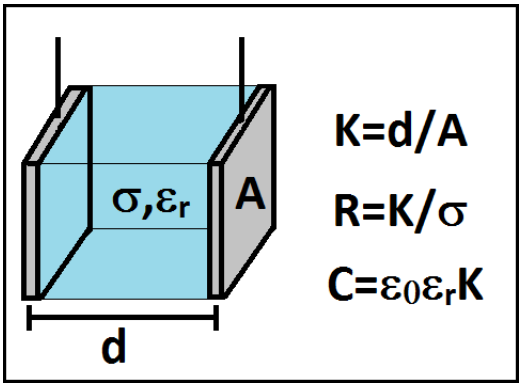

Figure 2-5 Schematic diagram of a simple electrolytic cell with two electrodes with area A, distant d, and medium electrolyte with conductivity σ and relative permittivity ε_r.

2.2.2 Thermal effects

The conductivity of an electrolyte is dependent on the ability of the ions in solution to transport charge across the system. This ability is affected by the number of ions present and by their mobility inside the solution, according to the equation [77]:

$$\Lambda_m^0 = (z_+\mu_+\nu_+ + z_-\mu_-\nu_-)F \qquad (2.41)$$

where Λ_m^0 is the infinite dilution molar conductivity, F is the Faraday's constant, ν is the number of ions, z is their valence, μ is their mobility and the subscript indicates the sign of their charge. Temperature variation can affect both the number of ions and their mobility:

- For pure water or weak acids/bases the temperature affects the dissociation constant and thus the number of ions present in solution.
- The temperature affects the random thermal fluctuations and thus the ability of an ion to move through the system.

To account for conductivity variations due to thermal effects, an empirical approach is based on fitting experimental resistivity data with an exponential function [78]:

$$\rho(T) = e^{A+\frac{B}{T}+\frac{C}{T^2}+\frac{D}{T^3}} \qquad (2.42)$$

Where ρ is the resistivity of the solution, A, B, C, D are empirical constants and T is the absolute temperature. The use of four terms in the exponential yields accurate value in the range 0-300°C. For small temperature variations, a simplified linear approach can be used for the conductivity σ:

$$\sigma_t = \sigma_0(1 + \alpha\,\Delta T) \qquad (2.43)$$

For fresh water at 25° it is assumed α =2 %/°C [79].

2.2.3 Electrode polarisation

Electrochemical reactions occur between an electrolyte and an electrode immersed in it. The quality and quantity of these reactions depend on the nature of the electrode and on the electrolyte.

Non-polarisable electrodes

An electrode is defined as ideally non-polarizable if its potential is independent of the current flowing through it. An electrode which has a behaviour similar to the ideally non-polarizable is the silver/silver-chloride (Ag/AgCl) electrode. This electrode is formed by a silver wire coated with its salt. The redox reaction:

$$AgCl(s) + e^{-} \Leftrightarrow Ag(s) + Cl^{-} \qquad (2.44)$$

occurs at the electrode when an electric potential is applied. This reaction is characterised by very fast kinetics: when a charge reaches the interface, it is immediately transferred into the electrolyte. Thus, no accumulation of charge is present at the interface and no polarisation occurs. This electrode is not well-suited for impedance spectroscopy of biological system because of the production of cytotoxic silver ions [80].

Polarisable electrodes

An electrode is defined as ideally polarizable if there is no Faradaic current (i.e. current generated by oxidation or reduction of molecules at the electrodes) flowing at the interface with the electrolyte. An electrode which is close to being ideally polarizable is the platinum (Pt) electrode. When an electric potential is applied, charge will accumulate at the interface. This charge will exert forces on the ions present in solution, causing their redistribution across the system to create an electrical double layer as shown in Figure 2-6 [81]. In biological measurements, this phenomenon is not desirable as this redistribution of ions will shield the bulk system from the applied electric field and completely dominate the signal at low frequencies (Figure 2-6). A complete understanding of this phenomenon has not yet been achieved, but physical and circuit models have been proposed.

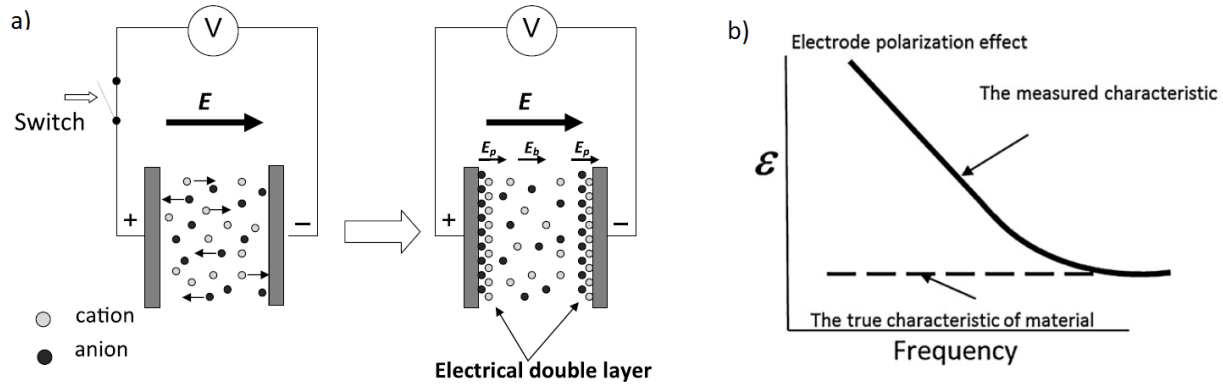

Figure 2-6 Effects of electrode polarisation, Ishai *et al.* [81]. a) Redistribution of the ions in the electrolyte under the application of an electric field. b) Comparison between true and measured characteristic for a measurement affected by electrode polarisation.

Physical models of the electrical double layer

Several models have been proposed to obtain the macroscopic behaviour of the system considering interactions on the microscopic level. The first model to describe the phenomenon was proposed by Helmholtz [82]. In this model the charges on the electrode attract ions with opposite charge from the solution. This attraction leads to the formation of a layer of adsorbed ions close to the surface of the electrode (Figure 2-7). Due to the presence of two layers of ions facing each other, this phenomenon is called an electrical double layer (EDL). The two facing layers of ions behave like a capacitor and the electric potential undergoes a linear drop in the region between them.

Another model was proposed by Gouy-Chapman [83]. They found that the constant capacitor model was not accurate enough. They considered a concentration of the ions which followed the Boltzmann distribution: the equilibrium between electrostatic attractions and diffusive thermal fluctuations in the system is then described by the Poisson-Boltzmann equation. Considering a charged plate with infinite extension along the y and z axes submerged in an electrolyte, the Poisson equation describing the electric potential Φ deriving from a charge density ρ is:

$$\rho_x = -\varepsilon_0 \varepsilon_r \frac{d^2\Phi(\mathrm{x})}{dx^2} \qquad (2.45)$$

whereas the Boltzmann distribution for the ions in the solution is:

$$\rho_x = N_A\, q\, \sum_i C_i^{bulk}\ \ z_i\, e^{\frac{-z_i\, q\, \Phi(x)}{k_B T}} \qquad (2.46)$$

where k_B is Boltzmann's constant, q is the charge of the electron, C_i^{bulk} is the concentration of an ion species in the bulk of the system, T is the temperature, N_A the Avogadro's number, z the valence of an ion species and the sum is extended to all the *i*-species of ions present in the solution. Combining the two equations:

$$\frac{d^2\Phi(x)}{dx^2} = \frac{N_A q}{\varepsilon_0 \varepsilon_r} \sum_i C_i^{bulk}\ \ z_i\, e^{\frac{-z_i\, q\, \Phi(x)}{k_B T}} \qquad (2.47)$$

which is the Poisson-Boltzmann equation for the system that defines the change in potential and charge with distance from the electrode. Considering only one ionic species ($|z^+| = |z^-|$), under the assumption of low potential ($q\,\Phi < k_B T$) and using the boundary conditions:

$$\begin{cases} x \to \infty & \Phi(x) = 0 \\ x \to \infty & \frac{d\Phi(x)}{dx} = 0 \end{cases} \qquad (2.48)$$

the differential equation can be solved analytically. The solution for the potential at a distance x from the charged plate is:

$$\Phi(x) = \Phi_0\ e^{-\frac{x}{\lambda_D}} \qquad (2.49)$$

where $\Phi_0$is the potential on the charged surface and $\lambda_D$is the Debye's length, defined as:

$$\lambda_D = \sqrt{\frac{\varepsilon_0 \varepsilon_r k_B T}{2 N_A\, q^2\, z_i\, C_i^{bulk}}} \qquad (2.50)$$

In this model, close to the electrode there is a diffuse layer with an exponentially decreasing concentration of ions. The Debye length characterizes the extension of the diffuse layer and the rate of the exponential decay of the potential form the plate.

A third model proposed by Stern combines the main features of the two previous models (Figure 2-7) [84]. Moving from the electrode surface towards the bulk solution the effects considered by this model are:

1. A layer of ions with the same charge of the electrode. These ions are specifically adsorbed on the electrode (Inner Helmholtz Plane).
2. A layer of solvated counter-ions held in place by electrostatic forces (Outer Helmholtz Plane).
3. A diffuse layer with an exponentially decreasing concentration of ions.

In this model the electric potential undergoes a linear drop in the first two layers and an exponential drop in the diffuse layer.

Electrical models

Circuit models derived from experimental data have been developed to characterize the electrode polarisation [85]. An evolution of Helmholtz's constant capacitor model was developed by Warburg [86]. This model was developed under the hypothesis of infinitely low current density and is based on a resistor and a capacitor in series. It states that the polarisation capacitance is inversely proportional to the square root of the frequency and that the phase angle of the system is constant and equal to 45°. Analysing experimental data, Fricke found that the Warburg model had limited applicability; to improve the model he proposed that the phase angle must be constant but it may be different from 45° [87]:

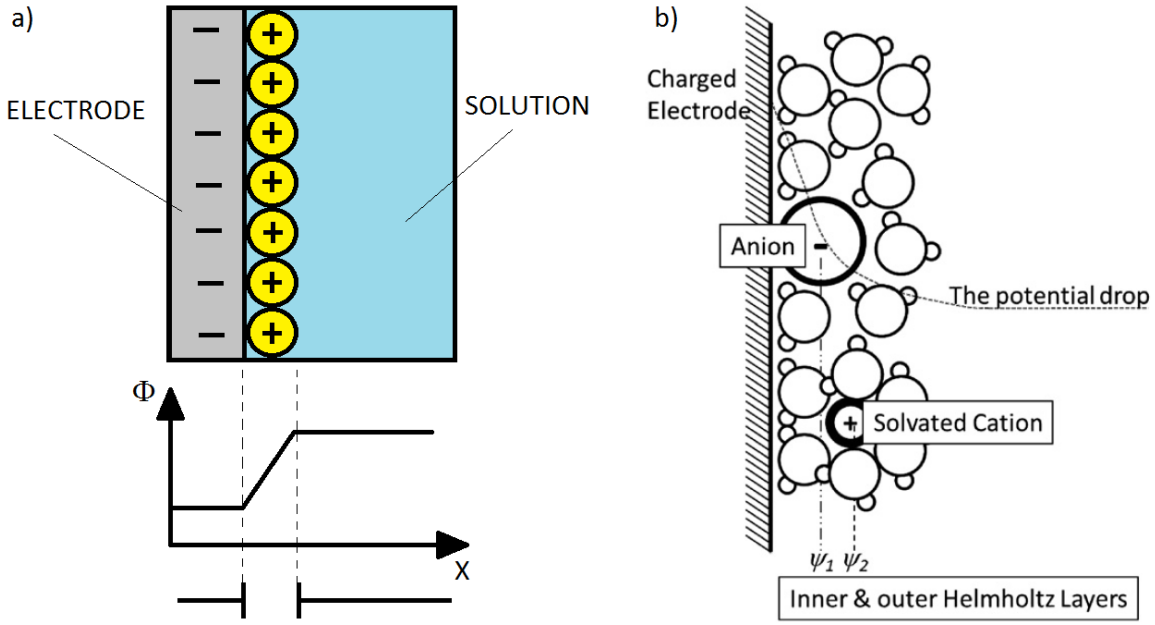

Figure 2-7 Two physical models for the electrical double layer. a) Helmholtz model: two layer of ions with opposite charge facing each other; b) Stern model by *Ishai et al.* [81]: a layer of specifically adsorbed ions with the same charge as the electrode (Inner Helmholtz plane), a layer of solvated counter-ions (Outer Helmholtz plane) and a layer of diffuse ions.

$$\zeta = \frac{m\pi}{2} \qquad (2.51)$$

$$C = \frac{k}{(2\pi f)^m} \qquad (2.52)$$

where ζ is the phase angle and m and k are constants which depend on the electrode metal. For the case m=0.5 the Fricke model reduces to the Warburg model. To satisfy equations 2.51 and 2.52 the polarisation resistance in series must be:

$$R = \frac{1}{k(2\pi f)^{1-m}\ \tan(\frac{m\pi}{2})} \qquad (2.53)$$

In the Fricke model the parameter m controls the overall response of the system:

- For m=1 the system is purely capacitive:

$$\zeta = \frac{\pi}{2} \qquad C = \frac{k}{2\pi f} \qquad R = 0$$

- For m=0 the system is purely resistive:

$$\zeta = 0 \qquad C = k$$

Both the Warburg and the Fricke models are composed of a resistor and a capacitor in series, thus in none of them is direct current allowed. Experimental evidence showed that m usually varies between 0.15 and 0.32 for a wide range of metals. The Fricke model is experimentally validated for low current densities and for frequencies in the range 100 - 3500 Hz. The Warburg and Fricke model are shown in Figure 2-8.

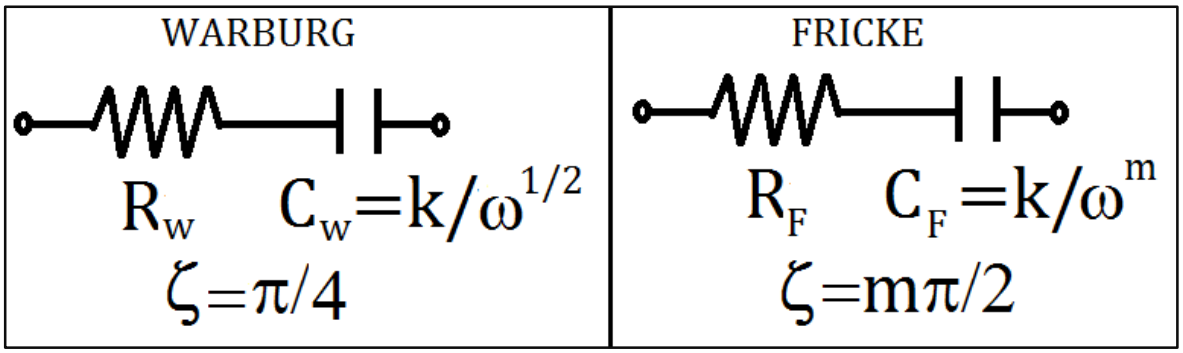

Figure 2-8 Electrical models for electrode polarisation. (Left) Warburg model (ζ=45°) and (Right) Fricke model ζ=constant). For m=1/2 the models are equivalent.

Effects of current density

All the models presented so far are based on the hypotheses of low applied potentials/current densities. Experimental evidence shows that the polarisation impedances have a current density threshold (for platinum electrodes it is approximately 0.1 mA/cm^2) as shown in Figure 2-9 [88]. For values below the threshold the polarisation impedance is not affected by the current density [89, 90]. For values above the threshold the polarisation capacitance increases and the resistance decreases with the current density. At high current densities the overall polarisation impedance is decreased and it affects the measurement to a lesser extent.

Polarisation correction

In biological measurements it is not common to use Ag/AgCl electrodes due to silver cytotoxicity. Instead, the use of polarizable electrodes such as platinum is widespread due to its good

cytocompatibility. Thus, electrode polarisation is a common problem in biological studies that needs to be addressed. Two possible solutions are presented:

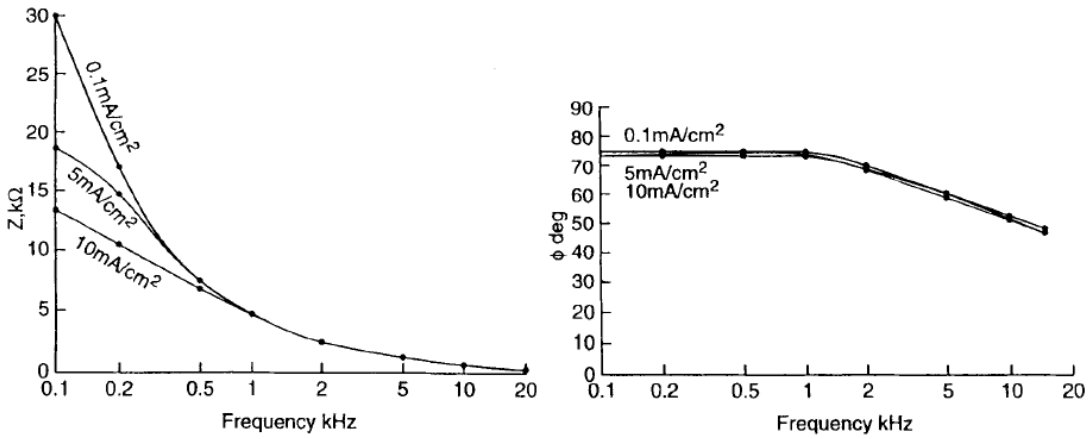

Figure 2-9 Effects of the current density on the electrode polarisation for Pt electrodes by Geddes [85]. While the phase angle is not affected, the magnitude of the impedance is decreased for higher current densities.

Four-electrode technique

In this approach two pairs of electrodes are used as shown in Figure 2-10. The first pair is used to drive a constant current through the system, and the second pair is used to measure the electric potential drop across the sample. If no current is drawn in the potential-measuring electrodes, then all the measured potential drop is localised across the sample, excluding polarisation effects from the measurement [81]. To ensure that no current flows in the potential-measuring electrodes, voltmeters with high input impedances are used.

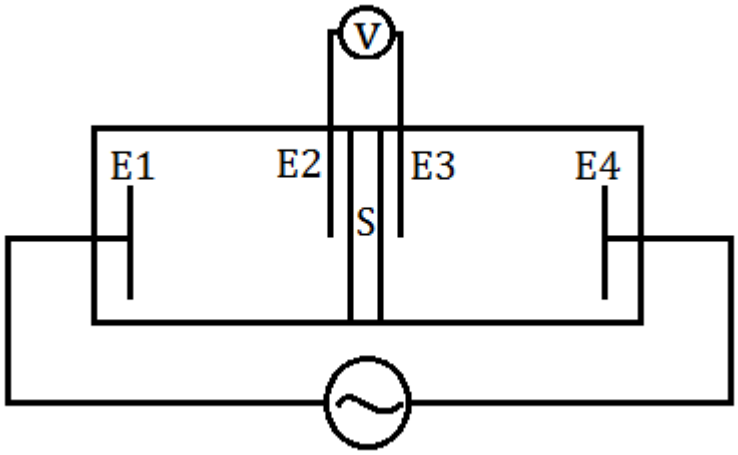

Figure 2-10 Four electrodes technique for polarisation correction. To measure the impedance of the sample S accurately, a constant current is flown between electrodes E1-E4 and the resulting potential drop between E2-E3 is measured.

Electrode coatings

To a first approximation, the double layer impedance can be considered as a capacitor in series with the system. Thus, it is possible to reduce the influence of the electrode polarisation on the measurement by increasing the electrode capacitance. This can be done by increasing the surface area of the electrodes. If the footprint of the electrodes can't be increased during the design, it is possible to coat the electrodes with porous material to increase the apparent surface area [81].

Several materials have been used to achieve this goal such as platinum black, titanium nitride (TiN), iridium oxide (IrOx) and polypyrrole/polystyrenesulfonate (PPy/PSS) [91]. The resulting polarisation capacitances were found to be increased by factors included in the range 75-790.

2.2.4 Nanoporous support

During the measurement of epithelial cells in organ-on-chip systems, the polymeric supports for tissue culture constitute an additional electrical resistance to be considered. The supports have nanopores with a size usually equal to 400nm in diameter which allow the perfusion of nutrients.

The electrical resistance of the pores has two components: one proportional to the field inside the pore and one due to the restricted access to the pore as shown in Figure 2-11.

$$R_{tot} = R_{pore} + R_{access} \quad (2.54)$$

The resistance inside the pore can be calculated simply as a cylindrical resistor:

$$R_{pore} = \frac{L}{\sigma A} = \frac{L}{\sigma \pi a^2} \quad (2.55)$$

where ρ is the resistivity of the solution inside the pore, while L and a are the length and the radius of the pore respectively. Several formulations have been developed to estimate the access resistance of a small circular pore:

- Hille [92] approximated the access surface of the pore as a hemisphere with the same radius. He computed the resistance from infinity to the hemisphere as:

$$R_{access}^{Hille} = \int_a^{\infty} \frac{1}{2\pi\sigma r^2} dr = \frac{1}{2\pi\sigma}\left[-\frac{1}{r}\right]_a^{\infty} = \frac{1}{2\pi\sigma a} \quad (2.56)$$

- Hall [93] calculated the access resistance using the transformation between resistance in conducting media and capacitance in insulating media under the assumption that the resisting medium fills the same medium that the electric field would [94]:

$$R = \frac{\varepsilon\rho}{C} \quad (2.57)$$

and then considering half the capacitance of a charged conducting disk which is:

$$\frac{C_{ChargedConductingDisk}}{2} = 4\varepsilon a \quad (2.58)$$

obtaining:

$$R_{access}^{Hall} = \frac{1}{4\sigma a} \quad (2.59)$$

The Hall access resistance is bigger than the Hille resistance of a factor π/2 which corresponds to a 60% larger value.

The total pore resistance is then:

$$R_{tot} = \frac{1}{\sigma a}\left(\frac{L}{a\pi} + \frac{1}{2}\right) \qquad (2.60)$$

where the access resistance has been doubled to take into account both pore ends. The total resistance is controlled by the pore radius for short pores and by the pore length for long pores. In a typical polymeric support for cell culture the pore radius is 200 nm and the pore length (i.e. the membrane thickness) is 12 µm: the access resistance (with σ =1.5 S/m) is R_{access}~1MΩ, while the pore resistance is R_{pore}~10MΩ.

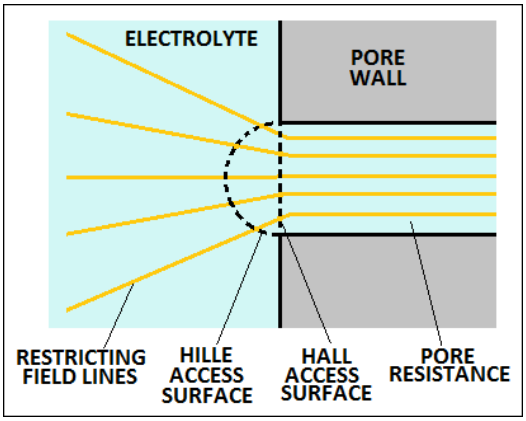

Figure 2-11 Electrical resistance of a small circular pore. An access resistance resulting from restricting electric field lines is present in addition to the pore resistance. Hille [92] and Hall [93] presented two methods to compute this additional component.

2.2.5 Cell layer structure

To analyse the electrical response of a cell layer it is necessary to develop a model for its structure, which is formed from both insulating and conductive components (Figure 2-12). An epithelial cell culture is formed from a layer of closely packed cells which are held together by complexes of proteins. These TJs regulate the passage of ions and act as resistors when an external electric field is applied. Each cell is formed from an outer phospholipid bilayer which is hydrophobic and prevents the passage of water molecules and ions. Inside the cell the cytosol which is a water-based conductive fluid. In the inner part of the cell, there is the nuclear membrane, which is another hydrophobic phospholipid bilayer, which separates the conductive cytosol-based DNA compartment from the rest of the cell.

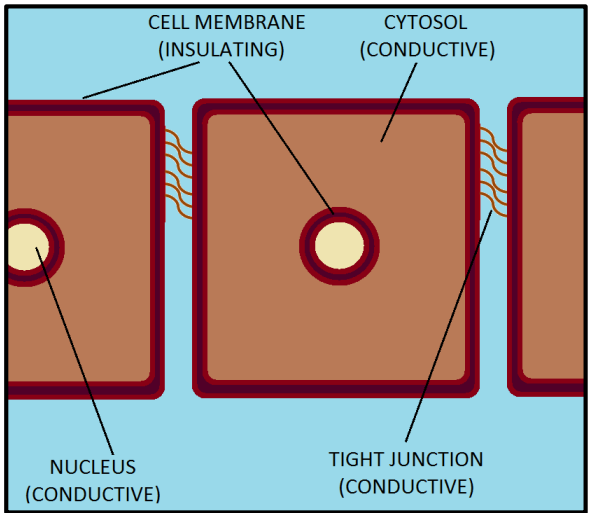

Figure 2-12 Schematic of electrical components of an epithelial cell layer. An insulating cell membrane surrounds the cell and the nucleus. The cytosol inside cells and the nuclei is conductive. TJs between cells regulate the passage of ions and are conductive.

2.2.6 Epithelial cell culture spectrum

Consider an epithelial cell culture on a porous support stimulated with an AC signal by two electrodes positioned in the different compartments of the culture. The generic setup together with the typical impedance spectrum and the equivalent circuit model are shown in Figure 2-13 [37]. The system is formed of two capacitors (i.e. the electric double layer and the cell layer capacitance) and two resistors (i.e. the medium and the trans epithelial resistance TEER). At high frequencies, the two capacitors act as short circuit and the overall impedance depends only on the resistance of the medium. At low frequencies, the impedance is dominated by electrode polarisation. A plateau is seen at intermediate frequencies: its height depends on the TJ resistance and the resistance of the medium while its width is dictated by the cell layer capacitance. Impedance spectra of growing epithelial cultures will be analysed in greater detail in the following chapters.

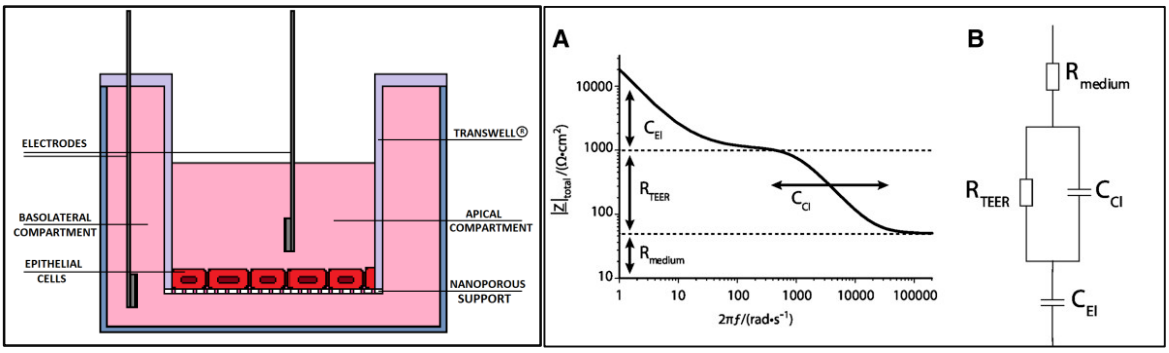

Figure 2-13 (Left) Typical setup for cell culture and TER measurement. (Right) Generic spectrum of the impedance for an epithelial cell culture and relative equivalent circuit model by Benson *et al.* [37]. At high frequencies the impedance of the system is dominated by the resistance of the medium, at intermediate frequencies by the resistance of the cell layer.

2.3 Chapter summary

This chapter examined two aspects of the theory of lab-on-a-chip, *i.e.* microfluidics and electrical measurement in biological systems.

The parameter that controls the fluidic behaviour of a system is the dimensionless Reynold number. Systems with Re bigger than 10^4 are described by Navier-Stokes equations and are subject to turbulence, while systems with Re smaller than 1 are in the laminar regime and can be described by the simpler Stokes equation. Most lab-on-a-chip devices operate in the laminar regime because their small scale translates into low Re. At low Re there is no turbulence, a closed steady-state solution for the flow exists and the flow is time-reversible. By solving the Stokes equations with no-slip boundary conditions on the wall, Poiseuille described the radial profile of the axial velocity for a pressure-driven flow in a cylindrical pipe. The resulting parabolic profile for the axial velocity is commonly used to compute the pressure drop for the flow in a pipe.

Diffusivity is another phenomenon that becomes important at the microscale. This phenomenon is caused by microscopic random motions of dispersed particles in solution that have the macroscopic effect of a tendency to reach homogeneity. The mean square displacement from the initial position over time due to diffusion can be quantified by Einstein's equation. Diffusion effects at the microscale can sometimes be as important as convection effects: the Péclet dimensionless number describes which of the two effects prevails in a given system. Both the Poiseuille parabolic profile and the diffusion process tend to cause dispersion of concentrations, in a synergistic effect described by Taylor-Aris.

Electrical effects that must be taken into account in measurements of biological systems were examined in the second section of this chapter. When an electric potential is applied between two electrodes submerged in an electrolyte, the resulting current depends on the system geometry, on the electrolyte conductivity and electrolyte permittivity. Temperature affects the mobility of ions in solution and thus affects the conductivity of the electrolyte with a variation of about 2 %/°C. The current flowing in an electrolytic cell also depends on the electrochemical phenomena that take place on the electrode surface. Polarizable electrodes are fully capacitive and do not allow the passage of direct current. When submerged in an electrolytic solution, a double layer of ions is formed at the electrode surface, shielding the system from the applied potential. Several models were proposed for this phenomenon, both theoretical and circuital. The first theoretical model consisting of behaviour of the ions similar to a parallel plate capacitor was proposed by Helhmoltz. Gouy and Chapman assumed that ions had an equilibrium distribution described by the Poisson-Boltzmann equation. Stern proposed a combination of the two previous models where the ions follow a linear distribution in proximity of the electrode surface and decay exponentially far from it. Circuit models describe this phenomenon with equivalent electric circuits showing similar behaviour. The first model proposed by Warburg is based on the series of a resistor and a capacitor with a constant phase angle for all systems, equal to 45°. Fricke improved the model by assuming that the constant phase angle could vary for different systems. In both models the passage of direct current is not permitted. Practically, electrode polarisation can affect the quality of the measurement and is avoided by electrode surface modifications or by performing 4 electrode measurements. When measuring the impedance of a tissue cultured on a nanoporous support, the current access resistance to the support holes must be considered in addition to the pore resistance. Hille and Hall gave two formulas to compute this added quantity.

Lastly, the electrical behaviour of cellular components was analysed. Cells and nuclei are enclosed by phospholipid membranes which act as insulators. The cytosol inside the cell is a conductive solution. Between epithelial cells, TJs regulate the passage of ions and are resistive components. The total impedance of the system is the sum of all these components and is low at high frequencies where the cell membrane is a short circuit and high at low frequency where the cell membrane is an open circuit and the current passes between the cells through epithelial TJs.

Chapter 3: Device Design

The aim of this project is to develop a microfluidic device for the culture and electrical analysis of epithelial barrier properties. The schematic of the microfluidic device is shown Figure 3-1. A circular nanoporous polymeric membrane is suspended on top of a microchannel 0.1 mm high. Cells are cultured on top of the nanoporous membrane. They receive nutrients from lateral diffusion of the medium perfused in the microchannel through the nanopores of the membrane (basolateral compartment). The cell apical compartment is defined by a polymeric structure and is open-access to allow the stimulation of the culture with chemicals during an experiment. It can be filled with liquid or with air, depending on the type of cells. Inlet and outlet ports are present in the same polymeric structure and have integrated tubing for connection with external equipment. The liquid is pumped using a syringe pump and is collected at the outlet in a collection tank. Long tubing connects the pump to the device and the device to the collection tank. Two pairs of electrodes are integrated on the bottom of the microchannel, one directly underneath the culture chamber (barrier) and one upstream of the culture chamber in the inlet channel (reference). Part of the electric field lines generated by the electrodes under the culture chamber flow in the channel and part flow through the cell layer. The total impedance measured by this electrode pair depends on the electrical properties of the cells and is used to monitor the status of the cell culture in terms of barrier properties. The electrodes in the inlet channel are distant from the culture chamber and are not affected by variation in the cell culture properties and are used as reference. The two pairs of electrodes are routed to one edge of the chip where they can be contacted by spring-loaded connectors for connection with the rest of the equipment. A three-dimensional rendered model of the target device is shown in Figure 3-2. In the following sections the design of the microfluidic channel and of the electrodes are examined in detail.

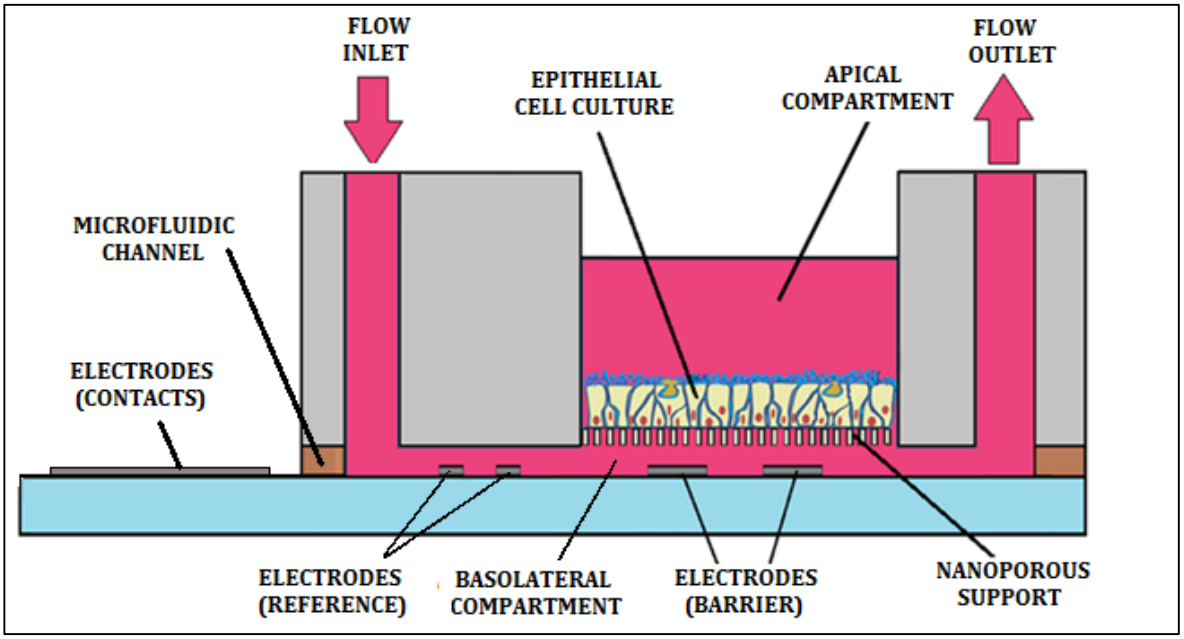

Figure 3-1 Schematics of the device: epithelial cells are cultured on a nanoporous support and nutrients are provided by the medium flowing in a microfluidic channel placed in the basolateral compartment. The apical compartment can be submerged or exposed to the air. Planar electrodes are integrated on the bottom of the channel under the support to measure the electrical properties of the culture.

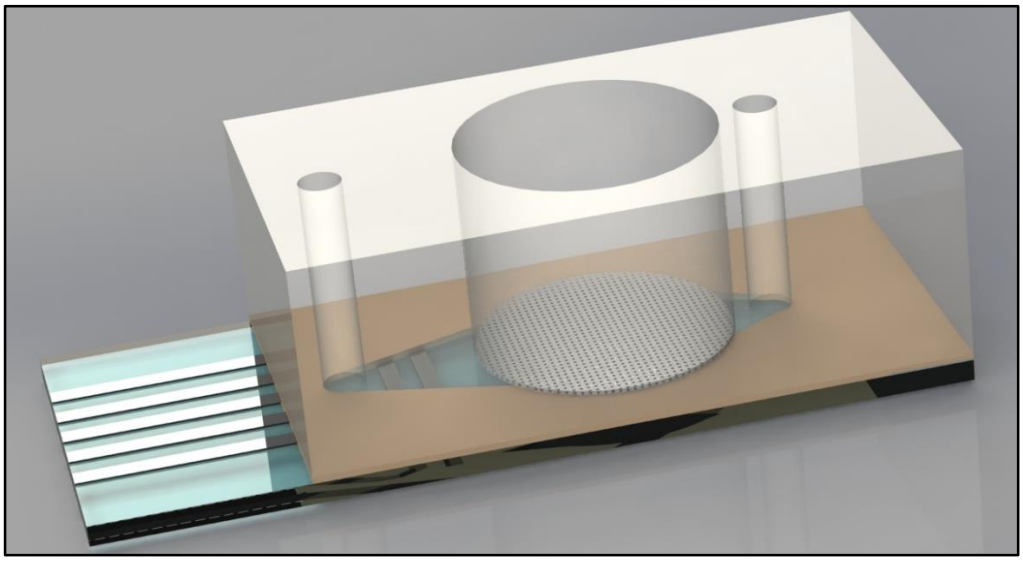

Figure 3-2 3D rendered model of the epithelia-on-a-chip. Platinum electrodes integrated on a glass chip measure the electrical properties of a tissue cultured on a polymeric nanoporous support. The tissue is fed by constant perfusion of medium in an underlying microfluidic channel.

3.1 Fluidic Design

The design of the microfluidic channel should provide a homogenous flow across the system with the lowest probability to trap air bubbles, in a compact space with minimum pressure variation across the cell.

3.1.1 Microchannel dimensions

The dimensions of the microchannel are shown in Figure 3-3. The culture chamber diameter is set to 5 mm, which is similar to the commercial Transwell® support (6.5 mm) but keeps the chip compact. The inlet and outlet diameters are 1.2 mm to ensure ease of connection to the external world. The inlet channel length is set to 3 mm to allocate the space for the conductivity electrodes. The outlet channel length is set to 1.6 mm to keep the device compact and reduce the backpressure on the culture chamber. The channel sidewalls are slanted to reduce discontinuities in the system and prevent possible stagnation points for air bubbles. The channel width at the midpoint is 2.5 mm. The channel height is 0.1 mm. This height is the minimum that was possible to reliably manufacture.

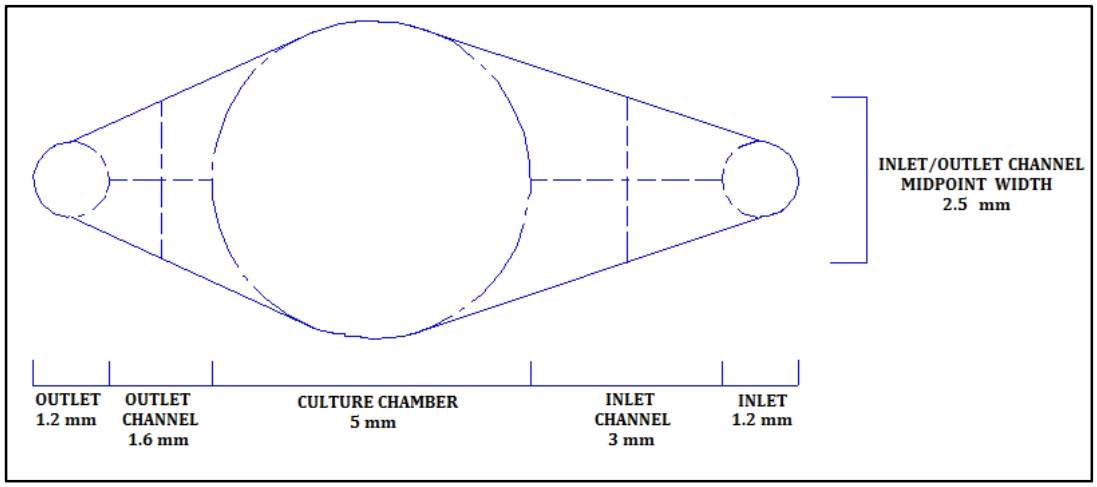

Figure 3-3 Technical drawing of the microchannel (dashed lines are for reference). Inlet and outlet are designed for connection with standard tubing. The size of the culture chamber is similar to the commercial Transwell®. The outlet channel is shorter than the inlet channel to reduce backpressure on the culture chamber. Channel walls are slanted to reduce stagnation points for bubbles.

3.1.2 Flow profile

The flow rate is set to 30 µl/hr to achieve a velocity in the channel in the range of the physiological interstitial flows (0.1-4 µm/s) [95, 96].

The resulting Reynolds number in the chamber is:

$$Re = \frac{\rho \frac{Q}{A} d}{\mu} = \frac{10^{-6} \frac{kg}{\mu l} \; \frac{30 \frac{\mu l}{hr}}{0.5 \; mm^2} \; 5 \; mm}{10^{-6} \frac{Kg}{mm \; s}} = 0.08$$

which is in the laminar regime.

Finite element method simulations (FEM) were performed with COMSOL Multiphysics® (see Appendix B for details) to analyse the flow in the microchannel and optimise the chip dimensions. Figure 3-4 shows a profile of the component of the velocity longitudinal to the channel in the chamber cross-section. The peak value is 35.1 µm/s, while the average of the section is 18.7 µm/s. No slip conditions were assumed on the porous support.

The cell layer must experience similar conditions across the chamber to prevent the introduction of artefacts due to cells having access to different amounts of medium. To calculate the uniformity of the flow, the velocity profile and its gradient are computed in the centre of the culture chamber as shown in Figure 3-4. Velocities are homogenous, with 84% of the channel section experiencing a velocity equal to ±25% of the mean. The same trend can be observed in the derivative of the velocity with respect to the chamber width, where the prevalent variations are localised in the few hundreds of micrometers close to the walls. Flow-induced shear stresses are applied to the nanoporous support which acts as a buffer between the flow and the culture. The tissue is therefore protected from mechanical stimuli.

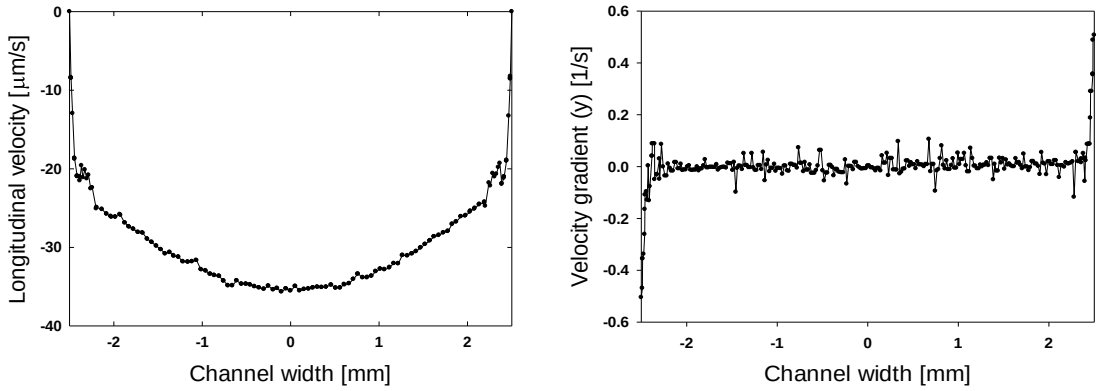

Figure 3-4 Finite Element Method (FEM) fluidic simulation. (Left) Velocity profile in the centre of the culture chamber. (Right) Velocity gradient in the centre of the culture chamber. Velocity gradient is close to zero in the central part of the channel.

3.1.3 Pressure drop

The FEM simulation of the pressure drop in the channel is shown in Figure 3-5. The pressure profile is homogenous across the channel cross section. The outlet port of the device is connected via tubing to an open reservoir, which causes additional backpressure on the membrane. The pressure drop in the tubing can be computed using the Poiseuille equation. Assuming a 10 cm long tubing with 1/32" (0.78 mm) inner diameter gives a pressure drop of:

$$\Delta P = \frac{128\,\mu\,Q}{\pi\,D^4}L = $$

$$= \frac{128 \quad 10^{-3}\,Pa\,s \quad 8.3\,10^{-3}\,\frac{\mu l}{s} \quad 10^{2}\,mm}{3.14 \quad (0.78\,mm)^4} \sim 10^{-1}\,Pa$$

Because of the very small flow rate the pressure drop is of the order of a single Pascal and therefore negligible in both the channel and the tubing.

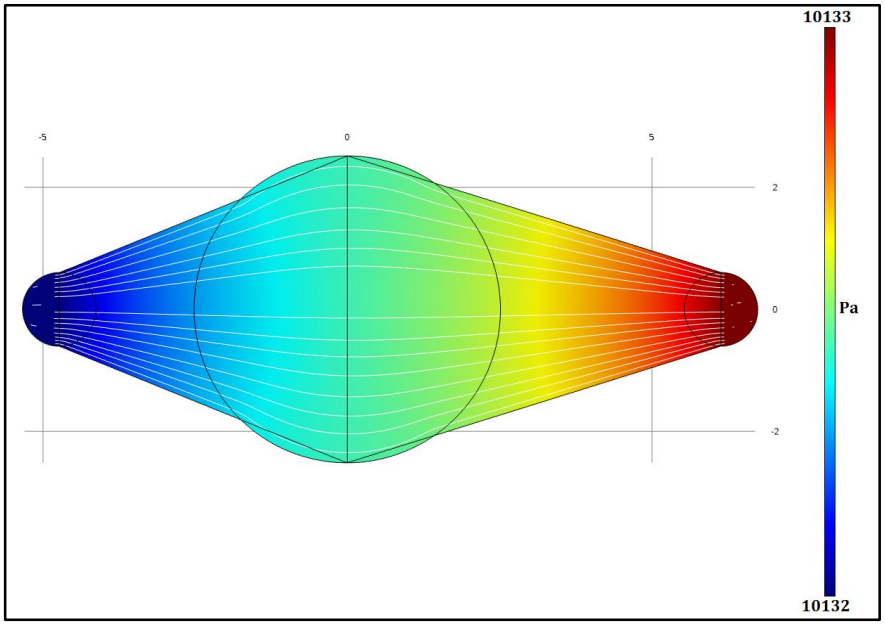

Figure 3-5 FEM simulation of the pressure profile along the channel. Pressure is reported as heat map. The pressure drop in the channel is in the order of single Pa.

3.1.4 Pressure analysis

Because the apical compartment is exposed to the atmospheric pressure, instabilities can arise in the system. The system shown in Figure 3-6 was analysed with and without the lid marked in red. Section 1 is the meniscus in the tank, section 2 is the meniscus of the apical compartment and section 3 is the meniscus at the outlet.

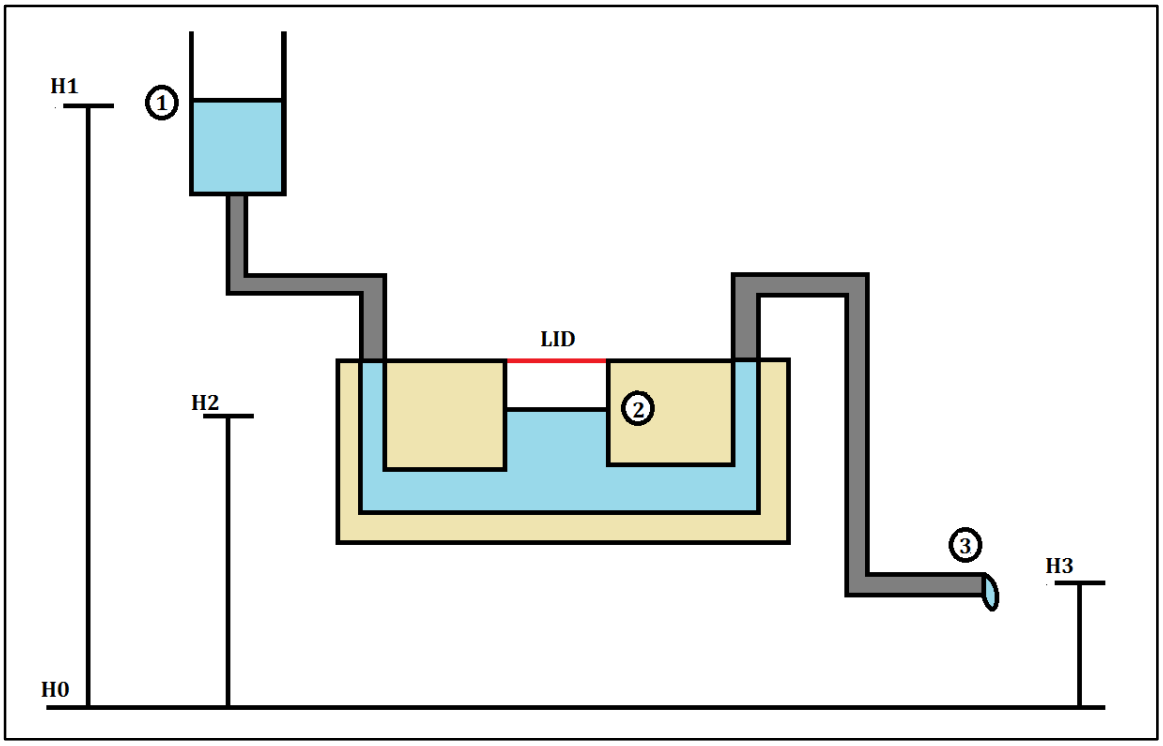

Figure 3-6 Schematic of the system for pressure analysis. Section 1 is the water level in the tank. Section 2 is the water level in the apical compartment. Section 3 is the height of the outlet tubing. The need for a lid in the apical compartment (Red) is analysed.

The Bernoulli energy balance [97, 98] is:

$$\frac{P_2}{\rho} + g\,(h_2 - h_0) + \frac{1}{2}v_2^2 = \frac{P_3 + \Delta P_L}{\rho} + g\,(h_3 - h_0) + \frac{1}{2}v_3^2 + W_{irr} \qquad (3.1)$$

where P, h and v are the pressure, the height and the velocity of the fluid at sections denoted by subscripts, ρ is the density, g is the gravity acceleration constant and W_{irr} is the irreversible work dissipated by friction:

$$W_{irr} = \frac{\Delta P_{irr}}{\rho} \qquad (3.2)$$

and ΔP_L is the Laplace pressure [99] at the outlet induced by the presence of a droplet of radius R:

$$\Delta P_L = \frac{2\,\gamma}{R} \qquad (3.3)$$

where γ is the water surface tension. Potential energies are computed with respect to the reference height h_0.

If there is no lid, the pressures are:

$$P_2 = P_3 = P_a \qquad (3.4)$$

where P_a is the atmospheric pressure. Assuming null velocity at section 2 and computing velocity at section with mass balance:

$$v_2 = 0 \qquad v_3 = \frac{Q}{A} \tag{3.5}$$

The resulting equation for the height difference is:

$$\Delta h = \frac{\Delta P_L + \Delta P_{irr}}{\rho\, g} + \frac{1}{2}\frac{v_3^2}{g} \tag{3.6}$$

This height difference depends on the Laplace pressure at the outlet, which is not constant but varies over time with the radius of the droplet that forms at the outlet tubing. The droplet slowly grows until it reaches a critical radius (which depends on the taper of the outlet), when it then detaches and drops into a container. Thus, the equilibrium height of the liquid in the apical compartment experiences cyclical variation and sudden changes in pressure which might affect the cell construct. To prevent this effect, the apical compartment can be sealed with a lid.

The Bernoulli equation then becomes:

$$\frac{P_2}{\rho} + g(h_L - h_0) = \frac{P_3 + \Delta P_L}{\rho} + g\,(h_3 - h_0) + \frac{1}{2}v_3^2 + W_{irr} \tag{3.7}$$

Considering the volume of gas enclosed in the apical compartment V_G and the total height of the apical compartment H:

$$V_G = h_G\ A \qquad h_L + h_G = H \tag{3.8}$$

where h_L is the height of the liquid, h_G is the height of the gas and A is the chamber area. The pressure in the apical compartment is:

$$P_2 = \frac{nR_{GAS}T}{V_G} = \frac{nR_{GAS}T}{(H - h_L)A} \tag{3.9}$$

The resulting equation is:

$$\frac{nRT}{(H - h_L)\rho A} + g(h_L - h_0) = \frac{P_a + \Delta P_L}{\rho} + g\,(h_3 - h_0) + \frac{1}{2}v_3^2 + W_{irr} \tag{3.10}$$

As in the previous case, an increased pressure in the system (right hand side term of the equation) leads to an increased pressure in the apical compartment (left hand side term of the equation). But, if the apical compartment is sealed, the increase in pressure will be distributed between the compression of the gas (first term) and the hydrostatic height (second term). Therefore, the lid maintains gas in the apical compartment, which acts as a buffer for the pressure and helps to maintain a constant liquid height. Sealing the apical compartment has the added benefit of reducing the risk of contamination and infection from airborne pathogens. The lid is removable to provide access to the apical compartment when needed.

3.1.5 Oxygen consumption

If the apical compartment is sealed it is necessary to ensure that there is enough oxygen for the cell construct to grow and remain viable. A schematic of the oxygen sources and consumption is shown in Figure 3-7.

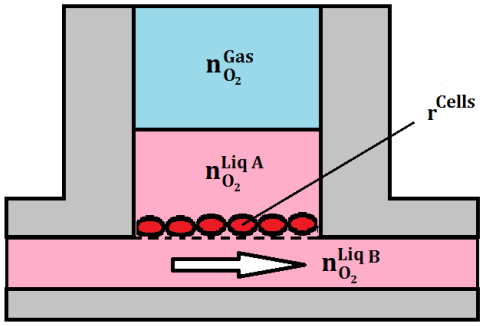

Figure 3-7 Cell culture chamber oxygen balance. Oxygen is present in the gas trapped in the chip $n_{O_2}^{Gas}$ and another in the apical compartment liquid $n_{O_2}^{Liq\ A}$. Oxygen is also dissolved in the pumped medium $n_{O_2}^{Liq\ B}$. Cells consume oxygen with a consumption rate r^{Cells}.

A typical value for the oxygen consumption for cells can be obtained from the literature. For example for the *NIH-H460 Human large epithelial lung cancer cell* [100] the consumption rate is:

$$r^{Cells} = 30 \cdot 10^{-18} \frac{mol}{s\ cell}$$

Cells are seeded on the support at confluence at 4.5 10^5 cells/cm^2. Therefore, the total daily oxygen consumption can be approximately estimated as:

$$n_{O_2}^{Daily} = c_{cells}\, A\, r^{Cells} = 4.5\ 10^5 \frac{cells}{cm^2}\ \ 0.19\ cm^2\ \ 30 \cdot 10^{-18} \frac{mol}{s\ cell}\ 86400 \cong 2.2\ 10^{-7} \frac{mol}{day}$$

where A is the area of the culture surface and c_{cells} is the concentration of cells on the surface. The oxygen in the gaseous phase of the apical volume (200 µl) is:

$$n_{O_2}^{Gas} = \frac{p_{O_2} V}{R_{GAS} T} = \frac{0.21\ atm\ 200\ \mu l}{0.082\ \frac{l\ atm}{K\ mol}\ \ 310\ K} \cong 1.6\ 10^{-6} mol$$

where p_{O_2} is the oxygen partial pressure at 1 atm, V is the gas volume, R_{GAS} is the gas constant and T is the absolute temperature.

Considering equilibrium at 298 K, the oxygen dissolved in the liquid phase of the apical volume (200 µl) is:

$$n_{O_2}^{Liq\ A} = c_{O_2}^{L} V = H p_{O_2} V = 1.3\ 10^{-3}\ \frac{mol}{l\ atm}\ \ 0.21\ atm\ \ 200\ \mu l \cong 5.5\ 10^{-8} mol$$

where $c_{O_2}^{L}$ is the O_2 concentration in liquid phase, V is the liquid volume, H is the Henry equilibrium constant for oxygen dissolved in water [101] and p_{O_2} is the oxygen partial pressure.

The oxygen dissolved in the cell culture media which is pumped through the basolateral channel in one day is:

$$n_{O_2}^{Liq\ B} = c_{O_2}^{L} V = H\ \ p_{O_2} V = 1.3\ 10^{-3}\ \frac{mol}{l\ atm}\ \ 0.21\ atm\ \ 30\ \frac{\mu l}{hr}\ \ 24\ hr \cong 2\ \ 10^{-7} \frac{mol}{day}$$

This shows that the amount of oxygen consumed daily by the cell construct is of the same order of magnitude as the amount of oxygen dissolved in the medium pumped in a day through the basolateral channel. A reservoir one order of magnitude bigger than the daily consumption is

present in the gas enclosed in the apical compartment, and is replenished every two days during growth medium replacement. Therefore, the oxygen consumed by the cells can be delivered by the system.

3.2 Electrodes Design

The microfluidic chips for cell growth have electrodes integrated into the base that are used to measure the electrical properties of the cell construct in real-time. The shape, size and position of the electrodes will determine the sensitivity of the measurement, therefore equivalent electric circuit (EEC) model and finite element method (FEM) simulation were performed to analyse the distribution of the electric field and to find the optimal design. It is important to maximize the sensitivity of the electrodes to enable the measurement of epithelia at the ALI, where the signal-to-noise ratio is low.

3.2.1 Trans-Epithelium and Cis-Epithelium impedance measurement

In a conventional Trans-Epithelium setup, the properties of the tissue are measured by the manual insertion of two electrodes placed in the apical and in the basolateral compartment respectively (Figure 3-8, left). When a voltage is applied between the electrodes a current flows through the system which depends on the electrical impedance of the culture. In this configuration, all the current flows through the tissue leading to a linear dependence between the current and the tissue impedance.

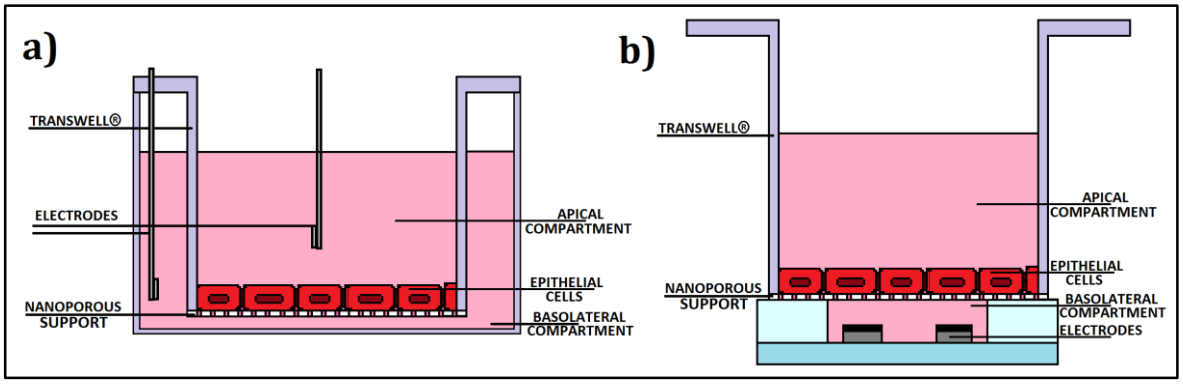

Figure 3-8 Trans-Epithelium vs Cis-Epithelium impedance measurement setup. In the Trans-Epithelium configuration (a) one electrode is placed in the apical compartment and one in the basolateral compartment, whereas in the Cis-Epithelium (b) both electrodes are in the basolateral compartment.

While this linear response of the system is desirable, this configuration requires the presence of an electrolyte in both the apical and basolateral compartment and is not suitable to measure properties of cells cultured at the ALI. Moreover, the manufacturing complexity of a device with this electrode configuration is challenging. For example, Hediger *et al.,* described the fabrication process of a device for cell culture with integrated trans-epithelium electrodes which required more than 10 manufacturing steps including deep plasma, wet etching, powder blasting, metal thin film deposition and a critical gluing process [60, 61]. On the other hand, only two simple steps are required to manufacture electrodes on the same side (Figure 3-8b). In this Cis-Epithelium planar electrodes configuration part of the current flows through the cell layer and part flows below it. This leads to a non-linear electrical response and to a more complex data analysis process. A schematic comparison between the two configuration is shown in Figure 3-9.

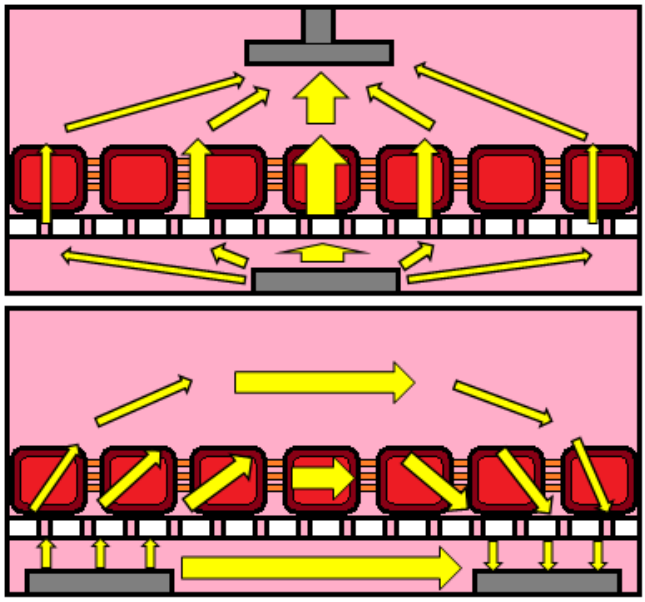

Figure 3-9 Field lines distribution in trans-epithelium and cis-epithelium electrodes configuration. (Top) In the trans-epithelium configuration all field lines go through the cell construct. (Bottom) In the cis-epithelium configuration part of the current flows through the tissue and part flows in the channel below it.

3.2.2 Equivalent Electrical Circuit

An equivalent electrical circuit (EEC) model is used to extrapolate the individual electrical parameters from the complex impedance spectrum. The choice of model is not unambiguous because of the complexity of the biological system. The finesse and level of details needed to describe the system is in part arbitrary (*e.g.* the inclusion of the nuclei, the inclusion of a current pathway across the cell layer, etc.). Nevertheless, not all the models perform in the same way and it is therefore necessary to have criteria to find the best model. Problems that might arise during fitting with an ill-suited model are [102]:

Under-Fit. A model without enough parameters fits the data poorly and will have high residual errors. It might miss important information and not be able to explain features of the experimental data.

Over-Fit. A model with too many parameters fits the data too well and might introduce features that are not real. Moreover, the fitting algorithm will be less stable because the same variation of the data can be explained with variation of different independent parameters.

The coefficient of determination is defined as:

$$R^2 = \sum_{i=1}^{N} \frac{\left(y_i^{Mod} - \bar{y}\right)^2}{\left(y_i^{Exp} - \bar{y}\right)^2} \qquad (3.11)$$

where the sum is extended to the N data points, y_i^{Exp} are the experimental values, y_i^{Mod} are the values predicted by the model and $\bar{y}$ is the mean of the experimental values. It quantifies how much of the total deviance is explained by the model, and is used to determine the goodness of a fit. Although this parameter yields good results for linear fit, it is not suitable as a tool to compare different models in non-linear regressions [103]. The Akaike Information Criterion (AIC) [104] is a well-suited parameter for the selection of the best model to fit a given set of data in non-linear

regressions [103]. This criterion aims to optimize the residuals errors while using only physically relevant parameters. A flowchart of the adopted algorithm is reported in Figure 3-10.

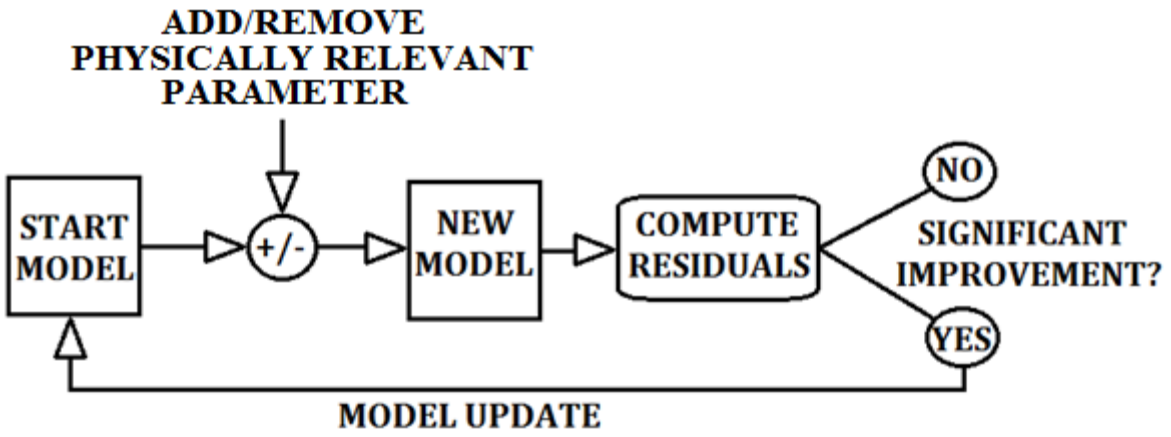

Figure 3-10 Algorithm for model selection. Parameters were added or removed from the starting model and the resulting effects on the fit were analysed. If there was a significant improvement the starting model was updated.

The AIC is defined as:

$$AIC = 2p - 2\ln(L) \qquad (3.12)$$

where p is the number of the parameters and $\ln(L)$ is the maximum log-likelihood of the estimated model which, under the assumption of normally distributed residuals, can be computed as [103]:

$$\ln(L) = -\frac{N}{2}\left[\ln(2\pi) + 1 - \ln(N) + \ln\left(\sum_{i=1}^{N}(y_i^{Mod} - y_i^{Exp})^2\right)\right] \qquad (3.13)$$

The AIC increases with the number of parameters and with the residual errors and decreases with increased experimental data points. The model with physiologically relevant parameters with the lowest AIC is the best-suited model to fit the data set. Five possible different EEC models of the system were considered, as shown in Figure 3-11.

The first model considered is the one used by Sun *et al.* [66], which has 12 parameters. This model uses a constant phase element (CPE) for the electrode polarisation. It includes both resistive and capacitive components for the basolateral compartment (R_{bm}, C_{bm}), the apical compartment (R_{am}, C_{am}), the nanoporous support (R_{tm},C_{tm}) and the cell layer (R_c,C_c). It also includes two paracellular pathways across the cell layer (R_{p1}, R_{p2}). This model leaves out the cytosolic resistance and the cellular nucleus: the former can be neglected because it's smaller than the other components, while the latter is only important at higher frequencies ($> 10^7\ Hz$.). One flaw of the model is that it includes two resistances in parallel (R_{p1} and R_c) which can't be determined univocally during the fit (i.e. for a given value of the resistance parallel there are infinite possible combinations of resistances values).

The second model considered assumes that capacitances of the basolateral compartment, nanoporous support, and apical compartment are only important for frequencies outside the measurement range (10^2 to $10^6\ Hz$) and that the respective capacitors can therefore be considered open circuits. Resistances that could not be determined univocally because either in series or in parallel were lumped together yielding a model with 6 parameters.

The third model considered uses a capacitor instead of a CPE to model the electrode polarisation. As stated previously, a single capacitor (C_{DL}) is not adequate to model this phenomenon: this model

with 5 parameters is expected to perform poorly and is used as a negative control for the AIC analysis.

The fourth and fifth models considered use 7 parameters each and are used to verify the likelihood of the assumptions made. One model includes the additional cytosol resistance in series with the cell membrane capacitance (R_{CS}), while the other assumes that the apical capacitance (C_a) cannot be neglected.

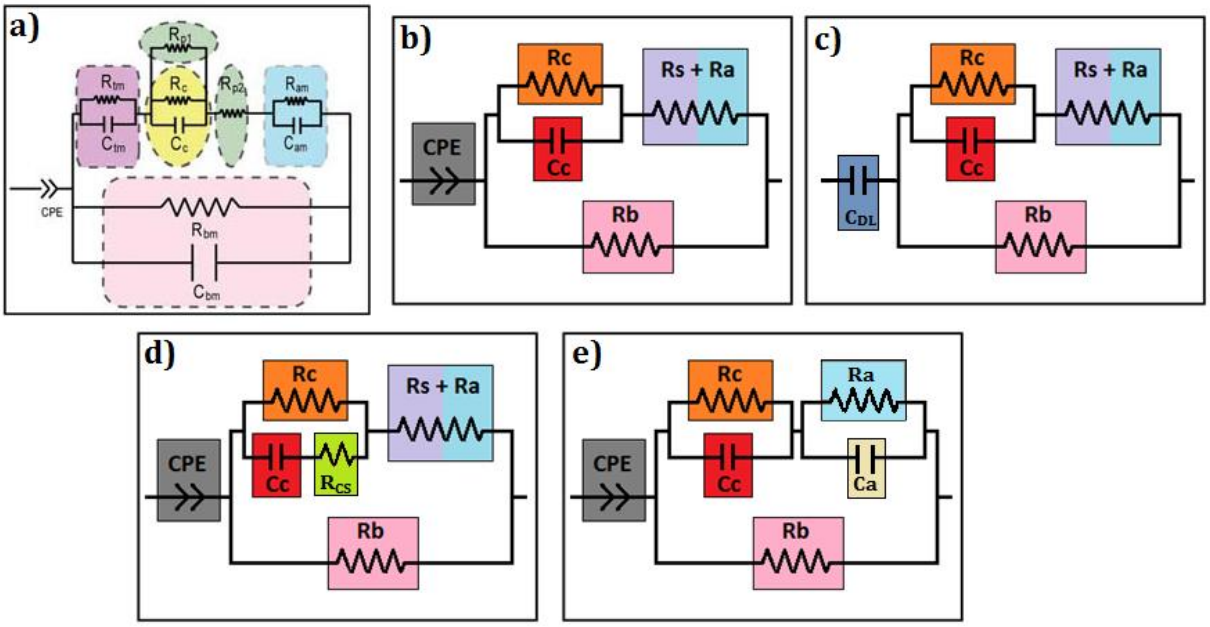

Figure 3-11 Five similar electric equivalent circuit (EEC) models that could represent the system. (a) Model reported by Sun *et al.* [66] with 12 parameters. (b) Proposed model with 6 parameters. (c) Model with 5 parameters with a simple capacitor for the electrodes polarisation. (d) Model with 7 parameters with the addition of the cytosol resistance. (e) Model with 7 parameters with the addition of an apical capacitance.

AIC were computed for each model using the same data set which represent a typical impedance spectrum of a cell construct with an established barrier (Figure 3-12). AIC values can be shifted by any additive constant, therefore it is not the absolute size of the AIC values that is important, but the relative values of the set of models considered, and particularly the differences between AIC values [102]. The model with 6 parameters gives the lowest AIC (461) and is therefore considered to be the one that performs best. The models with 7 parameters follow closely with AICs slightly bigger (463 for the model with cytosol resistance and 466 for the one with apical capacitance). The literature model with 12 parameters is fourth with an AIC of 490. The model with 5 parameters is the worst model considered with an AIC of 631.

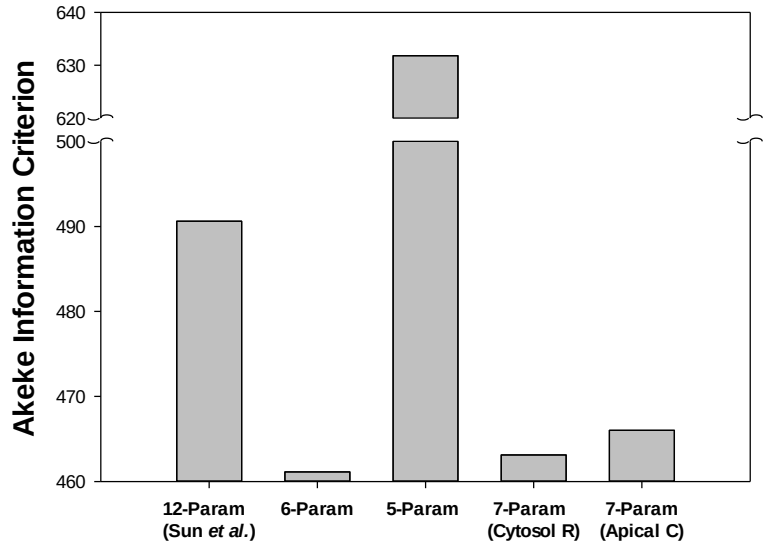

Figure 3-12 Akaike information criterion (AIC) calculated for the five proposed EEC models on a typical dataset of a confluent cell layer.

To better understand the information provided by Figure 3-12, the fit for model (a), (b) and (c) are shown in Figure 3-13 as magnitude and phase angle of the impedance. While model (a) and (b) fit the data nicely, model (c) fails to recapitulate some of the feature of the data (*e.g.* low frequency impedance and phase angle depth magnitude). This leads to bigger residual errors and an increased AIC. On the other hand, fits from model (a) and (b) are similar to each other, with the fitting curves almost superimposed. The greater number of parameters used without a significant improvement of the residual errors is penalised by the AIC which leans heavily towards the model with fewer parameters. The same process can be applied to explain the AIC differences between model (b) and the 7 parameter model. In this case the small difference in the number of parameters is reflected in the relatively small difference in AIC values. Model (b) is assumed to be the best model and used in all the following sections.

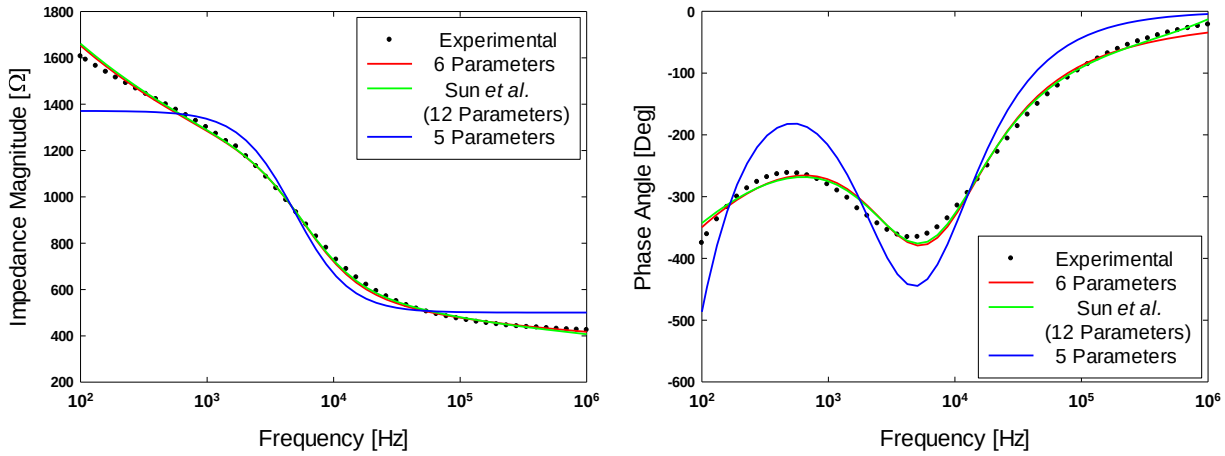

Figure 3-13 Comparison between fits performed with a model with 6 parameters (Red), 12 parameters (Green) and 5 parameters (Blue) on an experimental data set (Points).

The final equivalent circuit model for the epithelial construct (b) is shown in Figure 3-14. This model featuring only 6 parameters does not take into account some physiological parameters that have minor influence on the overall response, but provides a robust and accurate tool for the analysis of the parameters relevant to the application (i.e. the tissue resistance and capacitance, R_c and C_c). The model includes the electrodes, the basolateral medium in the channel, the polymer cell support, the cell culture and the medium in the apical compartment. As shown in the figure, there are two parallel pathways for the electrical current, one along the basal channel and a second through the nanoporous support, the cell culture and the apical compartment. The electrodes are polarisable and are modelled as a constant phase element (CPE). The cell layer is modelled as a parallel resistor-capacitor combination. The resistor represents the current flowing between the cells and through the TJs (R_c) and the capacitor describes the charging current flowing through the cell membrane and the cytoplasm (C_c). The reactive components of the polymer cell-support and of the medium in both the apical and basolateral channel are negligible in the experimental frequency range (10^2Hz-10^6Hz). The resistive components of the polymer support (R_s) and the medium in the apical compartment (R_a) are lumped together as a single resistor (R_s+R_a). The total impedance is not linearly dependent on the tissue construct parameters due to the presence of the other elements in the system. The equivalent electrical circuit is used to fit experimental impedance data and extract quantitative information for all the parameters. More details on the fitting process can be found in the Appendix. Typical values of the fitted parameters are reported in Table 1.

Not all the 6 parameters of the adopted model are relevant across all the frequency spectrum. At high frequencies (>10^5Hz) the cell membrane and the CPE are shunted and the model becomes the parallel of the apical and basolateral resistors. The presence of the tissue construct becomes important in the frequency range 10^3Hz-10^5Hz, where the cell membrane has its relaxation. The CPE becomes relevant at lower frequencies (<10^3Hz) and dominates completely the measurement at low frequencies (<10^2Hz).

Table 1 Typical values of fitted parameters for the circular segment electrodes design.

PARAMETER	PHYSICAL MEANING	TYPICAL VALUE
CPE Coefficient	Electrode Impedance	5000 [Ohm]
CPE Exponent	Electrode polarizability (resistive or capacitive)	0.51
R_b	Basolateral compartment resistance	8000 [Ohm]
R_a	Apical compartment resistance	500 [Ohm]
R_c	Construct resistance	0-300 [Ohm cm^2]
C_c	Construct capacitance	10^{-7}-10^{-6} [F/cm^2]

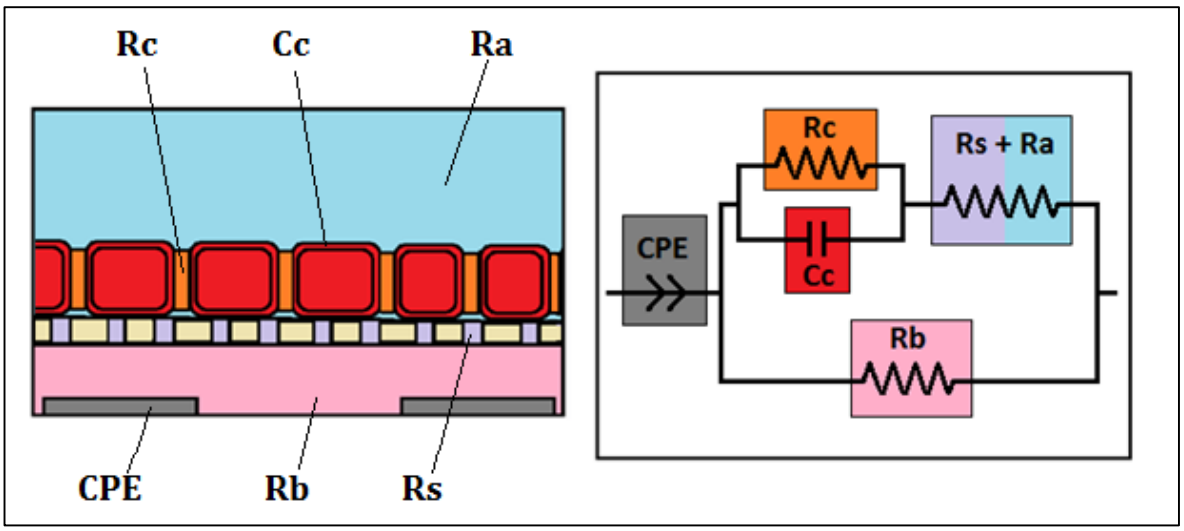

Figure 3-14 Schematic diagram and Equivalent Electrical Circuit (EEC) of the cell construct. The system consists of polarizable electrodes (Constant Phase Element, CPE) [Grey], the basolateral medium resistance in the channel (R_b) [Pink], the polymeric cell support (R_s) [Purple], the cell layer (R_c, C_c) [Orange, Red] and the medium in the apical compartment (R_a) [Blue]. The circuit corresponds to the two parallel current pathways: one along the bottom fluid channel and another through the cell layer.

3.2.3 Impedance spectra of a growing culture of epithelial cells

The equivalent circuit was used to simulate the evolution of the impedance spectrum as the epithelial barrier becomes established, to analyse the predicted response. Impedance spectra were computed keeping all the parameters constant except for one of the parameters relative to the cell culture (R_c or C_c) at a time. The simulated change in impedance for variation in R_c or C_c is shown in Figure 3-15. The baseline impedance spectrum shows that the reactive component of the impedance dominates at low-frequencies due to electrode polarisation. This leads to an exponential increase in the impedance magnitude at low frequency. R_c increases as the barrier is established. At high frequencies the cell membrane is short circuited, therefore the current flows through the cell cytoplasm and the total impedance magnitude will be almost independent of the cellular barrier. At low frequencies the cell membrane acts as an open circuit, therefore the current flows in between the cells and the impedance magnitude increases as intercellular TJs are formed. The frequency-dependent coupling between the signal and the culture leads to the formation of a trough in the phase angle. For increasing R_c values the magnitude of the trough increases and its peak frequency shifts towards lower values. Both the impedance magnitude and the phase angle shift towards lower frequencies for increasing values of C_c.

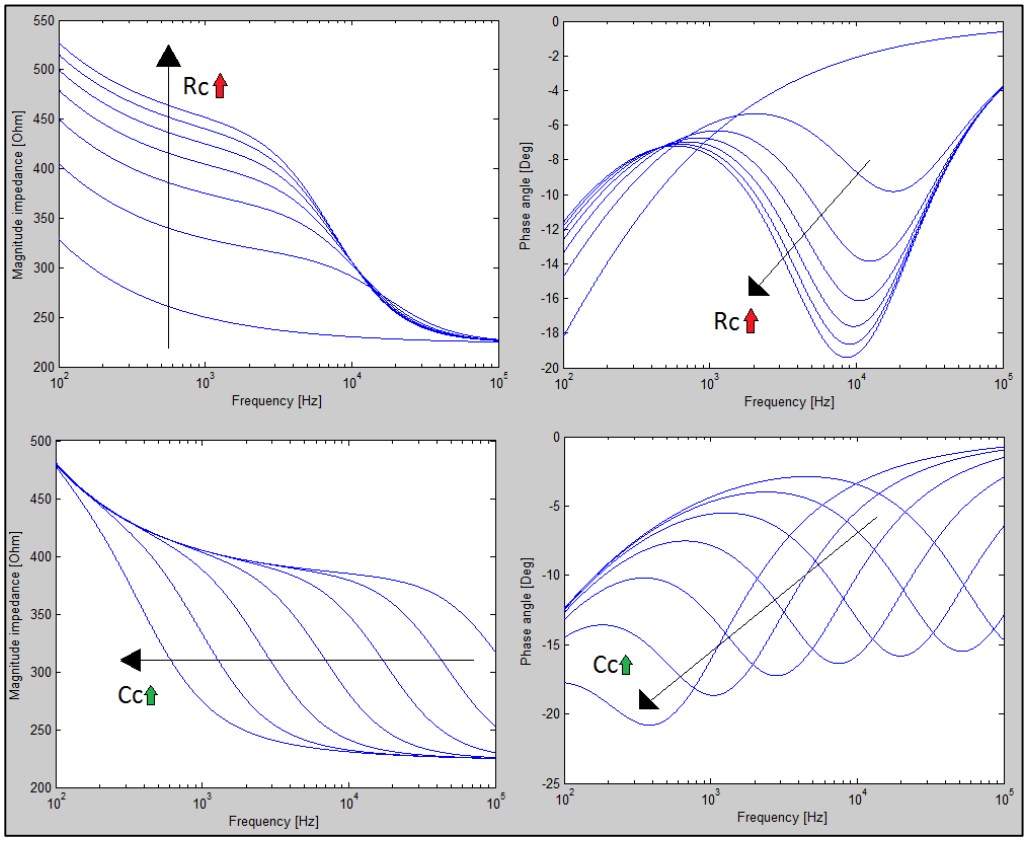

Figure 3-15 Simulated evolution of a growing culture. The equivalent electric circuit is used to predict the qualitative trend of the electrical properties of an establishing barrier. Evolution of impedance spectra for: (Top) increased R_c, (Bottom) increased C_c. All other model parameters are kept constant.

Simulated variations of the impedance magnitude at different frequencies for variation of the culture resistance are shown in Figure 3-16. At low frequencies (100 Hz) the impedance magnitude is directly proportional to the culture resistance, whereas at high frequencies (100 kHz) it is not affected by the culture resistance. At intermediate frequencies (3-7 kHz) there is a transition from one behaviour to the other.

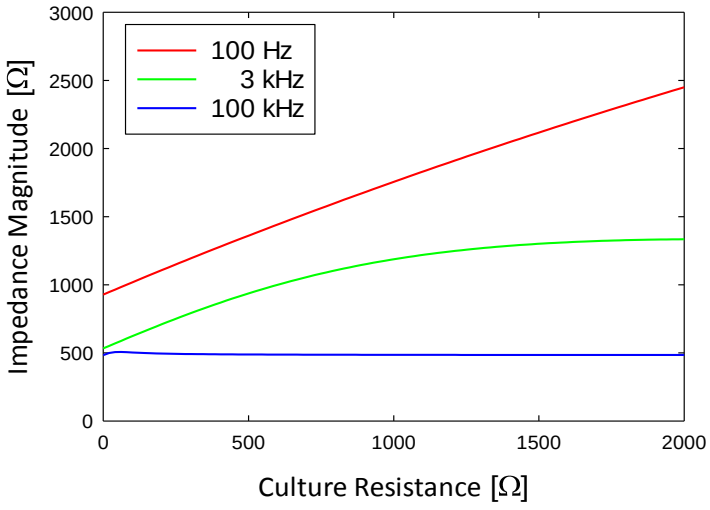

Figure 3-16 Frequency-dependent simulation for the impedance magnitude. At 100 Hz the impedance is directly proportional to the culture medium resistance, whereas at 100 kHz it is constant. In the 3-7 kHz range the measurement has a transition from one behaviour to the other.

To verify the trends predicted by the model for the impedance spectrum, experimental data for the typical evolution of the impedance spectra of a growing culture of epithelial cells is shown in Figure 3-17. All the trends predicted by the simulated model are observed in the experimental spectra. The impedance magnitude increases over time at frequencies <1 kHz and stays almost constant for frequencies >10 kHz. The trough in the phase angle shifts towards lower frequencies as the barrier is established.

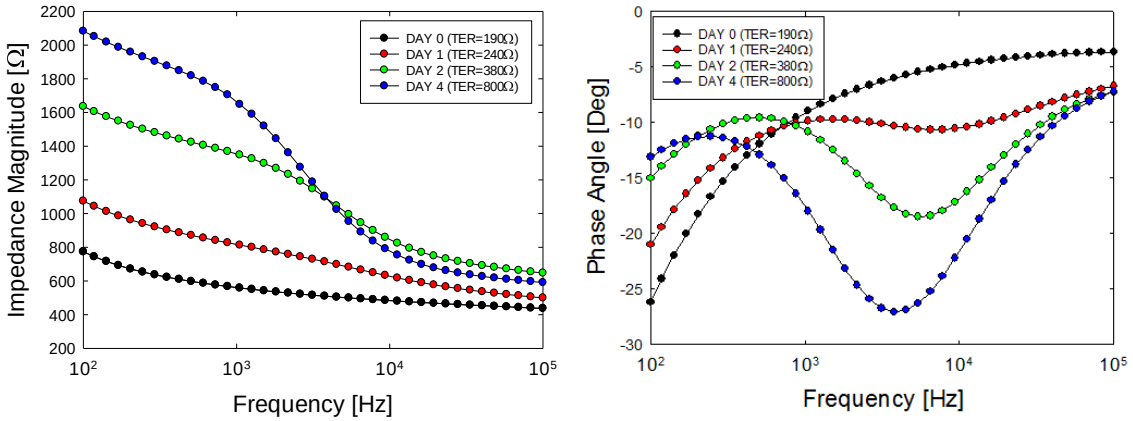

Figure 3-17 Typical experimental electrical impedance spectra of a growing submerged epithelial cell culture. The baseline (day 0) is dominated by the low frequency electrode polarisation. During the establishment of the barrier (day 1-4) the impedance modulus at low frequencies increases and a relaxation is observed in phase angle. At high frequencies the current flows predominantly through the cell membrane and the impedance is independent of the status of TJs.

3.2.4 Electrode Optimisation

The developed model of the system is used in this section to determine the optimum design of the measuring electrodes. The parameters that characterize the cell layer are the TJ resistance R_c and the cell layer capacitance C_c. The total impedance is not linearly dependent on these parameters due to the presence of the parallel basolateral resistor R_b and the series resistor R_a. To analyse the effects of these parameters on the measured impedance, a sensitivity can be defined as:

$$S_{R_b} = \frac{|Z_{1kHz}(R_c=1000\Omega)| - |Z_{1kHz}(R_c=0\Omega)|}{|Z_{1kHz}(R_c=1000\Omega)|} \qquad (3.14)$$

The sensitivity of the measurement to variations in the cell layer depends on the values of the basolateral resistance R_b and on the apical resistance R_a as shown in Figure 3-18. The highest sensitivity is obtained when both the basolateral resistance R_b and the current in the apical compartment is maximum, *i.e.* R_a is low. If the basolateral resistance is small most of the current will flow in the channel and the impedance measurement will be independent of the resistance of the cells. If the basolateral resistance is much higher than the culture resistance it will effectively behave as an open circuit and the optimal condition is obtained.

The values for the impedance are constrained in the range [(R_a//R_b), R_b]: the lower boundary is in the absence of cells (R_c=0); the upper boundary is the ideal case with $R_c \rightarrow \infty$.

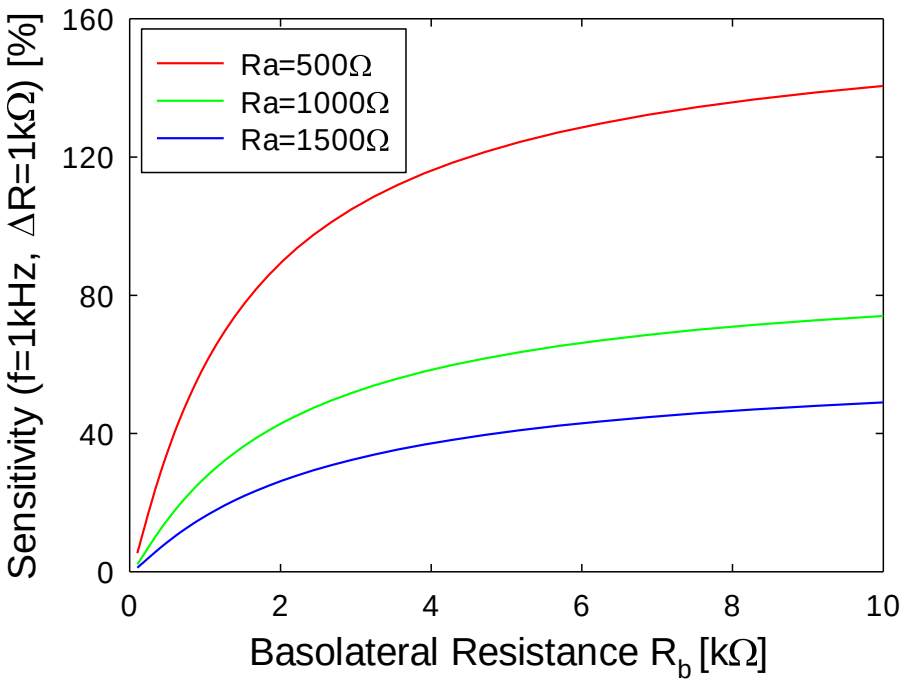

Figure 3-18 Sensitivity analysis S_{Rb} for variation in culture resistance (from 0Ω to 1000Ω) at 1 kHz: the sensitivity is affected by the basolateral and apical resistance Ra. The values for the impedance are constrained in the range [(R_a//R_b), R_b]. For small R_b and big R_a, small changes in the culture resistance can saturate all the measurement range. The sensitivity is maximised for R_a<<R_c<<R_b.

Therefore, the electrode and system geometry needs to maximise the basolateral resistance with minimum electrode polarisation effects. Electrode polarisation can be reduced by increasing the size of the electrode or by increasing the specific area with surface treatments, for example by Pt black coating. The geometrical parameters that affect the basolateral resistance are the reservoir height (set to 100 μm due to fabrication constrains) and the distance between the electrodes.

Figure 3-19 compares the original design of Sun et *al.* [66] with 4 new designs. The original design consists of two concentric electrodes of radii 1mm and 2mm, respectively. Design 1 has a pair of electrodes and a disk inner electrode. Design 2 consists of 3 interdigitated straight electrodes. The third design is formed of 2 large round electrodes and the fourth consists of two circular parallel strips.

FEM analysis was used to numerically evaluate the electrical characteristics of these different electrodes design (see Appendix for details). The percentage of the total current flowing through the culture medium was used as an indicator of sensitivity. When the ratio is 100% all the current flows through the cell layer and the sensitivity is maximum; if the ratio is 0% no current goes through the cells. The numerical integrals for the current density were evaluated at the electrode plane (z=0) and at the cell culture plane (support membrane) (z=0.1mm). Another way to assess the sensitivity is to measure the basolateral resistance. Simulated values for different geometries were calculated by dividing the applied potential by the numerical integral of the total current.

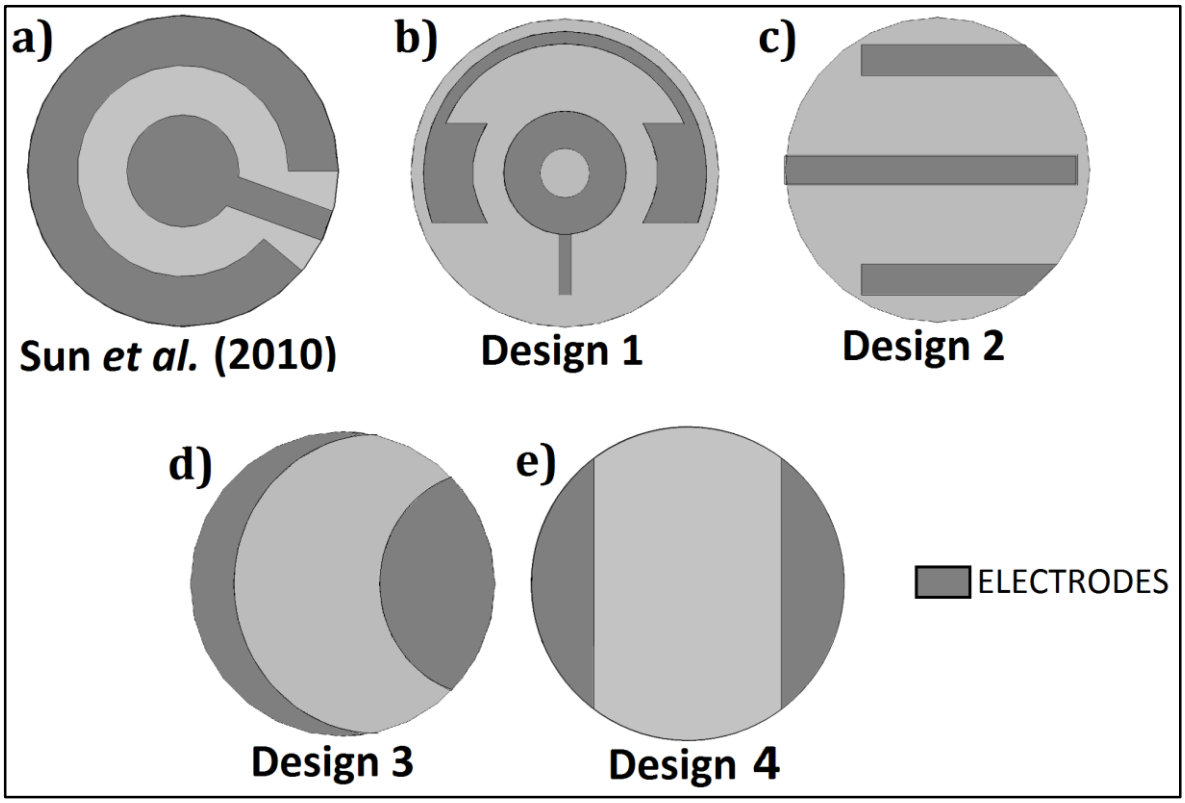

Figure 3-19 Proposed new electrodes geometries. (a) Original concentric electrode design from Sun *et al.*: dot radius = 1mm, ring inner radius = 2 mm, ring outer radius = 3 mm. (b) Concentric electrodes variation: dot radius = 1 mm, ring widths = 0.8 mm and 0.2 mm. (c) Interdigitated straight electrodes: width = 0.5 mm, gap = 1.3 mm. (d) Round electrodes: curvature radii = 2.5 mm and 1.9 mm. (e) Two parallel lines: width = 1 mm, curvature radius = 2.5 mm and gap = 3 mm.

Simulation results are shown in Figure 3-20: there is a large variation in sensitivities for the different designs. There is a correlation between the basolateral cell resistance and the sensitivity: the best designs have the largest distance between the electrodes. The optimal design is Design 4, which has a basolateral resistance of 6.7 kΩ and sensitivity of 71.3 %. In comparison, the original concentric electrode design has a basolateral resistance of 620 Ω and a sensitivity of 11.1 %. The circular segment electrodes design is therefore significantly more sensitive to variations in the electrical properties of the cell layer.

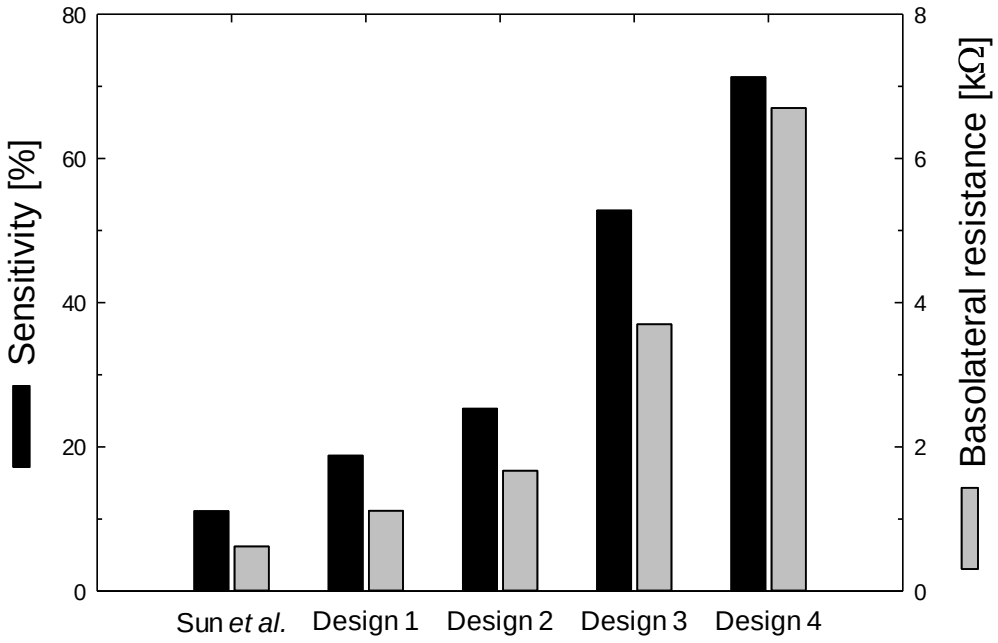

Figure 3-20 Results of the FEM electric simulation of the electrodes design. There is a correlation between the sensitivity and the basolateral cell resistance. The best design has symmetrical circular segments one (Design 4) which has a sensitivity of 71.3% versus 11.1% with the original concentric electrodes design [66].

Another parameter that should be considered is the uniformity of the current across the tissue construct. The best electrode design will create a uniform current density throughout all the tissue construct. Figure 3-21 shows the current density distribution in the cell plane (z=0.1mm) for design 4 (a) and the original design of Sun *et al*. (b). The standard deviation of current density in the plane is calculated as a measure of the uniformity. The resulting standard deviations are 6.28 A/m^2 (58% of the mean) for the concentric electrodes design and 4.63 A/m^2 (59% of the mean) for design 4.

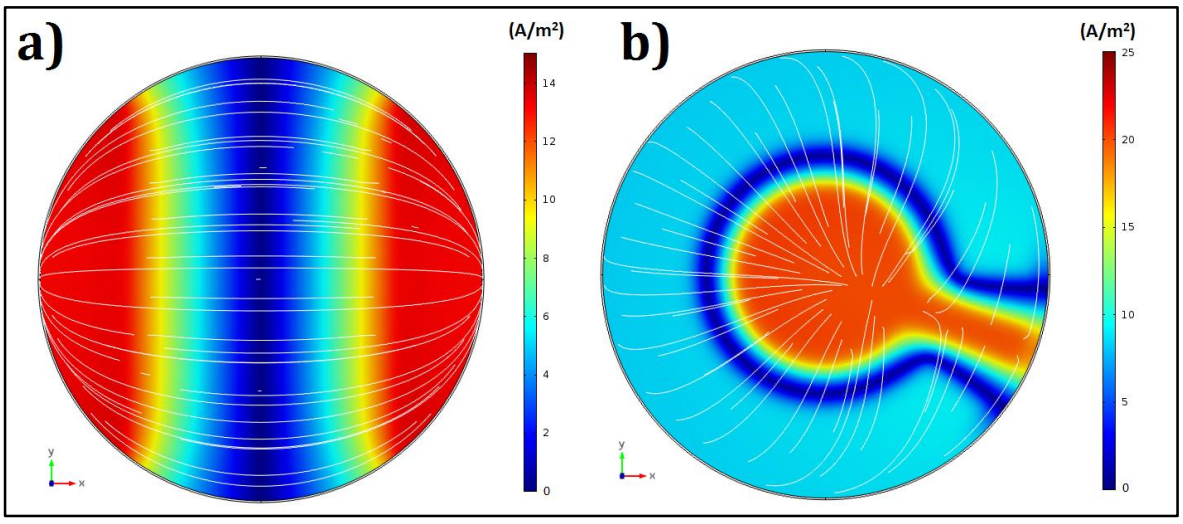

Figure 3-21 Finite element simulations for two different electrodes geometries – (a) Design 4 and (b) the original design of Sun *et al.*. The current density distribution in the cell plane (z=0.1mm) is shown as a colour-map. Current density field lines are in white. The standard deviation in the current density for Design 4 (4.63A/m^2) is lower than for the original design (6.28 A/m^2).

The performance of the new electrode design depends on the gap between the electrodes. To determine the optimal gap, the ratio between current flowing through the cell layer and the total current in the device was determined. Also the effects of the current density uniformity were analysed. As shown in Figure 3-22, when the gap between the electrodes is decreased the basolateral resistance decreases, resulting in a decreased sensitivity. On the other hand, when the gap between the electrodes is decreased, the electrode area increases (for a given cell membrane geometry), improving the current uniformity. The chosen gap is 3mm, resulting in 71.3% of the total current flowing through the cell layers, with a current density standard variation of 4.63 A/m^2 (59% of the mean).

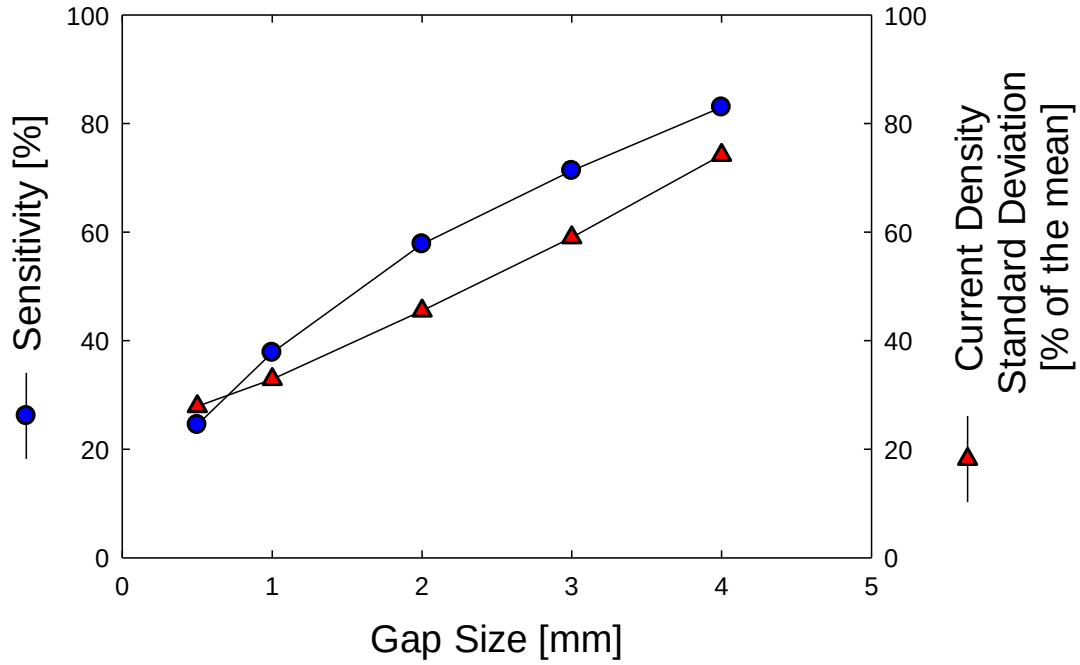

Figure 3-22 Effect of the gap between the electrodes for Design 4. As the gap is increased the basolateral resistance is increased so that more of the current flows through the cells. At the same time the electrode area decreases leading to a less uniform current distribution.

3.2.5 Design 5: Insulating Septum

It is possible to further increase the basolateral resistance of the system and therefore its sensitivity by adding an insulating barrier between the electrodes. This insulating obstacle prevents current from flowing through the basolateral compartment and forces the field lines to pass through the cell layer as shown in Figure 3-23. If the height of the obstacle is equal to the height of the reservoir spacer, no current can flow along the channel, $R_b \rightarrow \infty$ and the sensitivity is maximum. The current uniformity across the culture is improved as well by this addition: for a 0.1mm insulating septum the current density standard deviation is 3.41 A/m^2 (27% of the mean). The septum prevents the medium from flowing through part of the membrane pores above it and reaching the cells, therefore its effects on the viability of a long term culture must be assessed.

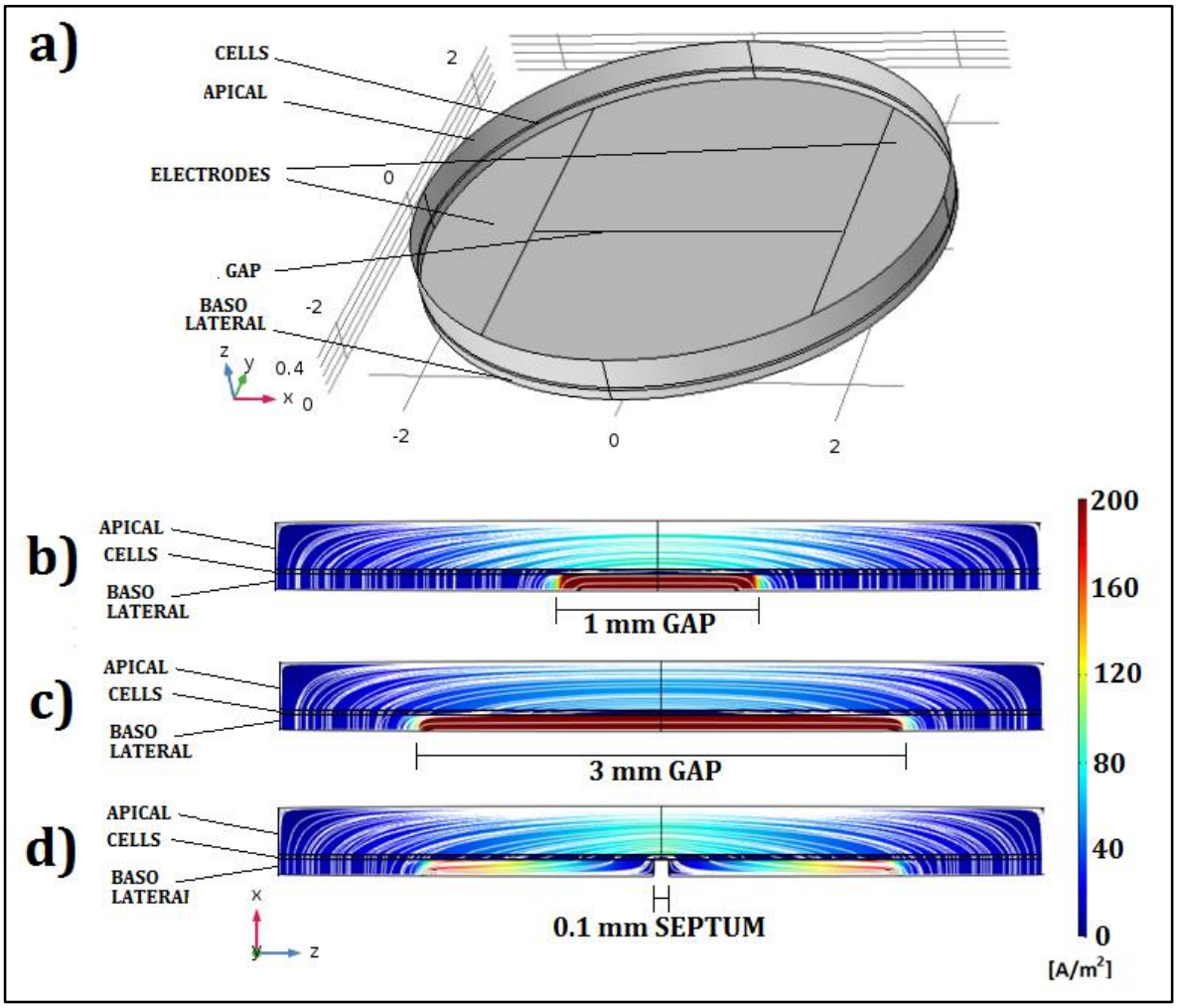

Figure 3-23 Finite element simulations of electrodes geometries with an insulating spacer. (a) Isometric view of the simulated system: electrodes are on the base of the basolateral cylinder on top of which there a cylinder representing the cells and a cylinder representing the apical compartment. (b,c,d) Effects of the gap between the electrodes. Current density distribution is shown as colour-map and field lines are shown in white. (b) 1 mm gap: the basolateral resistance is low and a large percentage of the current flows under the membrane. (c) 3 mm gap: the basolateral resistance is increased, the total current flowing through the system is decreased and the percentage of the current flowing through the cells is increased. (d) 0.1 mm wide insulating septum between the electrodes: the current can't flow in the channel and is forced through the culture. The basolateral resistance is the highest and the sensitivity is maximum. The cell-plane current density standard deviation is decreased to 3.41 A/m^2.

3.3 Chapter summary

In this chapter, the device design process was analysed. Two main aspects were considered: the microfluidics and the electrics. The channel shape diverges from the inlet to the culture chamber to avoid stagnation point for air bubbles and to obtain a homogeneous velocity profile across the culture chamber. The microfluidics flow was simulated with a finite element method. The flow rate is higher than the values of interstitial flows reported in the literature to ensure that the oxygen consumed by the cells is replenished. The backpressure on the culture support is negligible because a small flow rate is used. A lid is used to seal the apical compartment to damp the effects of variation in the outlet conditions (clogged tubing, different outlet height, droplet formation) which would otherwise cause a time-varying pressure in the apical compartment, disrupting the culture.

In the electric section an equivalent electric circuit was used to model the device. This analysis was important to guide the design of the planar electrodes. First, a typical experimental impedance spectrum of epithelial cells was used to determine which equivalent circuit fitted the data points best. A set of circuits was created starting from Sun *et. al.* [66] and changing the number of parameters. The Akaike Information Criterion was used as the metric to determine the goodness of the non-linear complex fits. The impedance spectrum was best described by a model with 6 parameters (2 to describe electrodes polarisation, 2 to describe the tissue construct and 2 to describe the resistive paths through the medium).

The final model was used to simulate the effects of each parameter on the total impedance. Variations in the cell culture resistance were found to increase the impedance magnitude at low frequency while leaving the high frequency values unaltered. This trend can be explained considering the frequency dependent electrical shielding of the cytoplasm offered by the capacitive cellular membrane: at low frequencies the membrane is an open circuit and the current follows a paracellular path and is thus affected by the paracellular resistance, while at high frequencies the membrane is an open circuit and the current follows a transcellular pathway and is independent from the paracellular resistance. This frequency-dependent effects of the cellular resistance on the total impedance was also observed in the evolution of the phase angle, where a trough in phase occurs, which becomes more pronounced as the tissue resistance increases. The simulated growth obtained with the selected equivalent electric circuit closely followed the experimental curves.

The effects of geometrical parameters on the total impedance were simulated and used to optimize the electrodes design. It was found that the basolateral resistance should be maximum and the apical resistance minimum in order to maximize the sensitivity of the measurement, and the measured impedance is constrained in the range $[(R_a//R_b), R_b]$. Basolateral resistance values were used to compare different electrodes designs. In the best design the electrodes have circular segment shapes and are separated by a gap. This design has a basolateral resistance 10 times bigger than the electrodes design reported by Sun *et. al.* [66]. The homogeneity of the current flowing through the cell construct are similar for the two designs. The effects of varying the gap between the circular segment electrodes was considered, and a 3mm gap gave the best compromise between sensitivity and current homogeneity.

Finally, an approach to increase the sensitivity of the measurement was introduced. This method consisted in inserting an insulating septum between the electrodes, thus setting the theoretical basolateral resistance to infinity. In a finite element method simulation, this approach over-performed the other designs in both sensitivity and current homogeneity.

Chapter 4: Methods

In this chapter the methods used in this thesis are discussed. First, the fabrication steps used to manufacture the microfluidic chip, then the experimental setup and the auxiliary machines required to operate the device and lastly the biological procedures for tissue culture are described.

4.1 Organ-on-chip fabrication

To impact on the drug research industry, the system throughput must be high. One way to increase the throughput is to use many devices in parallel at once, but the cost and production time of each one of them must be minimised. Some of the fabrication steps used to manufacture the device are already optimised for mass manufacturing, whereas others are still at the prototype scale. These methods are presented in this chapter, and for the latter the intended way to scale each step is presented together with the current production method. Detailed fabrication recipes of each step are described in Appendix C.

4.1.1 Clean-room processes

All the processes in this section are carried out in the Southampton University Nanofabrication Centre. They are performed on a 6 inch (15 cm) glass wafer to maximize the number of devices manufactured at once (76 chips can fit on a single wafer). A week is required to completely perform all the process steps on a wafer. A schematic of the clean-room fabrication steps is shown in Figure 4-1.

Electrode Patterning
The first manufacturing step consists in patterning the electrodes. A section of a photolithography mask for the electrodes for a single chip is shown in Figure 4-2. The final design consists of two circular segment electrodes to monitor cell culture electrical properties and two straight electrodes to measure the conductivity of the fluid in the channel. Each electrode has a track that connects it to the contact pins that will be buried under photoresist during the channel patterning. The material of choice for the electrodes is Platinum because of its high stability and biocompatibility. After the deposition of an adhesion promoting layer of Titanium (5 nm), a thin layer (≈100 nm) of Pt is deposited by sputtering using a Leybold Helios evaporator. Standard photolithography is performed to etch the platinum into the desired pattern: a positive photoresist (S1813) is spun on top of the wafer and then exposed to UV light under a mask. The photoresist degrades where the mask lets the light through and remains unaffected elsewhere. The wafer is then developed with a solvent that removes the degraded photoresist but not the unexposed one. The wafer is then etched using a reactive ion beam (IonFab machine): the exposed platinum is physically removed by the beam where there is no photoresist, whereas it is shielded and preserved by the photoresist elsewhere. A final cleaning step is used to strip the residual photoresist from the wafer. The resulting wafer after electrode patterning is shown in Figure 4-3.

Microfluidic Channel
After the electrodes were patterned, the microfluidic channel is defined. An adhesion promoter (Ti primer) is spun onto the wafer and the microchannel patterned from two sheets of 55 μm thick negative photoresist (TMMF®) laminated onto the wafer to obtain a channel height of ≈100 μm. To prevent the films detaching from the glass an adhesion promoter is used to improve the bonding. Photolithography is performed and the wafer is developed. The cross-linked photoresist which is left on the wafer is not cytotoxic and is used as the microfluidic channel for the culture media. A unit of the photolithography mask representing a single chip is shown in Figure 4-4.

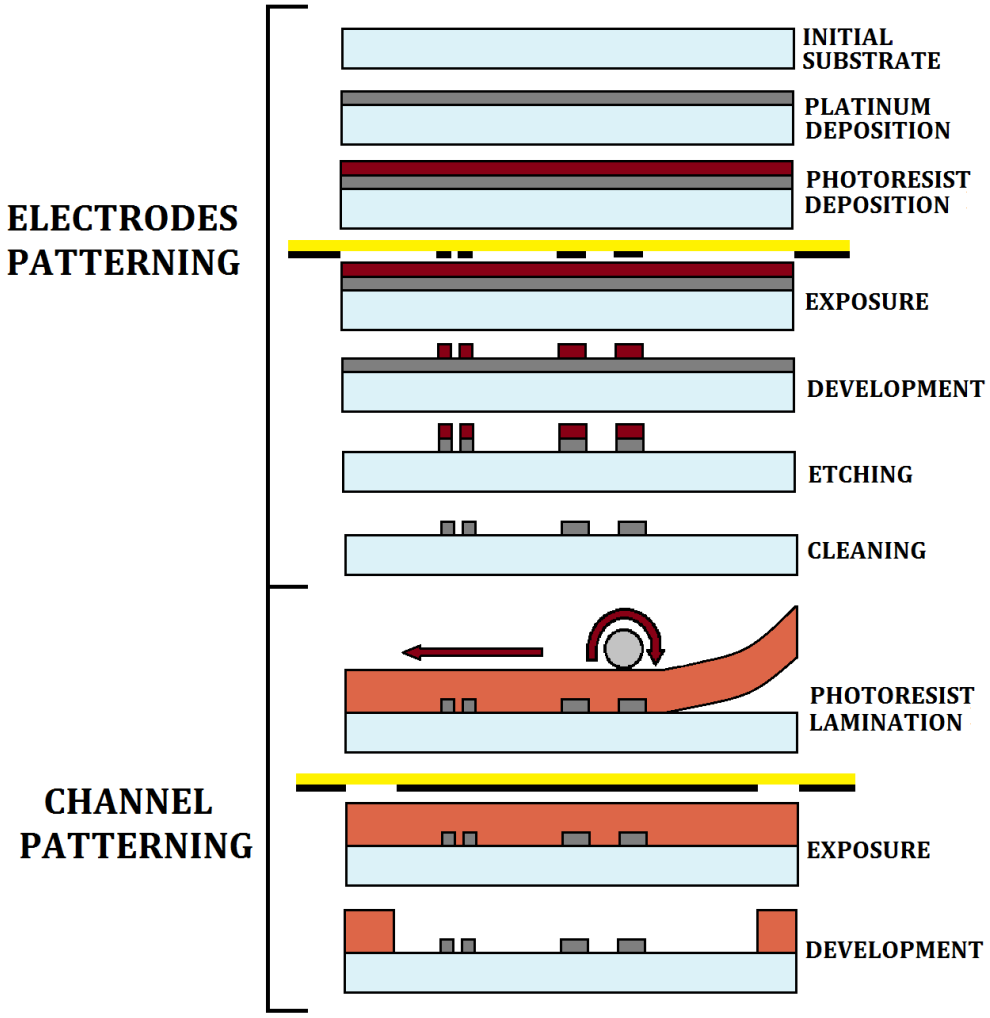

Figure 4-1 Clean-room steps of the fabrication process: Platinum is sputtered over the surface of a 6" glass wafer. Positive photoresist is spun on top of the wafer and photolithography is performed. The wafer is cleaned and exposed to the etching ion beam that removes all the metal not covered by photoresist. After cleaning, a negative photoresist is laminated on top of the wafer and photolithography is performed: only the exposed areas of the photoresist will be cross-linked and will not be removed the development.

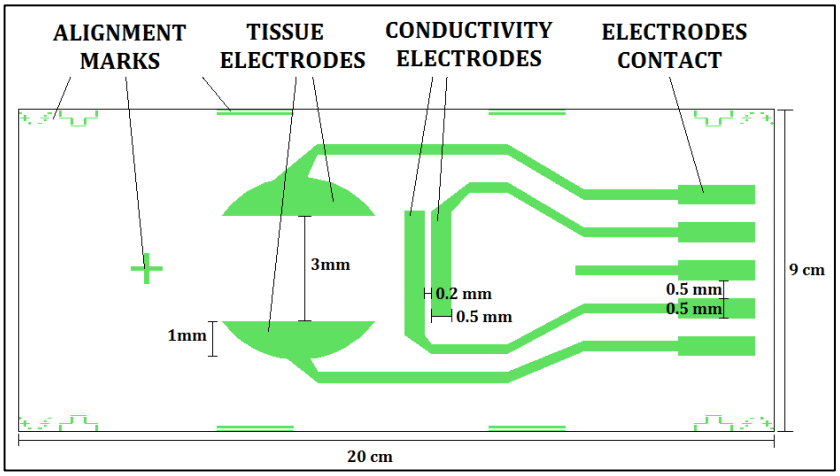

Figure 4-2 Diagram showing electrode design for a single chip. The crosses around the design are used as reference marks for the alignment with the other mask.

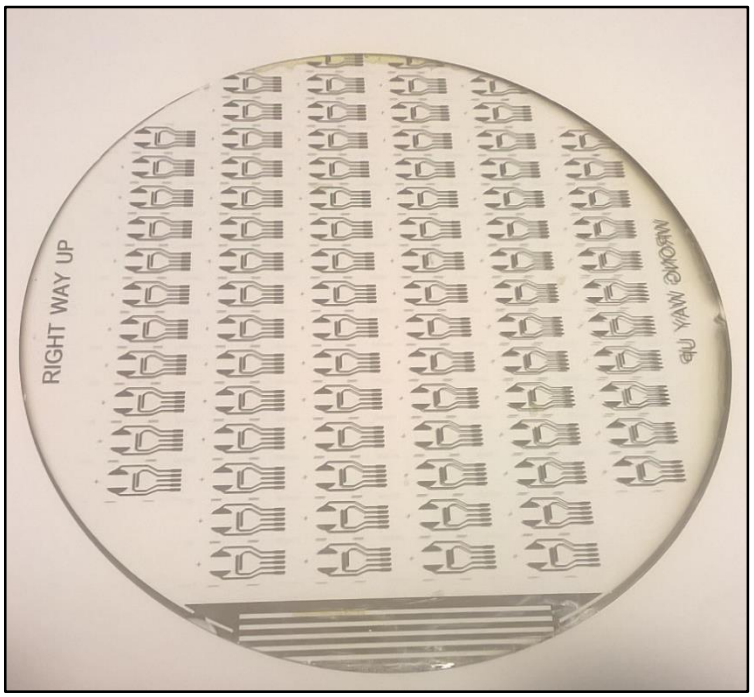

Figure 4-3 6" glass wafer after patterning the electrodes. 78 chips are present on each wafer.

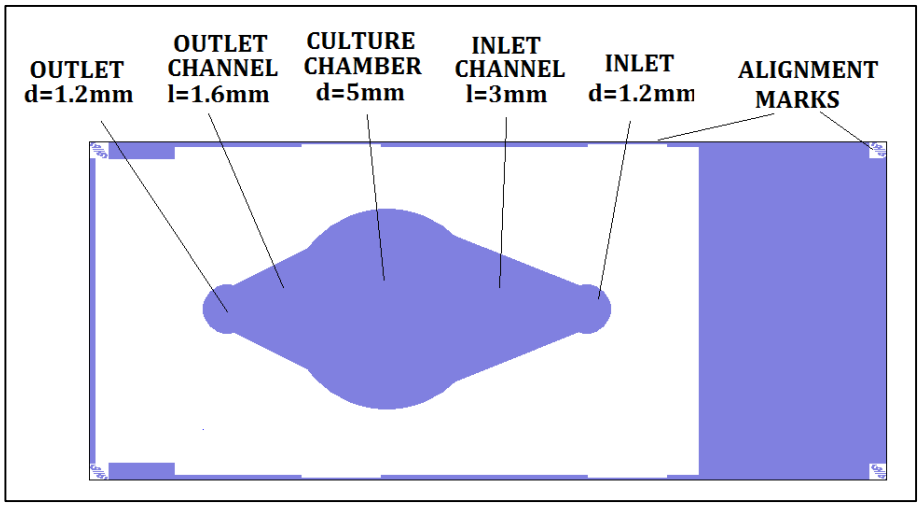

Figure 4-4 Single microfluidic channel unit of the photolithography mask. The alignment marks are complementary to the electrodes mask. The mask has been inverted because a negative photoresist is used to pattern the channel.

4.1.2 Laboratory processes

After the wafer is processed, it is diced into individual chips using a scriber. The resulting chips are ready to be processed in the laboratory. The remaining fabrication steps are performed in the Centre for Hybrid Biodevices in the order shown in Figure 4-5. First, the electrodes are electrochemically coated to improve their performances, then the culture chamber is fabricated.

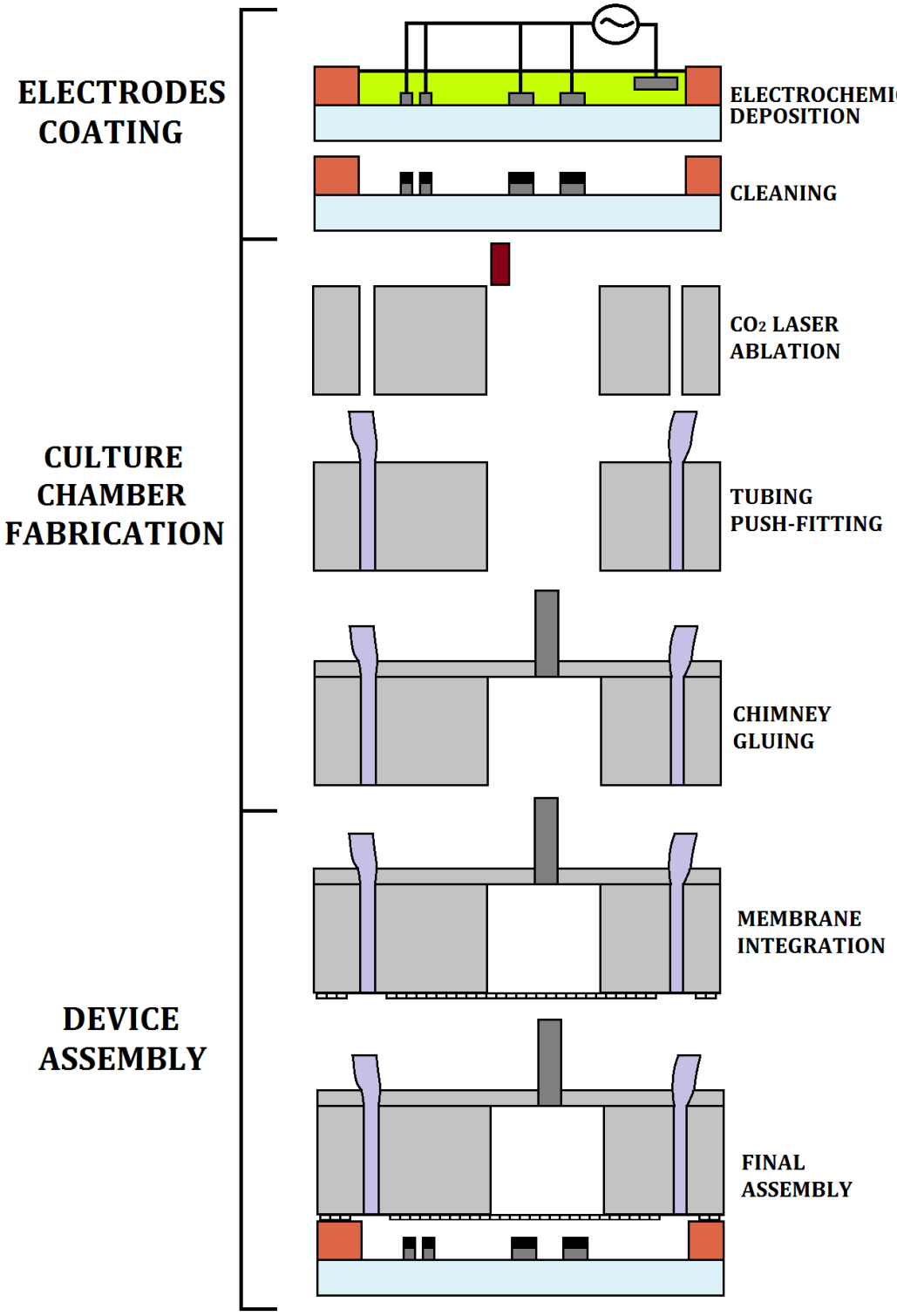

Figure 4-5 Laboratory steps of the fabrication process: Platinum black is electrochemically deposited on the electrodes. Inlet, outlet and culture chamber are ablated in a PMMA sheet using a CO_2 laser. Tubing are push-fit in the inlet and outlet and the chimney is glued on the assembly. A PET membrane is glued on the bottom of the PMMA and everything is glued to the chip.

Electrochemical deposition of platinum black

Platinum electrodes are nearly ideally polarizable electrodes, *i.e.* no Faradaic current can flow through them. This phenomenon completely controls the measured impedance at low frequencies (<100 Hz). To maximise the electrode capacitance, it is necessary to increase the electrode area.

The electrode footprint is fixed by size constrains, therefore the surface area is the only parameter that can be increased. To achieve this, a layer of platinum black is electrochemically deposited on top of the bright platinum electrodes [105]. Black platinum is highly nanostructured and thus has a high specific surface area. To perform the deposition, the platinum electrode to be coated and a platinum counter-electrode are immersed in a solution of Chloro-platinic acid and Lead-acetate (II) trihydrate (1 g and 8 g in 30 ml of de-ionized water to obtain concentration of 80 mM or 0.7 M, respectively). When an electric potential is applied between the electrodes (3.5 V for 210 seconds), lead imperfections act as nucleation sites on the bright platinum for the black platinum crystals to grow. The amount of platinum deposited on the electrodes depends on the total amount of current flowing through the electrolytic cell. Therefore, it is important that the distance between each electrode and the counter-electrode is the same to minimise non-uniformities in the final layer. The resulting chip is shown in Figure 4-6.

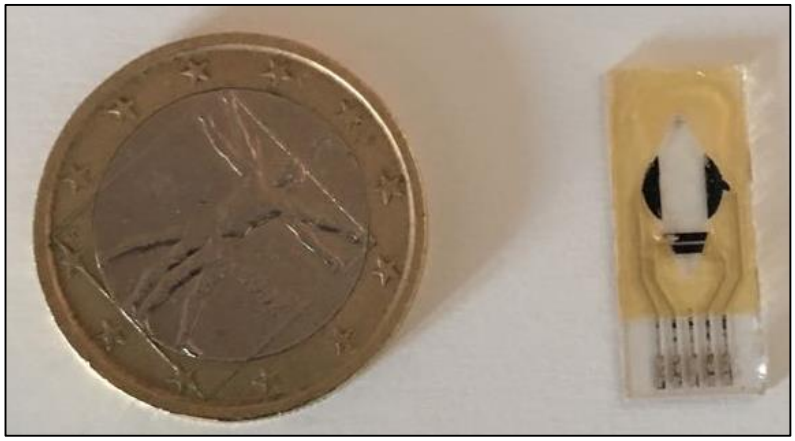

Figure 4-6 Chip after manufacturing. The TMMF defining the microfluidic channel is yellow, the sensing parts of the electrodes are black (coated) and the contacts are grey (uncoated). A one Euro coin is used as reference for dimensions.

Culture chamber fabrication

The bulk chip fabrication is performed in parallel to the glass chip fabrication. The function of this part of the device is to allocate the cell culture, the fluidic connectors, and to act as a structural support for the system. The material of choice for this part of the device is PolyMethylMethAcrylate (PMMA) for its cytocompatibility, low cost and ease of manufacturability. Cast sheets of PMMA were bought from TechSoft UK Ltd. 10 mm thick PMMA sheets are cut using CO_2 laser ablation. In laser ablation a CO_2 laser mounted on a xy-stage melts the underlying polymer along a 2D pattern. For thin substrates (1-2 mm) this technique is quick and accurate, but it loses resolution for higher thicknesses (>10mm) where the higher power warps the desired patterns because of localised heating. Given that the culture chamber diameter is 5 mm, to obtain an apical compartment of 200 μl of liquid and 200 μl of trapped air (as considered in the gas consumption model presented in Section 3.1.5) a 20 mm height is required. Therefore, 2 identical 10 mm thick PMMA pieces were etched and glued together to obtain the final device. The outer edges of the chip as well as the inlet, outlet and culture chamber through-holes are etched during the ablation process (Figure 4-7). The time required to cut all the features is about 30 seconds/piece.

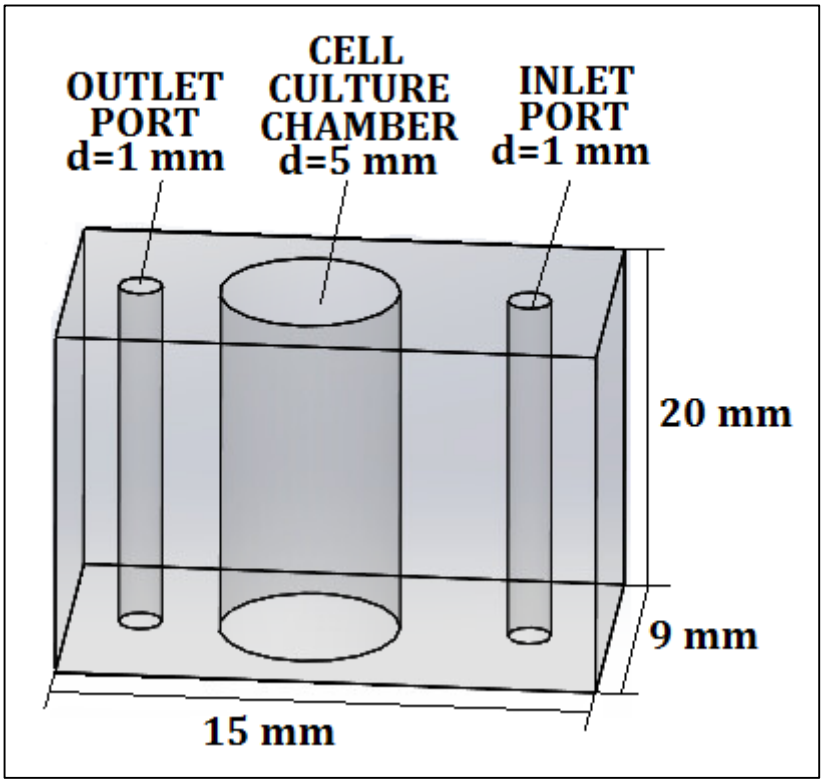

Figure 4-7 3D model of the PMMA unit. The inlet, outlet and cell culture chamber are ablated from a PMMA sheet using a CO_2 laser. Two 10 mm thick pieces are stacked together to obtain the final thickness.

Injection moulding

The industrial standard for mass manufacturing small polymeric parts is injection moulding. A thermoplastic polymer is heated above its glass transition temperature and pushed into a metallic mould where it is forced to assume a certain shape before cooling down. When cold, the part is removed and the cycle repeated. Moulds can be reused for millions of cycles and are the main cost associated with the process. They are usually made of aluminium, a workable material with medium cost and medium durability suitable for medium-sized production or steel, a hard material with high costs and high durability suitable for large volume production. Precautions needs to be taken to ensure uniformity across the manufactured pieces, because during the cooling step polymers tend to shrink and bend. Some guidelines for the mould design are:

- Avoid thick walls to prevent long cooling times.
- Adopt uniform wall thickness to prevent bending induced by differential cooling.
- Avoid sharp corners to prevent warping.
- Apply a draft angle to walls to facilitate mould release.
- Connect isolated part with bosses to reinforce them and prevent warping.

The PMMA part was redesigned according to these guidelines and models for the mould and the final device are shown in Figure 4-8.

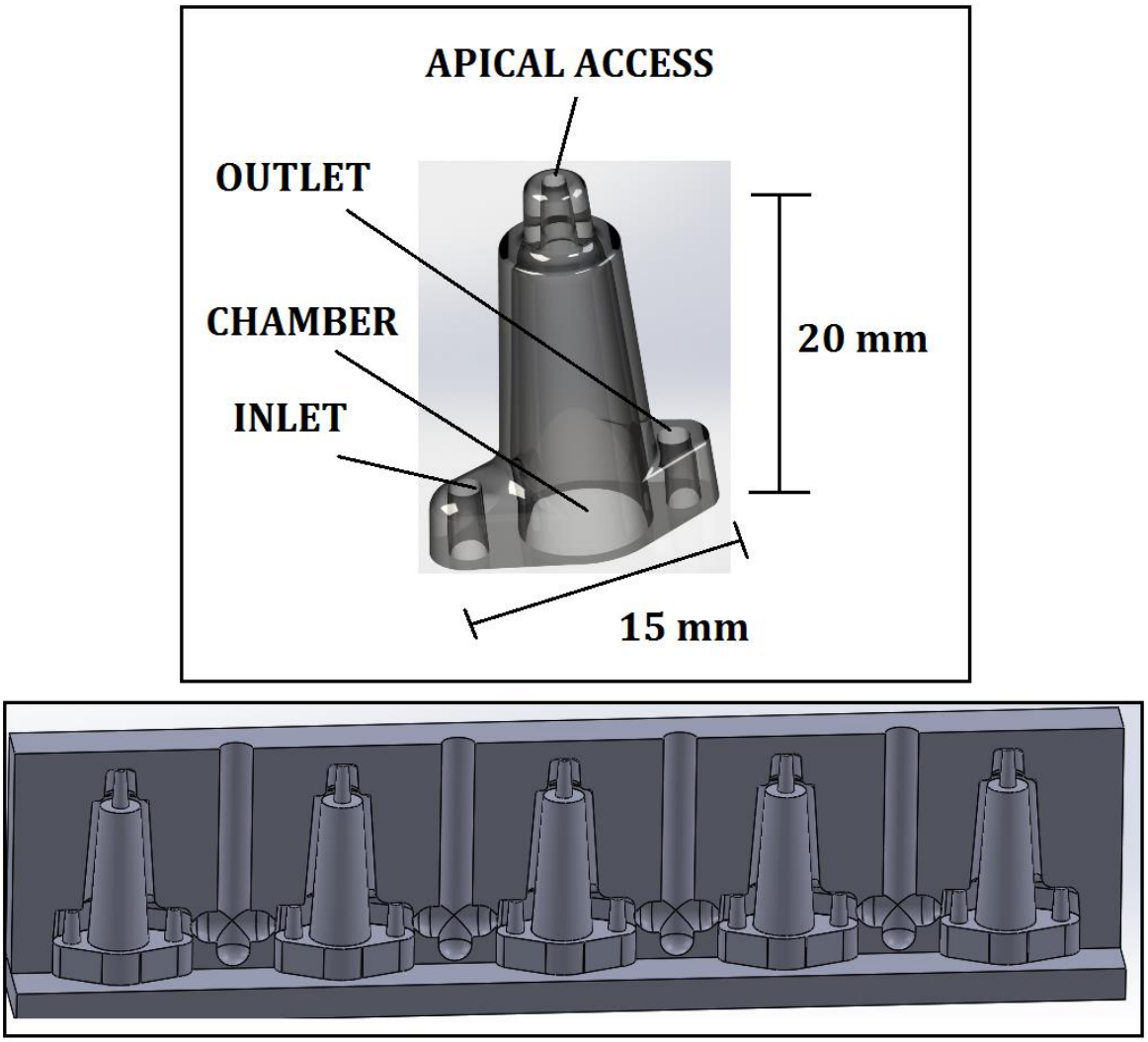

Figure 4-8 Injection moulding 3D models. (Top) 3D model of the device. Fillets and a draft angle are introduced for easier moulding. (Bottom) Model of the aluminium mould. The mould was kindly designed by Dr.Richard Alexander of Deakin University, Australia.

Culture support

In the device, cells are cultured on top of a membrane support which is suspended above the microfluidic channel. Several materials have been used in the literature to manufacture such supports. These include ceramic (Anopore™ [106], Silicon Nitride [107]), PolyEthyleneTherephtalated (Cyclopore™ [108], Transwell®) and PolyCarbonate (Nucleopore™ [109]). PolyEthylene-Therephtalated PET is the material of choice as this is the same material used in the commercial Transwell® system. The support needs to be porous in order for nutrients to diffuse from the microfluidic channel to the tissue construct. The higher the number of pores in the support the more homogeneous the nutrients distribution is across the culture. One technology to manufacture holes through a polymer is track-etching. This is a two-step process:

1. In the first step an energetic beam of heavy ions is shot at the polymer: the ions damage the polymeric chains as they pass through making them unstable.
2. In the second step the polymer is immersed in a chemical bath which etches the damaged chains but leaves the others unscathed.

The main advantage of this technique is the excellent degree of control of pore size, pore density and pore straightness [110]. For this project, hydrophilic PET track-etched membranes sheets were

purchased from it4ip S.A. (Louvain-la-Neuve, Belgium), a company specialised in track-etched membranes, with the parameters reported in Table 2. The membranes were cut to size with a scalpel.

Table 2 Parameters of the track-etched support

PARAMETER	**VALUE**
Thickness	12 μm
Pore size	400 nm
Pore density	10^8 holes/cm^2
Porosity	3%
Material	PET
Surface	Hydrophilic
Colour	Translucent

The apical compartment of the cell culture chip needs to be sealed to obtain a stable liquid meniscus, but there is also the requirement for an open access apical compartment that provides access for chemical stimulation and replacement of the medium. A removable lid addresses both these goals. A small metal 'chimney' compatible with disposable PDMS punched lids was added to the apical compartment as shown in Figure 4-9. This stainless steel chimney allows for easy application and removal of the lid, while granting a tight seal while the lid is in place. PDMS is gas permeable, but a 4 mm thick layer blocks gas permeation (in order to retain the pressure). In future injection moulded version of the design, the chimney for the lid will be integrated into the plastic.

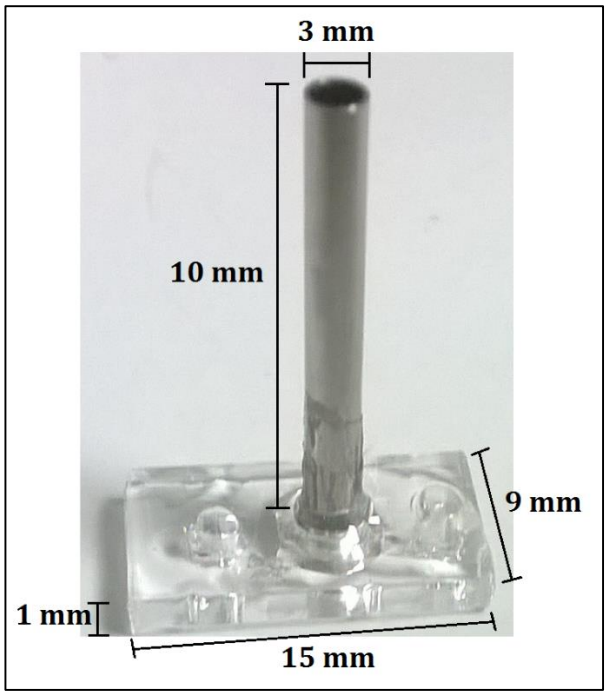

Figure 4-9 Metal chimney for the PDMS lid. A 10 mm long, 3 mm diameter stainless steel pin is glued into a 1 mm thick PMMA part in correspondence to the cell culture chamber.

Tubing

The device is connected to a pump with bubble trap and to a sample collection reservoir using PTFE tubing with inner diameter equal to 1/32" (≈0.8 mm) and outer diameter equal to 1/16" (≈1.6 mm) purchased from Cole-Parmer UK. Tubes are push-fit into the chips and are connected to the other components with Omni-Lok™ polypropylene (PP) connectors.

Bonding

Gluing the nanoporous support to the PMMA and chip is currently the rate limiting manufacturing step (requiring about one hour/chip). This process could be improved by implementing a wafer-scale gluing process or by adopting a different bonding technology. The bonding process is critical because:

- Three different materials (PET, PMMA and TMMF®) are bonded together.
- The nanoporous support must be flat and stretched after bonding.
- The bond must be able to maintain structural strength for 30 days at 37°C and 95% humidity (incubator).
- There must be no residuals that could harm the cells.

Several methods for bonding thermoplastic materials were examined [111].

Adhesive bonding

A common way to bond together parts of a microfluidic device is gluing. The glue must have chemical affinity for all components if different materials are bonded. A preliminary test on glues was performed to assess their cytocompatibility. The epithelial cell line, 16HBE were grown on the bottom of a standard cell culture well in the presence of the adhesive and their morphology examined. The results are shown in Figure 4-10. Morphologies of cells in contact with 3M double-sided tape, NOA81® and RS silicone rubber were similar to the control well; whereas Araldite 2-components epoxy, Loctite 435®, NOA61® and NOA65® induced cell death. In light of these experiment NOA81® was chosen to manufacture the device because of its low viscosity when liquid and its good strength when hardened. Norland Optical Adhesive 81 (NOA81®) is a UV glue that cures in seconds and whose use is widely reported [112, 113, 114].

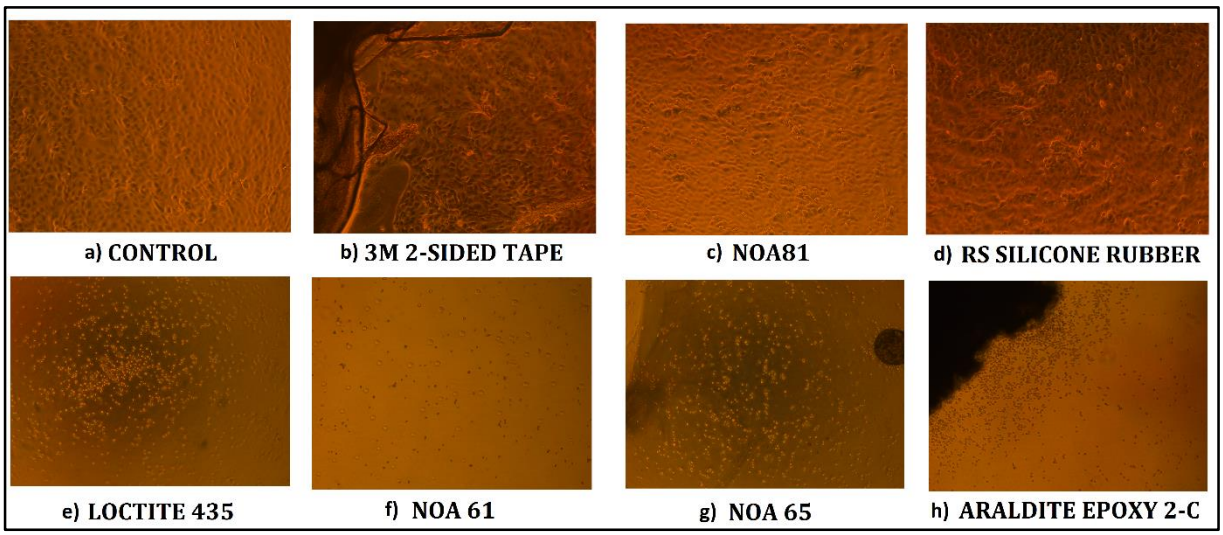

Figure 4-10 Glue cytocompatibility test. 16HBE were cultured on the bottom of a well plate. From a morphological analysis the 3M double-sided tape (b), NOA81 (c) and RS silicone rubber (d) were judged compatible, whereas Loctite 435 (e), NOA61 (f), NOA65 (g) and Araldite 2-components epoxy (h) were not compatible.

The glue dispensing process is critical since the culture area of the nanoporous support and the channel must be absolutely glue-free to prevent clogging. A procedure similar to the one reported by Lu *et al.* [115] was adopted to obtain a localised and accurate dispensing and shown in Figure 4-11. First, the chip, membrane and PMMA are aligned on top of each other. Then the glue is dispensed on one side of the system. Due to capillary action the low viscosity glue wicks into the nanopores and in the small gaps between the components. Then the chip is exposed to UV light hardening the glue. If the dispensing is carefully performed the glue will not wick into the channel due to the abrupt reduction of capillary forces.

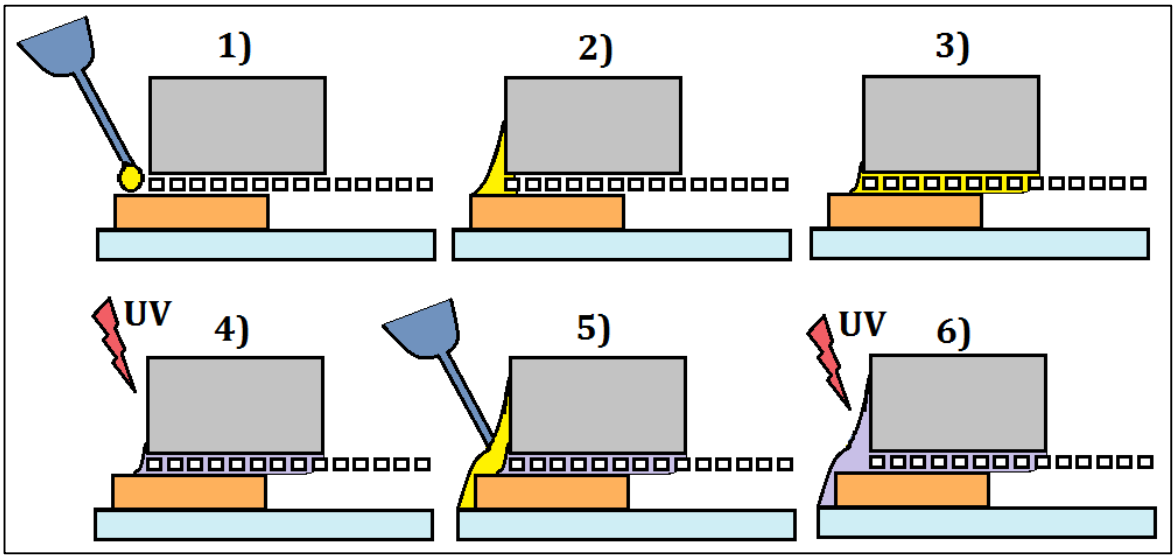

Figure 4-11 Gluing process. (1-2) The UV glue is dispensed on one side of the sandwich formed by the TMMF chip, PET membrane and PMMA part. (3) The low viscosity glue wicks into the small spacing between the components and inside the membrane pores due to capillary action. (4) The glue hardens after UV light exposure. (5-6) Additional glue is dispensed on the side and cured.

A weakening of the mechanical properties of the NOA81 was observed after a few days in the incubator which led to delamination of the device. To obtain a stronger device, another gluing step was added to the protocol. After the glue in the channel was dispensed and cured, more glue was added to the sides of the device and cured. The glass, the TMMF, the membrane and the PMMA part are strengthened by this additional gluing step. While in the first step the amount of glue dispensed must be accurately controlled to prevent channel blocking, in the second step excess glue can be used because there is no path available for the liquid glue to reach the channel. This process is currently performed manually one device at time. When performed by an experienced user the process yield is about 75%. The final assembled device is shown in Figure 4-12. The extension to wafer-scale gluing seems difficult to achieve, therefore alternative processes for mass manufacturing were analysed.

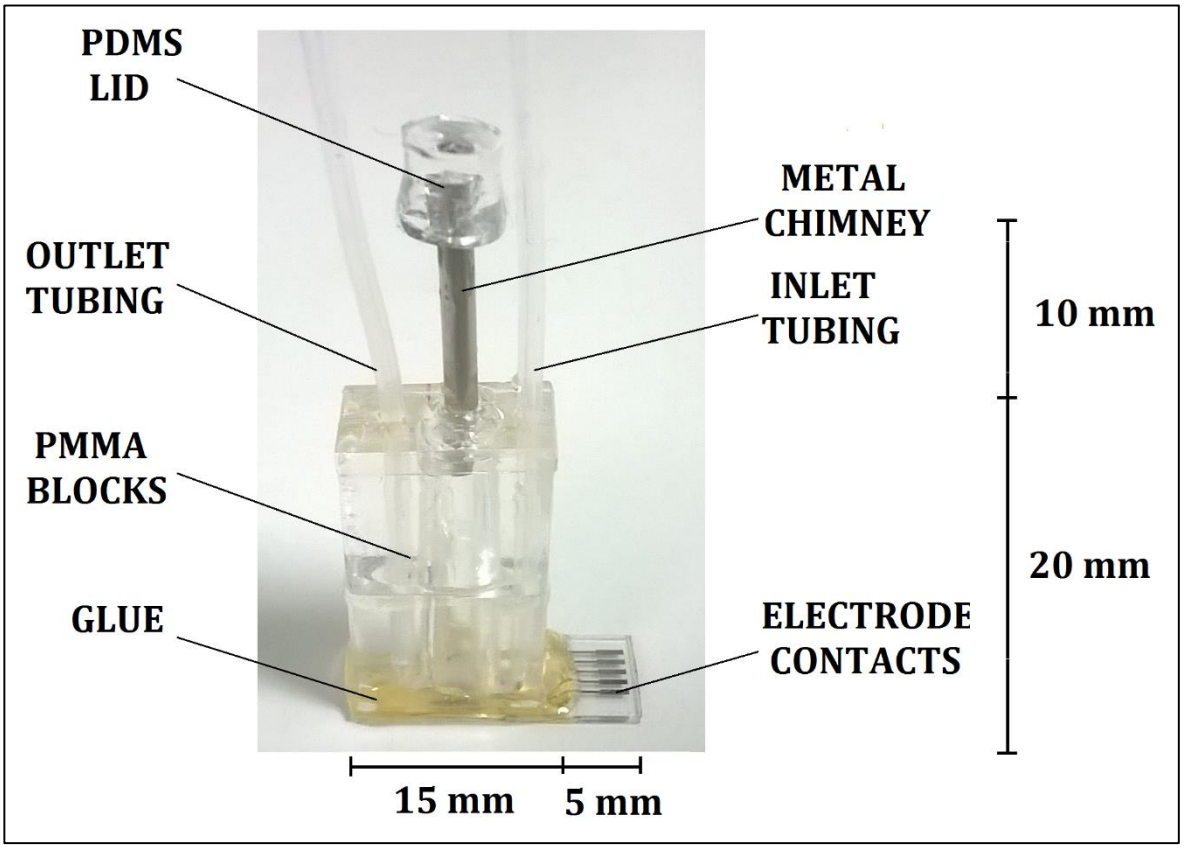

Figure 4-12 Assembled device. A PET membrane is sandwiched between the chip and the laser-cut PMMA piece. PTFE tubes are push-fitted inside the PMMA part. A metal chimney is added to allow apical stimulation and a PDMS lid is used to seal the system.

Alternative fabrication methods:

As mentioned above, alternative methods for device fabrication were investigated but not performed as part for this PhD thesis. These included the following:

1. **Off stoichiometry thiol-ene (OSTE)**

Off stoichiometry thiol-ene(OSTE) is a class polymeric components which has recently been developed in Stockholm at KTH Royal Institute of Technology. Two versions of the material are available on the market.

The first is a two liquid component mixture: one component has free thiols groups (the S-H bond) whereas the other has free allyl groups (R-C-CH-C_2). When this mixture is exposed to UV light in the presence of a photoinitiator, a cascade reaction occurs leading to solidification of the material in a short period of time (1-2 minutes). If the ratio between the two mixtures is stoichiometric, all the groups will react between them. If an off-stoichiometric ratio is adopted, some unreacted groups (with the quality and the quantity depending on the off-stoichiometry) will remain in the material and the surface will be easily functionalizable. The basic application is to mould a part of a device with a thiol excess (e.g. a microfluidic channel) and another one with allyl excess (e.g. the ceiling of the channel): the contact between the two parts will lead to a very fast bond. Many advanced features have been obtained with this technology, such as: tunable Young's modulus, tunable wetting properties, hydrophobic stops, integrated microfluidic connectors and pneumatic valves [116].

The second commercially available product is referred to as OSTE+ and is an upgraded version of the material featuring the addition of a third component with free epoxy groups to the mixture. This material works with a ratio of 1:2:1 of allyl:thiol:epoxy respectively. After mixing the material is liquid, and when exposed to UV light all the allyl groups will react with the thiols according to the previous reaction, leading to a soft solid material (Young's modulus comparable to PDMS). The thiols and epoxys will then react together after heating in a second curing step, leading to a fully

reacted solid network, as shown in Figure 4-13. The addition of the epoxy groups allows the material to bond to a wide range of substrates after the first curing step when the epoxys have not reacted yet. After the second curing step no groups are left unreacted, thus the presence of leachables is negligible leading to almost no cytotoxicity [117]. This material was not used due to difficulties in maintaining a clean membrane during the manufacturing process.

2. Chemical gluing

Chemical gluing is the process of bonding two heterogeneous polymers together by functionalising one substrate with ammine-terminated groups and the other with epoxy-terminated groups, as shown in Figure 4-13 [118, 119]. This process was tested to bond the nanoporous PET membrane to a PDMS block featuring an embedded microchannel. To this aim, both components were cleaned in deionized water and exposed to oxygen plasma to activate the surfaces and then functionalized in a 3-Aminopropyltriethoxysilane (APTES) or a 3-Glycidoxypropyltriethoxysilane (GPTES) bath, respectively for the PDMS block and the PET membrane. After application of a small compression force at room temperature, the process resulted in a strong bond between the two components. This process was not adopted due to difficulties in ensuring a conformal contact between the membrane and its seat during the bonding, leading to wrinkles and areas not bonded in the membrane which caused leakages during the experiments.

3. Thermal bonding

The structure of thermoplastic polymers can be modelled as a 'spaghetti-like' groove of chains. Weak inter-chains bonds control their relative mobility. When the temperature is increased, chains are less linked together and the material is less stiff. If the temperature is raised over a threshold (glass transition temperature, Tg) the polymer undergoes significant weakening. If two thermoplastic polymers are brought into contact, pressure applied and the temperature raised above both glass transition temperatures, it is possible for the chains to diffuse from one material to the other [111], thus creating a bond. Different methods have been reported to achieve a greater degree of control of the bonding, such as using high temperatures and low pressures [120] or high pressures and temperatures below the glass transition temperature [121]. The proposed manufacturing process for the device is to clamp the wafer together with a sheet of PET membrane (T_g≈80°C) and a wafer-sized PMMA block (T_g≈105°C). This is inserted into a hot-press at temperature higher than the T_gs (≈120°C) for sufficient time. This should be sufficient to ensure a good bonding of the system without sustained membrane modification.

4. Acoustic welding

In acoustic bonding heating is induced by acoustic means and thermal bond is obtained in localised regions [122, 123]. The process is shown in Figure 4-13. The machine is formed from a static base and a movable head: after the pieces are inserted, the head is brought into contact with the upper part and starts vibrating up and down at ultrasonic frequencies. These repeated movements generate friction in the contact spots between the parts. If the contacts spots are small enough, the heat generated can locally melt the polymer leading to bonding. In order to use this kind of technology, the pieces must be designed to have stress intensification regions. The protocol must also be optimised to obtain a wafer-scale process and to ensure that the PET membrane remains flat.

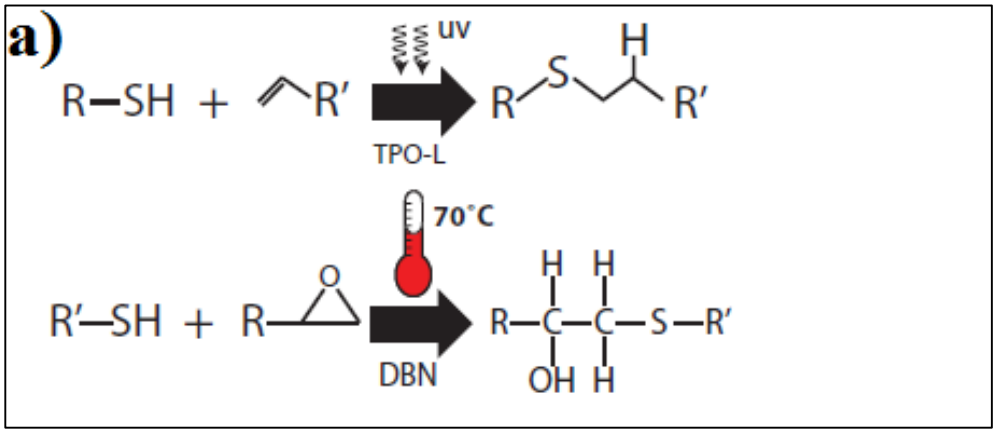

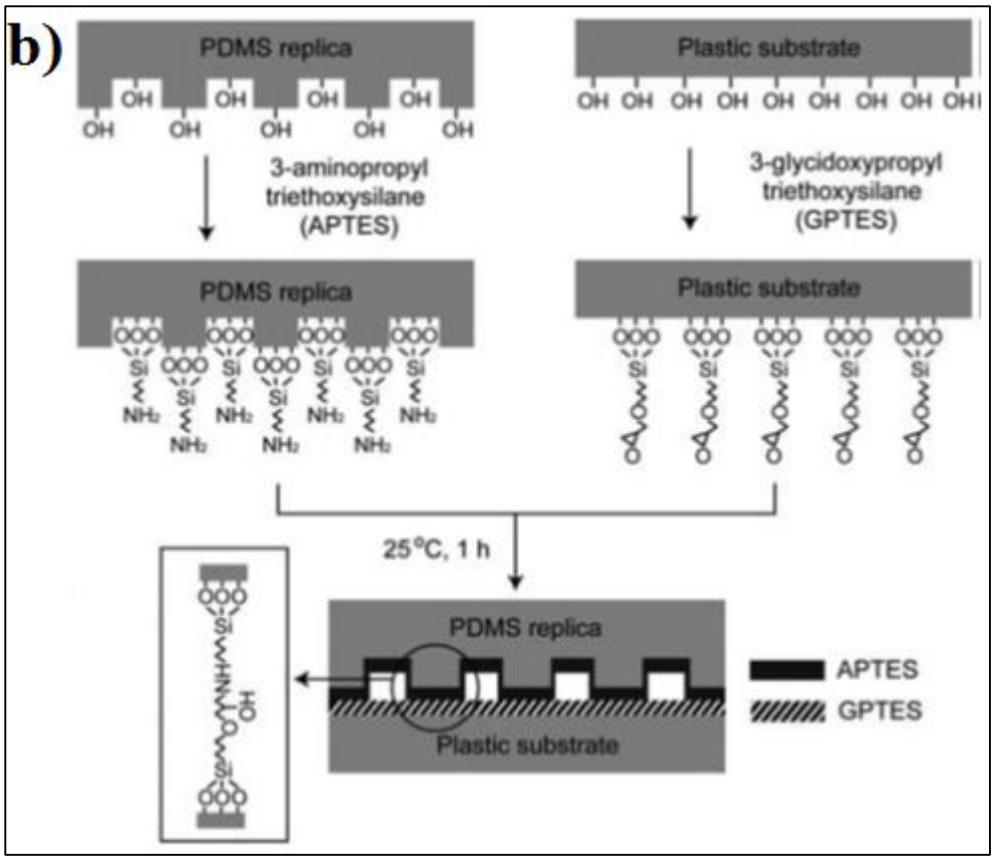

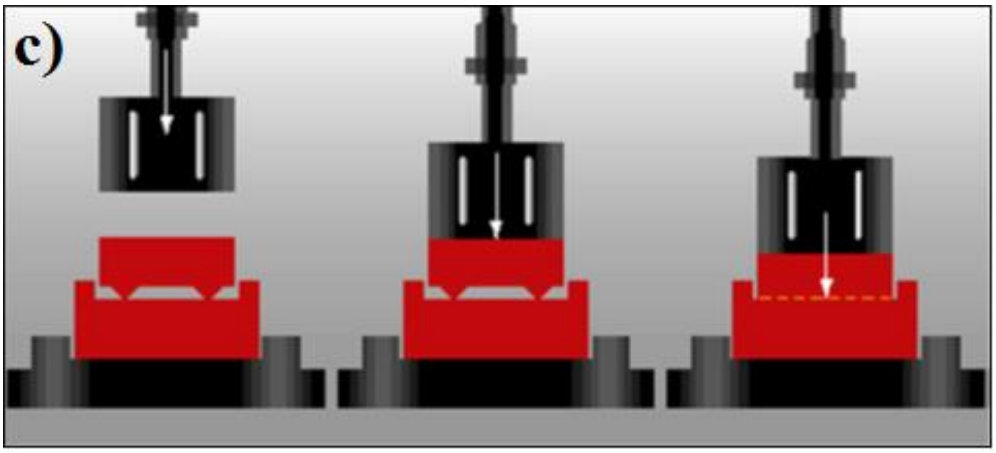

Figure 4-13 Alternative bonding technique. a OSTE+ dual cure polymer chemical reaction scheme [117]. b) APTES/GPTES chemical reaction scheme [119]. c) Ultrasonic bonding process from Trackenmuller *et al.* [122].

4.1.3 Static custom systems

Cells cultured in the device live in a constant perfusion regime which may affect the way they grow. Therefore, control systems are needed to rule out possible differences induced by the device or by the measurement before performing a direct comparison between microfluidic and Transwell® cultures.

Static support

The effects of the device structure and materials on the cell growth were assessed using custom static supports directly comparable to a commercial Transwell®, manufactured as shown in Figure 4-14. They are formed from the same PMMA and PET membrane glued together, but instead of the electrode chips they are equipped with two PMMA spacers that maintain the cell culture at a fixed distance from the base. This spacing is similar to the Transwell® system. These supports fit into a standard 24-well plate and the cell barrier impedance can be measured with standard chopstick electrodes.

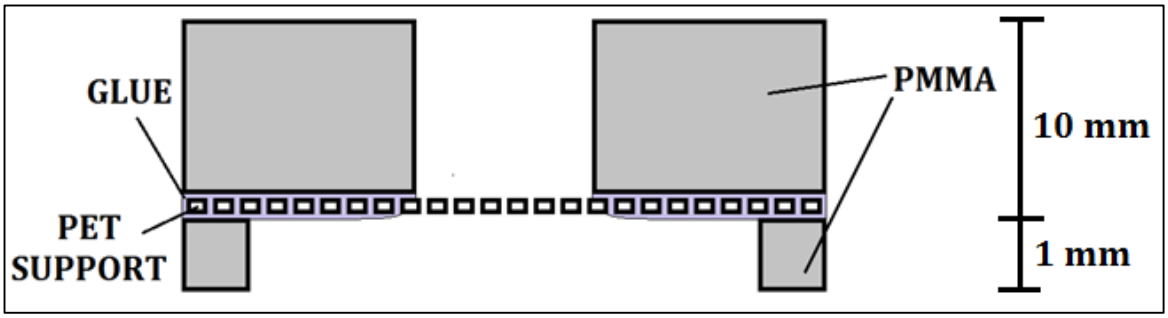

Figure 4-14 Custom support for the static culture of epithelia. A PET membrane is glued between a 10 mm thick PMMA ring that defines the cell culture chamber and two 1 mm thick PMMA supports that define the basolateral compartment.

Transwell® EIS measuring platform

Cells grown on Transwell® systems are considered the gold standard. Growing cells on these systems is relatively easy and reliable compared to the microfluidic system. It is useful to have a simple platform to perform electrical impedance spectroscopy on cells grown on Transwell® systems. This platform can be used to:

- Easily test and compare different electrodes design.
- Analyse the effects of variation in the measuring setup.
- Obtain preliminary measurements when a new type of cells is adopted.

Two measuring platforms were manufactured.

1. Electrodes with reservoir

Some of chips were not used to create a full device but as part of the measuring systems as shown in Figure 4-15. For the measurement, a drop of medium is placed on top of the electrodes and the Transwell® is carefully placed on top of the chip.

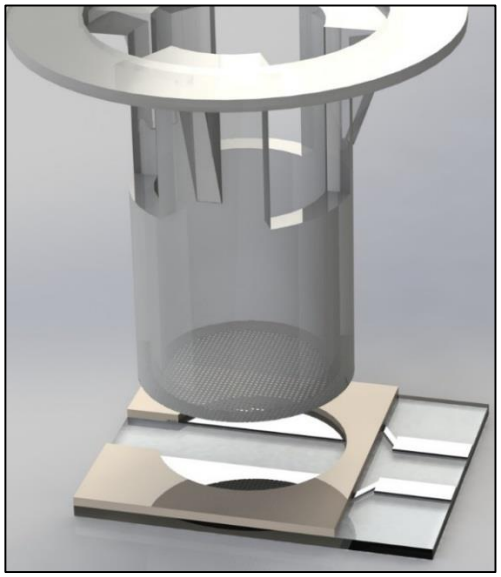

Figure 4-15 3D model of the Transwell® EIS measuring platform. The photoresist on the chip acts as a spacer for the Transwell®. A drop of medium is placed on top of the electrodes to perform the measurement.

2. Electrodes with insulating septum

This platform was used to analyse the effects of an insulating septum between the electrodes. To manufacture this platform the TMMF microfluidic channel is removed from a chip. A 4 mm thick PDMS sheet is cast and two 2mm holes are punched through. The two parts are then cleaned, activated with oxygen plasma for 30 seconds, aligned and bonded. The holes correspond to the platinum electrodes in the chip as shown in Figure 4-16. The holes are filled with liquid and the Transwell® is carefully placed on top of the PDMS to perform the measurement.

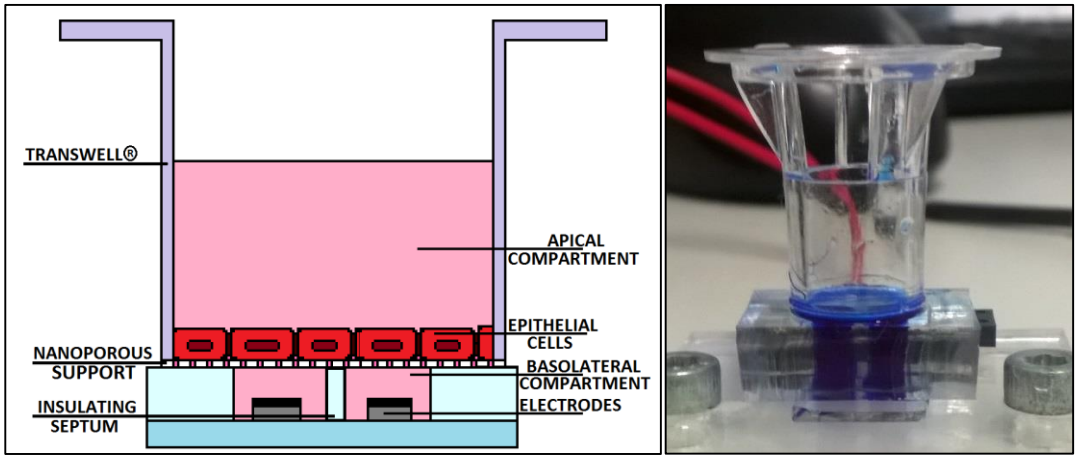

Figure 4-16 Transwell measuring platform with integrated insulating septum. Two 2mm holes are punched through the septum on top of the electrodes and filled with liquid (blue dye in the figure).

4.2 Experimental Setup

In this section are analysed the auxiliary components required by the chip to function. The device needs to be inserted into a setup that:

1) Provides a well-regulated medium flow. The setup must control flow rate, temperature and air bubbles of the medium.
2) Performs automated impedance measurements over time on the tissue.

A schematic diagram of the setup is shown in Figure 4-17. A 20 ml syringe is loaded onto a syringe pump. The pump is connected to a 3-way valve which is able to open each port independently. One outlet of the valve is connected to the waste collection, while the other feeds into a bubble trap. The bubble trap has one outlet on the top-side which is connected to the waste collection and one outlet on the lateral side which is connected to the device. Each outlet from the bubble trap has an in-line shut-off valve. The outlet from the device feeds into a collection tank. The electrodes of each device slide into a push-fit connector. The device is connected to a multiplexer which switches the channels for the impedance analyser measurement. The multiplexer is controlled by a data acquisition card and is powered by a portable power supply. The syringe pump, valves, bubble trap, device and collection tank are placed inside an incubator, whereas all the other components are place above or below it as shown in Figure 4-18. Before an experiment, all the microfluidic equipment is sterilised. After sterilisation, all tubings are connected and the system is primed with cell growth medium. After the bubble trap is filled, the device is connected and primed until stable flow conditions are reached. Successively, the electrodes are connected with the impedance analyser and an impedance measurement of the device without cells is performed. After the system has reached steady flow conditions (~15 min) cells are suspended and seeded. Impedance spectra are measured every hour until the cells become polarised.

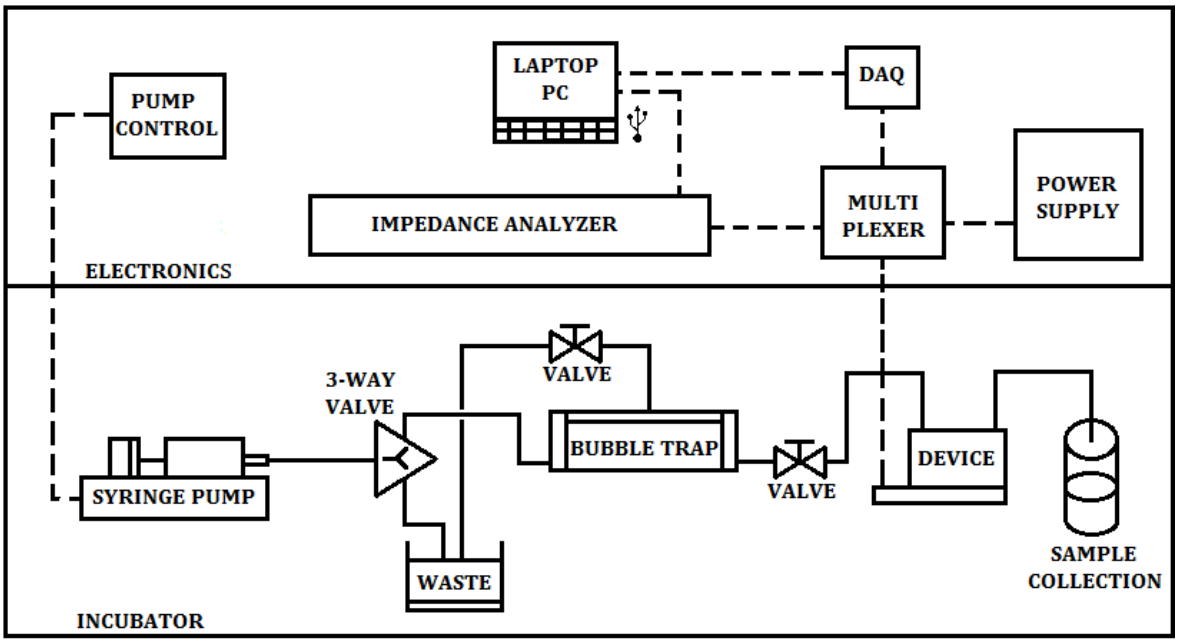

Figure 4-17 Schematics of the complete experimental setup. Fluid flows are shown as full lines; electric signals are shown as dashed lines. Inside the incubator the syringe pump actuator pushes the liquid and a trap removes air bubbles from the flow. Two tanks collect the waste and the sample. Outside the incubator a laptop controls a multiplexer and the impedance analyser.

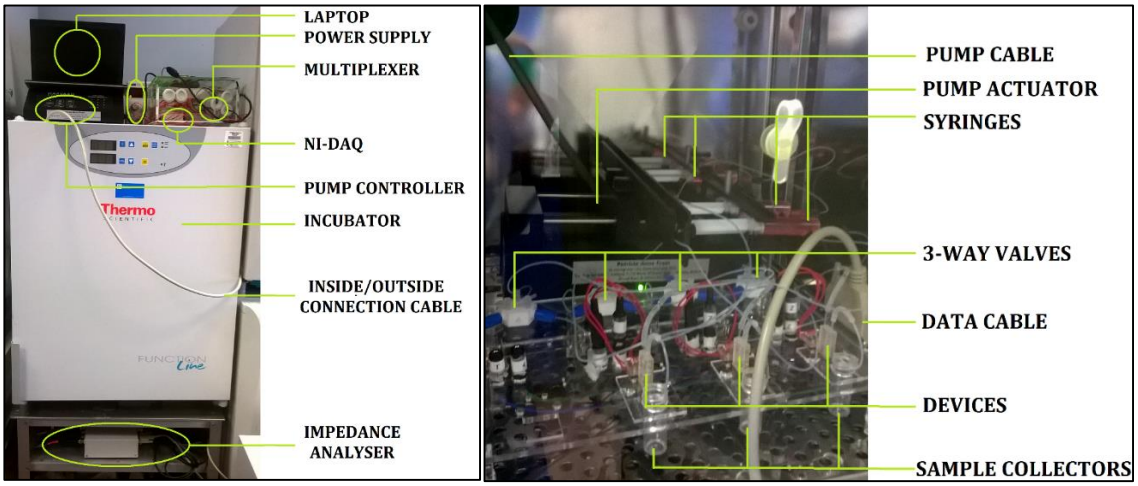

Figure 4-18 Picture of the experimental setup. (Top) View of the outside of the incubator. The laptop, the pump controller, the multiplexer and the power supply are placed on top of the incubator while the bulky impedance analyser is placed below. The data cable goes from the inside to the outside through the front door. (Bottom) View of the inside of the incubator. The syringe pump actuator is placed on the back of the top tray at an angle. A custom PMMA support is used to host the remaining setup. The pump cable goes from the inside to the outside through a hole in the back of the incubator.

4.2.1 Fluidic Components

Incubator

The incubator Function Line from Thermo Scientific is used to regulate the environmental parameters to physiological levels. Cells are kept at 37°C and 5% CO_2. To obtain a relative humidity of about 95%, autoclaved water is inserted in the incubator and replenished every few weeks. The incubator has a hole on the back to allow for the passage of electric cables.

Syringe Pump

The syringe pump (PHD2000 from Harvard Apparatus) was kindly donated by the Asthma Allergy & Inflammation Research charity. It can run up to 10 syringes in parallel with a minimum flow rate of 0.1nl/hr (using a 0.5 µl syringe). The control unit is placed outside the incubator and the actuator is placed inside. To minimize the amount of air bubbles in the system, the actuator unit is placed in the incubator at a small angle so that the buoyant bubbles accumulate at the top of the syringe.

Bubble Trap

Air bubbles are a common issue affecting the reliability of cell culture microfluidic devices [124]. The most common causes for the presence of air bubbles are:

- Incomplete filling of the system during priming.
- Inclusion during connections.
- Formation due solubility difference induced by temperature variations.

If an air bubble reaches the culture chamber it has two main adverse effects: if the bubble is underneath the nanoporous support it will block nutrient diffusion causing stress and eventually inducing death of some tissue areas; a bubble on top of an electrode will prevent the passage of current and completely disrupt the system impedance measurement. For these reasons, a bubble trap is inserted in the setup near the chip to prevent bubbles from reaching the microfluidic channel.

The working principle of the bubble trap is described in Figure 4-19. The trap has two outlets, one on the top to waste and one on the bottom to the microfluidic device. A shut-off valve is placed in

each line. The trap is first filled with medium: the bottom valve is closed, the top one is opened, and liquid is pumped through. When the chamber is completely filled, the top valve is closed and the trap is ready for operation. If there is a bubble in the inlet it will be trapped in the chamber due to higher buoyancy compared to the liquid. The trap chamber dimensions are 5 mm x 5 mm x 40 mm with a total volume of 1 ml. The volume is designed to be sufficient to ensure the removal of all the bubbles formed during a week; after this time the trap needs to be refilled. The residence time is the average amount of time spent by the fluid in the chamber, and can be computed as:

$$\tau_{res} = \frac{V}{Q} = \frac{1ml}{30\mu l/hr} \sim 3.3\ hr$$

the higher the residence time and the more time bubble have to be trapped, improving the efficiency of this gravity-based trap. The bubble trap was manufactured using laser-cut PMMA glued with a solvent welding process which leaves no residuals after solvent evaporation.

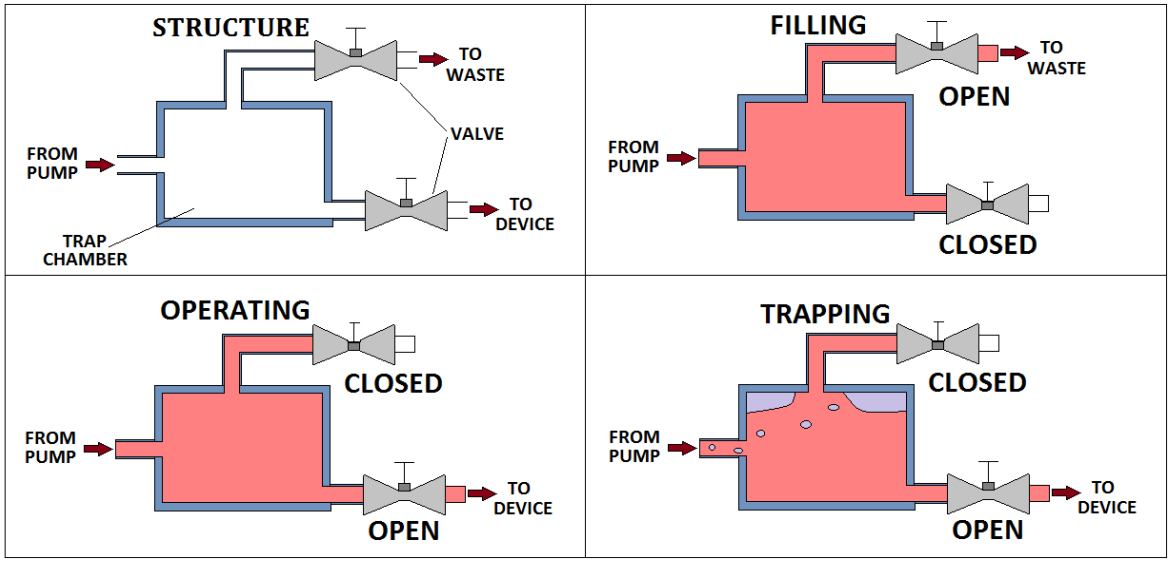

Figure 4-19 Working principle of the custom bubble trap. First the trap is filled with medium. During operation the valve to the waste is shut. When a bubble is present in the inlet medium it will move up because it has higher buoyancy and it will be trapped.

Sample collection

The liquid at the outlet of the device carries molecular targets that are important markers of cellular activity. Currently, the outlet medium is collected in a reservoir, but it might be of interest to collect fractions in a time-resolved manner for off-chip analysis as reported by Blume *et al.* [125, 126]. The main goal of the process is to separate different fractions and prevent diffusion of proteins between them. In this way, a fraction of the basolateral medium carries information regarding protein production rates and tissue permeability over time. While Blume *et al.* used a mechanical fraction collector as a way to prevent inter-fraction diffusion, another method could be to use phase immiscibility by intercalating a droplet of oil between the fractions. Similar processes have been developed in different applications [127]. Practically, this method consists of connecting the outlet of the device together with a fluorinated oil-phase to a T-junction to create a plug-flow. Compared to a robotic stage used by Blume *et al.* this method appeal lies in its simple setup (only an additional T-junction and syringe required).

4.2.2 Electronic Components

Several electronic components are needed to measure the impedance. The signal is generated, routed, acquired and measured. The components used in the setup and their connections are described in this section.

Impedance Analyser

The impedance analyser is a machine able to measure the impedance between two ports in a wide range of frequencies. The used impedance analyser is an Alpha-A (Novocontrol Technologies) which is able to operate in the frequency range 10^{-5} - 10^{7} Hz with an impedance magnitude accuracy of ±0.01% and a phase angle accuracy of ±0.06° [128].

Multiplexer

A custom designed multiplexing circuit was used to switch the impedance analyser to different devices running in parallel. The PCB shown in Figure 4-20 was designed using DesignSpark PCB (RS components) and was fabricated by Newbury Electronics. The multiplexer is an ADG726, which is a dual 16 to 1 channel with a typical transition time of 23 ns [129]. The multiplexer can switch one of the S1-S16 pins to the output A and the corresponding S17-S32 pin to output B. In the setup pins S1-16 are the left pins of each pair of electrodes and pins 17-32 are the right ones. The pair routed to the output is controlled by the multiplexer. The multiplexer has 9 control pins: A0, A1, A2, A3, CSA, CSB, WR, EN, GR. Of those, 4 (A0-A3) are used to select the channel, 1 (GR) is the ground, 1 (EN) puts the multiplexer in a safe state and 3 are left un-used. The control signals are provided by a Data Acquisition Card (National Instrument) which is controlled by the computer. Ferrite inductors are placed between the control pins and the multiplexer to cancel high frequency noise. The multiplexer is powered by an external power supply with voltage regulators of +2.5V and -2.5V between the power pins and the multiplexer.

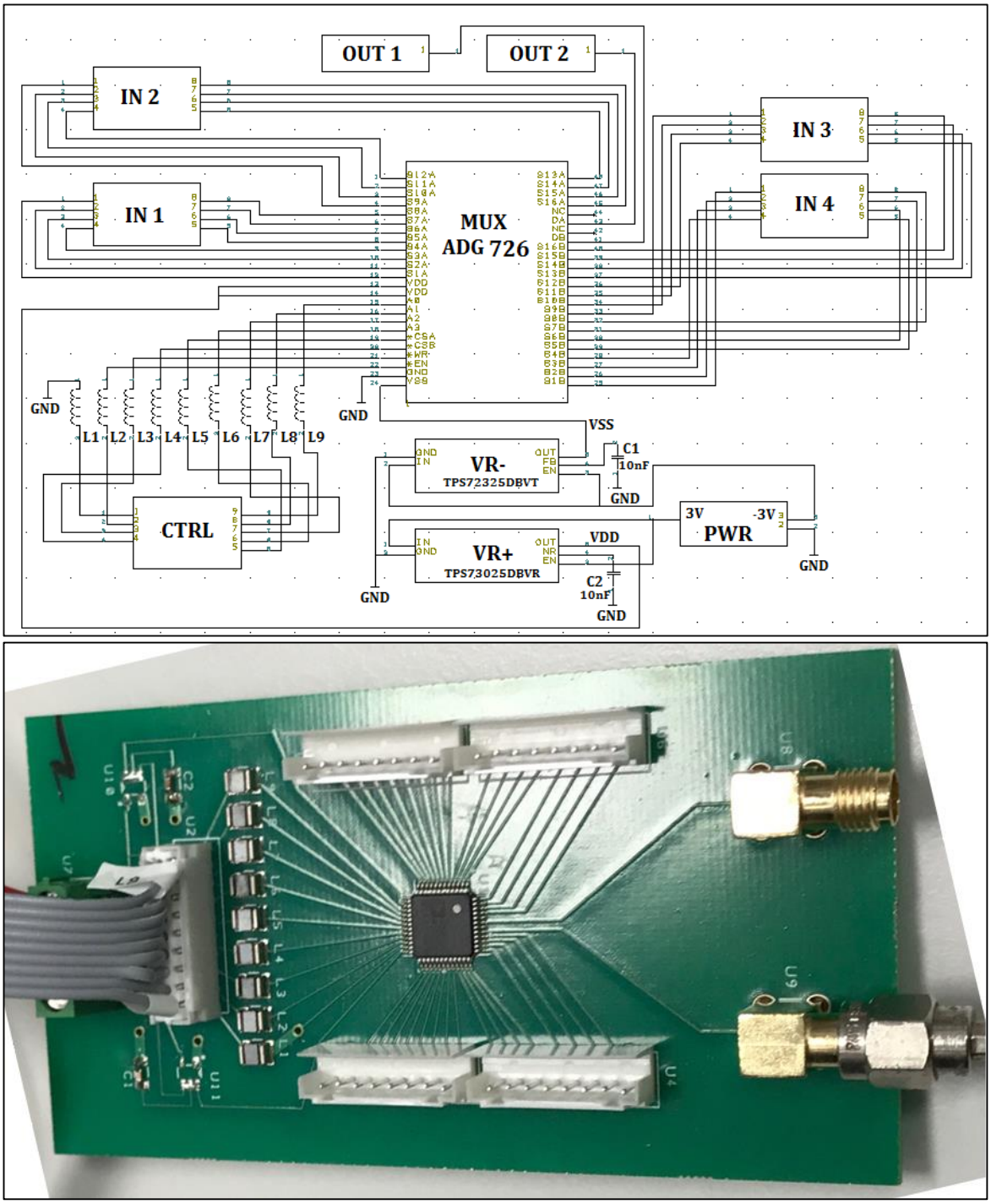

Figure 4-20 Custom multiplexing PCB. (Top) Electric Circuit. The multiplexer MUX (ADG726) is powered by 2 voltage regulator (VR+, VR-) and controlled by the digital signals CTRL from the NI-DAQ. The multiplexer switches the different imputs IN1-IN2 to output OUT 1 and IN3-IN4 to OUT 2 respectively. Capacitors C1-C2 and inductors L1-L8 are inserted in the circuit to filter external noise. (Bottom) Picture of the manufactured PCB.

Electronic connections

The diagram of the connections in the setup is shown in Figure 4-21. Spring-loaded connectors (SAMTEC) are used to contact each chip. These connectors have five 1mm-wide gold-coated pins underneath allowing a single chip to slide in. When the chip is inserted the spring is under slight compression, ensuring a good electric contact. A jack connector is used to connect the system inside the incubator. Signal cables are connected to a 37-pin serial cable, with a single cable from the inside to the outside of the incubator. The impedance analyser is connected to the multiplexing

board with 2 coaxial cables and to the computer with a USB cable. Connections from the multiplexer to the power supply and the NI-DAQ are made with individual wires.

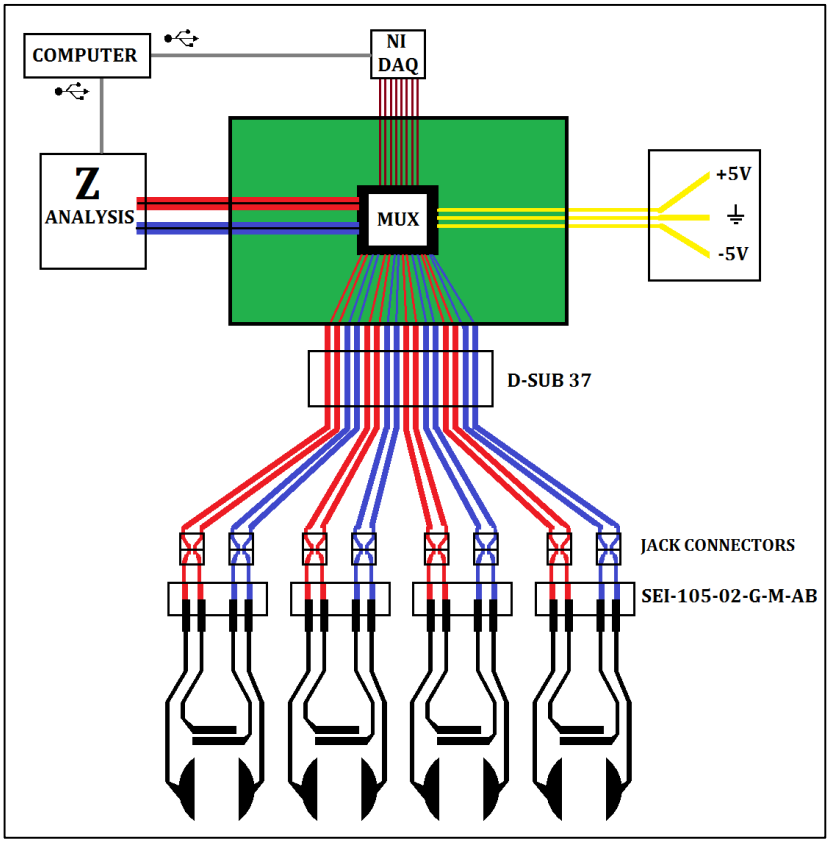

Figure 4-21 Connection diagram. Chips are contacted with SEI-series single piece interface connectors (Samtec). Each chip electrode pair is connected to a jack connector so it can be removed independently. All the wires are routed to a single serial 37-pin cable.

Computer Software

A computer controls both the impedance analyser and the multiplexing board. WinDETA is the proprietary software provided by the manufacturer of the Alpha-A impedance analyser to run the machine. It allows for measurement and real time plotting and customisation of frequency range, applied voltage and time points. The multiplexer was controlled using a custom Matlab script. The two software could not be merged and are run separately. The greatest inconvenience in running two different software to control the system is timing. There is no absolute time and the software need to be launched at the same time to ensure that they are in sync.

4.3 Tissue Cell Culture

In this section, the biological procedures used during the continuous culture of cells and during the experiments are discussed. All the cell culture was performed in the Brooke Laboratory within the Academic Unit of Clinical and Experimental Sciences (CES), Faculty of Medicine, University of Southampton at the University Hospital Southampton.

4.3.1 Tissue Models

Airway-derived epithelia were used for this study because they can be cultured submerged or at an ALI and form a physical barrier, thus being the best test subject for the new measuring system. Two different sources of bronchial epithelial cells were analysed using the device: an immortalised epithelial cell line (16HBE14o-) and PBECs derived from volunteers undergoing fiberoptic bronchoscopy. Compared to the primary cell culture, the cell line is less physiologically relevant but easier and faster to culture to a polarised epithelial barrier and it was therefore used as a preliminary experimental subject.

Human epithelial cell line (16-HBE14o-)
The main cell line used in this study was the human bronchial epithelial cell line 16-HBE14o- (16HBE). This cell line was immortalised using SV40 T-antigen from a 1 year old heart-lung patient and was originally described by Prof. Gruenert, UCSF, USA [130]. These cells are about 20 μm wide. When grown on collagen-coated nanoporous membrane filters these cells retain important epithelial cell morphology including the ability to form TJs polarised on the apical surface [131]. This cell line is commonly used to study several aspects of BEC biology including drug transport [132], gene delivery [133] and membrane channels activity [134]. This cell line develops TJs submerged and, once established, can maintain them at the ALI [131].

Primary human bronchial epithelial cells (PBECs)
Primary bronchial epithelial cells (BECs) were obtained as part of the EVITA/Merck study (study #888), approved by the Southampton and South West Research Ethics Committee (REC No. 09/H0504/109). All donor samples were obtained following written informed consent and were anonymised with a donor code. They were obtained by outgrowth from bronchial brushings harvested using fiberoptic bronchoscopy. The 4 cultures of primary cells used in this study were derived from to 2 asthmatic and 2 healthy donors. The cells were kindly prepared and seeded on Transwells® by the two Brooke Laboratory technicians, Dr. Natalie P. Smithers and Dr.Rob A. Ridley.

4.3.2 Cell culture

Continuous culture of the epithelial cell line (16-HBE14o-, 16HBE)
A previously cryopreserved frozen cell stock was thawed by pipetting pre-warmed cell culture medium (MEM+L-glut, 10%FBS + penicillin/streptomycin) into a cryovial and transferring into a falcon tube containing cell culture medium (10 ml). Cells were sedimented by centrifugation (300 x *g*, 5 min), the cell-free supernatant removed and the cells pellets resuspended in cell culture medium (10ml) and cultured in a T75cm^2 flask in a humidified atmosphere at 37°C, 5% CO_2. Cell culture medium was replaced every 2 days until 70-80% confluency was reached, after which cells were ready for subculturing.

Subculture of 16-HBE cells on filter supports
During subculture, the medium was removed and the flask was washed with a salt solution (HBSS without calcium and magnesium ions) to remove dead cells and residual proteins. The adherent culture of 16HBEs was detached from the surface of the flask with trypsin in ethylene-diamine-tetraacetic acid (EDTA) (1x 1 ml, 37°C, 10 min). After the cells detached, the residual trypsin is neutralised with fresh medium (10 ml) and the cell solution was transferred into a conical tube and

centrifuged (300 x *g*, 5 min). The cell-free supernatant was removed and the cell pellet resuspended in fresh medium (1 ml). A 10 µl aliquot was removed and used for cell counting using a haemocytometer. Once calculated, an aliquot of cells (200,000) were seeded in a flask coated with a collagen 1 solution (2mM in ultrapure water, 5 ml, 30 min at 37°C) for continuous culture, while the remaining cells were used for experiments.

The fraction of cells dedicated to the experiments was seeded onto commercial or custom made (as previously explained) filter supports. All the supports were previously coated with a collagen I solution in ultrapure water (2 mg/ml, 200 µl, 30 min at 37°C). The amount of cells seeded in each device was chosen to ensure confluency: 150,000 are seeded in Transwells® (surface area ≈ 33mm^2) and 90,000 in the custom supports (surface area ≈ 19mm^2). Cell culture medium was added basolaterally and apically and was replaced every 2 days. These cells achieve maximum barrier properties after 4-5 days of submerged culture on a nanoporous support [125, 126].

Subculture of PBECs on filter supports

Subculturing of PBECs was performed by Dr Natalie Smithers and will be briefly described here.
After removing cryopreserved cells from liquid nitrogen and thawing, cells were grown as monolayers in collagen-coated T75cm^2 flask in Bronchial Epithelial growth medium (2x BEGM from Lonza). Once cells at passage 1 were 60-65% confluent, they were detached from the surface with trypsin/EDTA and seeded onto Transwells® (70,000). Once 100% confluent, the primary cells are taken to ALI: the apical media was removed and media for the ALI culture was prepared (50% 2x BEGM w/o retinoic acid:, 50% DMEM+NEAA+NaPy+ penicillin/streptomycin +L-Glut+BSA) with the addition of retinoic acid (50nM) prior to replacement of basolateral medium. The basolateral cell culture medium was replaced daily. These cells achieve maximum barrier properties after 21 days of ALI culture on a nanoporous support.

Sterilisation

Prior to use, all custom supports are first washed in 10% bleach for 10 minutes followed by rinsing in sterile water, then washed three times in 70% Industrial Methylated Spirits, a HBSS rinse prior to collagen coating and cell seeding.

4.3.3 Barrier Disruption

Disruption of the barrier was induced in some confluent cell cultures to assess if the device is able to measure the drop in impedance. Two different chemical stimuli are used to achieve this effect: ethyleneglycol-bis(β-aminoethylether)-N,N,N',N'-tetraacetic acid) (EGTA) and polyinosinic:polycytidylic acid (Poly(I:C)).

EGTA

TJs are protein complexes that are regulated by the concentration of calcium ions Ca^{++} [135, 136]. One way to disrupt these complexes is by depleting the surrounding media of calcium. The depletion of these metal ions can be achieved with the addition of a chelating agent such as EGTA, which is a chemical able to remove free ions in solution and associate them into heterocylical rings. The addition of EGTA to a confluent culture of epithelial cells is known to induce strong TJ disruption and TER drop [66, 137]. Experimentally, an amount of EGTA required to reach a concentration of 0.5 M in the basolateral compartment was added. The typical required time for EGTA to induce a barrier drop is 10 minutes.

Polyinosinic:polycytidylic acid (Poly(I:C))

This synthetic analogue of double-stranded RNA, a molecular pattern associated with the replication of viruses and mimics a viral infection [138]. The physical barrier function of epithelial cells is known to decrease following exposure to poly(I:C) [126, 139]. Experimentally, a stock solution of Poly(I:C) (1 mg/ml in ultrapure water) was stored at -20°C and further diluted to the desired final concentration (5µg/ml) in cell culture media and added apically to both Transwell and

static supports containing cells. Typically, the first effects of poly(I:C) stimulation are visible after 3 hours.

4.3.4 Microscopic analysis

Analysing the size and shape of cells gives information on the status of the culture. For example, cells deriving from a cell line which have been cultured for several passages (>50) and are old start to show abnormal features such as incremented cell size and aberrant protuberances.

(i) Epithelial cell line (16HBE)

Morphologies for this type of cells are shown in Figure 4-22. When cultured on a planar surface, these cells are skewed along a preferential axis (Top-Left). They grow as an irregular plane with small valleys and mountains. During growth, the cells start to form small clusters that expand over time, adhering to neighbour clusters until they reach a confluent monolayer. Cell-cell contacts are clearly visible. The proteins that maintain the cell adherence to the surface are degraded when the cell dies, resulting in detachment (Bottom-Left). In addition, dead cells lose the preferential axis elongation and assume a spherical shape. When cultured on a nanoporous support these cells grow as a uniform culture and it is no longer possible to observe cell-cell interfaces (Top-Right). If the culture is healthy, the surface is mostly homogenous with minor imperfections. If the culture is not healthy (Bottom-Right), the surface shows marked differences between the areas where the cells are tight and a barrier is being formed and the areas where the cells are disrupted and the barrier is leaky.

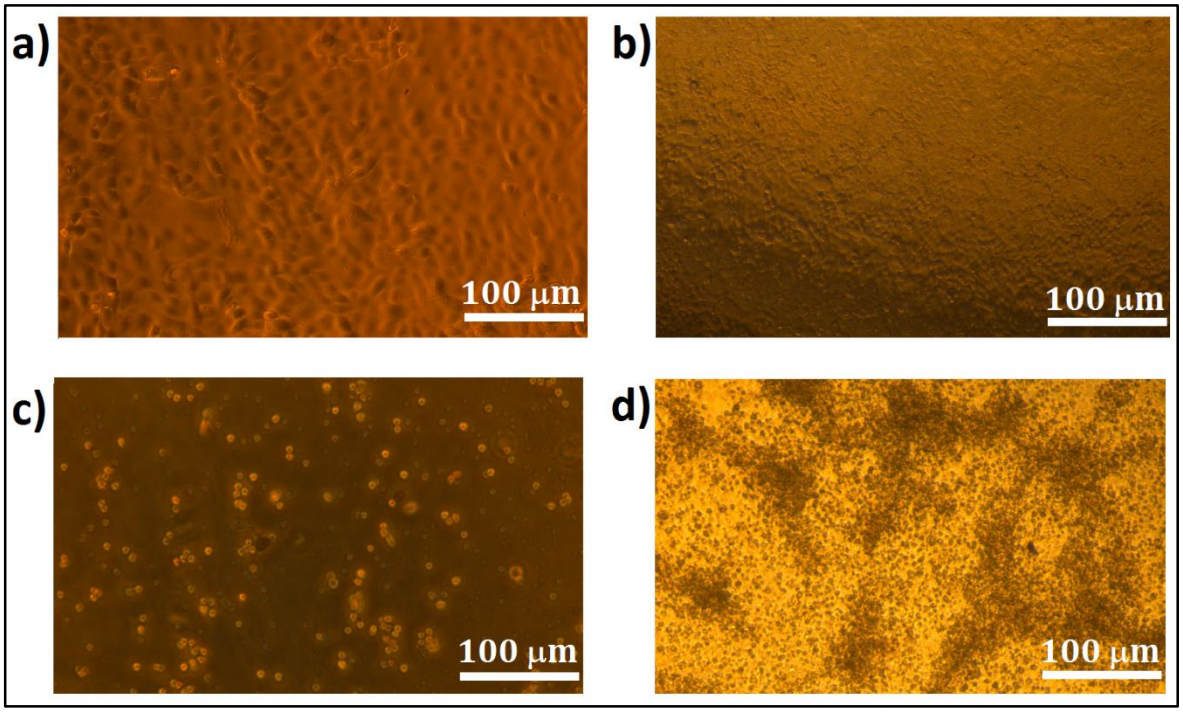

Figure 4-22 Morphologies of 16HBE14-o- cells. (a) Healthy cells cultured on a planar surface. (b) Healthy cells cultured on a nanoporous support. (c) Dead cells detached from the culture flask. (d) Disrupted culture of cells on a nanoporous support.

(ii) PBECs

Morphologies for this type of cells are shown in Figure 4-23. When first seeded on a nanoporous support, these cells form small clusters which spread over time. These clusters are clearly visible after the first week of culture (a), tend to disappear after the second week (b) and are absent after the third week (c). Cell-cell contacts are clearly visible at all growth stages. After cells form a confluent monolayer, they start forming an additional layer starting from the edges of the support

towards the centre. After the second week these cells start to develop mucus-producing goblet cells and mucus builds up on the apical surface.

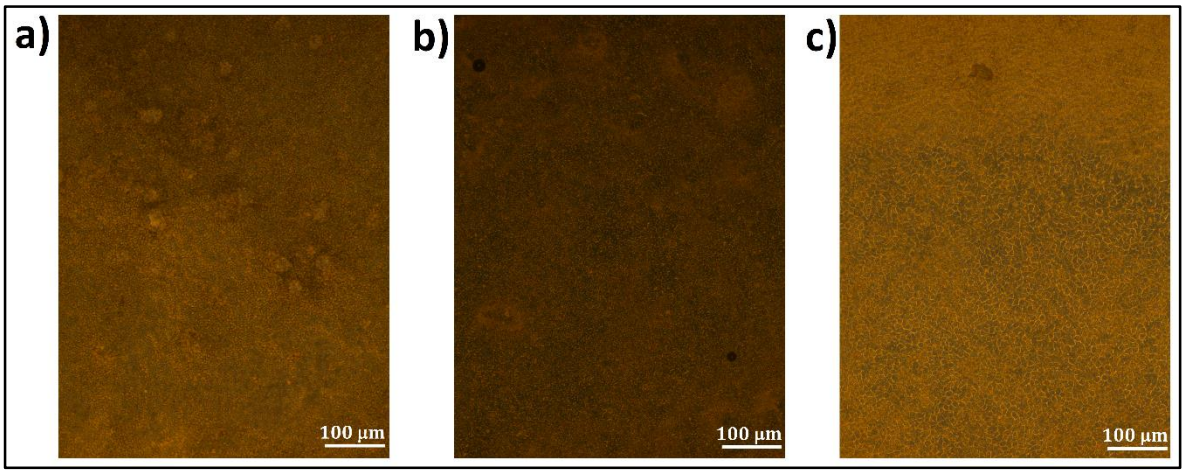

Figure 4-23 Morphologies of PBECs. At day 7 (a) small clusters deriving from the cell seeding are present. At day 14 (b) the residual cluster are less numerous and the cells are well distributed. At day 21 (c) no clusters are visible and cells start to produce mucus.

Cytocompatibility

Cellular morphology can be also used as a preliminary indicator for the cytocompatibility of different materials. A preliminary assessment of the cytotoxicity of glue was reported in the fabrication chapter. From this test, it was observed that cells grown in contact with certain glues died after 2 days. A similar test was performed for all the materials of the device. In particular, platinum black which was reported as a potential carrier of cytotoxic effects [140], did not affect the morphology of the culture.

Fungal infection

Microscopy inspection was used to verify the presence of any fungal infection. In the first stages of infection fungi are rod-shaped. As the infection proceeds, they produce more filaments from the edges of the pre-existing ones. At the final stage of infection, fungi produce spores that spread to the surrounding environment. Given the ease of fungal contamination and the high risk associated with it, it is necessary to discover any infection and promptly isolate and destroy the infected culture. An example of infected culture is shown in Figure 4-24.

Figure 4-24 Example of a culture of 16HBE cells infected by fungi for 4 days.

Immuno-fluorescent staining

This technique consists of the selective staining of different proteins in the cell with different fluorescent markers and subsequent microscopic analysis. This procedure yields information on the presence or absence of proteins and on their spatial organisation in relation to other cells. An example is shown in Figure 4-25 where three components of the system have been stained with different fluorescent markers: actin filament are marked in red, zona occludens-1 in green and the DNA in the nuclei in blue. With the superimposition of the images it is possible to gather information regarding the order of the TJs and of the 3D structure of the cells.

Before staining cells were fixed by the addition of paraformaldehyde (4% PFA in PBS). This is an organic compound able to form covalent bonds between dissolved proteins and the cytoskeleton, blocking the cellular structure and preventing cellular decomposition. Once fixed, the membranes were permeabilised using a surfactant (Triton X-100, 0.1% in PBS, 15 minutes), the non-specific binding sites were blocked by addition of Bovine Serum Albumin (BSA) (PBS + 1% BSA+ 0.1% Tween20, 30 minutes), the conjugated antibody for occludin (AF647-labelled-occludin) and Acti-stain 670 (Cytoskeleton Inc.) was added and left to incubate overnight. After washing (5 x 5 minutes, 0.1% Tween 20 in PBS), a drop of ProLong Gold Antifade Reagent (with DAPI) was added on the cells and the system covered with a cover slip.

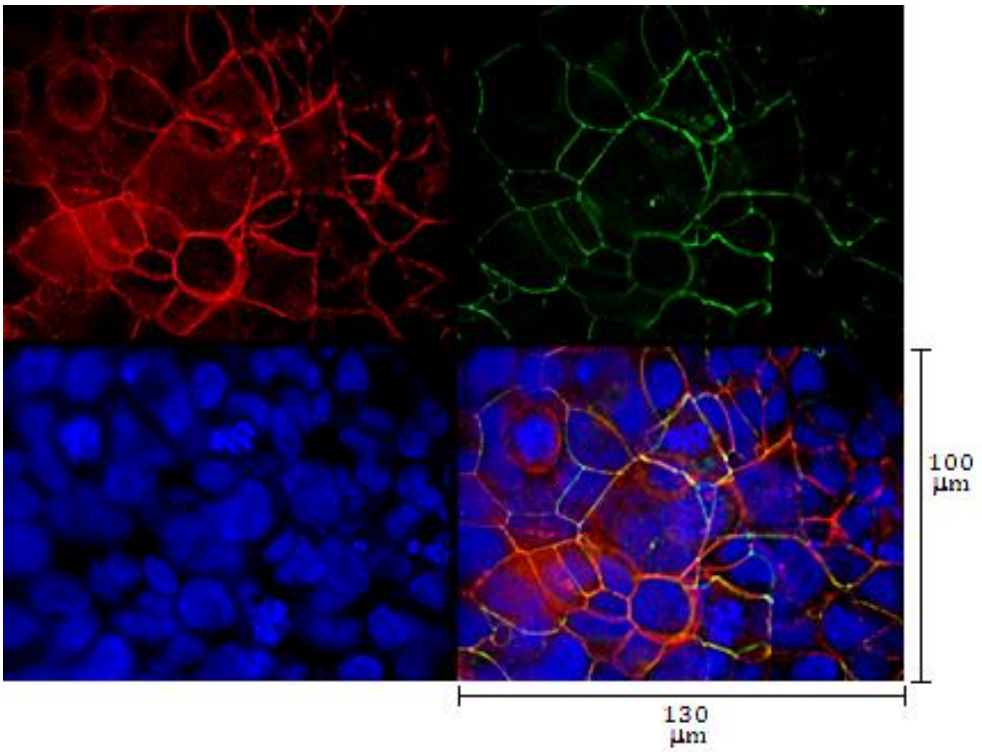

Figure 4-25 Immunofluorescent staining of 16HBE cells cultured on Transwell® for 6 days. Actin filament are stained in red, occludin is stained in green and the DNA in the nuclei is stained in blue.

Z-stacks were taken using LSM 6000 microscope (Leica Microsystems, Wetzlar, Germany). After deconvolution using Leica Application Suite software z-projections were performed using ImageJ software. This assumes that the light originated from one point spread according to a point spread function which is the same for all the sample. This allows for analysis of different sections of the tissue and for 3-dimensional reconstruction of the cells such the one shown in Figure 4-26. Immunofluorescence staining was performed in collaboration with Dr. Robert A. Ridley and Dr. Cornelia Blume.

Immuno-fluorescence staining images can also be used to obtain quantitative estimates of the status of the tight junctions. For example, it is possible to quantify the effects of a disruptive stimulus by comparing images of treated and untreated cultures. One approach to compute this disruption is to consider how many cells in each image contribute to the tight-junctional barrier, i.e. are surrounded by an interrupted perimeter of TJs, as shown in Figure 4-26. The advantage of this approach is that it accounts for both TJs destruction (which lead to cells with an incomplete perimeter of TJs) and for TJs redistribution (which lead to TJs located around a cluster of more than one cell). While in this work the count was performed by visual inspection, it is possible to implement an automated image processing routine capable of counting the cells. This routine should first remove the image background and then perform Fourier or Hough transforms to obtain matrixes that can be analysed for patterns. To obtain a robust analysis, at least 3 different areas should be imaged for each sample and a statistical analysis of the measurements should be conducted.

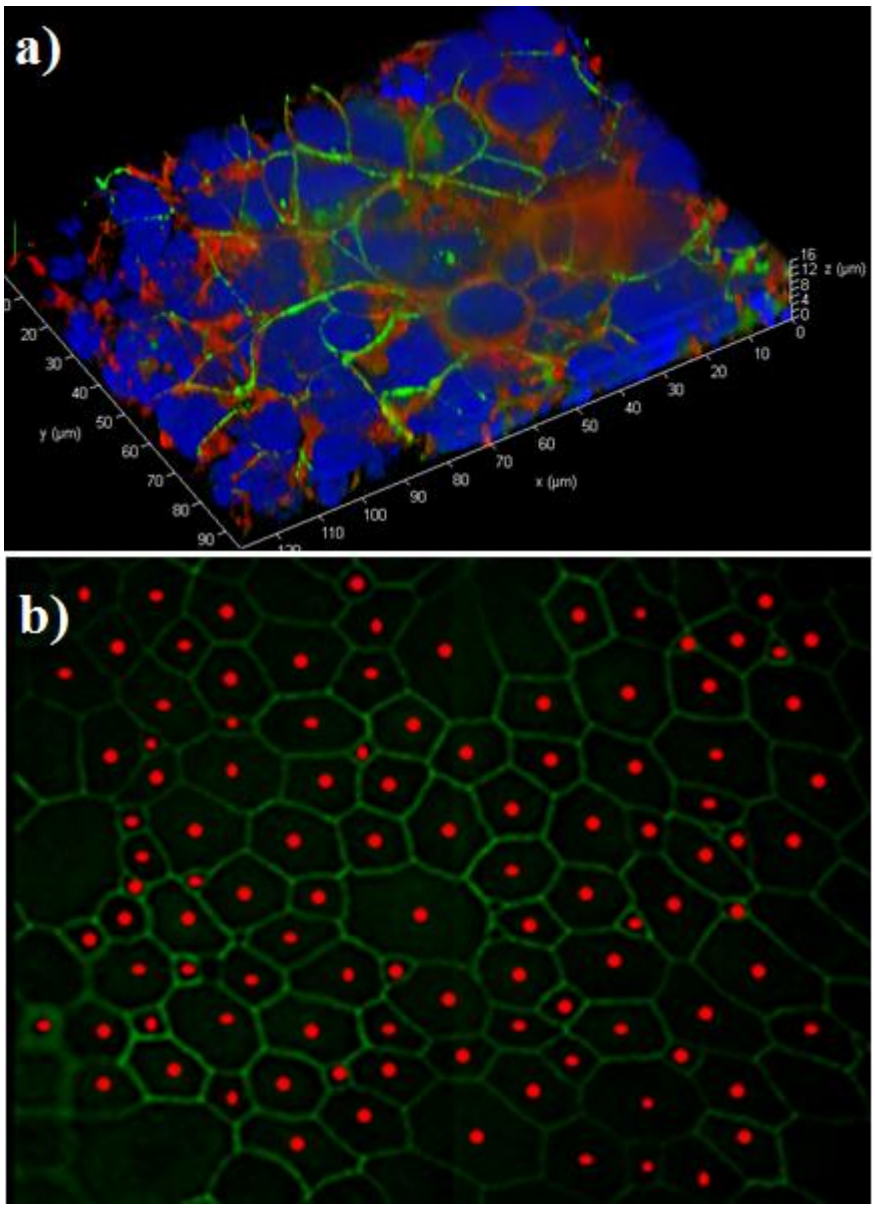

Figure 4-26 Quantitative information from immunofluorescence stained tissues. a) Tissue construct thickness obtained by 3D reconstruction of 16HBE cells created by obtaining multiple images at different heights. b) Cell count for tight junction status evaluation: the red dots represent cells surrounded by an interrupted perimeter of occludin.

4.4 Chapter summary

In this chapter, the experimental apparatus and the techniques required to manufacture the device and culture the cells are described. Currently, the manufacturing process for the device is divided between the clean-room and the laboratory. In the clean-room, the process is performed on a 6" wafer which can yield up to 76 devices. Platinum electrodes are patterned and then the TMMF channel is defined using photolithography. After dicing, each chip is coated with platinum black and glued integrated with a nanoporous membrane and a polymeric part. At the moment, the integration of the nanoporous membrane by manual gluing is the critical and production–limiting factor. It might be possible to improve process time and yield by the adoption of a different process such as acoustic welding or thermal bonding. Also, while the production of the polymeric part by laser ablation is sufficient for prototyping, it is necessary to switch to injection moulding for higher manufacturing volumes.

During an experiment, the chip is placed inside an incubator, and growth medium is pumped by a syringe pump. Air bubbles are removed with a bubble trap before reaching the device. Electrodes are connected with a serial cable to a multiplexer and to an impedance analyser outside the incubator. A commercial impedance analyser provides great sensitivity but it is over-specified for the task and a cheaper alternative could be used in future setups. At the moment, samples at the outlet of the device are collected in a single reservoir. In this way, information regarding protein production rates are lost: it would therefore be interesting to integrate the device with a system to collect and store liquid fractions produced over time for subsequent off-chip analysis, in order to compare the electrical and chemical response of the cells. A simple setup to perform time resolved fraction collection using an oil-phase similar to what is used for capillary liquid chromatography was proposed.

Two sources of human bronchial tissue were considered: a human bronchial epithelial cell line (16HBE14o-) and PBECs. Chemical stimuli to induce a cellular barrier disruption were described. This artificial disruption was used to test the capability of the device to measure drop in tissue barrier properties. While EGTA chelates the free calcium ions required by the TJs and completely disrupts the barrier, Poly(I:C) mimics a viral infection and induces a mild barrier disruption caused by an inflammatory response. Conventional microscopy was used to observe the growth of the culture, to detect eventual infections and to test material cytocompatibility. Fluorescence analysis was used to obtain spatial information on tight junctional complexes.

Chapter 5: RESULTS – Electrical characterisation of epithelia

This chapter describes the experimental results for characterising the electrical properties of epithelial cell cultures. Firstly, baseline measurement without cells was investigated to calibrate the system. Secondly, characterisation of cells grown in fluid and static conditions on commercial Transwell® supports or on custom fabricated supports are examined before finally characterising the electrical properties of cells grown under microfluidic conditions. Details of the statistical methods used during data analysis can be found in Appendix D.

5.1 Baseline measurements without cells

The first set of experiments was performed in the absence of cells and used to calibrate the system and establish a baseline.

5.1.1 Conductivity measurement

The bright Pt electrodes used to measure cellular impedance were calibrated with increasing concentrations of salt solutions (NaCl, 50-500 mM). The measured impedance spectra are shown in Figure 5-1. When the salt concentration was increased, the Debye length decreased by a square root and the number of charge carrier increased. This was reflected experimentally by a decreasing impedance magnitude and a decreasing phase angle with increasing salt (and therefore ions) concentration. Impedance spectra were fitted with an equivalent electric circuit formed by a CPE representing the electrode polarisation and by a resistor in series. The phase of the CPE is 0.51 for a 500 mM solution and 0.32 for a 50 mM solution.

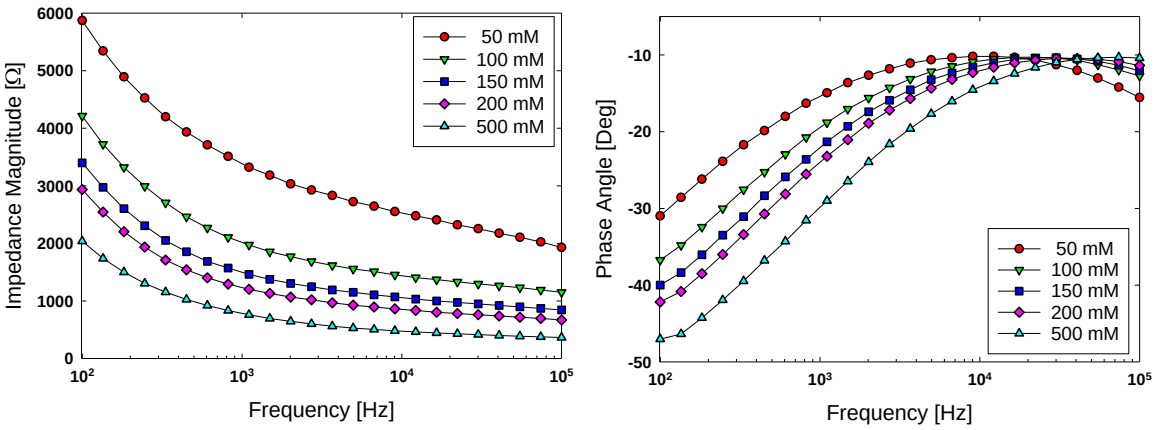

Figure 5-1 Impedance spectra for solution with different concentration of NaCl. As the concentration is increased more charge carriers are present in solution leading to a decreased impedance magnitude and phase angle.

For dilute electrolytes the solution conductivity is directly proportional to salt concentration. Therefore, the admittance (the reciprocal of the impedance) and the salt concentration should correlate linearly. This is verified in Figure 5-2 where admittance magnitude values are plotted against increasing NaCl concentration and fitted linearly. At high frequencies (100 kHz) the linear correlation was strong (R^2=0.98) while at low frequencies (100 Hz) the correlation was poor (R^2=0.94) attributed by the strong effect of the electrode polarisation in absence of the platinum black coating.

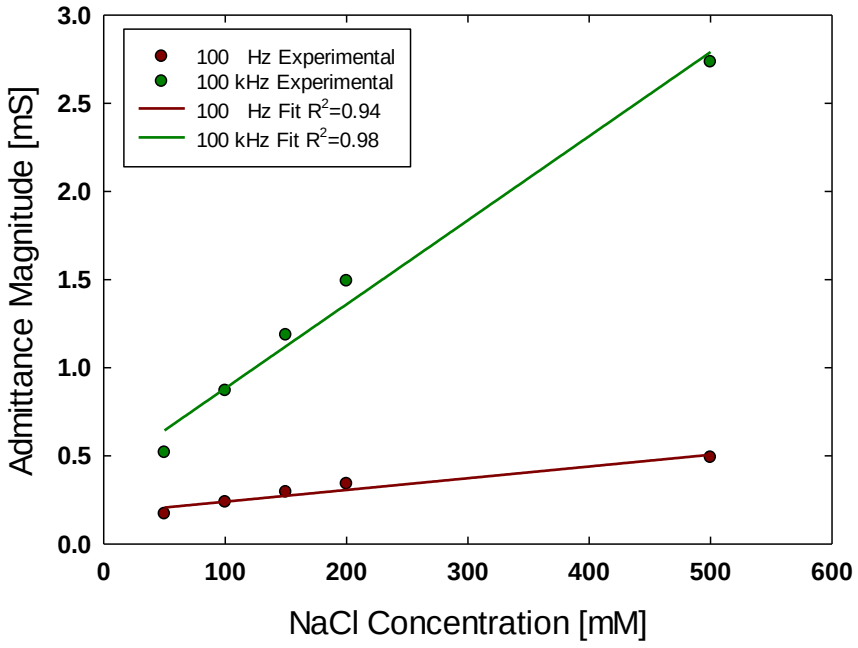

Figure 5-2 Measured admittance for solutions with different sodium chloride concentration. At 100 kHz double layer effects are small and the linear correlation of the data is good (R^2=0.98). At 100 Hz double layer effects affect the measurement and the correlation is worse (R^2=0.94).

5.1.2 Temperature effects

For a salt solution, temperature variations affect the ability of charges carrier to move through the solution and thus its electrical conductivity. At high temperatures the ions have higher random fluctuations and the resistivity is low, while at low temperatures the opposite happens. To test the effect of temperature on impedance measurements a 500 mM solution of KCl was measured at different temperatures to measure the variation in the impedance spectrum. The results are shown in Figure 5-3. When the temperature was increased from 22°C to 27°C, the magnitude of the impedance spectrum decreased by ≈30 Ω, while the phase angle stayed constant at high frequencies and was decreased by ≈1° at lower frequencies (100 Hz). Admittance magnitude at 100 Hz and at 100 kHz were fitted linearly against the temperature. The equations were:

$$|Y|_{100\,Hz} = 1.47 + 0.040\ T \qquad R^2 = 0.993$$
$$|Y|_{100\,kHz} = 2.11 + 0.076\ T \qquad R^2 = 0.998$$

where $|Y|$ indicates the admittance magnitude in milliSiemens and T the temperature in degrees Celsius. The temperature correction factor at 25°C and 100 kHz is α_{KCl}=1.97 %/°C. This value is comparable with the values found in the literature (α≈2 %/°C [79]).

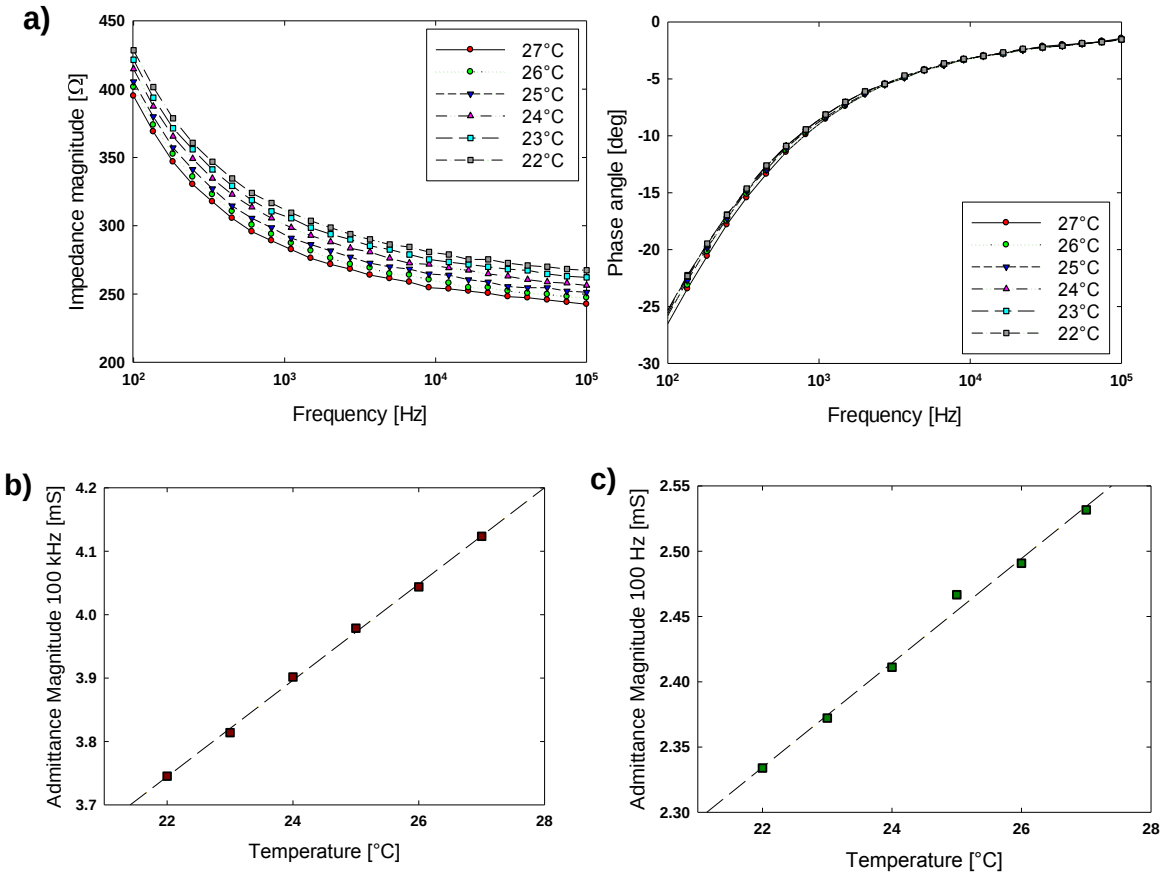

Figure 5-3 Effects of temperature on the impedance spectrum of a 500 mM solution of KCl. (a) Solutions at different temperatures were pumped through the device and impedance spectra are measured. Admittance magnitudes at 100 kHz (b) and at 100 Hz (c) against the temperatures and fitted linearly (R^2>0.99 for both regressions).

Temperature can also affect dissociation constants of weak acids, therefore the effects that the temperature has on the electrical properties of growth medium might differ from a salt solution. To assess these effects, a similar analysis was performed on cell culture medium and is shown in Figure 5-4.

A linear fit to the admittance magnitude data with the temperature gives:

$$|Y|_{100\,Hz} = 1.09 + 0.045\ T \qquad R^2 = 0.998$$
$$|Y|_{100\,kHz} = 1.35 + 0.124\ T \qquad R^2 = 0.991$$

The obtained temperature correction factor at 25°C and 100 kHz is α_{Medium}=3.01 %/°C, and is greater than for the salt solution, indicating the presence of additional effects caused by the complexity of the culture medium components. The highest temperature variation in the system is observed during the opening of the incubator to operate the setup. The resulting temperature is in the 35.5-37°C range. This 1.5°C temperature variation can induce a 4.5% variation in the measured impedance.

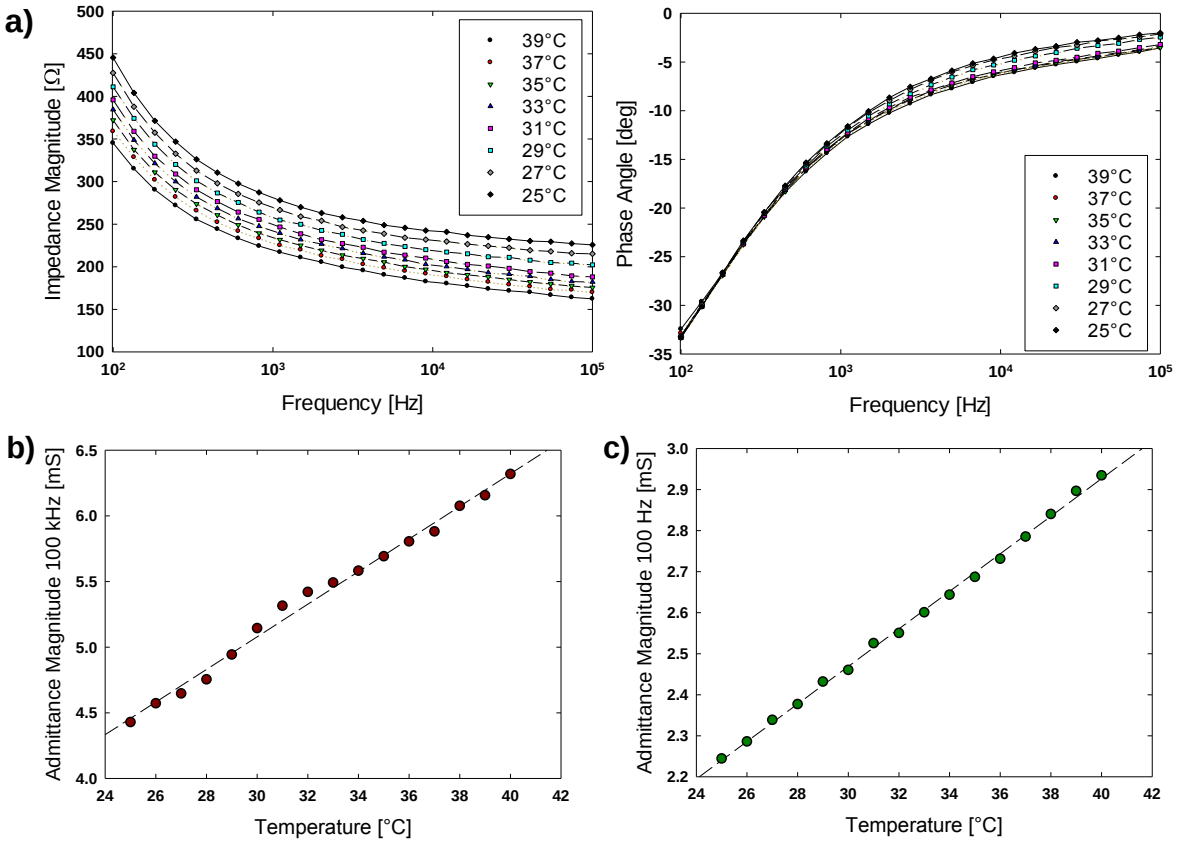

Figure 5-4 Effects of temperature on the impedance spectrum of 16HBE cell growth medium. (a) Medium at different temperatures is pumped through the device and impedance spectra are measured. Admittance magnitudes at 100 kHz (b) and at 100 Hz (c) are reported against the temperatures and fitted linearly (R^2>0.99 for both regressions).

5.1.3 Platinum black deposition

Platinum (Pt) black was deposited on the platinum electrodes to reduce electrode polarisation effects. To assess the quality of the deposition and the performance improvement after coating, the impedance of a 10 µl droplet of 16HBE medium was measured with coated and uncoated platinum electrodes. The resulting spectra are shown in Figure 5-5. For the uncoated electrodes at low frequencies, the impedance magnitude increases exponentially (>3500 Ω at 100 Hz) and the phase angle decreases (<-50° at 100 Hz). Variations between high and low frequency values due to electrode polarisation were of the same order of magnitude as the variation caused by TJ formation (~1 kΩ). Uncoated electrodes are therefore not suitable to monitor small variations in cell culture impedance because they are covered by double layer effects.

Compared to the uncoated electrodes, the polarisation of Pt-black coated electrodes is negligible at the frequencies of interest. When the two spectra are plotted on the same scale, the impedance magnitude of the coated electrodes appears constant (120 Ω at 100 Hz) and the variation of phase angle smaller (-10° at 100 Hz). The improvement can be quantified analysing the values of the fitted capacitances for the two spectra. For uncoated electrodes it is $C_{Bright\ Pt}$~$0.3\ F/m^2$ which is in agreement with values from the literature [141, 142], and it is $C_{Pt\ Black}$~ $27\ F/m^2$ for coated electrodes. This is a 90-fold increase in the electrode surface, which is lower than the values reported in the literature (140-fold) [91]. The lower improvement in electrode area compared to the literature might be a consequence of non-optimal deposition conditions and could be improved

by optimizing the deposition process. Nevertheless, the obtained electrodes were deemed suitable for the application and the deposition protocol was left unaltered. All subsequent impedance spectra presented were obtained with Pt-black coated electrodes.

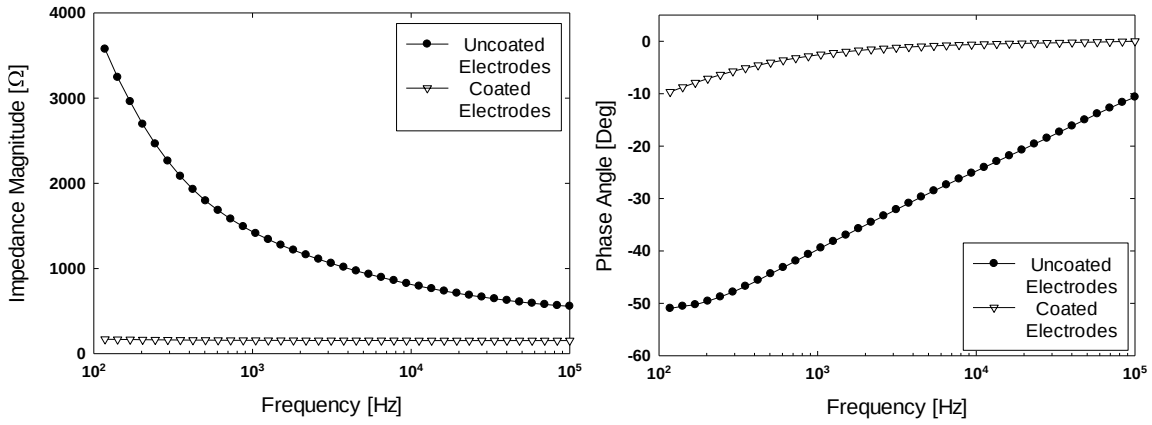

Figure 5-5 Comparison between bright platinum electrodes (Uncoated) and platinum black electrodes (Coated). Uncoated electrodes are heavily affected by polarisation effects. The Pt-black coating improves the electrode performances reducing polarisation effects by a factor 75.

5.2 Submerged epithelia

The 16HBE cell line was analysed in submerged, static conditions. These experiments are necessary to understand the behaviour of tissues grown in standard condition and give a reference point for the analysis of more complex systems. First, the effects of materials and the measurement system on cellular viability were measured, followed by an analysis of the performance of different measurement setups. Impedance measurements in this section were performed with both the systems discussed in Section 4.1.3.

5.2.1 Tissue growth on custom supports

To assess if the materials and the structure of the device affected cell growth, the TER of cell cultures grown on commercial Transwell® supports and on custom static supports were compared. This is shown in Figure 5-6, where TERs were measured using commercial chopstick electrodes at 1, 3 and 6 days after seeding. For statistical analysis, the experiment was repeated 3 times with 4 replicates for each condition each time. Measured TERs were subtracted from the blank values of an empty support and normalised with respect to the surface area of the membrane: 0.33 cm^2 for the commercial Transwell® system and 0.19 cm^2 for the custom system. Averages and standard deviations (SD) of replicates were computed for each experiment. Grand means and standard deviations of biological replicates across the experiments were computed and are shown. On the third day after seeding, cells cultured on Transwell® had TER values of 332±98 Ωcm^2 and cells cultured on custom supports had values of 453±74 Ωcm^2. After the sixth day these values became respectively 830±215 Ωcm^2 and 655±211 Ωcm^2. These values are in the standard range observed in the literature for this type of cells [126]. A paired Student's *t*-test was performed to assess the statistical significance between the two systems. For the sixth day the *t*-value was 1.458, with an associated double-tailed cumulative probability with 11 degrees of freedom of 82.8%. The data suggests that the static support does not have a statistically significant effect on the cell culture growth.

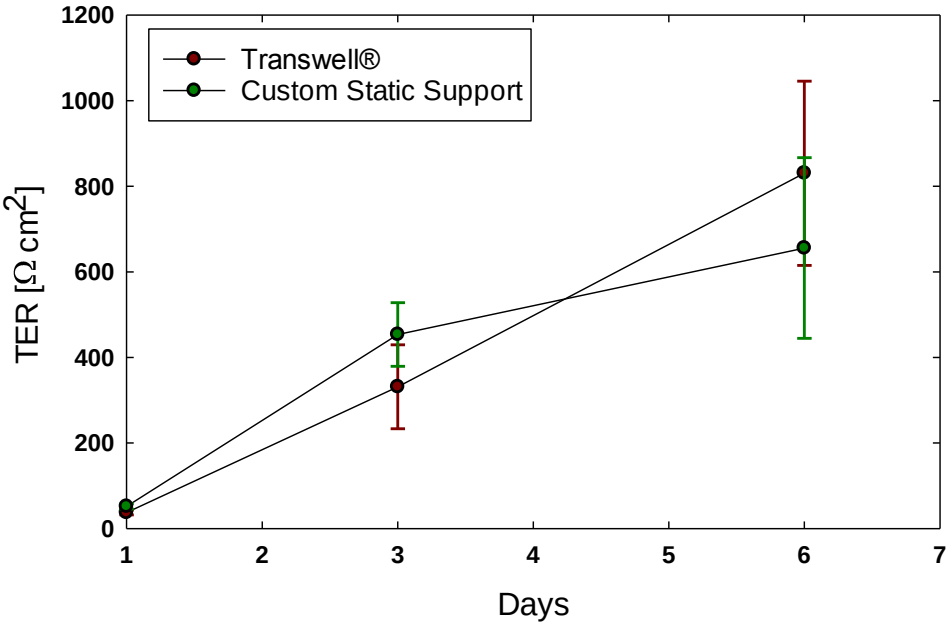

Figure 5-6 Comparison between the development of an epithelial barrier of epithelial cell cultures grown on commercial and static supports over time. Epithelial cells (16HBE) were grown on commercial supports with 10^6 holes/cm^2 or custom made culture supports with 10^8 holes/cm^2 and grown for 6 days at 37˚C. On day 0, 3 and 6, ionic permeability was determined by TER measurements where values were normalised with respect to the blank and to the surface areas. Results shown are means ± SD of 3 independent experiments performed in quadruplicate. Day 6 values are not statistically different (p=0.172).

5.2.2 Support pore density effects on tissue morphology

The effect of the support pore density on the cells was analysed by immunofluorescence staining of cultures grown on commercial supports, custom supports with low pore density (10^6 holes/cm^2), and custom supports with high pore density (10^8 holes/cm^2). A comparison between morphologies of cells cultured for 6 days on the 3 different supports is shown in Figure 5-7. Z-stacks of images were obtained at different focal planes and 3D structures were reconstructed after deconvolution. Even though TJs are formed in all culture conditions, the morphologies are different. Tissues cultured on Transwell® and on custom supports with high pore density have more than one layer of cells and are 17 and 16 μm thick, respectively. Tissues cultured on custom supports with low pore density are formed by a single cell layer and are 9 μm thick. This difference could be caused by the non-uniformity of medium distribution, or by effects derived from manufacturing process, such as difference in mechanical properties or in glue distribution. Therefore, high pore density membranes were used to obtain cellular cultures similar to the ones obtained on the current Transwell® standard.

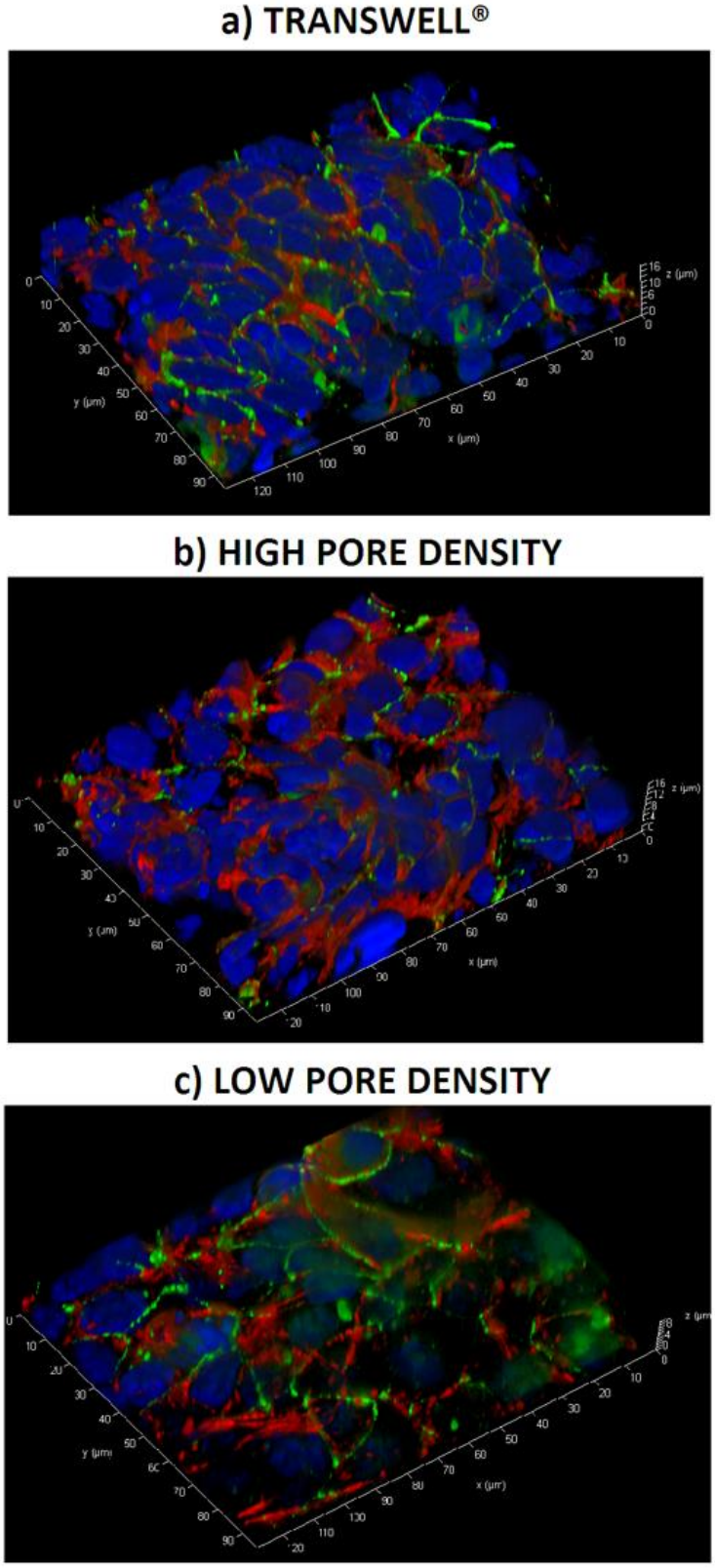

Figure 5-7 Effects of membrane pore density on the tissue structure as observed by immunofluorescence staining of 16HBE cells. Epithelial cells (16HBE) were grown on static commercial supports with 10^6 holes/cm^2 (a) or custom made culture supports with 10^8 holes/cm^2 (b) or 10^6 holes/cm^2 (c) and grown for 6 days at 37C. After which, 16HBEs were fixed and assessed for occludin (green), actin (red) distribution with nuclei staining (blue) by immunofluorescent microscopy. Images were deconvoluted and are representative of 4 technical replicates of 3 biological replicates experiments. 100x magnification.

5.2.3 Barrier disruption induced by electric fields

Biological systems can be affected by exogenous fields and care must be adopted in the choice of the signal shape and magnitude. Experiments were performed to verify that the signal applied during the impedance measurement did not perturb the electrical properties of the examined cell culture. The epithelial cell line, 16HBE, was grown on commercial Transwell supports for 6 days and impedance was measured using the impedance spectroscopy chip system described in Section 4.1.3, Figure 4-15 using a stimulation signal with frequency 1 kHz and amplitude 0.7 V_{rms}. TERs of the cell cultures were measured with commercial chopstick electrodes before, 30 seconds and 10 minutes after the impedance measurement. 4 biological replicates of the experiment were measured and are shown in Figure 5-8 as averages and standard deviations. A two-tailed paired Student's *t*-test was used for statistical analysis.

A significant drop ($p<0.001$) in the measured TER was observed after 30 seconds, from 1685±44 Ω to 1127±47 Ω. Cells recover over time from the initial perturbation: TER values measured 10 minutes after the application of the signal show a significant increase ($p=0.027$) compared to the original values, up to 1772±85 Ω.

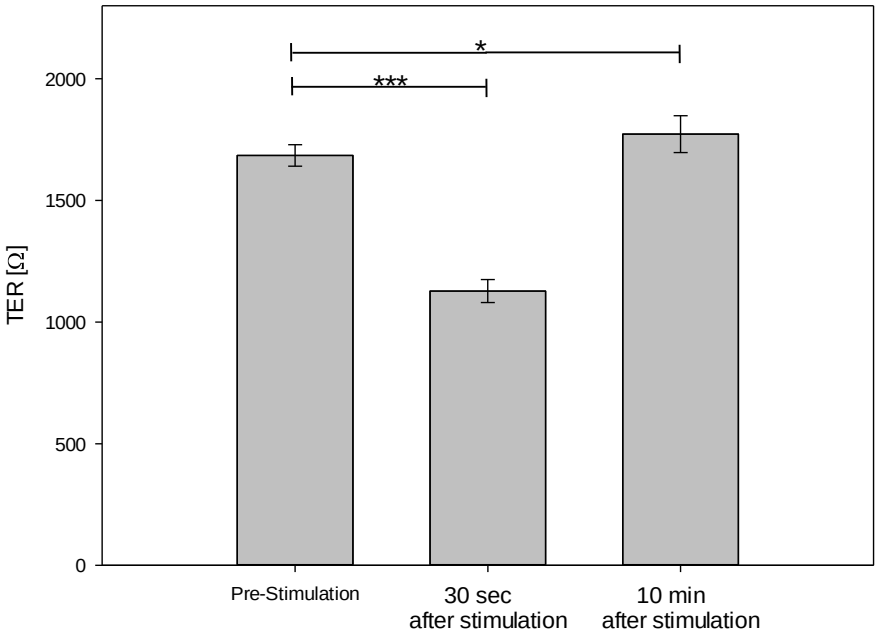

Figure 5-8 Effects of an external electric field on the barrier properties of epithelial cells. Ionic permeability as determined by TER measurements using the EVOM and chopstick electrodes of confluent cell cultures on Transwell® were measured before, 30 seconds and 10 minutes after the measurement of the impedance using a signal with frequency 1 kHz and amplitude 0.7 V_{rms} (4 replicates). Results are means ± SD. A significant drop is observed 30 seconds after the impedance measurement (***$p<0.001$), followed by a significant increase 10 minutes after the impedance measurement (*$p=0.027$) (two-tailed paired Student's *t* test).

The application of the electric signal disrupts the barrier of the culture. It is necessary to minimize this effect in order to avoid the introduction of artefacts during the monitoring of the culture. To assess if this effect depends on the intensity of the applied signal the experiment was repeated with signal amplitudes in the 0-1 V_{rms} range. The TER drop after the impedance measurement are shown in Figure 5-9 as percentage of the initial value.

There is a marked variability in the drop induced by the external field across the cultures. An applied voltage of 1 V_{rms} induces a drop in the TER of the barrier of 67±5 %. The higher the amplitude of the signal applied, the higher the resulting drop in the TER measurement. Data fit to an exponential curve, with R^2=0.967as follows:

$$y = 8.3 + 1.27\, e^{3.78x}$$

A drop of 7±4 % was observed for the control (i.e. no measurement performed). This is probably due to mechanical stresses during the displacement of the support from the 24-well plate to the measuring chip. This should not be present in the microfluidic chip measurement where cultures are measured *in-situ* and no displacement of the support is required.

A one-tailed homoscedastic Student's *t*-test for data obtained with applied voltage of 0.1 V_{rms} or 0 V_{rms} gives a cumulative distribution probability p=0.26 indicating a non-significant effect. Therefore, all subsequent measurements are performed with an applied voltage of 0.05 V_{rms} to avoid the introduction of artefacts in the measurement.

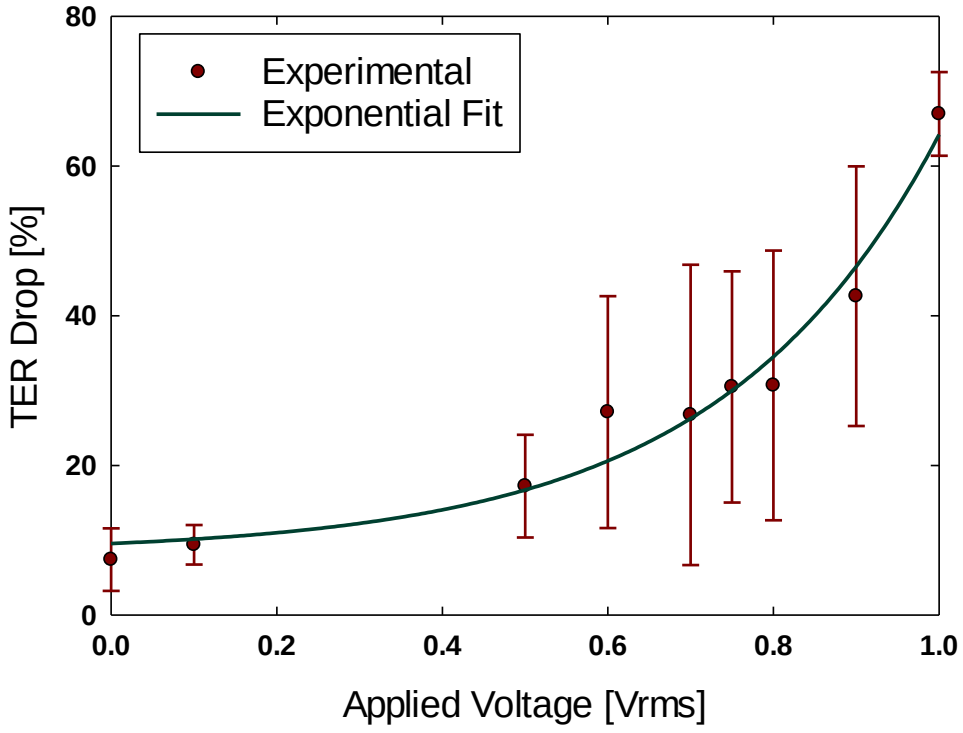

Figure 5-9 Effects of the applied field intensity on the induced barrier disruption. The ionic permeability of epithelial cell cultures grown on commercial supports for 6 days was determined by TER measurements before and after the application of an electrical stimulus (1kHz, 2 seconds). The amount of induced TER drop can be correlated exponentially with the field applied voltage (R^2=0.967). Even when no field is applied, there is a small barrier disruption induced by mechanical stresses during the measurement. Barrier disruption for V_{rms}=0 (no measurement performed) and V_{rms}=0.1 are not statistically different. Results are means ± SD of 3 independent biological measurements.

5.2.4 Comparison between Trans-Impedance and Cis-Impedance measurements

The performances of cis-epithelium and trans-epithelium electrodes on a growing culture of epithelial cells were compared. A Transwell® was placed on top of the measuring chip with circular segment electrodes to measure cis-epithelium impedance, and an additional electrode was added in the apical compartment to measure trans-epithelium impedance as shown in Figure 5-10. This third electrode was a platinum wire (diameter 0.5mm) coated with platinum black submerged to a depth of ≈5mm in the apical medium. The trans-epithelium impedance was measured using the additional electrode and one of the two planar electrodes. The field lines for this configuration were not symmetrical, but the artefact is considered negligible. The submerged area of the platinum wire was ≈4mm^2 compared to ≈3mm^2 of each planar electrode.

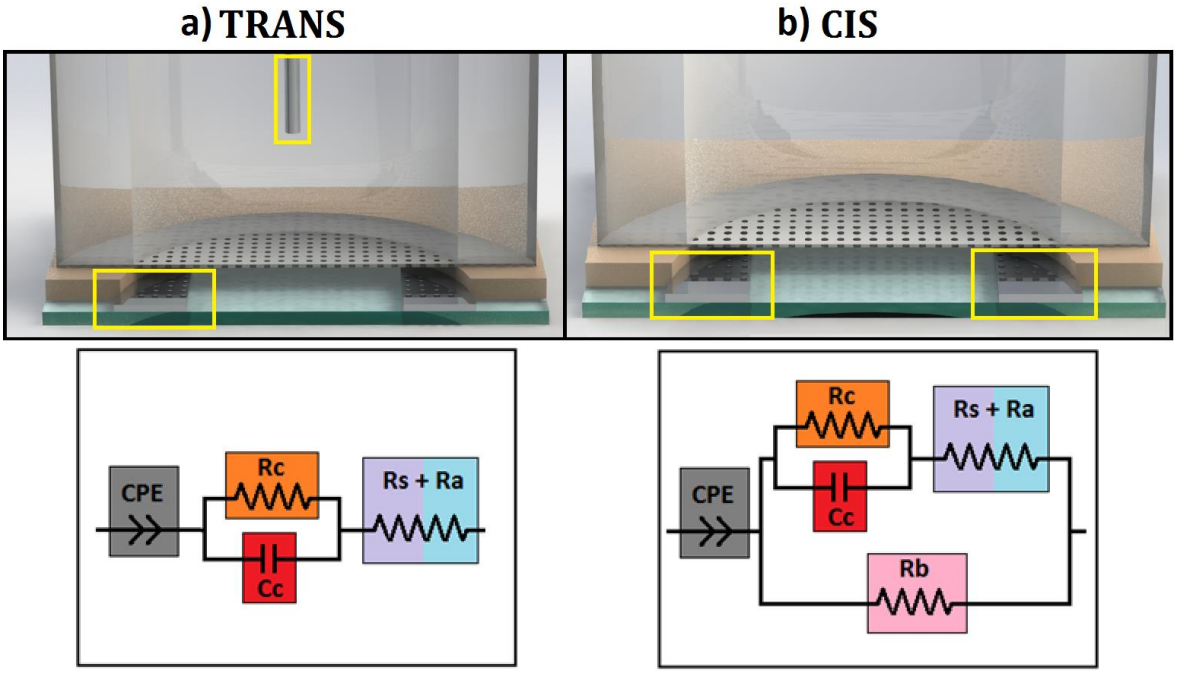

Figure 5-10 Schematic of the two measuring setups and respective equivalent circuits (active electrodes framed in yellow): in the cis-configuration (b) two planar electrodes are used, while in the trans-configuration (a) a third Pt/Pt-black electrode is submerged in the apical compartment.

The electrical properties of epithelial cell cultures grown on a Transwell® were measured daily from the day after seeding with both electrode configurations and with commercial electrodes. The typical evolution of measured spectra over time are shown in Figure 5-11 (only selected curves are shown to improve graph readability). TER values measured with standard chopstick electrodes increased steadily from day 1 to 5 (from 270 Ω to 820 Ω) and decreased on day 6, indicating that the cells established a polarised barrier with decreased ionic permeability.

Impedance measured with the two electrode configuration show the same qualitative behaviour: the impedance magnitude stayed constant at frequencies >10^4 Hz and increased with increasing TER at frequencies <10^3 Hz. At 100 Hz, the impedance magnitude measured with trans-epithelium electrodes increased from 1065 Ω on day 1 to 1760 Ω on day 5, while the impedance magnitude measured with the cis-epithelium electrodes increased from 1360 Ω on day 1 to 2490 Ω on day 5 The characteristic depth in the phase angle for the trans-epithelium electrodes changed from -10° at 7 kHz at day 1 to -27° at 1.5 kHz at day 5 (Figure 5-11a), and for the cis-epithelium electrodes changed from -12° at 9 kHz at day 1 to -27° at 2.5 kHz at day 5 (Figure 5-11b).

In both systems, small variations in the high frequency impedance magnitude values (66 Ω for the trans-epithelium and 71 Ω for the cis-epithelium) can be explained by temperature differences between measurements or by difference in the relative position between electrodes and Transwell®.

The impedance magnitude sensitivity can be defined as:

$$|Z|\ Sensitivity = \frac{|Z|_{Low\ Freq}^{Day\ 5} - |Z|_{Low\ Freq}^{Day\ 1}}{TER^{Day\ 5} - TER^{Day1}}$$

this value is equal to 1.22 for the trans-epithelium configuration and 2.01 for the cis-epithelium configuration. This difference can be explained by considering the different field distribution in the systems, as already discussed in 3.2.1.

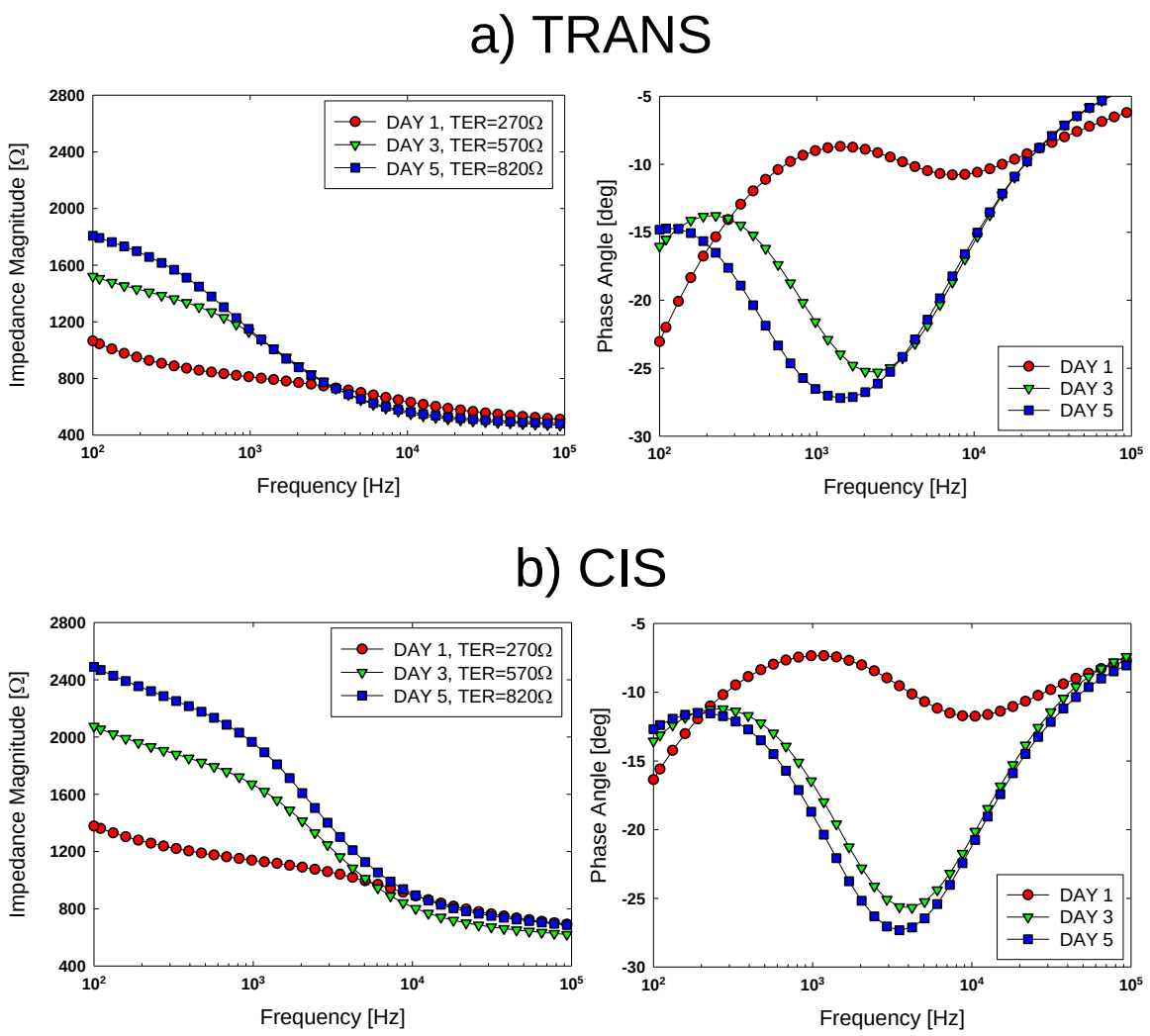

Figure 5-11 Comparison between measurement setups. Typical impedance spectra of a culture of epithelial cells growing on Transwell® measured with the trans-epithelium (a) or with cis-epithelium electrodes (b). Spectra are representative of 2 independent experiments.

It is important to verify that after the fitting procedure the system yields the same quantitative information on the tissue electrical resistance and capacitance. The data from the two configurations were fitted to their respective electric equivalent circuits (Figure 5-10) and the fitted

parameters are shown in Figure 5-12 as equivalent resistance values together with the TER measurement for each day. Values of the equivalent resistance obtained with the trans-electrodes configuration closely follow the experimental TER, while values obtained with the cis-electrodes configuration overestimate the experimental TER. It is possible to correlate the equivalent resistances obtained with the two configuration. The regression curve is:

$$R_{EQ}^{TRANS} = 124 + 0.44\, R_{EQ}^{CIS}$$

with an R^2=0.968. The difference in the fitted values is caused by differences in the sensitivities of the systems.

Equivalent capacitance values for both configurations are constant after the first day. The values were ≈0.6 μF/cm^2 for the trans configuration and ≈0.2 μF/cm^2 for the cis configuration. In the literature, a wide range of values for capacitance of epithelial cell cultures has been reported. In his original study on a suspension of red blood cells, Fricke reported a value for the cell membrane capacitance of 0.81 μF/cm^2 [143]. This value was demonstrated to be constant over a wide range of cell membranes and has since been used as reference. Nevertheless, the capacitance of an epithelial cell culture is not simply the sum of single cell capacitances, because more complex phenomena are involved (such as the asymmetrical subdivision of the cell membrane into apical and basolateral compartments [144]). Currently, there is not a standard method for the measurement of epithelial capacitance in the same way there is a standard method for the measurement of epithelial resistance, and capacitance values found in the literature can be affected by methodology differences. Schmid *et al.* [144] reported the capacitance for a Madin-Darby canine kidney cells type I (MDCK-I) epithelial cells culture to be 0.51 μF/cm^2. Henry *et al.* [64] reported the capacitance of a culture of primary human airway epithelial cells (hAECs) to be 7.33 μF/cm^2. Sun *et al.* [66] reported the capacitance of a culture of 16HBE cells to be 1.26 μF/cm^2. Tellez *et al.* [145] reported the capacitance of a culture of 16HBE14o- to be 0.151 μF/cm^2. The capacitance values obtained in this work with both electrodes configurations are in the range reported in the literature. Overall, the two configurations yield quantitatively similar information demonstrating that the planar electrode configuration can be used to monitor the epithelial barrier.

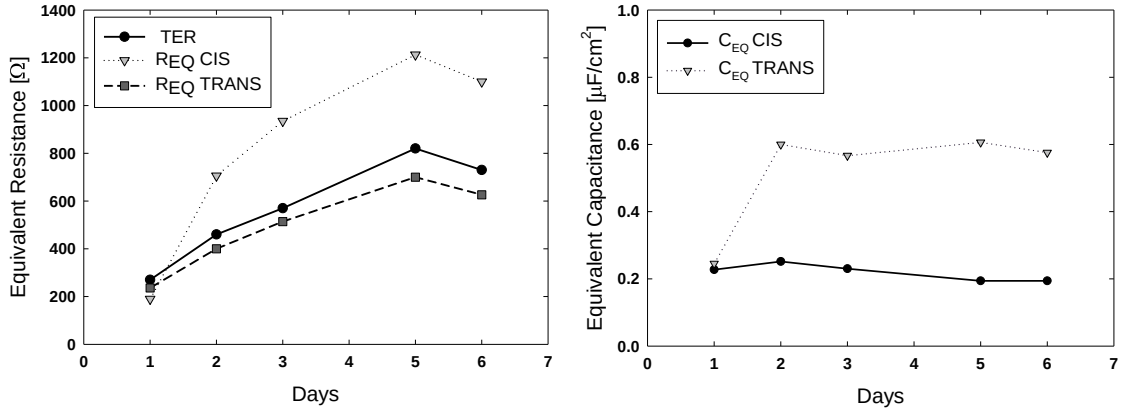

Figure 5-12 Comparison between trans-epithelium and cis-epithelium equivalent parameters. The cell resistance and capacitance for the two configurations are obtained fitting their impedance spectra with the respective equivalent electric circuit. Equivalent resistances measured with the two configurations correlate linearly (R^2=0.968) follow TER values. Equivalent capacitance values are constant after the first day and lower than the commonly assumed value of 1 μF/cm^2, indicating the presence of more than one layer of cells. Data are representative of 2 independent experiments.

5.2.5 Comparison between planar electrodes design

As analysed in the design Chapter-3, the shape of the electrodes strongly affects the sensitivity of the measurement. Two new designs were compared with the design from Sun *et al.* [66] (Design1) as shown in Figure 5-13. The first new design (Design2) consists of two 1 mm-wide symmetrical circular segments, while the second has the same planar electrodes but with the addition of an insulating polydimethylsiloxane (PDMS) barrier between them (Design3). Both designs aim to reduce the current flowing underneath the tissue thus increasing the sensitivity of the measurement.

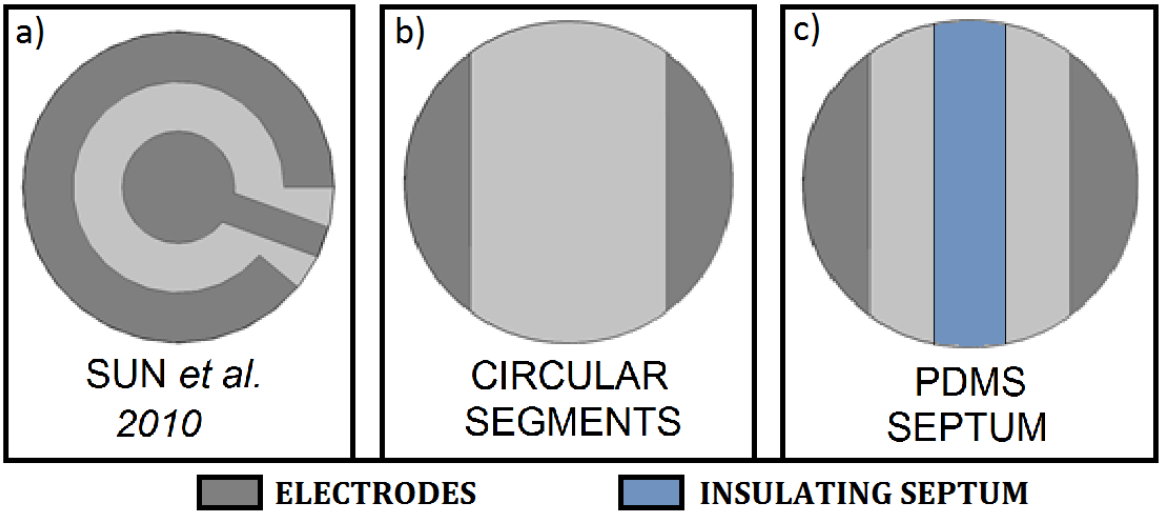

Figure 5-13 Schematic drawings of the compared electrode design. (a) Design by Sun et *al.* [66] formed by a central dot and an external ring, (b) circular segments design, (c) circular segments design with insulating septum between the electrodes.

Measurement of an empty Transwell® and of a support with a confluent layer of polarised epithelial cells (TER=2000Ω) was performed for each system. The impedance spectra are shown in Figure 5-14.

Design1 has the lowest basolateral resistance and therefore the lowest baseline for an empty Transwell® (210 Ω). By increasing the distance between the electrodes the basolateral resistance is increased, resulting in higher baselines for Design2 (420 Ω) and for Design3 (1800 Ω), where the current is physically blocked by the insulating septum.

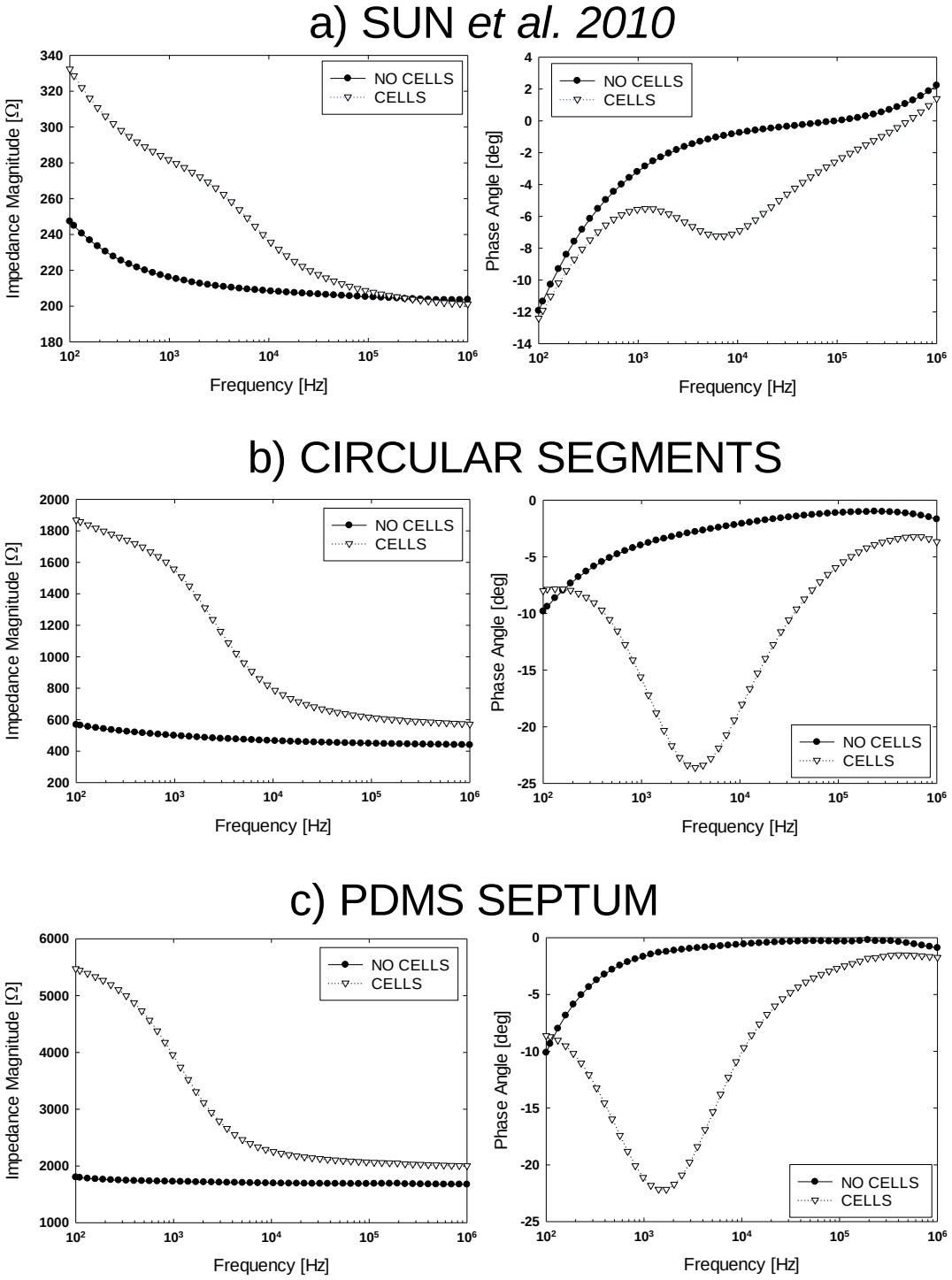

Figure 5-14 Comparison between impedance spectra of 16HBE cells cultured for 5 days on static Transwell® supports, measured with different electrodes design: (a) the one from Sun et *al.* [66], (b) the proposed optimum planar electrodes design, (c) and the proposed optimum planar design with the addition of an insulating PDMS barrier between the electrodes. Impedance spectra of an empty Transwell® and one with a polarised cell layer (TER=2000 Ω) are measured with each setup. With respect to the design from the literature, the increase in measured impedance magnitude at 100 Hz for the same variation of epithelial resistance is 10-fold and 30-fold, respectively without and with the insulating PDMS septum. The phase angle depth magnitude for both proposed design is 3-fold compared to the literature design.

Electrode areas are comparable across the systems. The increase in low-frequency impedance magnitude due to electrode polarisation effects is 44 Ω for Design1, 130 Ω for Design2 and 127

Ω for Design3. To assess the effects that electrode polarisation has on the measurement, these variations must be considered relative to variations measured when a confluent cell layer is present, as:

$$Relative\ Electrode\ Polarization\ = \frac{|Z|^{Blank}_{Low\ Freq} - |Z|^{Blank}_{High\ Freq}}{|Z|^{Cells}_{Low\ Freq} - |Z|^{Cells}_{High\ Freq}}$$

this value is 34% for Design1, 10% for Design2 and 3% for Design3. Thus, similar electrode polarisation effects can be neglected in the new designs.

When used to measure a polarised tissue with TER= 2000 Ω, the value of the low frequency impedance magnitude was 330 Ω for Design1, 1870 Ω for Design2 and 5400 Ω for Design3.
The impedance magnitude spectrum of a confluent layer of 16HBE cells measured with the geometry proposed by Sun et *al.* is equivalent to the one reported in the same study [66].

The impedance magnitude sensitivity can be defined as:

$$|Z|\ Sensitivity = \frac{|Z|^{Pol}_{Low\ Freq} - |Z|^{Blank}_{Low\ Freq}}{TER^{Pol} - TER^{Blank}}$$

The impedance magnitude sensitivity gives information on the measured impedance variation for a given input variation of TER. It is calculated at the low-frequency maximum of the phase angle, where the signal variation induced by the presence of the cells is saturated and the electrode polarisation effects are minimum. The performance comparison is shown in Figure 5-15 together with the phase angle depth normalised against the blank. The impedance magnitude sensitivity is 0.04 for Design1, 0.65 for Design2 and 1.83 for Design3, while the phase angle depth is 6.42° for Design1 and 21° for both Design2 and Design3. The two new electrode designs exhibit improved performances compared to the design from the literature: the impedance magnitude sensitivity increases 16-fold for the circular segments electrodes and 45-fold with the addition of insulating septum. The phase angle depth increase is 3-fold for both designs.

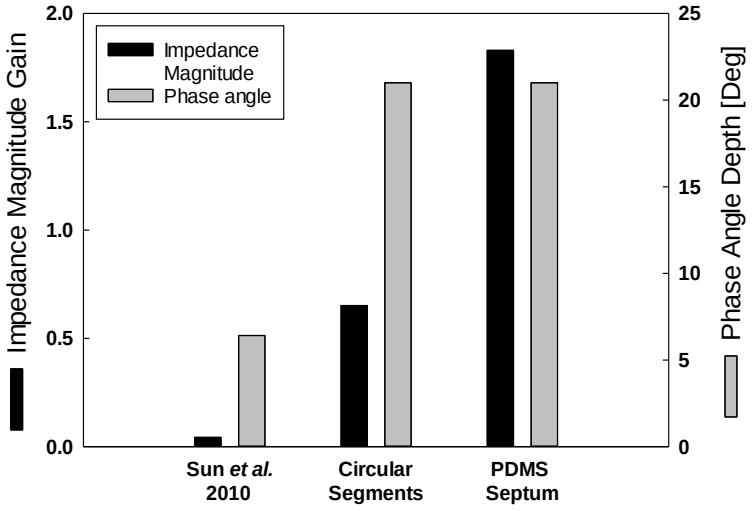

Figure 5-15 Performance comparison between different electrodes design. The impedance magnitude sensitivity is 0.04 for the design from the literature, 0.65 for the simple circular segments and 1.83 for the circular segments with insulating septum. The phase angle depth normalised to the blank is 6.42° for the design from the literature and 21° for the other two.

5.3 Air-Liquid Interface epithelia

Airway epithelia are physiologically exposed to an ALI. Primary BEC require this condition to proliferate and differentiate *in vitro*: it is therefore important to have a method to measure tissue electrical properties of cells at the ALI. Conventional measuring systems cannot probe the ALI for the lack of apical electrolyte. To perform a measurement with these systems it is necessary to temporarily cover the cells with growth medium which is a labour intensive and disruptive process. As an alternative to overcome this barrier, planar electrodes only need electrolyte on one side to probe the cells and could be suitable for direct measurement of impedance for cells growing at the ALI.

5.3.1 Effects of the apical medium volume on the measurement sensitivity

The amount of medium present in the apical compartment affects the system impedance spectrum: the higher the volume of electrolyte, the lower the electrical resistance. This relation is not linear because of the planar geometry of the electrodes. The apical resistance is in series with the tissue electrical parameters and affects the sensitivity of the measurement. The higher the ratio between the apical resistance and the basolateral resistance, the lower the current flowing through the cell layer.

To assess the effects of the apical compartment volume and to determine a minimum detection limit, a polarised cell culture of 16HBE cells were grown on a commercial support (TER=3000 Ω) and impedance was measured with different amounts of liquid in the apical compartment (0, 10, 20, 30, 40, 50 or 200 µl) using the planar circular segments electrode as previously examined. As shown in Figure 5-16, the variation of impedance magnitude measured at 100 Hz was ≈150 Ω and was lower than the variation of impedance magnitude measured at 100 kHz which was ≈1200 Ω. The measured trough in the phase angle changed from -30° to -5° when measured with 200 µl or an empty apical compartment, respectively. The experiment was repeated 4 independent times, obtaining the same trend.

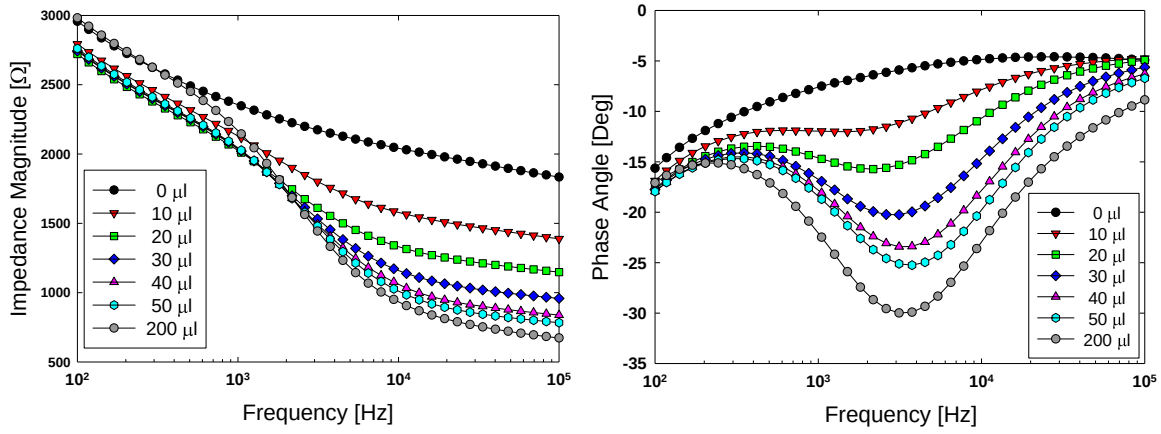

Figure 5-16 Effects of the apical medium volume on the impedance spectrum. A Transwell® with a polarised cell layer (TER=3000 Ω) is measured using the novel planar electrodes design with different volumes of medium in the apical compartment (0, 10, 20, 30, 40, 50, 200 µl). Results are a representative plot of 4 independent experiments.

To analyse the response of the system it is useful to consider the high frequency and the low frequency equivalent circuits shown in Figure 5-17. At low frequencies, the capacitance is an open circuit. The resulting series resistance R_c+R_a in parallel with the basolateral resistance R_b is dominated by the paracellular resistance R_c because $Rc>>R_a$. Therefore, the impedance does not depend on the value of the apical resistance R_a. At high frequencies, the capacitance is an open

circuit. R_a is in parallel with the basolateral resistance R_b. Therefore, the impedance magnitude depends on the value of the apical resistance R_a.

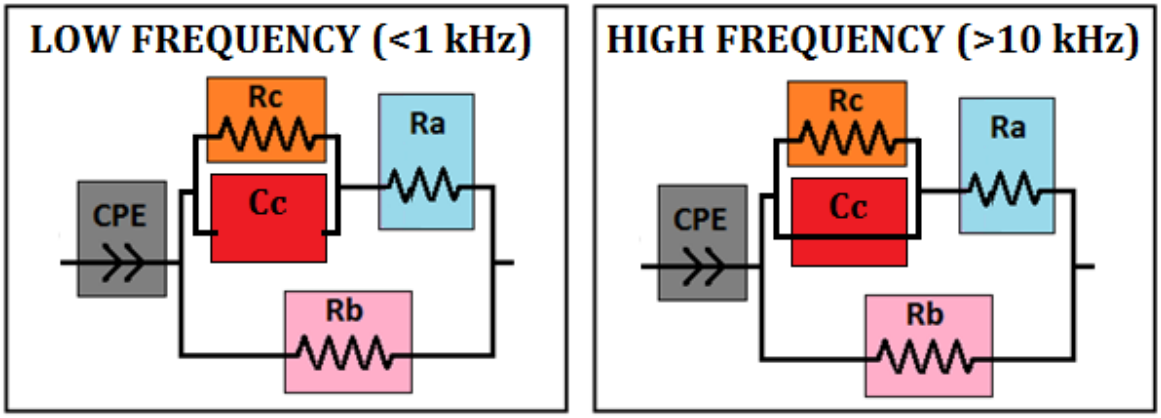

Figure 5-17 Low and high frequency equivalent circuits. At low frequencies, the capacitance C_c is an open circuit and the current flows through the paracellular resistance R_c. At high frequencies, the cell membrane capacitance C_c is a short circuit and bypasses the paracellular resistance.

To quantify the effect of the apical volume a sensitivity factor is introduced:

$$Apical\ Volume\ Sensitivity = \frac{|Z(100Hz)| - |Z(100kHz)|}{|Z(100kHz)|}$$

This takes into account the difference between the high frequency and low frequency values of the impedance magnitude. Both the sensitivity (S) and the change in the phase angle increase logarithmically with increasing apical compartment volume as shown in Figure 5-18. Data correlates with the logarithm of the apical volume with R^2=0.98 for impedance magnitude and R^2=0.95 for phase angle (the system is more sensitive to variations of the apical resistance when the apical resistance is small).

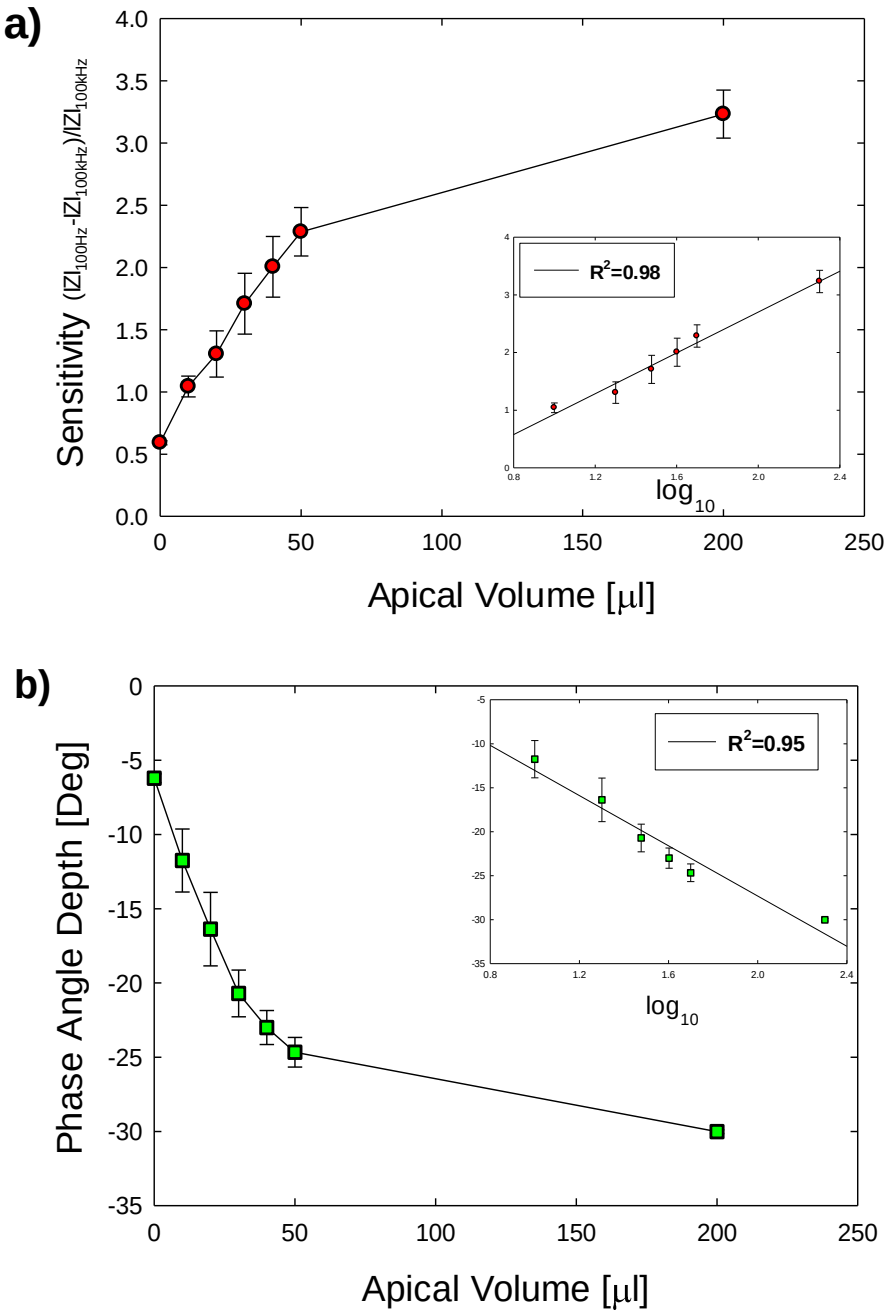

Figure 5-18 Effects of the apical volume on the measurement sensitivity of the impedance magnitude (a) and in the phase angle (b). In the inset the apical volume is reported on a logarithmic scale and data are correlated linearly. The correlation factors are R^2=0.98 for the impedance magnitude and R^2=0.95 for the phase angle (zero values excluded from the log plots). Results are means ± SE of 4 replicate experiments.

5.3.2 Effects of the apical medium volume on 16HBE cells barrier detection

The minimum amount of electrolyte needed to probe the tissue electrical properties needs to be determined. To assess this, cultures of 16HBE cells were seeded onto commercial supports and impedance was measured daily with different amounts of medium in the apical volume using the planar circular segments electrode design (second design from Figure 5-13). Cells are normally cultured with 200 µl of medium in the apical compartment. Before an impedance measurement the apical medium was removed and replaced with different volumes of either 200, 50, 20 or 10 µl of fresh medium (topped up to 200 µl at the end of the measurement for normal culture). Typical

impedance spectra measured with 200 µl or 10 µl of medium in the apical compartment are shown in Figure 5-19. As already stated, increasing the apical resistance reduces the sensitivity. As shown in the figure, it is possible to observe the typical features of an establishing epithelial cell barrier (i.e. an increasing impedance magnitude and a decreasing phase angle trough) with only 10 µl of medium in the apical compartment. The experiment was repeated two times in duplicates for each apical volume, and similar spectra were observed.

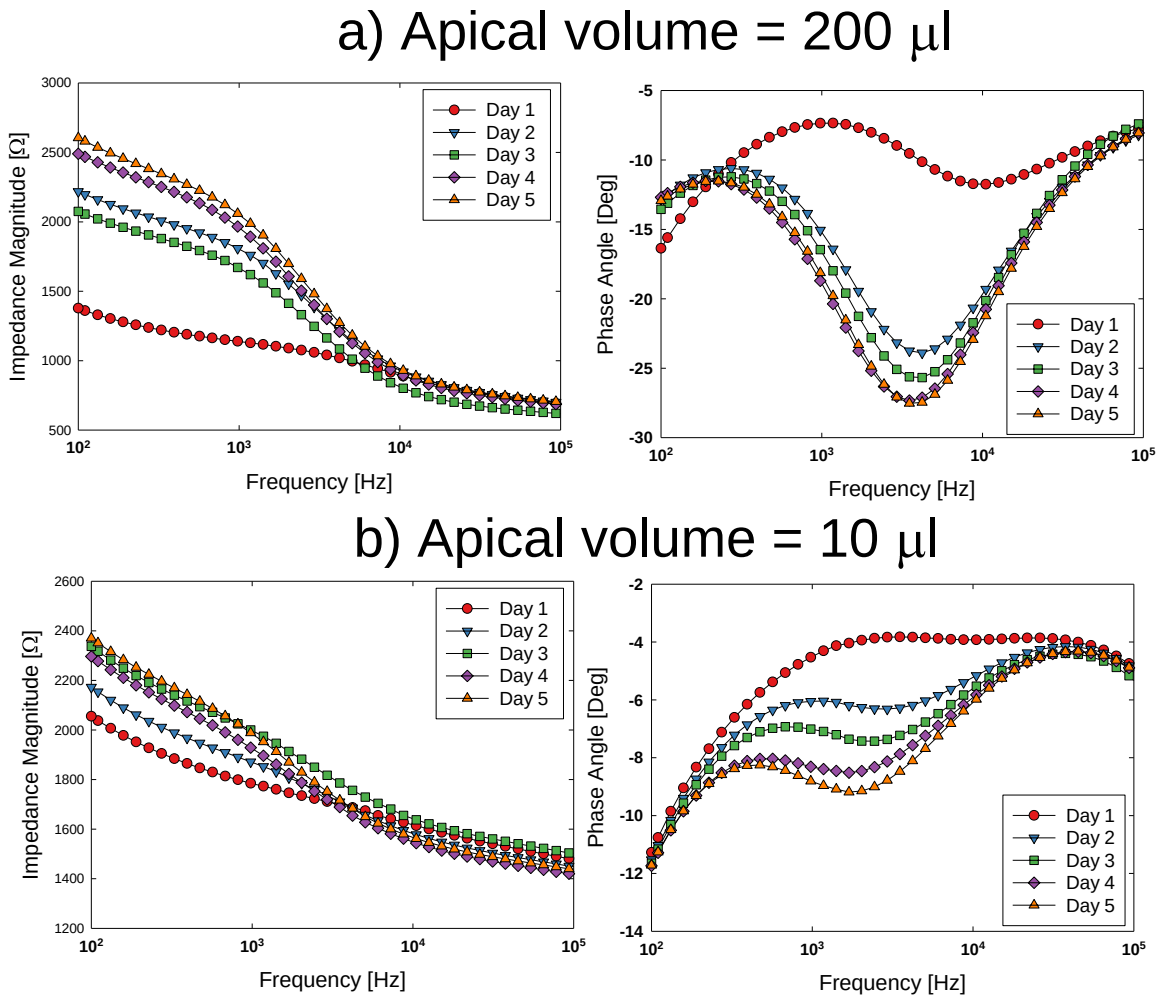

Figure 5-19 Comparison between impedance spectra of a growing culture of 16HBE cells measured with 200 µl (a) or 10 µl (b) of medium in the apical compartment. Cells were cultured on Transwell® supports for 5 days with 200 µl of medium in the apical compartment and impedance spectra were measured daily. Before the measurement, the medium in the apical compartment was temporarily replaced with either 200 µl (a) or 10 µl (b) of fresh medium. Spectra are representative of 2 independent experiments performed in duplicate.

Figure 5-20 compares the equivalent parameters extracted from impedance spectra obtained with different apical resistances (n=4). The equivalent apical resistance (averaged over the days) decreases with increasing apical volume, and varies from 1780 Ω for the smallest apical volume considered (10 µl) to 600 Ω for the largest volume. The fitted parameters obtained with 200 µl or 50 µl are similar because of the small difference in sensitivity between these two volumes. Cell equivalent resistances Rc for all the experimental conditions are similar to the TER measured with commercial electrodes. Equivalent cell capacitances are constant over time in the range 0.3-0.8 µF/cm^2, indicating the presence of a multi-layered tissue. Both the equivalent parameters of the culture R_c and C_c have the same artefact from the fitting procedure: they clearly depend on the apical volume while the apical resistance R_a should be the only parameter affected by the apical

volume. This artefact does not affect the ability of the system to monitor the establishment of the barrier of a growing epithelium but requires the use of a conversion factor when comparing epithelial barriers measured with different apical volumes.

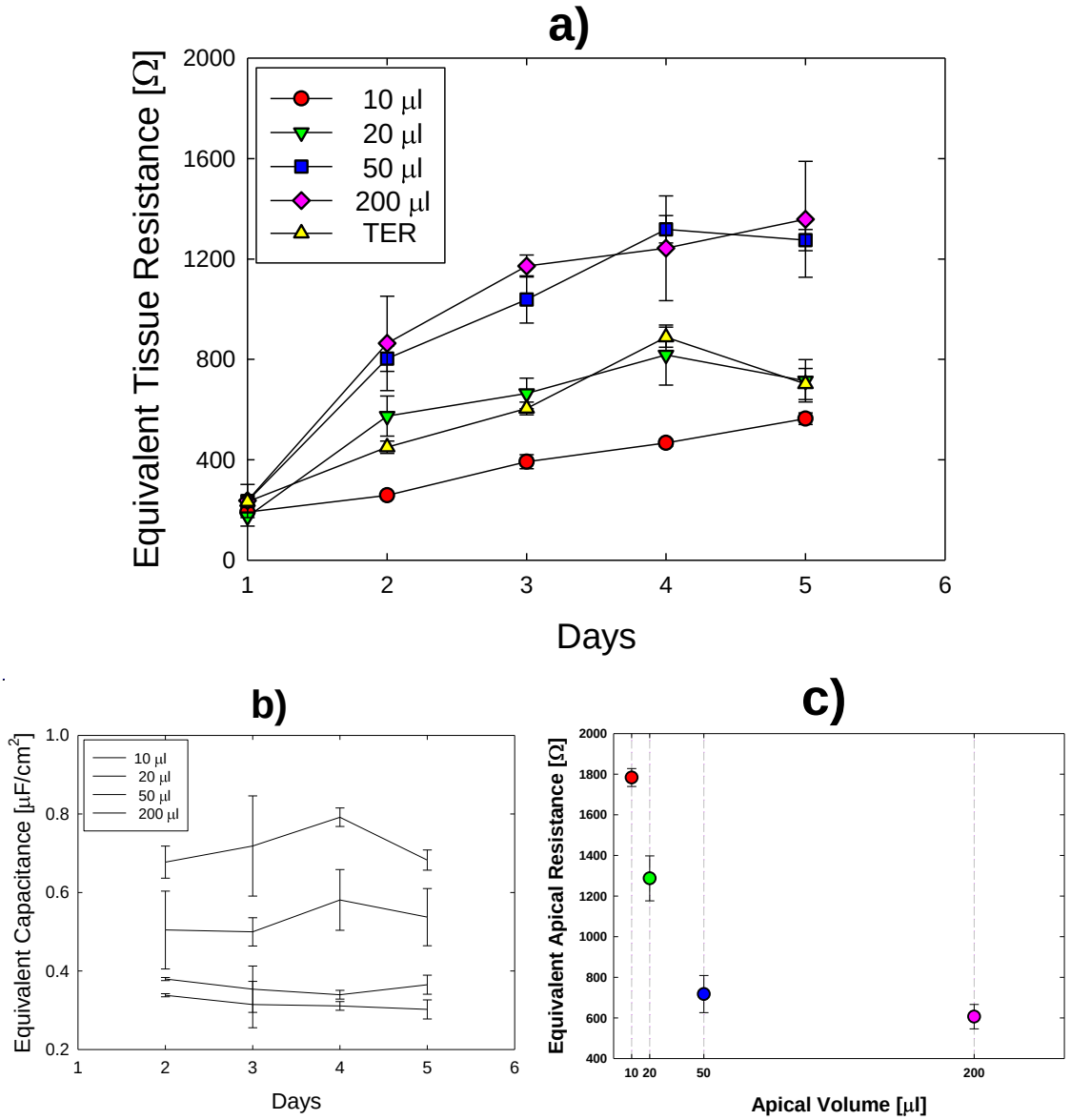

Figure 5-20 Effects of the apical volume on monitoring growth of 16HBE14o-. Impedance spectra of growing cells measured daily with 10, 20, 50 or 200 µl of medium in the apical compartment. Spectra are fitted and equivalent resistances (a), equivalent tissue capacitances (b) and equivalent apical resistances (c) are extracted. The experiment was repeated 2 independent times in duplicates for each condition. Results are means ± SD of the 4 data sets.

5.3.3 Measurements at the air-liquid interface

The improved sensitivity of the planar circular segment electrodes allows monitoring of the development of the tissue barrier for an epithelial cell line (16HBE) that are submerged with a thin film of liquid (10 µl).

As previously demonstrated, it is possible to significantly increase the sensitivity of the system by inserting an insulating septum between the electrodes. The septum blocks the current flowing in

the basolateral compartment and forces it to pass through the tissue. This system was used to measure the electrical properties of ALI cultures of PBEC. Cells were cultured for 21 days on commercial supports at the ALI and the formation of the epithelial barrier was determined by TER measurements with conventional electrodes (EVOM system) and with the custom system with the insulating septum (previously described in Figure 4-16, Section 4.1.3) both submerged or at the ALI. The experiment was repeated 4 independent times in quadruplicates. 2 of the 4 biological samples were from healthy donors and 2 were from asthmatic donors. TERs of cultures from healthy donors increased over time, from 362±86 Ω on day 7 to 1228±79 Ω on day 14 and 1317±87 Ω on day 21. TERs of cultures from asthmatic donors decreased over time, from 1266±115 Ω on day 7 to 810±20 Ω on day 14 and 519±17 Ω on day 21.

As shown in Figure 5-21, if the culture is submerged, the impedance spectra for primary cells has the same features as for cell lines (i.e. to high TERs correspond high low frequency impedance magnitude values and more pronounced depths in the phase angle). However, for the ALI cultures there is a difference >2000 Ω between high-frequency values of the same culture over time. These differences might be due to several factors:

- Setup related variation: differences in measurement parameters such as temperature, relative position between the support and the electrodes or electrodes wearing.
- Culture related variation: the biology of primary cells is more complicated than a cell line. Primary cells undergo polarisation and differentiation and start to produce mucus during the 3 weeks that they grow on a support. All these variations could affect the measurement.

The variation of the impedance spectrum as cell grow is small compared to the other factors resulting in instability in the fitting algorithm and making impossible a consistent fitting. Such analysis would be possible if all the setup-related artefacts are cancelled.

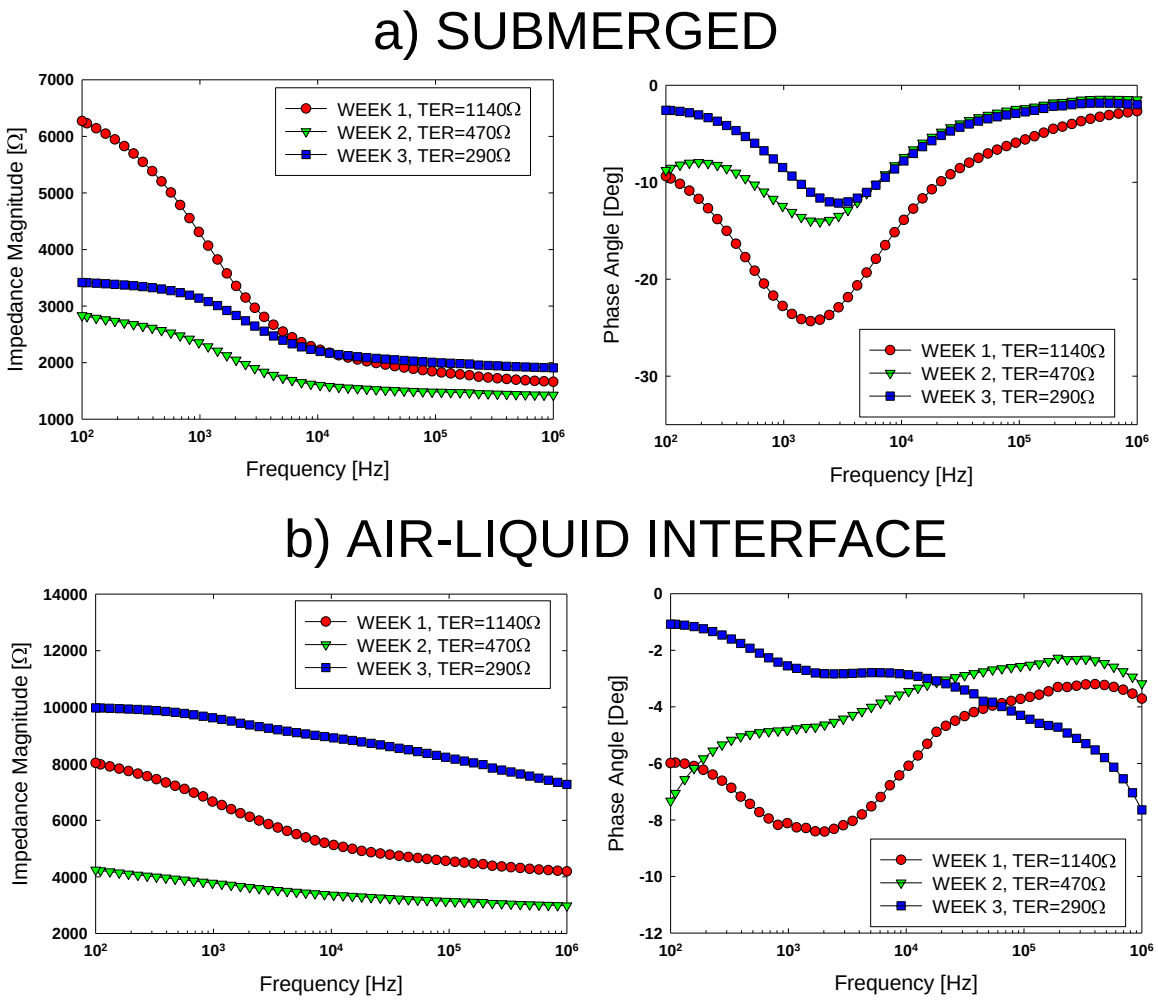

Figure 5-21 Impedance spectra of a growing culture of primary bronchial epithelial cells at the ALI. Impedance spectra are measured after 7, 14 and 21 days both submerged (a) or at the ALI (b) together with standard TER. The plots are representative of 2 independent experiments performed in quadruplicate from asthmatic donors.

Barrier disruption

After the cells were cultured for 21 days on a commercial support, their barrier was disrupted with EGTA. In each experiment, 2 replicates are treated with EGTA and 2 replicates are used as control (same amount of growth medium added). To assess if the system can measure EGTA disruption, cells were measured with conventional electrodes and with the custom system (third design from Figure 5-13), with the tissue submerged or at the ALI, before and 10 minutes after the stimulation. Impedance spectra are shown in Figure 5-22. A marked drop in impedance (IZI_{before}=6500 Ω, IZI_{after}=2000 Ω) was observed for the treated submerged cells (TER_{before}=1680 Ω, TER_{after}=340 Ω), while 2 overlapping curves were measured for the submerged control (TER_{before}=1490 Ω, TER_{after}=1210 Ω). Similarly, the ALI control spectra overlaps, while the EGTA treated cells show a small variation in both impedance magnitude and phase angle (IZI_{before}=7000Ω, IZI_{after}=5800Ω).

A quantitative analysis of the drop of the barrier induced by EGTA is described in Figure 5-23. Data relative to cultures deriving from healthy or asthmatic donors were segregated to analyse the different responses to EGTA. Equivalent resistances are determined from a fit to the impedance spectra, before and after addition of EGTA or growth medium. It is possible to compare the ALI spectra before and after stimulation because the measurements are performed in a single experiment, thus limiting the number of artefacts. Barrier change is computed as the ratio of post-

stimulation to pre-stimulation equivalent resistances. Averages and standard errors of the mean were obtained from 2 independent experiments with 2 replicates for each type of cells (healthy, asthmatic).

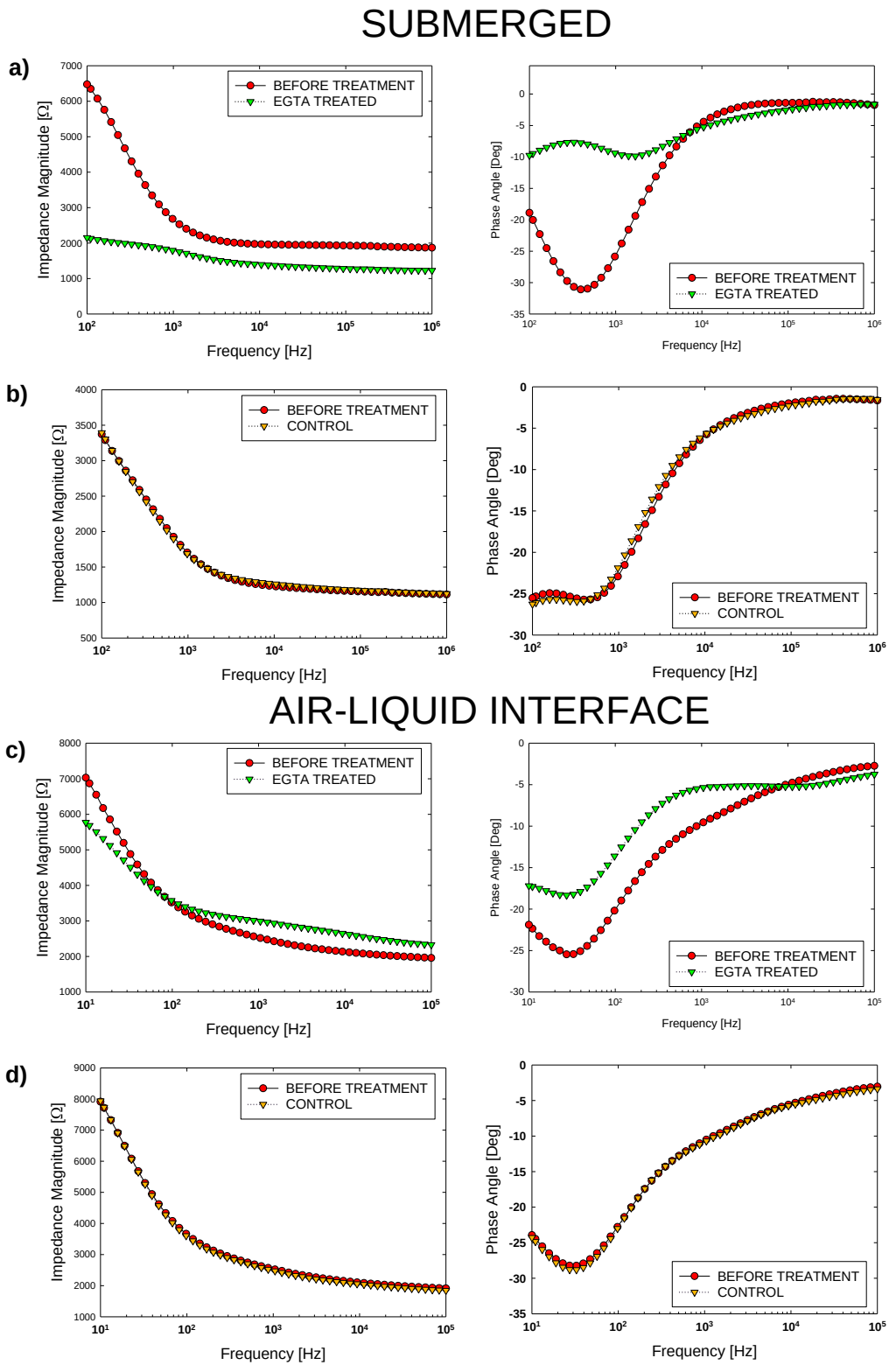

Figure 5-22 Effects of EGTA on differentiated PBECs (Day 21) measured under submerged (a, b) or ALI conditions (c, d). Impedance spectra are measured before (Red) and after (Green) addition of EGTA (Treated, a, c) or growth medium (Control, b, d). Curves are representative of 4 independent experiments in duplicate for treated and controls.

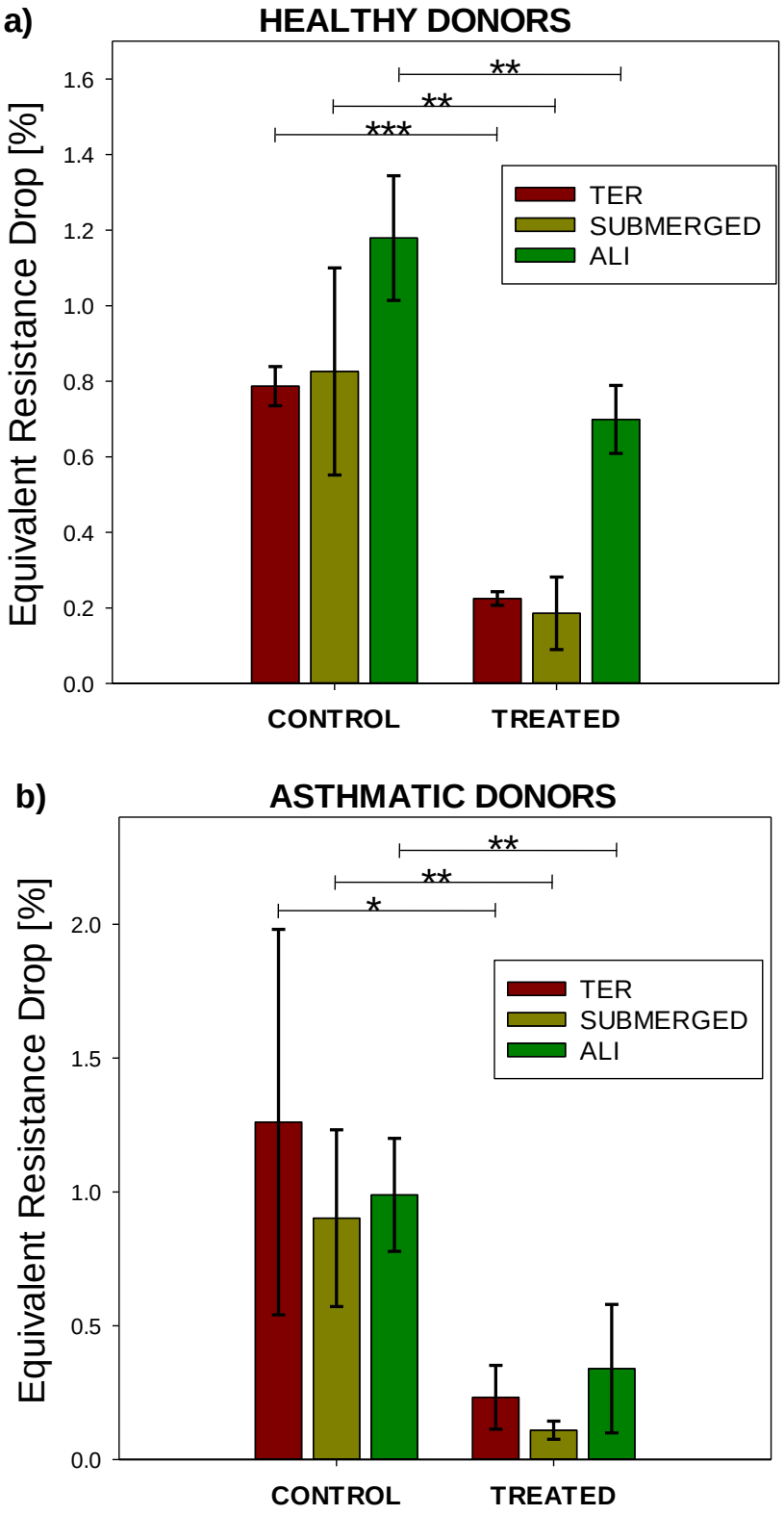

Figure 5-23 Differentiated PBECs barrier disruption with EGTA. Equivalent resistances are fitted from impedance spectra of differentiated (a) healthy or (b) asthmatic PBEC cultures measured before and after addition of EGTA or medium. The drop is calculated as the ratio of the post-stimulation value to the pre-stimulation equivalent resistance. Results are means ± SE of 4 independent experiments performed in duplicates for control and treated conditions (*p<0.05, **p<0.01, ***p<0.001 for comparison between control and EGTA stimulated cultures using a one-tailed paired Student's *t* test).

Healthy and asthmatic cultures shown a similar response to EGTA, with each measurement of the treated cultures being statistically lower than its control. For the healthy cells, the measurements of control cultures shown small differences from pre-stimulation values, with ratios of 79±5% for the TER, 82±27% for the submerged impedance and 118±16% for the ALI impedance. The measurements of healthy cultures treated with EGTA shown a marked drop from pre-stimulation values, with ratios of 22±2% for the TER, 18±9% for the submerged impedance and 70±10% for the ALI impedance. Treated values were lower than the controls with significance p=0.00001, p=0.002 and p=0.001 for TER, submerged impedance and ALI impedance, respectively. For the asthmatic cells, the measurements of control cultures had ratios of 126±72% for the TER, 90±33% for the submerged impedance and 98±21% for the ALI impedance, whereas the measurements of cultures treated with EGTA had ratios of 23±11% for the TER, 11±3% for the submerged impedance and 34±24% for the ALI impedance. For the asthmatic cells treated values were lower than the controls with significance p=0.015, p=0.001 and p=0.003 for TER, submerged impedance and ALI impedance, respectively. The amount of EGTA added to the cultures was sufficient to chelate all the calcium ions from the solution and completely disrupt all the tight junctions, therefore a uniform response for healthy and asthmatic cells was expected. In the future, smaller amount of EGTA could be added to study the different dose-dependent response of the two cell types.

Values for EGTA-induced drop of epithelial electrical properties can be found in the literature for primary cells and cell lines: Coyne *et al.* [146] reported a drop of TER for a primary, static culture of human airway epithelial (HAE) cells down to 12.5% of the original value; Sun *et al.* [66] reported a drop for a static culture of 16HBE cells to 20% of the original value when measured with conventional TER methods and down to 80% of the original value if measured with a cis-impedance system. Henry *et al.* [64] reported a drop in trans-impedance of a microfluidic culture of intestinal cells down to 35% of the pre-stimulation value. The experimental measured drop in TER is in agreement with the ones reported in the literature. The drop measured with cis-impedance is lower than the one reported by Sun *et al.* because of the different sensitivities of the two systems, as previously explained.

To verify the barrier disruption induced by EGTA, control and stimulated cultures were fixed and immunofluorescently stained for actin, occludin (a protein component of the tight junctional complex) and DNA (nuclei). A comparison between a treated and a control culture is shown in Figure 5-24. In control, unstimulated cultures the images show that TJs are homogenously distributed across the tissue and form an organised honeycombed structure with strong pericellular staining of occludin. This is representative of an established epithelial barrier. It can be observed in the superimposed images that TJs are properly located on top of the intercellular actin filament. After EGTA treatment, there are areas where the occludin and the actin networks are completely disrupted. In this condition there is no barrier and the tissue is extremely leaky. This morphological analysis for cultures of PBECs is confirmed in the literature: the control is equivalent to the one observed by Hardyman *et al.* [147], whereas the effects of the EGTA stimulation are similar to the ones reported by Vermeer *et al.* [148]. The number of cells surrounded by an uninterrupted perimeter of occludin was 105±21 for the control and 35±25 for the treated culture. The drop down to 33% of the original value was statistically significant and similar to the electrical measurement.

The sensitivity of the planar circular segments electrodes with an insulating septum is sufficient to measure variation in the electrical properties of a primary bronchial epithelial tissue cultured on a commercial support at the ALI. Large variations in signal associated with EGTA barrier disruption can be quantified, whereas small variations associated with barrier establishment over time that are also affected by the previously described setup-related errors lead to instability of the fitting algorithm.

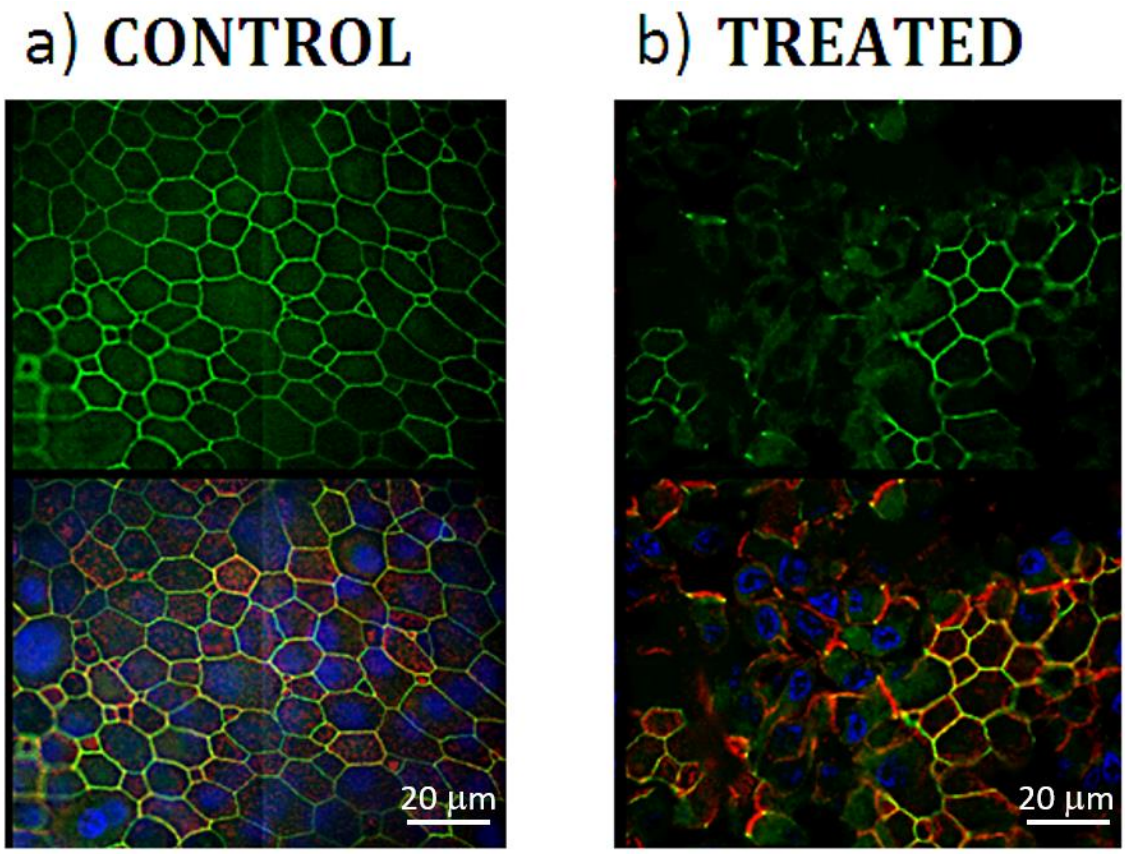

Figure 5-24 Immunofluorescence staining of PBEC cultured at the ALI on commercial supports 10 minutes after addition of growth medium (a, Control) or EGTA (b, Treated). TJs (occludin) are stained in Green, while nuclei are stained in Blue and actin in Red. TJs are reported as stand-alone (Top) or in superimposition with actin filaments and nuclei(Bottom). In the treated condition, the tissue present areas where TJs are heavily disrupted. Images are representative of 4 independent experiments performed in duplicate for control and treated conditions. 100x magnification.

5.4 Electrical characterisation of epithelia cultured in fluidic conditions

This section describes the experimental results obtained with cells cultured under constant perfusion conditions (30 µl/hr). All the experiment reported in this section were performed with the microfluidic device from Figure 4-12, with integrated circular segments coplanar electrodes (second design in Figure 5-13) coated with Pt-black.

5.4.1 Electrodes fouling

The microfluidic device was operated for 66 hours under constant perfusion with cell culture medium to assess the extent of electrode fouling. Selected impedance spectra over time are shown in Figure 5-25 together with the fitted values for the constant phase element parameters. The system showed a reduction in electrode polarisation over time. The impedance magnitude at 100 Hz decreased from a starting value of 1170 Ω to 1050 Ω after 86 hours, while the phase angle at the same frequency varied from -25.7° to -24.2°. The fitted parameters also show a reduction of electrode polarisation with the constant phase element amplitude decreased by 10% while the exponent increased from 0.476 to 0.493 indicating a more resistive behaviour. This variation does not have a detrimental effect on the measurement and is automatically accounted for during the fitting of the impedance spectra.

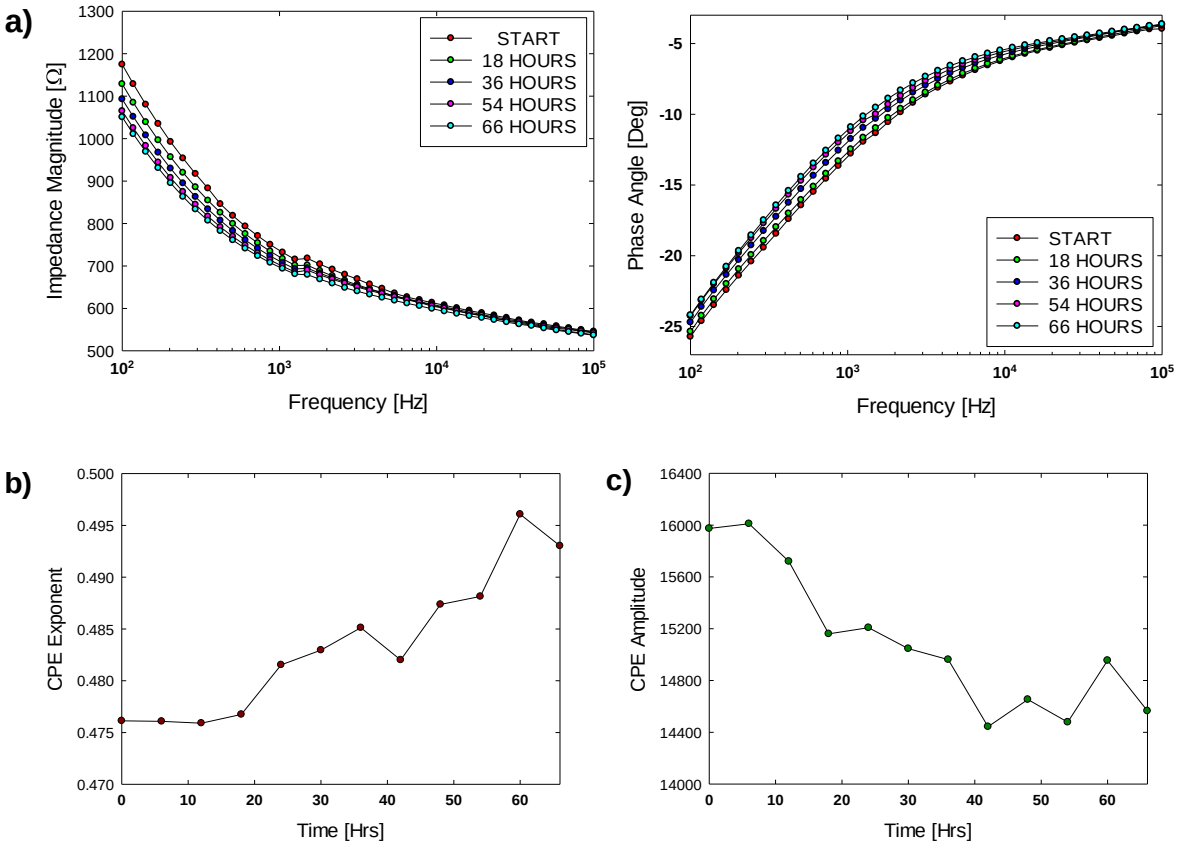

Figure 5-25 Assessment of electrodes fouling effects. A device is operated with cell culture medium for 66 hours and the impedance spectrum is measured every 6 hours. Selected spectra are reported (a). Fitted values for the exponent (b) and amplitude (c) of the constant phase element relative to electrodes polarisation are reported as functions of time.

5.4.2 Continuous monitoring of 16HBE cells

Cells were cultured in microfluidic conditions to assess if the system is capable of supporting and monitoring cellular growth and barrier formation. 16HBE cells were cultured in the device for 6 days and impedance spectra measured every 6 hours. The evolution of measured electrical properties is shown Figure 5-26. The impedance magnitude at 300 Hz was 610 Ω when cells were seeded, increased to 1230 Ω after 24 hours, to 1430 Ω after 54 hours and stayed constant afterwards. The phase angle depth decreased from the initial baseline to -20° after 24 hours and to -27° after 54 hours. A similar trend was observed in the fitted equivalent resistance which increased over the first 2-3 days up to 1100 Ω and stayed constant afterwards. Data points where the equivalent resistance reaches high values (>2000 Ω) were sometimes observed and were deemed dependent from the measurement apparatus rather than from actual biological variations of the epithelial barrier.

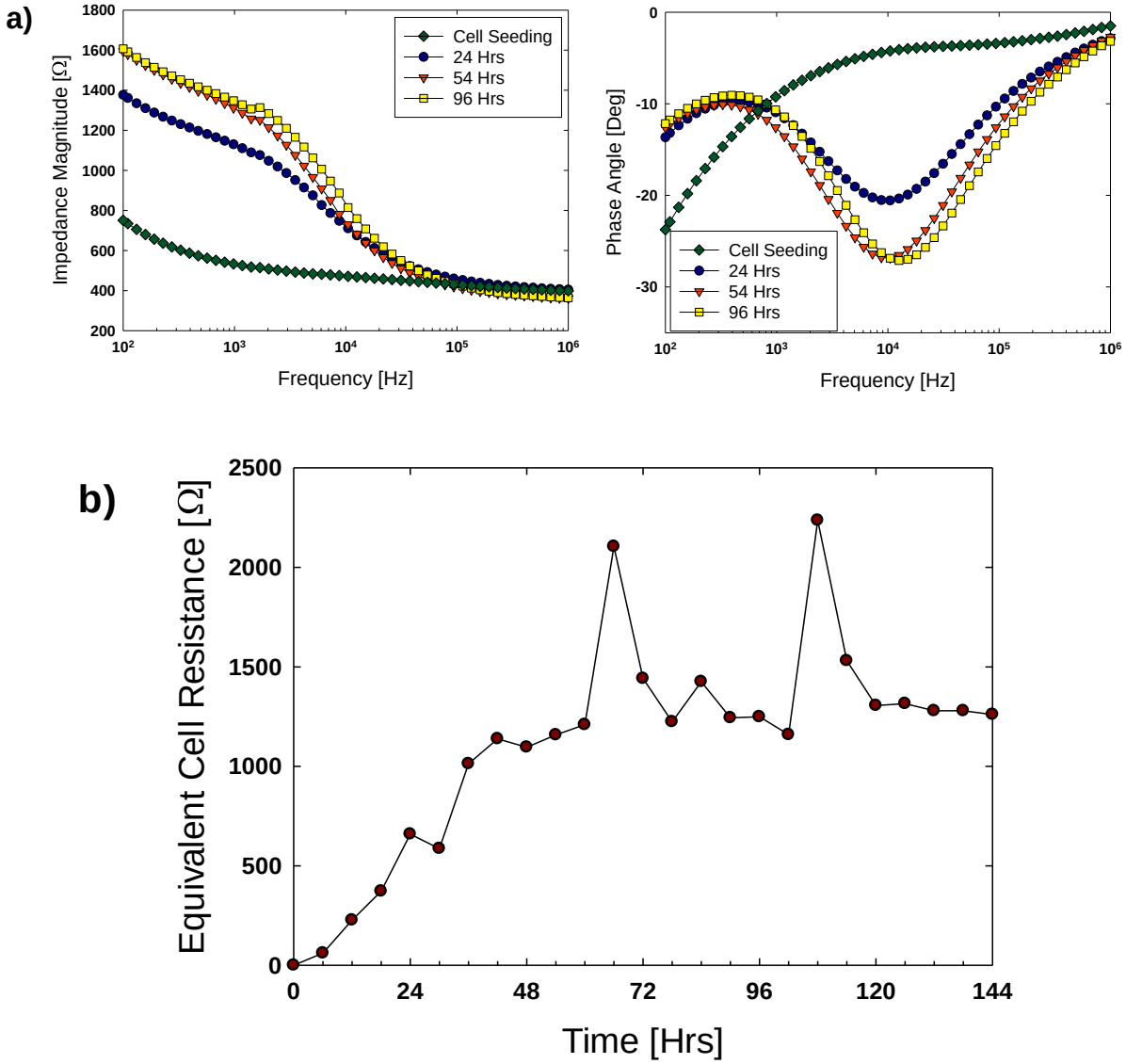

Figure 5-26 Continuous monitoring of 16HBE14o- growth. Cells are cultured in the device in microfluidic conditions for 6 days and impedance spectra are measured every 6 hours. Impedance spectra for selected time-points (a) and fitted cell resistance parameters over time (b) are shown. Results are representative traces of 3 independent experiments.

To compare tissue grown in microfluidic or static conditions, cells were cultured on 4 standard Transwell® supports in parallel with the microfluidic device. The experiment was repeated 3 times and data are shown in Figure 5-27.

Equivalent cell resistance values obtained with the two systems were comparable: both systems indicated the establishment of a barrier in the first 3 days, followed by a small decrease in electrical properties in subsequent days, in agreement with the literature. A t-test was performed to compare means obtained with the different measuring systems after 3, 5 or 6 days (assuming equal variance of the two populations). The two cultures were not statistically different because the null-hypothesis of equal mean couldn't be rejected in any of the cases

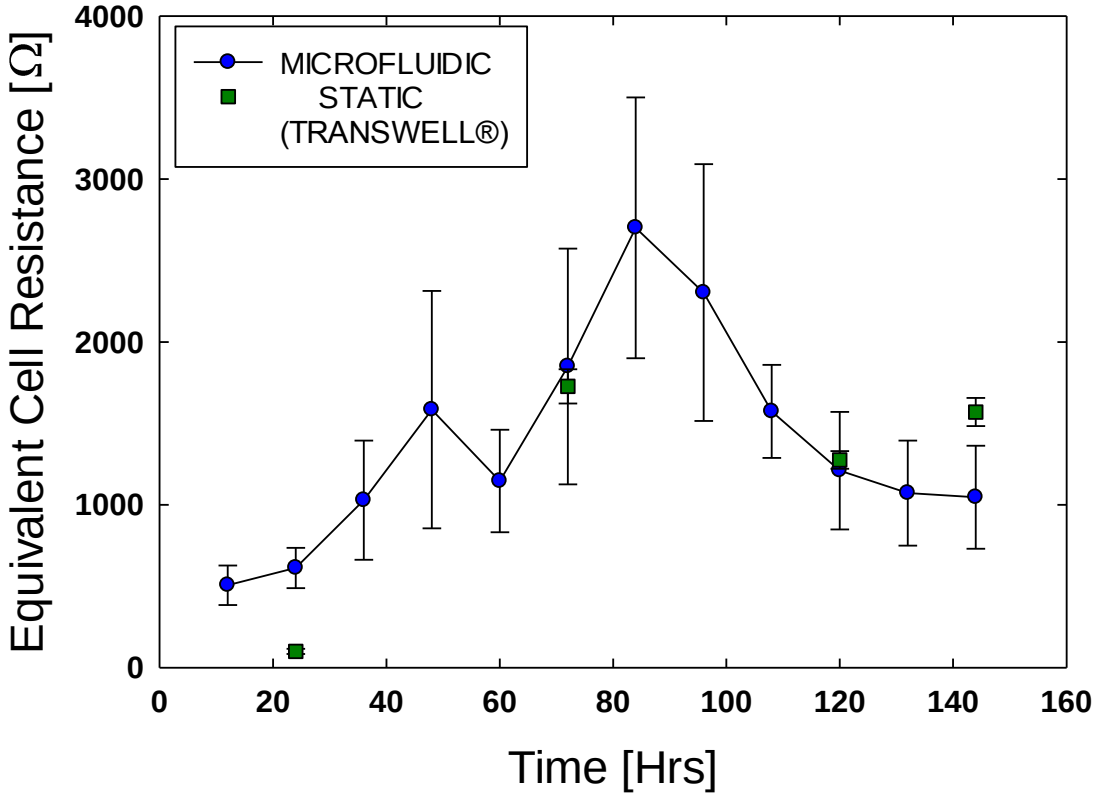

Figure 5-27 Comparison of 16HBE cell growth and polarisation in microfluidic or static (Transwell®) conditions. Cells were cultured in parallel in a microfluidic device and in 4 static Transwell® for 6 days. Tissue electrical properties are measured every 12 hours for the automated impedance system or at selected days for the commercial system. Results are means ± SE from 3 independent experiments (blank are subtracted from the static data). The two cultures are not statistically different after 3, 5 or 6 days.

5.4.3 Monitoring Poly(I:C)-induced barrier disruption

After 6 days of culture, the barrier was disrupted for cells growing in the microfluidic device and in 2 static Transwell® supports by stimulation with Poly(I:C). The other 2 static supports were used as control.

Electrical properties of cultures were monitored over time after stimulation, as shown in Figure 5-28. Impedance spectra of the microfluidic chip were measured every hour with integrated planar electrodes, while commercial electrodes were used to measure TER of static cultures after 3 and 17 hours. Impedance spectra indicated a drop in barrier properties after 3 hours, which continued after 9 and 15 hours. Equivalent cell resistance values were computed and compared with TER values of static cultures. All values were normalised to pre-stimulation values to obtain information on the resistance change induced by poly(I:C) stimulation. Post stimulation resistances of control static cultures were not statistically different from pre stimulation ones. Treated static cultures show significant changes down to 61±8% of the original value after 3 hours and to 22±4% after 17 hours. Microfluidic cultures show the first significant drop after 3 hours down to 84±5% of the original value and a continued drop over time, reaching 54±10% after 17 hours. These values are in good agreement with values of poly(I:C) disruption of static cultures of 16HBE found in the literature. Rezaee *et al.,* [139] reported a drop in TER of 50% after 3 hours and 80% after 24 hours, *Blume et al.,* [126] reported a drop in TER of 50% after 3 hours and 70% after 24 hours; and Heijink *et al.,* [149] reported a drop of 20% after 3 hours and 60% after 24 hours.

To verify the poly(I:C)-induced barrier disruption, cultures were fixed and stained for occludin, actin and nuclei 17 hours after stimulation. Representative fluorescence images are shown in Figure 5-29. In control static cultures, TJs had a well-organised structure, were located in correspondence to intercellular actin filament and formed a uniform and continuous network, indicating good barrier properties. In treated static cultures, the intensity of intercellular occludin signal was low. TJs were located only in small regions of the tissue, indicating poor barrier properties. In treated microfluidic cultures, a TJs network was present and corresponded to the actin structure. The network was less homogenous than the control static culture and TJs were rearranged around clusters of cells rather than individual cells. The disruptive effects of poly(I:C) on occludin disposition on 16HBE cells shown in Figure 5-29 are equivalent to the ones reported by Rezaee *et al.* [139]. The number of cells surrounded by an uninterrupted perimeter of occludin was 20±9 for the control static culture, 1±1 for the treated static culture and 5±1 for the treated microfluidic culture.

From immunofluorescence images and electrical data, it is possible to infer that cultures in the microfluidic device undergo a smaller barrier disruption compared to the static cultures after poly(I:C) stimulation. This effect can be explained considering that the long-term effective concentration of poly(I:C) in the microfluidic device is smaller than in the static supports. The amount of poly(I:C) present in the static supports is constant over time, while it is not in the microfluidic device where molecules that permeate through the tissue are removed by the basolateral flow. A similar effect is present for synthesised pro-inflammatory proteins, which can accumulate in the static cultures over time causing negative feedback effects but are removed from the microfluidic culture [125].

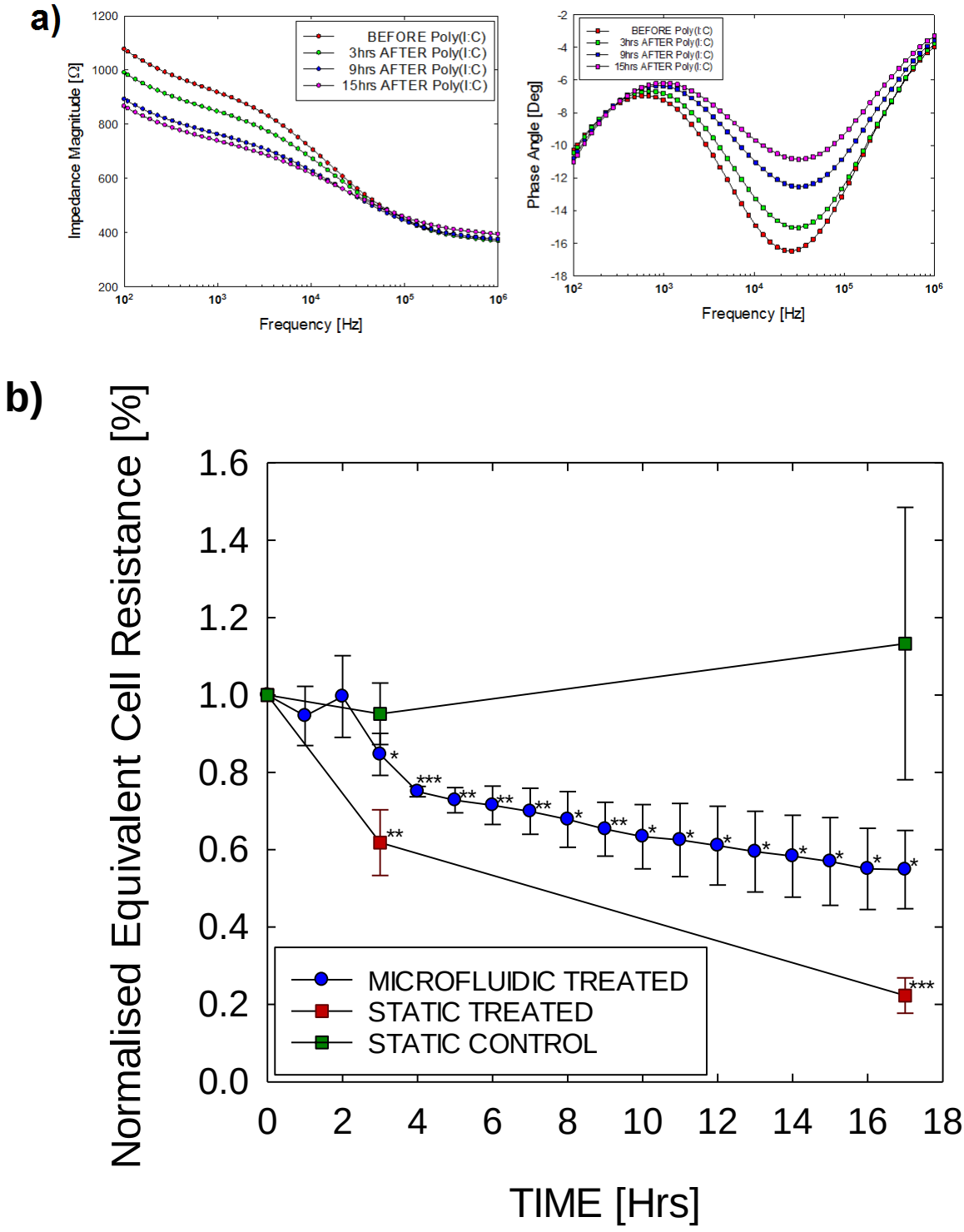

Figure 5-28 Effects of Poly(I:C) on tissue electrical parameters. Cells are grown in parallel cultures of a microfluidic device and 4 static Transwell® supports. After 6 days of culture, the microfluidic culture and 2 static supports are stimulated with Poly(I:C) (5 μg/ml), while 2 static supports are used as control. The microfluidic culture is monitored with impedance measurement every hour, while TER is measured on commercial supports after 3 and 17 hours. Selected impedance spectra (a) and evolution over time of equivalent cell resistances (b) are shown. Equivalent cell resistances are normalised to pre-stimulation values. Results shown are representative traces or means ± SD of 3 independent experiments. *p<0.05, **p<0.01 and ***p<0.001 for comparison between pre- and post-poly(I:C) stimulation.

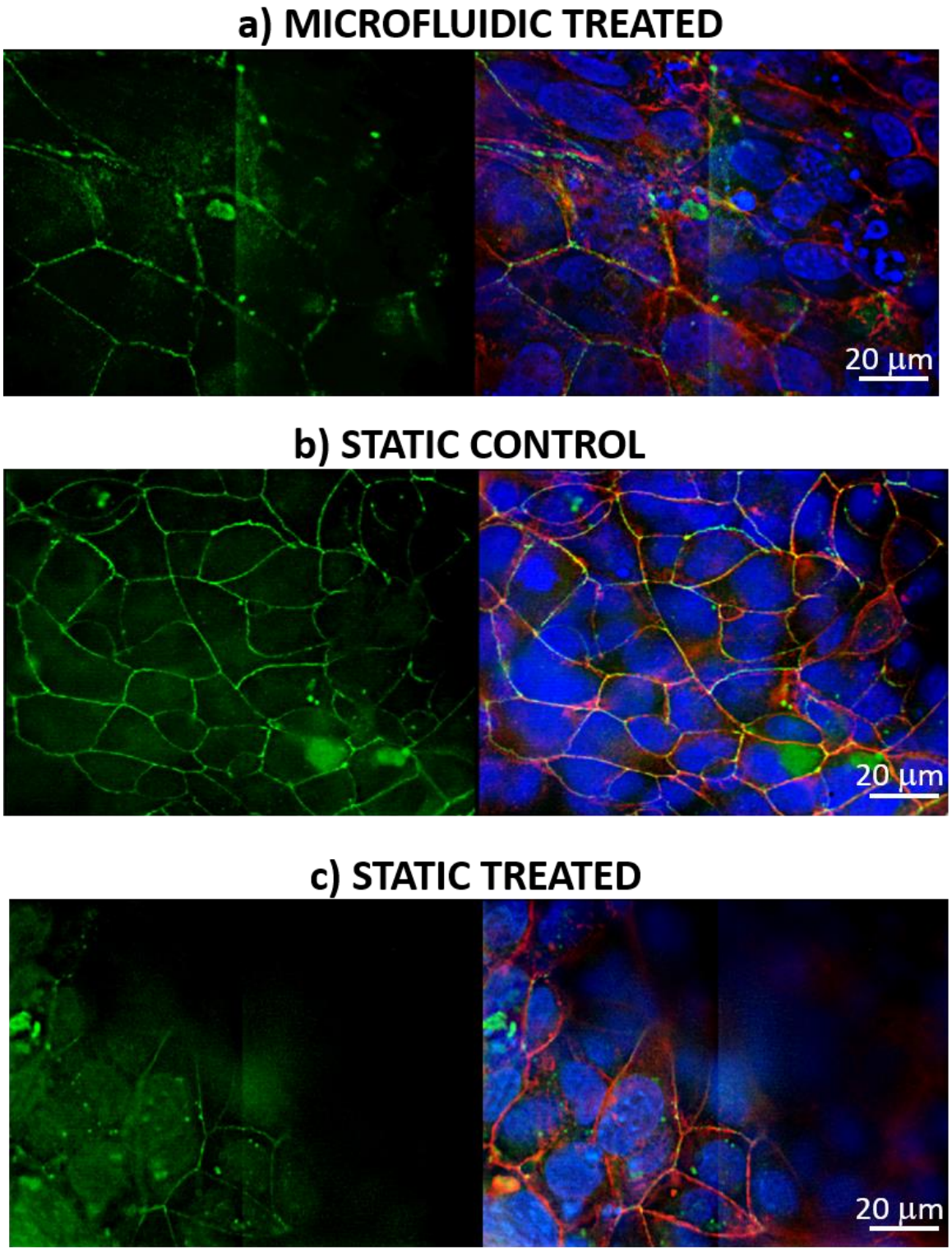

Figure 5-29 Immunofluorescence staining of 16HBE cells. Cells were cultured in parallel on a microfluidic device and on static Transwell® supports. After 6 days of culture, cells are stimulated with Poly(I:C) to induce a barrier disruption. 17 hours after the stimulus, cells were fixed and stained for occludin (Green), actin (Red) and nuclei (Blue). A treated microfluidic culture (a), a control static culture (b) and a treated static culture (c) are shown. Images are representative of 3 independent experiments. 100x magnification.

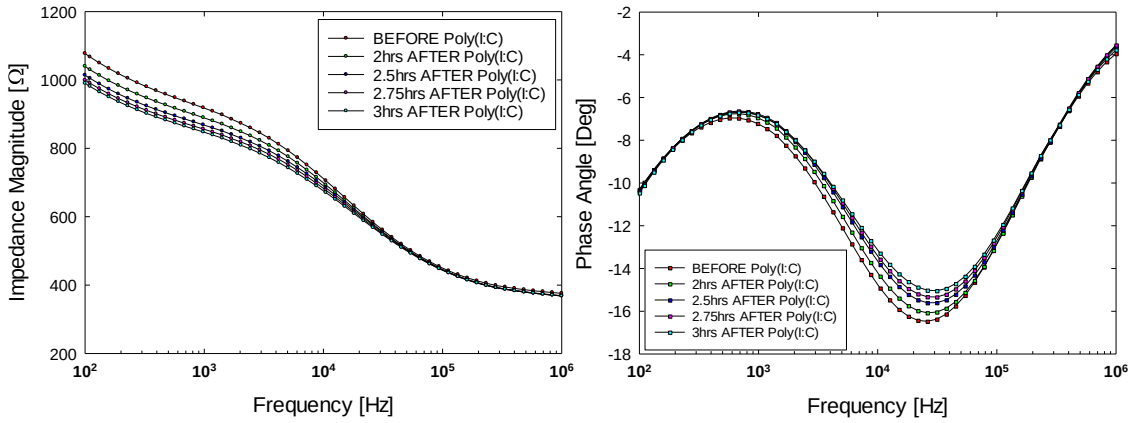

Figure 5-30 Effects of poly(I:C) on impedance spectra. Measurements are performed every 15 minutes after the poly(I:C) stimulation. Spectra for the significant impedance drop from 2 to 3 hours are shown. The high sensitivity of the electrodes design allows barrier disruption to be closely observed.

The automation and sensitivity of the device allowed measurements of tissue electrical properties variation with a fine temporal resolution. This can be observed in Figure 5-30, where the drop in impedance after poly(I:C) challenge is observed with a 15 minutes resolution.

In summary, the proposed microfluidic device was suitable to monitor the barrier establishment of a submerged culture of 16HBE cells for 6 days and for the measurement with fine temporal resolution of the extent of barrier disruption induced by poly(I:C) stimulation.

5.5 Discussion and conclusions

This chapter described the experimental characterisation of the platform for epithelial cell culture and barrier monitoring developed in the project. First, the electrodes were tested without cells to establish a baseline. Then, they were used to monitor electrical properties of epithelial cells cultured in static conditions on commercial supports under submerged or ALI conditions. Lastly, cells were cultured in the device under submerged, constant perfusion condition and monitored with the integrated electrodes.

Characterisation of the device in the absence of cells was performed to analyse the effects that system parameters have on the impedance measurement. The 4 parameters considered were solution temperature, solution concentration, electrode polarisation, and electrodes fouling under perfusion. Temperature variations affect the mobility of the ions, modulating the solution conductivity. An increase in temperature caused a decrease in measured impedance which was linear both at low and at high frequencies, in agreement with the literature. Increasing the salt concentration of a solution results in higher conductivity and lower Debye's length. The impedance at high frequencies depended linearly on the concentration, because polarisation effects were negligible. A Pt black coating was used to reduce low frequency electrode polarisation. The coated electrodes show good performance down to 100 Hz, in agreement with the literature. The system shows no relevant electrode fouling after 84 hours under constant cell culture medium perfusion. Preliminary characterisation highlighted the necessity of the Pt black coating and suggested that, in a controlled environment, minimal variation of the measured impedance induced by variation in the system parameter are to be expected.

A preliminary characterisation of static cultures was performed to assess the soundness of the proposed methods. The possibility of material cytotoxic effects was excluded by comparing cell growth on commercial and on custom static supports. After 6 days the two cultures had similar barrier properties, as indicated by a non-significant difference in TER values and by similar structures after immunostaining. The electric field applied during the measurement was found to disrupt the cell construct barrier. The disruption was dependent on the applied potential but was recovered over time. A potential that had no significant effects on the culture barrier properties was determined and used in all the other experiments. The feasibility to monitor the establishment of the cell culture barrier with planar electrodes was confirmed by the linear correlation between the impedance spectra measured with a trans-epithelium or cis-epithelium electrodes configuration. The device materials, structure and electrical measurements yielded responses comparable to those obtained with current standards in tissue culture.

Different planar electrodes geometries were tested to validate the numerical optimisation performed in the modelling chapter. The general guideline of increasing the basolateral resistance proved effective and led to the circular segment electrode design, with a sensitivity 16 times larger than the design from the literature. The sensitivity was found to increase to 45-fold compared to the design from the literature with the insertion of an insulating septum between the electrodes.

The effects of different medium volume in the apical compartment was analysed for a static cell culture. The measured sensitivity decreased logarithmically with decreasing apical volume. The minimum amount of apical liquid in required for a measurement with the circular segments planar electrode was found to be 10 μl. If the apical volume is above this limit, impedance spectra can be used to monitor the establishment of the barrier, and tissue equivalent electric parameter are qualitatively and quantitatively comparable to values measured with the commercial system. Otherwise the variation in impedance induced by the barrier formation cannot be detected. The measurement of electrical properties at the ALI was demonstrated on a primary culture of bronchial epithelial cells using the circular segments electrodes with an insulating septum. The establishment of the barrier induced an observable variation in the impedance spectra, but this could not be quantified due to week-to-week variation in the setup which altered the baseline and hindered a

consistent fit. The EGTA stimulation induced a significant drop in barrier that was comparable with the drop measured by the current standard in biology TER methods. Healthy and asthmatic cells did not show different responses to the EGTA challenge. The increased sensitivity obtained with the new electrodes design was not sufficient to allow measurement of cell electrical properties at the ALI; an insulating barrier will be required to reach that goal.

Finally, the monitoring of a culture of 16HBE cells grown under constant perfusion was demonstrated with integrated electrodes. Polarisation and barrier formation were comparable to standard systems. Cells cultured in the microfluidic system showed a response to a viral infection equivalent to the one normally observed in static cultures. The device provided more information than the standard measuring systems because time-points could be collected more frequently and because the complex impedance was measured.

Chapter 6: Conclusions and future work

In this thesis, the design, simulation, modelling, optimisation, fabrication and experimental characterisation of a novel organ-on-chip device for epithelial cells culture and epithelial barrier monitoring were described. In the device, cells cultured on top of a nanoporous support were fed by constant perfusion of growth medium in a basolateral microchannel and barrier properties were monitored in real-time with integrated coplanar Pt/Pt-black electrodes. Finite element method (FEM) simulations were used to guide the development of a new coplanar electrode design formed by 2 circular segments electrodes divided by a polymeric septum. The high sensitivity of the novel electrode design enabled the measurement of epithelial electrical properties directly ALI and was used to measure the drop in barrier properties of PBEC cultured on Transwell®, induced by stimulation with EGTA. The microfluidic device was used to culture 16HBE cells for 6 days and to monitor the establishment of the epithelial barrier under submerged conditions. Moreover, the barrier drop induced by stimulation with a viral mimic (poly(I:C)) was observed.

6.1 Contributions to the field of organs-on-chip

In this work, several original contributions that improved the state of the art of the organ-on-chip technology were presented. These contributions were developed as solutions to application-specific problems but the adopted approach can be extended to different organ-on-chip systems.

A new equivalent electric circuit was developed to enable a robust interpretation of tissues electrical impedance spectra. Prior models were not optimized and over-fitted the system by using an excessive number of independent parameters, yielding inaccurate or unreliable results. The proposed model was obtained by considering the frequency-dependent behaviour of several biological parameters and by discarding the parameters which had a second-order effect on the total impedance. In this way, only the relevant parameters were fitted. A similar approach can be used to develop EEC models for other organs-on-chip systems.

A new coplanar electrode design was developed to obtain a system capable of performing real-time electrical measurement with high sensitivity of submerged or ALI cultures. Previous systems which used trans-epithelium electrodes required a momentarily submersion of the tissue and could not provide a good temporal resolution, whereas previous systems which used coplanar electrodes did not have a sufficient sensitivity to probe the ALI. To determine the best electrode design, a circuital analysis was performed and it was found that the basolateral resistance of the system should be maximized in order to increase the sensitivity of the measurement. By following these design rules, two novel electrode design with increased sensitivity were developed, one with parallel electrodes separated by a gap and another with the addition of an insulating septum between the electrodes. The design rules developed in this work can be used to optimize the electrode design of any organ-on-chip which aims at measuring electrical properties of cells.

A new fabrication technique for the integration of porous support in microfluidic devices was developed. The technique used a cell-friendly UV curable glue dispensed with a self-terminating approach to ensure a glue-free culture area. The technique used 2 gluing steps to ensure a strong and moisture resistant device. This technique can be used to integrate porous support in any organ-on-chip system.

In this work, novel measurements of biological systems were also performed. The measurement of electrical properties of epithelia cultured at the ALI was demonstrated for the first time. The EGTA-induced epithelial barrier disruption was analysed in these conditions. This measurement is relevant for all studies focusing on epithelia from the respiratory tract. Moreover, the measurement of cell lines, healthy primary cells and asthmatic primary cells was demonstrated with the same

approach, illustrating the flexibility of the technology. Lastly, the study of the temporal kinetic of poly(I:C)-induced epithelial barrier disruption of cells cultured in a microfluidic device was demonstrated, showing the unique capabilities of the proposed microfluidic device with integrated electrodes.

6.2 Setup improvements

Moving forward, some features of the device and of the setup can be improved to ensure a more robust and reliable experimentation.

Experimental setup and device parallelisation

Currently, only one device at time was used. This was sufficient to demonstrate the feasibility of growing and monitoring cells on-chip, but it will not be sufficient for future drug discovery experiments, where a high-throughput is required. The main obstacle towards increased parallelization was the unreliability of the setup combined with the high sterility requirements. The electrical connectors were difficult to align and to fix in place, leading to the need to repeatedly access the inside of the incubator to move the connector with a screwdriver. Several times, this compromised the experiment due to contamination or chip breakage. Improvements could be made to the setup to solve this issue. The new setup will ideally have better connectors, have built-in bubble traps and valves, and will be compact enough to fit entirely inside a sterile hood, so that any adjustment required can be performed in a sterile way, minimizing the risk of infections.

Mass-manufacturing

Currently, the components of the device are manufactured in the clean-room or in the laboratory and the device assembled by manual gluing. This process is satisfactory to manufacture a few prototypes, but the throughput must be increased for eventual commercialization. Several improvements could be introduced to increase the production rates.

Electrochemical deposition of platinum black must be moved from single chip to wafer scale. The deposition time of 3.5 minutes is amplified dramatically by coating one chip at time. To perform wafer-scale coating, it is necessary to modify the photolithography mask and introduce tracks connecting every device, which will be cut off during dicing. The wafer can then be submerged in a beaker with the platinization solution and contacted on one edge. To ensure good deposition uniformity, connecting tracks must be wide enough to ensure that the same potential is applied to all chips. A platinum coated wafer mounted on a rack facing the working wafer can be used as counter-electrode.

The production of PMMA chips could be improved by switching from laser ablation to injection moulding. This technology change requires small differences in the design of the pieces, but increases the production rate. Lastly, device assembly must be improved. This is currently the bottleneck of the manufacturing process, requiring about 2 hours per chip. It would be possible to improve this either by wafer-scale gluing or by adopting a different technology such as ultrasonic welding.

Sterilisation

The sterility of each device is critical to avoid infections. Each device must be in a sterile package before entering the lamina flow hood and opened only in sterile environments. Currently, each device is sterilised with bleach and ethanol before use. This operation is time consuming and is not feasible for high-throughput experiments. Commercial gamma radiation is available and would constitute a better option for sterilization of higher volumes of devices.

Control software

The Alpha-A from Novocontrol Technologies impedance analyser was used to perform measurements. This machine is over-specified for this application, is bulky and can only be run with the proprietary WinDeta software. In the future, the cheaper, smaller and lighter impedance analyser C60 from Cypher [150] could be used. The specifics of this instrument are sufficient for this application and it has the added advantage that it can be controlled with Matlab, allowing the integration of the two control software packages. Additionally, all the valves in future setups will be electric and, together with the syringe pump, controlled automatically by the same software during experiments.

Conductivity measurements and additional sensors

The device has a pair of electrode additional to the electrodes used to monitor the cell construct. These electrodes are designed to monitor the conductivity of the medium in the channel and detect variation in the temperature during a long-term measurement. Additional electrodes could be integrated to monitor other properties such as dissolved oxygen or pH.

Fraction collector

Electrical measurements give information on the overall culture barrier properties over time. To better understand drug effects, it is of interest to couple this information with a time-resolved analysis of cellular protein production rates. A fraction collector can be used to achieve this goal. Fraction collector are systems that collect and store liquid fractions from the outlet of the devices. Their main function is to prevent diffusion between two temporally different fractions. Two options for a fraction collector have been presented in the method sections. The first consists of a robotic xyz stage that moves a collection well plate underneath the device as reported by Blume *et al.* [125]. The second is a microfluidic system where a fluorinated oil droplet is intercalated between two medium fractions with a T-junction.

6.3 Biological experiments

This thesis focused on the technical aspects of the development of a microfluidic device for culture and monitoring of epithelial cells. All the experiments performed involving biological samples were aimed at the validation of the device, and used procedures or targets with examples in the literature that could be used as comparisons. in this section some biological studies that could be performed on this platform after its preliminary characterization are described.

Analysis of PDMS septum on culture

It was demonstrated on a Transwell® that the addition of an insulating septum between the electrodes increases the sensitivity of the planar electrodes measurement. The septum needs to be in contact with the support membrane to completely prevent electrolyte passage and be fully effective. The integration of this septum in a microfluidic device might lead to problems concerning the culture media distribution uniformity across the culture chamber. Cells growing on areas of the nanoporous membrane in contact with the septum might not receive adequate nutrients and be affected by the septum. The effects of a septum integrated in the microfluidic device must therefore be investigated. It is important to note that the width of the septum is not a critical parameter in the electrode design and it can be reduced to decrease the number of cells in contact with it.

Microfluidic cultures of primary epithelial cells

It was demonstrated that the device is able to sustain and monitor the growth of an epithelial cell line. Additionally, it was demonstrated that the circular segments electrodes design is sensitive enough to measure electrical properties of a culture at the ALI. Future experiments would be to monitor the growth of PBECs cultured on-chip at the ALI for 21 days, as recently performed by Henry *et al.* [64] (2017).

Effects of stimuli on epithelial barrier

It was demonstrated that the device is able to detect the establishment of an epithelial barrier and the drop associated with poly(I:C) or EGTA stimulation. It is biologically relevant to test which other stimuli (e.g. pollen, cigarette smoke, nanoparticles) might have detrimental effects towards the epithelial barrier. At the same time, it is possible to see which drug candidates have positive effects on a disrupted culture and prompt a recovery of the epithelial barrier.

6.4 Future directions

Up to this moment, the full integration of electrodes within organ-on-chip devices was challenging [64], but the proposed device might change this perspective. In fact, the new electrode design is equipped with a high sensitivity and the unique flexibility to operate under submerged or ALI conditions. Moreover, any organ-on-chip system aimed at culturing epithelial cells on a porous membrane could benefit from the straightforward integration of the coplanar electrodes chip in the basolateral side of the device. In fact, the core sensing element, i.e. the rectangular glass chip with platinum electrodes, can easily be adapted to the geometries and bonded to the materials of most common organ-on-chip devices. This integration could enable electrical measurements in organ-on-chip devices focused on other features, becoming a shared standard and enabling a multi-parametric analysis of epithelial tissues required to achieve high model predictivity.

Appendix A Data Fitting

Complex impedance spectra are fitted with electric equivalent circuits to obtain values for the tissue equivalent parameters. A custom MATLAB script is developed to perform the fitting. Every fitting problem can be transformed in a minimisation one by introducing an objective function defined as the sum of residuals between the experimental data and the theoretical model: values of the model parameters that best fit the curve are the ones for which the objective function is minimum.

A.1 Weighted Complex Non-linear Least Squares (CNLS)

In impedance fitting there are two sets of data (real and imaginary parts) that need to be fitted at the same time by the same parameters. One way to define the objective function in this case is with the complex non-linear least squares (CNLS) approach. In this approach, the objective function is defined as the sum of squared residuals deriving both from real and imaginary parts:

$$\Phi = \sum_{i=1}^{f_N} \sqrt{\left(Re_i^{EXP} - Re_i^{MOD}\right)^2 + \left(Im_i^{EXP} - Im_i^{MOD}\right)^2}$$

where the sum is extended to all the experimental frequency points measured. If real and imaginary parts are of different order of magnitudes, the CNLS will fit only the biggest variable (which has the biggest residuals associated with it) and disregard the smaller variable. To prevent this effect, the two parts are commonly weighted to obtain comparable values [151]. One way to weight the data is by proportional weighting, where each term is normalised to its experimental value: the objective function becomes:

$$\Phi = \sum_{i=1}^{f_N} \sqrt{\left(\frac{Re_i^{EXP} - Re_i^{MOD}}{Re_i^{EXP}}\right)^2 + \left(\frac{Im_i^{EXP} - Im_i^{MOD}}{Im_i^{EXP}}\right)^2}$$

A.2 Minimisation algorithm

Once the objective function is defined, it needs to be minimised. To perform this task, the Nelder-Mead simplex algorithm was used. This algorithm is widely used even though convergence has not been demonstrated for it [152]. This algorithm is an unconstrained direct search method (does not use derivatives) which uses a low number of function evaluations at each iteration. In *n* dimensions, the algorithm builds a simplex defined by *n*+1 vertices. At each iteration the algorithm computes function values in the vertices, then considers allowed transformation of the simplex (reflection, contraction, expansion and shrinkage) and computes function values in the new points: if the function value in the new point is smaller than the function value in one of the vertices, the new point becomes a vertex. The algorithm proceeds until no new points with lower associated functions can be found or the maximum number of iterations is reached [153]. Computationally, the algorithm is built-in in the “fminsearch” MATLAB function and is therefore straightforward to implement.

A.3 Matlab script

The script has the following structure:

1. Software initialisation.
2. Global variables are defined.

3. The names of the external comma separated values (CSV) files containing the data are loaded.
4. A first guess on the fitting parameters is provided.
5. External impedance data are loaded.
6. Impedance magnitude and phase angle data are transformed in real and imaginary parts of the impedance.
7. The objective function for the first guess parameters is evaluated.
8. The Nelder-Mead algorithm minimizes the function.
9. The fitted parameters are stored.

The custom script is provided below:

```
%%%%%% COMPLEX NON-LINEAR FITTING
% Script to fit cellular impedance spectra. This script fits the real and the imaginary part
% of the impedance at the same time with a custom weighted complex fit using squared residuals sum
minimization.
% Calls Zcells.m function which must be present in the same folder, together with the data as .txt
files.

% Initialise Matlab
close all
clear
clc

% Define global variables (is not elegant but works). f is the frequency,
% re is the real part of the signal and im is the imaginary part of the
% signal. I could not use 'real' or 'imag' names because they are reserved.
% by Matlab.
global f;
global re;
global im;

% Data file names. Must be .txt in 3 columns and no headers. See example.
% All filenames must be of the same length.
filenames=['30UL0.txt';'50UL0.txt'];
% Number of files to analyse.
D=size(filenames);

% Initialise fitted parameters on the number of files to analyse.
br          =zeros(1,D(1));
ar          =zeros(1,D(1));
rc          =zeros(1,D(1));
cc          =zeros(1,D(1));
CPE_Factor  =zeros(1,D(1));
CPE_Exponent=zeros(1,D(1));

% Cycle on the number of files to analyse.
for i=1:D(1)

 % First guess parameters for the fit. br is the basolateral resistance[Ohm], ar is the
 % apical resistance[Ohm], rc is the cell resistance [Ohm](Tight Junctions),cc is the
 % cell capacitance [F], CPE_Factor and CPE_Exponent are the dpuble layer
 % parameters.
 br_guess=1000;
 ar_guess=50;
 rc_guess=100;
 cc_guess=10e-8;
 CPE_Factor_guess=10000;
 CPE_Exponent_guess=0.5;
 % Pack all the first guess parameters in a single variable
 p_guess=[br_guess,ar_guess,rc_guess,cc_guess,CPE_Factor_guess,CPE_Exponent_guess];

 % Load Data
 filename=filenames(i,:);
 display(filename);
 data=dlmread(filename,'\t');
 % Transform from impedance magnitude and phase angle to real and imaginary
 % parts.
 re=data(:,2).*cos(data(:,3).*3.14/180);
 im=data(:,2).*sin(data(:,3).*3.14/180);
 f=data(:,1);
% f2 is the frequency expressed as log
 f2=log10(f);

 % Custom complex fit function. Finds the minimum of the objective function
 % defined as the weighted complex sqaured residuals sum.
 % Uses Zcells.m function.
%  Returns all fitted parameters packed in p.
 p=fminsearch(@Zcells,p_guess);

 % Compute model to compare with fitting

 % Capacitance of the cell layer
 Capacitance_cell=1./(1j*2*pi*f*p(4));
```

```
 % Impedance of the cell layer. Parallel CC//RC
 Z_cell=p(3)*Capacitance_cell./(p(3)+Capacitance_cell);
 % Impedance of the electrodes. Constant phase element.
 Z_CPE=p(5)*(1j*2*pi*f).^(-(p(6)));
 % Total impedance of the system. CPE + (ZC+RA)//RB
 Z_total= Z_CPE+(p(2)+Z_cell)*p(1)./((p(2)+Z_cell)+p(1));

 % Plot fitted data vs real data. ALWAYS CHECK!
 figure()
 plot(f2,real(Z_total))
 hold on
 scatter(f2,re)
 figure()
 plot(f2,imag(Z_total))
 hold on
 scatter(f2,im)

 % Plot residuals. Should ideally be randomly distributed.
 figure()
 plot(f2,zeros)
 hold on
 scatter(f2,(re-real(Z_total)),3,[0 0 1])
 hold on
 scatter(f2,(im-imag(Z_total)),3,[0 1 0])
 legend('Real Part','Imaginary Part')
 ylabel('Residual')
 xlabel('Frequency [Hz]')

 % Store parameter values
 br(i)=p(1);
 ar(i)=p(2);
 rc(i)=p(3);
 cc(i)=p(4);
 CPE_Factor(i)=p(5);
 CPE_Exponent(i)=p(6);

end

% Plot fitted parameters for different files (if files are in chronological
% orde gives evolution of TER over time
figure()
plot(rc(:))
figure()
plot(cc(:))


function Fce = Zcells(p)

% Define global variables (is not elegant but works). f is the frequency,
% re is the real part of the signal and im is the imaginary part of the
% signal. I could not use 'real' or 'imag' names because they are reserved.
% by Matlab.
global f;
global re;
global im;

% Set objective funtion to zero
obj=0;

% Capacitance of the cell layer
Capacitance_cell=1./(1j*2*pi*f*p(4));
% Impedance of the cell layer. Parallel CC//RC
Z_cell=p(3)*Capacitance_cell./(p(3)+Capacitance_cell);
% Impedance of the electrodes. Constant phase element.
Z_CPE=p(5)*(1j*2*pi*f).^(-(p(6)));
% Total impedance of the system. CPE + (ZC+RA)//RB
Z_total= Z_CPE+(p(2)+Z_cell)*p(1)./((p(2)+Z_cell)+p(1));

% Compute squared residuals sum.
% Real and imaginary parts are weighted to obtain similar values and have a
% good fit on both plots.
for i=1:length(f)
  obj=obj+sqrt( (( (real(Z_total(i))-re(i))/re(i) )^2 + ( (imag(Z_total(i))-im(i))/im(i) )^2));
end

% Returns the objective function
Fce=obj;

end
```

Appendix B Finite Elements Simulation

Finite element simulations are performed with COMSOL Multiphysics®.
The Creeping Flow module was used to perform the fluidic simulations while the AC/DC module was used for the electric ones.

B.1 Fluidic simulations

Geometry
The geometry of the channel was reconstructed in the software using the model builder.

Materials
"Water, liquid" from the built-in material library was assigned at all domains.

Mesh
An "Extremely fine" mesh was adopted.

Boundary Conditions:

- A normal mass flow rate of $8.3\ 10^{-9}$ kg/s was assigned to the inlet
- Atmospheric pressure was assigned to the outlet.
- No-slip conditions were assigned to all other boundaries.

Study
The steady state was considered.

B.2 Electric simulations

Geometry
The geometry of the measuring chamber was reconstructed in the software using the model builder:

- Electrodes were recreated on the bottom geometry plane.
- A 100mm cylinder (C1) was created on top of the electrodes. It represents the basolateral compartment.
- A 30mm cylinder (C2) was created on top of the previous cylinder (C1). It represents the cell layer.
- A 300mm cylinder (C3) was created on top of the previous cylinder (C2). It represents the apical compartment.

Materials

- Conductivity was set to 1.47 S/m in the apical and basolateral compartment and to $9\ 10^{4}$ S/m in the cell layer.
- Relative electric permittivity was set to 1 on all the domains.

Mesh
An "Extremely fine" mesh was adopted.

Boundary Conditions:

- One electrode was set to 1 V and the other was set to the ground potential.
- Electric insulation was assigned to all other boundaries.

Study
The steady state was considered.

Appendix C Fabrication Recipes

The microfluidic device fabrication steps, their order and location are reported in the following table:

Table 3 Device fabrication steps

Step Number	Step Name	Location
1	Wafer Cleaning	Cleanroom
2	Platinum Deposition	Cleanroom
3	S1813 Photolithography	Cleanroom
4	Platinum Etching	Cleanroom
5	Wafer Cleaning	Cleanroom
6	TMMF Photolithography	Cleanroom
7	Scribing	Cleanroom
8	Manual Dicing	CHB lab
9	Pt-Black Deposition	CHB lab
10	Device assembly	CHB lab

C.1 Clean Room

Wafer cleaning

- Submerge the wafer in a beaker filled with fuming nitric acid (FNA) 99.5% for 2 minutes.
- Rinse in D.I. water.
- Spray each side of the wafer with alternate washing of acetone and isopropanol for 3 times and dry with nitrogen.
- Leave overnight in dehydration oven.

Platinum deposition

After the deposition of an adhesion promoter layer of Titanium (5 nm), a 100nm film of platinum is deposited using the sputtering Helios machine (Buhler Inc.). This step was kindly performed by 3 different cleanroom technicians: Miss Katie Chamberlain, Miss Sarah Helps and Miss Ying Tran. To achieve the deposition, a platinum target is bombarded with energetic particles (Argon) in a high-vacuum environment. The collision between a particle and the target causes the physical release of platinum ions. Such ions are not stable and tend to deposit on all surfaces, including the substrate.

S1813 photolithography

- Spin-coat S1813 photoresist (Microposit) at 500 RPM for 30s with 5000acc.
- Softbake at 95°C for 1 minute.
- Align the wafer and expose with a dose of 92mJ with the EVG620TB mask aligner (EV group).
- Develop for 50s in MF319505 developer (Microposit) bath.
- Rinse for 50s in a DI water bath for 2 times.

Platinum etching
The platinum etching step is performed with an ion beam etch with the Ionfab 300 (Oxford Instruments) machine. The etching parameters are reported in the following table:

Table 4 Platinum etching parameters

Beam Neutralizer Current	552 mA
Beam Neutralizer Bias	15.6 V
Beam Neutralizer Discharge	610 mA, 18 V
Beam Neutralizer Heater	24.94 A, 4 V
RF Generator	570 W, 2 W reflected
Beam Current	200 mA
Voltage	603 V
Accelerator	2 mA, 301 V
Faraday Cup	0.07mA/cm^2
Time	27 min

TMMF photolithography

- Spin-coat the adhesion promoter TI-Prime (Microchemicals GmbH) at 500 RPM for 30s with 5000acc.
- Laminate 2 films of TMMF S2055 (TOK Ltd.) on top of the wafer (Mount=ON, Speed=1, T=80°C).
- Align the wafer and expose with a dose of 480mJ with the EVG620TB mask aligner (EV group).
- Post-exposure bake: ramp up to 90°C in 3 min, dwell for 6 min, ramp down to 50°C in 4 min.
- Develop for 16 min in EC solvent UN3272 (Microposit) followed by a quick rinse in isopropanol and nitrogen drying.
- Hardbake: ramp to 170°C in 10 min, dwell for 15 min, ramp down to 20°C in 15 min.

Scribe & Dice
Wafer are scribed using a precision scriber (speed=40mm/s, pressure=0.15, depth=0.2mm) and diced manually into single chips.

C.2 Platinum black deposition

Electrochemical deposition of platinum black is obtained by submersion of the working electrode and a platinum counter electrode in a solution composed by 8 mg of lead (II) acetate trihydrate and 1 g of chloroplatinic acid hexahydrate in 30 ml of deionized water. Deposition parameters:

- Working electrode potential = 0 V
- Counter electrode potential = 3.5 V
- Maximum current limit = 2 mA
- Deposition time = 210 sec

Appendix D Statistical analysis

Statistical methods were used in the analysis of experimental data to assess if an observed trend was statistically relevant. In this section, test used, adopted formulas and brief explanations are presented.

D.1 Standard deviation

The standard deviation (SD) of a data set is a measure of its dispersion around the mean. It gives information on data variability. The formula used to compute the SD is:

$$\mathrm{SD} = \sum_{1=1}^{N} \sqrt{\frac{1}{N-1}(x_i - \bar{x})^2} \qquad (6.1)$$

where N is the number of samples, $x_1, \ldots, x_i, \ldots, x_N$ are the observed values and $\bar{x}$ is the mean of the N observed values. When the number of samples is big enough (ideally $N \to \infty$), the SD of the observed values approaches the standard deviation of the population [154].

D.2 Standard error

The standard error of the mean (SE) of a data set is a measure of the confidence on the value of the mean. It gives information on how distant is the sample mean from the population mean. The formula used to compute the SE is:

$$\mathrm{SE} = \frac{1}{\sqrt{N}} \sum_{1=1}^{N} \sqrt{\frac{1}{N-1}(x_i - \bar{x})^2} = \frac{\mathrm{SD}}{\sqrt{N}} \qquad (6.2)$$

When the number of samples is big enough (ideally $N \to \infty$), the sample approaches the population, the mean of the sample approaches the mean of the population and the $\mathrm{SE} \to 0$ [154].

D.3 Student's *t*-test

Student's *t*-test is a method that can be used to find the probability associated with the mean of a sample being equal to a certain value [155]. The formula used to find the *t*-value is:

$$t = \frac{\bar{x} - \mu_0}{\mathrm{SD}/\sqrt{N}} = \frac{\bar{x} - \mu_0}{\mathrm{SE}} \qquad (6.3)$$

where μ_0 is the reference value. The *t*-value follows a *t*-distribution with $N - 1$ degrees of freedom. The cumulative probability p associated with the *t*-distribution is the probability that the sample occurred by chance. The threshold $p < 0.05$ is assumed as the limit for statistical significance if the value $\bar{x}$ can differ from the reference μ_0 only in one direction (one-tailed), whereas the values $p < 0.025$ and $p > 0.975$ are used as thresholds if the mean of the sample can be higher or lower than the reference value (two-tailed) [156].

Paired *t*-test

This test can be used to compare the means of 2 paired groups. The *t*-test becomes:

$$t = \frac{\bar{d}}{\mathrm{SE}} \qquad (6.4)$$

where $\bar{d}$ is the mean of the differences between the paired samples.

Homoscedastic *t*-test

This test can be used to compare the means of 2 groups deriving from populations with equal variance. The *t*-test becomes:

$$t = \frac{\bar{x}_1 - \bar{x}_2}{\mathrm{SD}\sqrt{\frac{1}{N_1} + \frac{1}{N_2}}} \qquad (6.5)$$

where $\bar{x}_1$ and $\bar{x}_2$ are the means of the samples and N_1 and N_2 are the numbers of samples in each group.

References

[1] S. Morgan, P. Grootendorst, J. Lexchin, C. Cunningham and D. Greyson, "The cost of drug development: A systematic review," *Health Policy,* vol. 100, pp. 4-17, 2011.

[2] J. A. DiMasi, R. W. Hansen, H. G. Grabowski and L. Lasagna, "Cost of innovation in the pharmaceutical industry," *Journal of Health Economics,* vol. 10, pp. 107-142, 199.

[3] J. A. DiMasi, R. W. Hansen and H. G. Grabowski, "The price of innovation: new estimates of drug development costs," *Journal of Health Economics,* vol. 22, pp. 151-185, 2003.

[4] S. M. Paul, D. S. Mytelka, C. T. Dunwiddie, C. C. Persinger, B. H. Munos, S. R. Lindborg and A. L. Schacht, "How to improve R&D productivity: the pharmaceutical industry's grand challenge," *Nature Reviews Drug Discovery,* vol. 9, pp. 203-214, 2010.

[5] A. Sertkaya, H.-H. Wong, A. Jessup and T. Beleche , "Key cost drivers of pharmaceutical clinical trials in the United States," *Clinical Trials,* vol. 13, no. 2, pp. 117-126, 2016.

[6] A. P. Li, C. Bode and Y. Sakai, "A novel in vitro system, the integrated discrete multiple organ cell culture (IdMOC) system, for the evaluation of human drug toxicity: comparative cytotoxicity of tamoxifen towards normal human cells from five major organs and MCF-7 adenocarcinoma breast," *Chemico-Biological Interactions,* vol. 150, pp. 129-136, 2004.

[7] S. K. Doke and S. C. Dhawale, "Alternatives to animal testing: A review," *Saudi Pharmaceutical Journal,* vol. 23, pp. 223-229, 2015.

[8] I. W. Mak, N. Eveniew and M. Ghert, "Lost in translation: animal models and clinical trials in cancer treatment," *American Journal of Translational Research,* vol. 6, no. 2, pp. 114-118, 2014.

[9] C. G. Persson, J. S. Erjefalt and F. Sundler, "The mouse trap," *Trends in Pharmacological Sciences,* vol. 18, pp. 465-467, 1997.

[10] J. C. L. Schuh, "Trials, Tribulations, and Trends in Tumor Modeling in Mice," *Toxicologic Pathology,* vol. 32, pp. 53-66, 2004.

[11] A. D. van der Meer and A. van der Berg, "Organs-on-chips: breaking the in vitro impasse," *Integrative Biology,* vol. 4, pp. 461-470, 2012.

[12] J. Edwards, M. Belvisi, S.-E. Dahlen, S. Holgate and A. Holmes, "Human tissue models for a human disease: what are the barriers?," *Thorax,* vol. 0, pp. 1-3, 2015.

[13] S. Wenzel and S. T. Holgate, "The Mouse Trap: It Still Yields Few Answers in Asthma," *American Journal of Respiratory and Critical Care Medicine,* vol. 174, no. 11, pp. 1171-1173, 2006.

[14] P. J. Barnes, S. Bonini, W. Seeger, M. G. Belvisi, B. Ward and A. Holmes, "Barriers to new drug development in respiratory disease," *European Respiratory Journal,* vol. 45, pp. 1197-1207, 2015.

[15] D. Huh, Y. Torisawa, G. A. Hamilton, H. J. Kim and D. E. Ingber, "Microengineered physiological biomimicry: Organs-on-Chips," *Lab on a Chip,* vol. 12, pp. 2156-2164, 2012.

[16] E. W. Esch, A. Bahinski and D. Huh, "Organs-on-chips at the frontiers of drug discovery," *Nature Reviews Drug Discovery,* vol. 14, no. 4, pp. 248-260, 2015.

[17] C. Y. Chan, P.-H. Huang, F. Guo, X. Ding, V. Kapur, J. D. Mai, P. K. Yuen and T. J. Huang, "Accelerating drug discovery via organs-on-chips," *Lab on a Chip,* vol. 13, no. 24, pp. 4697-4710, 2013.

[18] H. Jastrow, "A tour of the cell," The Open University, 2016. [Online]. Available: http://www.open.edu/openlearn/ocw/mod/oucontent/view.php?id=13785&printable=1. [Accessed 8 8 2017].

[19] T. J. Yeatman, "A renaissance for SRC," *Nature Reviews Cancer,* vol. 4, pp. 470-480, 2004.

[20] K. J. Green and J. C. Jones, “Desmosomes and hemidesmosomes: structure and function of molecular components.,” *Official publication of the Federation of American Society for Experimental Biology,* vol. 10, no. 8, pp. 871-881, 1996.

[21] J. Diamond, “The Epithelial Junction: Bridge, Gate, and Fence,” *The Physiologist,* vol. 20, no. 1, pp. 10-18, 1977.

[22] M. Koval, “Tight Junctions in Lung Barrier Function,” [Online]. Available: http://kovallab.org/ic.html. [Accessed 22 07 2017].

[23] J. M. Anderson and C. M. Van Itallie, “Physiology and Function of the Tight Junction,” *Cold Spring Harbor Perspectives in Biology,* vol. 1, no. 2, pp. 1-16, 2009.

[24] M. Furuse, “Molecular Basis of the Core Structure of Tight Junctions,” *Cold Spring Harbor Perspectives in Biology,* vol. 2, no. 1, pp. 1-14, 2010.

[25] D. W. Powell, “Barrier function of epithelia,” *American Journal of physiology,* vol. 241, pp. 275-288, 1981.

[26] A. M. Marchiando, W. V. Graham and J. R. Turner, “Epithelial Barriers in Homeostasis and Disease,” *Annual Review of Pathology Mechanisms of Disease,* vol. 5, pp. 119-144, 2010.

[27] S. T. Holgate, “Epithelium dysfunction in asthma,” *Journal of Allergy and Clinical Immunology,* vol. 120, no. 6, pp. 1233-1244, 2007.

[28] C. Xiao, S. M. Puddicombe, S. Field, J. Haywood, V. Broughton-Head, I. Puxeddu, H. M. Haitchi, E. Vernon-Wilson, D. Samut, N. Bedke, C. Cremin, J. Sones, R. Djukanovic, P. H. Howarth, J. E. Collins, S. T. Holgate, P. Monk and D. E. Davies, “Defective epithelial barrier function in asthma.,” *The Journal of allergy and clinical immunology,* vol. 128, no. 3, pp. 546-556, 2011.

[29] E. J. Swindle and D. E. Davies, “Artificial airways for the study of respiratory disease,” *Expert Review of Respiratory Medicine,* vol. 5, no. 6, pp. 757-765, 2011.

[30] C. Blume and D. E. Davies, “In vitro and ex vivo models of human asthma,” *European Journal of Pharmaceutics and Biopharmaceutics,* vol. 84, pp. 394-400, 2013.

[31] Corning, “Transwell® Permeable Supports Selection and Use Guide,” [Online]. Available: http://csmedia2.corning.com/LifeSciences/Media/pdf/transwell_guide.pdf. [Accessed 24 03 2017].

[32] C. Moon, K. L. VanDussen, H. Miyoshi and T. S. Stappenbeck, “Development of a primary mouse intestinal epithelial cell monolayer culture system to evaluate factors that modulate IgA transcytosis,” *Mucosal Immunology,* vol. 7, no. 4, pp. 818-828, 2014.

[33] A. A. Pezzulo, T. D. Starner, T. E. Scheetz, G. L. Traver, A. E. Tilley, B.-G. Harvey, R. G. Crystal, P. B. McCray, Jr and J. Zabner, “The air-liquid interface and use of primary cell cultures are important to recapitulate the transcriptional profile of in vivo airway epithelia,” *American Journal of Physiology Lung Cellular and Molecular Physiology,* vol. 300, no. 1, pp. 25-31, 2010.

[34] W. P. Instruments, “EVOM2 Epithelial Volt-Ohmmeter Instruction Manual,” [Online]. Available: https://www.wpiinc.com/clientuploads/pdf/EVOM2_IM.pdf. [Accessed 24 03 2017].

[35] B. Jovov, N. K. Wills and S. A. Lewis, “A spectroscopic method for assessing confluence of epithelial cell cultures,” *American Journal of Physiology,* vol. 261, pp. 1196-1203, 1991.

[36] nanoAnalytics, “cellZscope - How it works,” [Online]. Available: http://www.nanoanalytics.com/en/products/cellzscope/how-it-works.html. [Accessed 24 03 2017].

[37] K. Benson, S. Cramer and H.-J. Galla, “Impedance-based cell monitoring: barrier properties and beyond,” *Fluids and Barriers of the CNS,* vol. 10, no. 1, p. 5, 2013.

[38] Applied BioPhysics Inc., “ECIS theory,” [Online]. Available: http://www.biophysics.com/ecis-theory.php. [Accessed 26 03 2017].

[39] D. D. Nalayanda, C. Puleo, W. B. Fulton, L. M. Sharpe, T. H. Wang and F. Abdullah, “An open-access microfluidic model for lung-specific functional studies at an air-liquid interface.,” *Biomedical Microdevices,* vol. 11, no. 5, pp. 1081-1089, 2009.

[40] D. Huh, B. D. Matthews, A. Mammoto, M. Montoya-Zavala, H. Y. Hsin and D. E. Ingber, “Reconstituting organ-level lung functions on a chip.,” *Science,* vol. 328, pp. 1662-1668, 2010.

[41] D. Huh, H. Fujioka, Y. C. Tung, N. Futai, R. Paine, J. B. Grotberg and S. Takayama, “Acoustically detectable cellular-level lung injury induced by fluid mechanical stresses in microfluidic airway systems.,” *Proceedings of the National Academy of Sciences USA,* vol. 104, pp. 18886-18891, 2007.

[42] Z. Xu, Y. Gao, Y. Hao, E. Li, Y. Wang, J. Zhang, W. Wang, Z. Gao and Q. Wang, “Application of a microfluidic chip-based 3D co-culture to test drug sensitivity for individualized treatment of lung cancer.,” *Biomaterials,* vol. 34, no. 16, pp. 4109-4117, 2013.

[43] S. H. Kim, S. M. Hwang, J. M. Lee, J. H. Kang, I. Y. Chung and B. G. Chung, “Epithelial-to-mesenchymal transition of human lung alveolar epithelial cells in a microfluidic gradient device.,” *Electrophoresis,* vol. 34, no. 3, pp. 441-447, 2013.

[44] C. G. Sip, N. Bhattacharjee and A. Folch, “Microfluidic transwell inserts for generation of tissue culture-friendly gradients in well plates.,” *Lab on a Chip,* vol. 14, no. 2, pp. 302-314, 2014.

[45] G. Karsenty and R.-W. Park, “Regulation of Type I Collagen Genes Expression,” *International Reviews of Immunology,* vol. 12, no. 2, pp. 177-185, 1995.

[46] W. Zhang, Y. Gu, Y. Hao, Q. Sun, K. Konior, H. Wang, J. Zilberberg and W. Y. Lee, “Well plate-based perfusion culture device for tissue and tumor microenvironment replication.,” *Lab on a Chip,* vol. 15, no. 13, pp. 2854-2863, 2015.

[47] X. Wu, J. R. Peters-Hall, S. Bose, M. T. Peña and M. C. Rose, “Human bronchial epithelial cells differentiate to 3D glandular acini on basement membrane matrix.,” *American Journal of Respiratory Cellular Molecular Biology,* vol. 44, no. 6, pp. 914-921, 2011.

[48] E. T. Osei, C.-A. Brandsma, J. A. Noordhoek, W. Timens, D. Postma and I. Heijink, “Crosstalk between epithelium and fibroblasts; implications for COPD,” *European Respiratory Journal,* vol. 44, no. 58, 2014.

[49] B. Sacramento, F. Andrade, S. B. da Silva, F. Rodrigues, J. das Neves and D. Ferreira, “Cell-based in vitro models for predicting drug permeability.,” *Expert Opinion on Drug Metabolism & Toxicology,* vol. 8, no. 5, pp. 607-621, 2012.

[50] C. Mobley and G. Hochhaus, “Methods used to assess pulmonary deposition and absorption of drugs.,” *Drug Discovery Today,* vol. 6, no. 7, pp. 367-375, 2001.

[51] B. Forbes, A. Shah, G. P. Martin and A. B. Lansley, “The human bronchial epithelial cell line 16HBE14o- as a model system of the airways for studying drug transport.,” *International Journal of Pharmaceutics,* vol. 257, pp. 161-167, 2003.

[52] K. J. Jang, A. P. Mehr, G. A. Hamilton, L. A. McPartlin, K. Y. Suh and D. E. Ingber, “Human kidney proximal tubule-on-a-chip for drug transport and nephrotoxicity assessment.,” *Integrative Biology,* vol. 5, no. 9, pp. 1119-1129, 2013.

[53] W. J. Polacheck, R. Li, S. G. M. Uzel and R. D. Kamm, “Microfluidic platforms for mechanobiology,” *Lab on a Chip,* vol. 13, no. 2, pp. 2252-2267, 2013.

[54] E. K. Chu, J. S. Foley, A. S. Patel, J. M. Drazen and D. J. Tschumperlin, “Bronchial Epithelial Compression Regulates Epidermal Growth Factor Receptor Family Ligand Expression in an Autocrine Manner,” *American Journal of Respiratory Cell and Molecular Biology,* vol. 32, pp. 373-380, 2005.

[55] B. Ressler, R. T. Leet, S. H. Randell, J. M. Drazen and R. D. Kamm, “Molecular responses of rat tracheal epithelial cells to transmembrane pressure,” *American Journal of Physiology, Lung Cellular and Molecular Physiology,* vol. 278, pp. 1264-1272, 2000.

[56] T. J. Carlson and M. B. Fisher, “Recent advances in high throughput screening for ADME properties,” *Combinatorial Chemistry & High Throughput Screening,* vol. 11, pp. 258-264, 2008.

[57] J. H. Sung and M. L. Shuler, “A micro cell culture analog (mCCA) with 3-D hydrogel culture of multiple cell lines to assess metabolism-dependent cytotoxicity of anti-cancer drugs,” *Lab on a Chip,* vol. 9, pp. 1385-1394, 2008.

[58] Y. Imura, K. Sato and E. Yoshimura, “Micro Total Bioassay System for Ingested Substances: Assessment of Intestinal Absorption, Hepatic Metabolism, and Bioactivity,” *Analitical Chemistry,* vol. 82, pp. 9983-9988, 2010.

[59] M. B. Esch, T. L. King and M. L. Shuler, “The Role of Body-on-a-Chip Devices in Drug and Toxicity Studies,” *Annual Reviews Biomedical Engineering,* vol. 13, pp. 55-72, 2011.

[60] S. F. Hediger, A. Sayah, W. Hunziker and M. A. M. Gijs, “Biosystem for the culture and characterisation of epithelial cell tissues,” *Sensors and Actuators B,* vol. 63, pp. 63-73, 2000.

[61] S. Hediger, A. Sayah, J. D. Horisberger and M. A. M. Gijs, “Modular microsystem for epithelial cell culture and electrical characterisation,” *Biosensors & Bioelectronics,* vol. 16, pp. 689-694, 2001.

[62] R. Booth and H. Kim, “Characterization of a microfluidic in vitro model of the blood-brain barrier (mBBB),” *Lab on Chip,* vol. 12, pp. 1784-1792, 2012.

[63] M. Odijk, A. D. van der Meer, D. Levner, H. L. Kim, M. W. van der Helm, L. I. Segerink, J. P. Frimat, G. A. Hamilton, D. E. Ingber and A. van den Berg, “Measuring direct current trans-epithelial electrical resistance in organ-on-a-chip microsystems.,” *Lab on a Chip,* vol. 15, no. 3, pp. 745-752, 2015.

[64] O. Y. F. Henry, R. Villenave, M. J. Cronce, W. D. Leineweber, M. A. Benz and D. E. Ingber, “Organs-on-chips with integrated electrodes for trans-epithelial electrical resistance (TEER) measurements of human epithelial barrier function,” *Lab on a Chip ,* vol. 17, no. 13, pp. 2264-2271, 2017.

[65] B. M. Maoz, A. Herland, O. Y. F. Henry, W. D. Leineweber, M. Yadid, J. Doyle, R. Mannix, V. J. Kujala, E. A. FitzGerald, K. Kit Parker and D. E. Ingber, “Organs-on-Chips with combined multi-electrode array and transepithelial electrical resistance measurement capabilities,” *Lab on a Chip,* vol. 17, pp. 2294-2302, 2017.

[66] T. Sun, E. J. Swindle, J. E. Collins, J. A. Holloway, D. E. Davies and H. Morgan, “On-chip epithelial barrier function assays using electrical impedance spectroscopy,” *Lab on a chip,* vol. 10, pp. 1611-1617, 2010.

[67] N.-T. Nguyen and S. T. Wereley, Fundamentals and Applications of Microfluidics, Artech House Integrated Microsystems Series, 2006.

[68] C. M. Casciola, “Micro-Nano Fluid Dynamics and Micro-Nano Flow Devices,” unpublished, Università degli Studi di Roma 'La Sapienza', 2011.

[69] O. Reynolds, “An Experimental Investigation of the Circumstances Which Determine Whether the Motion of Water Shall Be Direct or Sinuous, and of the Law of Resistance in Parallel Channels,” *Philosophical Transactions of the Royal Society of London,* vol. 174, pp. 935-982, 1883.

[70] Y. A. Cengel and J. M. Cimbala, Fluid Mechanics Fundamentals and Applications, 2013.

[71] M. C. Annesini, Transport Phenomena: fundamentals and application, Rome: Edizioni Ingegneria 2000, 2004.

[72] A. Fick, “On liquid diffusion,” *Philosophical Magazine and Journal of Science,* vol. 10, pp. 31-39, 1855.

[73] A. Einstein, “Über die von der molekularkinetischen Theorie der Wärme geforderte Bewegung von in ruhenden Flüssigkeiten suspendierten Teilchen,” *Annalen der Physik,* vol. 322, no. 8, pp. 549-560, 1905.

[74] S. Cerbelli, “Transport by advection and diffusion,” unpublished, Università degli Studi di Roma 'La Sapienza', 2011.

[75] G. Taylor, “The Dispersion of Matter in Turbulent Flow through a Pipe,” *Proceedings of the Royal Society of London A: Mathematical, Physical and Engineering Sciences,* vol. 223, pp. 446-468, 1954.

[76] R. Aris, “On the Dispersion of a Solute in a Fluid Flowing through a Tube,” *Proceedings of the Royal Society of London A: Mathematical, Physical and Engineering Sciences,* vol. 235, pp. 67-77, 1956.

[77] P. Atkins and J. de Paula, Atkin's Physical Chemistry, New York: W. H. Freeman and Company, 2006.

[78] T. S. Light, “Temperature Dependence and Measuement of Resistivity of Pure Water,” *Anal. Chem.,* pp. 56, 1138-1142, 1984.

[79] S. H. Smith, “Temperature Correction in Conductivity Measurements,” *Limnology and Oceanography,* vol. 7, p. 3, 2003.

[80] K. Loza, C. Sengstock, S. Chernousova, M. Köller and M. Epple, “The predominant species of ionic silver in biological media is colloidally dispersed nanoparticulate silver chloride,” *RSC Advances,* vol. 4, pp. 35290-35297, 2014.

[81] P. B. Ishai, M. S. Talary, A. Caduff, E. Levy and Y. Feldman, “Electrode polarization in dielectric measurements: a review,” *Measurement Science and Technology,* vol. 24, no. 10, 2013.

[82] H. Helmholtz, “Ueber einige Gesetze der Vertheilung elektrischer Ströme in körperlichen Leitern mit Anwendung auf die thierisch-elektrischen Versuche,” *Physik und Chemie,* vol. 165, pp. 211-233, 1853.

[83] Z. Stojek, Electroanalytical Methods - The Electrical Double Layer and Its Structure, F. Scholz, 2010.

[84] H. Morgan and N. G. Green, AC Electrokinetics: Colloids and Nanoparticles, Research Studies Press, 2003.

[85] L. A. Geddes, “Historical Evolution of Circuit Models for the Electrode-Electrolyte Interface,” *Annals of Biomedical Engineering,* vol. 25, pp. 1-14, 1997.

[86] E. Warburg, “Ueber das Verhalten sogenannter unpolarisirbarer Elektroden gegen Wechselstrom,” *Annalen der Physik,* vol. 303, no. 3, pp. 493-499, 1899.

[87] H. Fricke, “The theory of electrolytic polarization,” *Philosophical Magazine,* vol. 14, pp. 310-318, 1932.

[88] H. P. Schwan and J. G. Maczuk, “Electrode polarization impedance: limits of linearity.,” in *Proceedings of the 18th*, Philadelphia, PA,, 1965.

[89] M. Stern and A. L. Geary, “Electrochemical Polarization. A theoretical Analysis of the Shape of Polarization Curves,” *Journal of The Electrochemical Society,* vol. 104, no. 1, pp. 56-63, 1957.

[90] H. P. Schwan, “Electrode polarization impedance and measurements in biological materials,” *Annals of the New York Academy of Sciences,* vol. 148, no. 1, pp. 191-209, 1968.

[91] D. Malleo, J. T. Nevill, A. van Ooyen, U. Schnakenberg, L. P. Lee and H. Morgan, “Note: Characterization of electrode materials for dielectric spectroscopy,” *Review of Scientific Instruments,* vol. 81, no. 1, 2010.

[92] B. Hille, “Ionic channels in nerve membranes,” *Progress in Biophysics and Molecular Biology,* vol. 21, no. 1, 1970.

[93] J. E. Hall, “Access Resistance of a Small Circular Pore,” *The Journal of General Physiology,* vol. 66, no. 4, pp. 531-532, 1975.

[94] W. R. Smythe, Static And Dynamic Electricity, Toronto: McGraw-Hill Book COmpany, 1950.

[95] S. R. Chary and R. K. Jain, “Direct measurement of interstitial convection and diffusion of albumin in normal and neoplastic tissues by fluorescence photobleaching,” *Proceedings of the National Academy of Science USA,* vol. 86, no. 14, pp. 5385-5389, 1989.

[96] H. Dafni, T. Israely, Z. M. Bhujwallw, L. E. Benjamin and M. Neeman , “Overexpression of vascular endothelial growth factor 165 drives peritumor interstitial convection and induces lymphatic drain: magnetic resoresonance imaging, confocal microscopy, and histological tracking of triple-labeled albumin,” *Cancer Research,* vol. 62, no. 22, pp. 6731-6739, 2002.

[97] H. Lamb, Hydrodynamics, Cambridge: University Press, 1916.

[98] D. Bernoulli, Hydrodynamica.

[99] R. Defay, I. Prigogine, A. Bellemans and D. H. Everett, Surface Tension and Adsorption, New York: Wiley, 1966.

[100] B. A. Wagner, S. Venkataraman and G. R. Buettner, “The rate of oxygen utilization by cells,” *Free Radical Biology & Medicine,* vol. 51, no. 3, pp. 700-712, 2011.

[101] R. Sander, “Compilation of Henry’s law constants (version 4.0) for water as solvent,” *Atmospheric Chemistry and Physics,* vol. 15, pp. 4399-4981, 2015.

[102] K. P. Burnham and D. R. Anderson, Model selection and multimodel inference: A Practical Information-Theoretic Approach. Second edition, New York: Springer, 2002.

[103] A.-N. Spiess and N. Neumeyer, “An evaluation of R2 as an inadequate measure for nonlinear models in pharmacological and biochemical research: a Monte Carlo approach,” *BMC Pharmacology,* vol. 10, no. 6, 2010.

[104] H. Akaike, “A new look at the statistical model identification,” *IEEE Transactions on Automatic Control,* vol. 19, no. 6, pp. 716-723, 1974.

[105] B. D. Ilic, P. Neuzil, T. Stanczyk, G. Blough and G. J. Macly, “Preparation and characterisation of platinum black electrodes.,” *Journal of Materials Science,* vol. 35, pp. 3447-3457, 2000.

[106] F. Ingels, S. Defereme, E. Destexhe, M. Oth, G. Van der Mooter and P. Augustijns, “Simulated intestinal fluid as transport medium in the Caco-2 cell culture model,” *International Journal of Pharmaceutics,* vol. 232, no. 1, pp. 183-192, 2002.

[107] S. H. Ma, L. A. Lepak, R. J. Hussain, W. Shain and M. L. Shuler, “An endothelial and astrocyte co-culture model of the blood–brain barrier utilizing an ultra-thin, nanofabricated silicon nitride membrane,” *Lab on a Chip,* vol. 5, pp. 74-85, 2004.

[108] W. I. De Boer, J. M. Rebel, M. Vermey, C. Thijssen and T. Van der Kwast, “Multiparameter analysis of primary epithelial cultures grown on cyclopore membranes.,” *The Journal of Histochemistry and Cytochemistry,* vol. 42, no. 2, pp. 277-282, 1994.

[109] R. Cornell, “The use of Nucleopore filters in ultrastructural studies of cell cultures.,” *Experimental Cell Research,* vol. 56, no. 1, pp. 156-158, 1969.

[110] P. Apel, “Track etching technique in membrane technology,” *Radiation Measurements,* vol. 34, pp. 559-566, 2001.

[111] C.-W. Tsao and D. L. DeVoe, “Bonding of thermoplastic polymer microfluidics,” *Microfluidics and Nanofluidics,* vol. 6, pp. 1-16, 2009.

[112] L.-H. Hung, R. Lin and A. P. Lee, “Rapid microfabrication of solvent-resistant biocompatible microfluidic devices,” *Lab on a Chip,* vol. 8, pp. 983-987, 2008.

[113] P. Wägli, B. Y. Guélat, A. Homsy and N. F. de Rooij, “Microfluidic devices made of UV-curable glue (NOA81) for fluorescence detection based applications,” in *14th International Conference on Miniaturized Systems for Chemistry and Life Sciences*, Groningen, 2010.

[114] Z. T. Cygan, J. T. Cabral, K. L. Beers and E. J. Amis, “Microfluidic Platform for the Generation of Organic-Phase Microreactors,” *Langmuir,* vol. 21, pp. 3629-3634, 2005.

[115] C. Lu, L. J. Lee and Y.-J. Juang, “Packaging of microfluidic chips via interstitial bonding technique,” *Electrophoresis,* vol. 29, pp. 1407-1414, 2008.

[116] C. Carlborg, T. Haraldsson, K. Öberg, M. Malkoch and W. van der Wijngaart, “Beyond PDMS: off-stoichiometry thiol-ene (OSTE) based soft lithography for rapid prototyping of microfluidic devices.,” *Lab on a Chip,* vol. 11, no. 18, pp. 3136-47, 2011.

[117] F. Saharil, F. Forsberg, Y. Liu, P. Bettotti, N. Kumar, F. Niklaus, T. Haraldsson, W. van der Wijngaart and K. B. Gylfason, “Dry adhesive bonding of nanoporous inorganic membranes to microfluidic devices using the OSTE(+) dual-cure polymer,” *Journal of Micromechanics and Microengineering,* vol. 23, no. 2, 2013.

[118] N. Y. Lee and B. H. Chung, “Novel poly(dimethylsiloxane) bonding strategy via room temperature "chemical gluing".,” *Langmuir,* vol. 25, no. 6, pp. 3861-6, 2009.

[119] L. Tang and N. Y. Lee, “A facile route for irreversible bonding of plastic-PDMS hybrid microdevices at room temperature,” *Lab on Chip,* vol. 10, pp. 1274-80, 2009.

[120] Y. Sun and N. T. Nguyen, “Low-pressure, high-temperature thermal bonding of polymeric microfluidic devices and their applications for electrophoretic applications,” *Journal of Micromechanics and Microengineering,* vol. 16, no. 8, pp. 1681-1688, 2006.

[121] C. H. Ahn, J. W. Choi, G. Beaucage, J. H. Nevin, J. B. Lee, A. Puntambekar and J. Y. Lee, “Disposable Smart lab on a chip for point-of-care clinical diagnostics,” *Proceedings IEEE,* vol. 92, no. 1, pp. 154-173, 2004.

[122] R. Truckenmuller, R. Ahrens, Y. Cheng, G. Fischer and V. Saile, “An ultrasonic welding based process for building up a new class of inert fluidic microsensors and actuators from polymers,” *Sensors and Actuators A Physicals,* vol. 132, no. 1, pp. 385-392, 2006.

[123] R. Truckenmuller, P. Henzi, D. Herrmann, V. Saile and W. K. Schomburg, “Bonding of polymer microstructures by UV irradiation and subsequent welding at low temperatures.,” *Microsystem Technologies,* vol. 10, no. 5, pp. 372-374, 2004.

[124] Y. Wang, D. Lee, L. Zhang, H. Jeon, J. E. Mendoza-Elias, T. A. Harvat, S. Z. Hassan, A. Zhou, D. T. Eddington and J. Oberholzer, “Systematic Prevention of Buble Formation and Accumulation for Long-Term Culture of Pancreatic Islet Cells in Microfluidic Device,” *Biomedical Microdevices,* vol. 14, no. 2, pp. 419-426, 2012.

[125] C. Blume, R. Reale, M. Held, T. M. Millar, J. E. Collins, D. E. Davies, H. Morgan and E. J. Swindle, “Temporal Monitoring of Differentiated Human Airway Epithelial Cells Using Microfluidics,” *PLoS ONE,* vol. 10, no. 10, 2015.

[126] C. Blume, R. Reale, M. Held, M. Loxham, T. M. Millar, J. E. Collins, E. J. Swindle, H. Morgan and D. E. Davies, “Cellular crosstalk between airway epithelial and endothelial cells regulates barrier functions during exposure to double-stranded RNA.,” *Immunity, Inflammation and Disease,* 2017.

[127] Q. Li, J. Pei, P. Song and R. T. Kennedy, “Fraction Collection from Capillary Liquid Chromatography and Off-line Electrospray Ionization Mass Spectrometry Using Oil Segmented Flow,” *Analytical Chemistry,* vol. 82, pp. 5260-5267, 2010.

[128] “Technical Specification Alpha-A Mainframe,” Novocontrol Technologies, 2010. [Online]. Available: http://www.novocontrol.de/pdf_s/alph_a_spec.pdf. [Accessed 10 02 2017].

[129] “ADG726 Data Sheet,” Analog Devices, [Online]. Available: http://www.analog.com/media/en/technical-documentation/data-sheets/ADG726_732.pdf. [Accessed 13 02 2017].

[130] A. L. Cozens, M. J. Yezzi, K. Kunzelmann, T. Ohrui, L. Chin, K. Eng, W. E. Finkbeiner, J. H. Widdicombe and D. C. Gruenert, “CFTR expression and chloride secretion in polarized immortal human bronchial epithelial cells.,” *American Journal of Respiratory Cell and Molecular Biology,* vol. 10, pp. 38-47, 1994.

[131] B. Forbes, “HUman airway epithelial cell lines for in vitro drug transport and metabolism studies,” *Pharmaceutical Science & Technology Today,* vol. 3, no. 1, 2000.

[132] B. Forbes and A. B. Lansley , “Transport characteristics of formoterol and salbutamol across a bronchial epithelial drug absorption model.,” *European Journal of Pharmaceutical Sciences,* vol. 6, 1998.

[133] M. Stern, N. J. Caplen, J. E. Browning, U. Griesenbach, F. Sorgi, L. Huang, D. C. Gruenert, C. Marriot, R. G. Crystal, D. M. Geddes and E. W. Alton, “The effect of mucolytic agents on gnene transfer across CF sputum barrier in vitro,” *Gene Therapy,* vol. 5, pp. 91-98, 1998.

[134] J. Wine, W. E. Finkbeiner, C. Haws, M. F. Krouse, S. Moon, J. H. Widdicombe and Y. Xia, “CFTR and other Cl- channels in human airway cells.,” *The Japanes Journal of Physiology,* vol. 44, pp. 199-205, 1994.

[135] L. Gonzalez-Mariscal, R. G. Contreras, J. J. Bolivar, A. Ponce, B. Chàvez De Ramirez and M. Cereijido, “Role of calcium in tight junction formation between epithelial cells,” *American Journal of Physiology,* vol. 259, pp. 978-986, 1990.

[136] M. Bleich, Q. Shan and N. Himmerkus, “Calcium regulation of tigh junction permeability,” *Annals of the New York Academy of Sciences,* vol. 1258, pp. 93-99, 2012.

[137] B. Rothen-Rutishauser, F. K. Riesen, A. Braun, M. Günthert and H. Wunderli-Allenspach, “Dynamics of Tight and Adherens Junctions Under EGTA Treatment,” *Journal of Membrane Biology,* vol. 188, pp. 151-162, 2002.

[138] M.-E. Fortier, S. Kent, H. Ashdown, S. Poole, P. Boksa and G. N. Luheshi, “The viral mimic, polyinosinic:polycytidylic acid, induces fever in rats via an interleukin-1-dependent mechanism,” *American Journal of Physiology - Regulatory, Integrative and Comparative Physiology,* vol. 287, pp. 759-766, 2004.

[139] F. Rezaee, N. Meednu, J. A. Emo, B. Saatian, T. J. Chapman, N. G. Naydenov, A. De Benedetto, L. A. Beck, A. I. Ivanov and S. N. Georas, “Polyinosinic:polycytidylicacid induces protein kinase D-dependendt disassembly of apical junctions and barrier dysfunction in airway epithelial cells,” *Journal of Allergyand Clinical Immunilogy,* vol. 128, no. 6, pp. 1216-1224, 2011.

[140] M. Schuettler, T. Doerge, S. L. Wien, S. Becker, A. Staiger, M. Hanauer, S. Kammer and T. Stieglitz, “Cytotoxicity of Platinum Black,” in *10th Annual Conference of the International FES Society*, 2005.

[141] W. Franks, “Impedance characterization and modeling of electrodes for biomedical applications.,” *IEEE Transactions on Biomedical Engineering,* vol. 52, no. 7, pp. 1295-1302, 2005.

[142] H. Morgan, T. Sun, D. Holmes, S. Gawad and N. G. Green, “Single cell dielectric spectroscopy,” *Journal of Physics D: Applied Physics,* vol. 40, pp. 61-70, 2007.

[143] H. Fricke, “The electric capacity of suspensions of red corpuscles of a dog.,” *Physical Review,* vol. 26, no. 5, pp. 682-687, 1925.

[144] T. Schmid, D. Günzel and M. Bogdan, “Automated Quantification of the Capacitance of Epithelial Cell Layers from an Impedance Spectrum,” in *Biotechno 2015 : The Seventh International Conference on Bioinformatics, Biocomputational Systems and Biotechnologies*, 2015.

[145] G. F. Tellez, B. W. M. Willemse, U. Brouwer, S. Nijboer-Brinksma, K. Vandepoele, J. A. Noordhoek, I. Heijink, M. de Vries, N. P. Smithers, D. S. Postma, W. Timens, L. Wiffen, F. van Roy, J. W. Holloway, P. M. Lackie, M. C. Nawijn and G. H. Koppelman, “Protocadherin-1 Localization and Cell-Adhesion Function in Airway Epithelial Cells in Asthma,” *PLOS ONE,* vol. 11, no. 10, pp. 1-21, 2016.

[146] C. B. Coyne, M. M. Kelly, R. C. Boucher and L. G. Johnson, “Enhanced Epithelial Gene Transfer by Modulation of Tight Junctions with Sodium Caprate,” *American Journal of Respiratory Cell and Molecular Biology,* vol. 23, no. 5, pp. 602-609, 2000.

[147] M. A. Hardyman, E. Wilkinson, E. Martin, N. Jayasekera, C. Blume, E. J. Swindle, N. Gozzard and S. T. Holgate, “TNF-α–mediated bronchial barrier disruption and regulation by src-

family kinase activation," *Journal of Allergy and Clinical Immunology,* vol. 132, no. 3, pp. 665-675, 2013.

[148] P. D. Vermeer, L. Panko, M. J. Welsh and J. Zabner, "ERBB1 Functions as a Sensor of Airway Epithelial Integrity by Regulation of Protein Phosphatase 2A Activity," *The Journal of Biological Chemistry,* vol. 281, pp. 1725-1730, 2006.

[149] I. H. Heijink, M. R. Jonker, M. de Vries, A. J. M. van Oosterhout, E. Telenga, N. H. T. ten Hacken, D. S. Postma and M. van den Berge, "Budesonide and fluticasone propionate differentially affect the airway epithelial barrier," *Respiratory Research,* vol. 17, no. 2, pp. 1-13, 2016.

[150] "C60-Technical Specification," Cypher Instruments, [Online]. Available: http://www.cypherinstruments.co.uk/c60-technical.asp. [Accessed 10 02 2017].

[151] E. Barsoukov and J. R. Macdonald, Impedance Spectroscopy Theory, Experiment and Applications (Second Edition), John Wiley & Sons, Inc., Publication, 2005 .

[152] J. C. Lagarias, J. A. Reeds, M. H. Wright and P. E. Wright, "Convergence properties of th Nelder-Mead simplex method in low dimensions," *SIAM Journal of Optimization,* vol. 9, no. 1, pp. 112-147, 1998.

[153] J. A. Nelder and R. Mead, "A simplex method for function minimaztion," *Computer Journal,* vol. 7, pp. 308-313, 1965.

[154] D. Bowers, Medical Statistics from Scratch - Second Edition, John Wiley & Sons Ltd, 2008.

[155] Student, "The Probable Error of a Mean," *Biometrika,* vol. 6, no. 1, pp. 1-25, 1908.

[156] J. A. Rice, Mathematical Statistics and Data Analysis - Third Edition, Thomson Brooks/Cole, 2007.